THESE DE DOCTORAT DE L'UNIVERSITE DE STRASBOURG

Discipline:

Astronomie et Astrophysique

Présentée par:

Audrey Galametz

Pour obtenir le grade de
Docteur en sciences de l'Université de Strasbourg

The Environments of AGN out to z=2

Soutenue publiquement le 26 Mars 2010

Membres du jury:

Directeur de thèse: Dr. Mark Allen (Observatoire de Strasbourg, France)
Rapporteur interne: Dr. Bernd Vollmer (Observatoire de Strasbourg, France)
Rapporteur externe: Dr. Philip Best (Institute for Astronomy, Edinburgh, UK)
Rapporteur externe: Dr. Simona Mei (Observatoire de Paris, France)
Examinateur: Dr. Adriano Fontana (Osservatorio Astronomico di Roma, Italy)
Examinateur (et encadrant de thèse): Dr. Carlos De Breuck (ESO, Garching, Allemagne)

Membres invités:

Encadrant de thèse: Dr. Joël Vernet (ESO, Garching, Allemagne)
Encadrant de thèse: Dr. Daniel Stern (JPL, Pasadena, CA, USA)

'Of course, they say every atom in our bodies was once part of a star. Maybe I'm not leaving... maybe I'm going home.'
Gattaca -

Acknowledgements/Remerciements

I am very grateful to the three organizations that host me during this PhD. Thanks to the staff of the Observatory of Strasbourg, my home university. I would like to express my gratitude to the Jet Propulsion Laboratory in Pasadena and its staff (in particular Charles Lawrence) for welcoming me a year. It was one of the most enriching experience in my life, both scientifically and humanly. Thanks at last to the European Southern Observatory in Garching and its members, in particular Bruno Leibundgut and Robert Fosbury. I feel really honored to have been a member of the big ESO family both for my master thesis project and for my PhD.

I would never be able to express with a few words the gratitude and admiration I feel for you, my four PhD advisors: Mark Allen, Carlos De Breuck, Joël Vernet and Daniel Stern. It has been a pleasure to work with you during these years and benefit for your expertise on science and life. Thanks to Mark for welcoming me in these last months of my PhD at the Observatory of Strasbourg so that I could take advantage of this additional time to write this thesis and papers therein serenely. Thank you, Dan for welcoming me at the JPL for a year and for always having been present during the rest of my thesis despite the 9 hours delay. I liked very much the year I spent in California and a big part of it was thanks to you. A special thanks for your tremendous help when I was writing my papers; they just became Shakespearian works after your English expertise. Thanks to your wonderful family too, your wife Cynthia and your two adorable Asher and Eden. A vous deux maintenant, Carlos et Joël. Vous avez assisté à mes tous débuts en science quand je suis arrivée en stage de master à l'ESO. Je mesure la chance d'avoir été votre étudiante. Vous avez été à l'écoute et je souhaite que beaucoup d'autres étudiants/es aient cette merveilleuse opportunité de vous avoir comme directeurs de thèse. Merci également à vos épouses Myha et Elise ainsi qu' à vos adorables petits bouts de chou, Fenno, Emmi, Laora et au petit dernier qui va bientôt s'ajouter à la famille SHzRG.

Four years have passed since I first stepped a foot in Munich and became this fantastic adventure. And I would like to thank people I met along the way. Thanks to my collaborators Adam Stanford, Peter Eisenhardt, Lexi Moustakas, Mark Brodwin, Alessandro Rettura, Tadayuki Kodama, Alain Omont, Chiara Marmo, Bram Venemans, Jaron Kurk, Nina Hatch, George Miley, Roderik Overzier, Andrew Zirm and a special thanks to Nick Seymour (and his wife, Fran). It has been an honor to work with all of you and benefit from your experience and advice. Thanks to the young generation of scientists, students and fellows I met at the JPL, at ESO, at the Observatory or in conferences, in particular Jouni, Jarek, Yuri, Sune, Gerrit, Suzanna, Francesco, Stefano, Giovanni, Silvia, Tina, Amanda, Jack and Veronica. I wish you all the best for your life and career. A particular thought to my ESO officemate, Heidi. We shared much more than just our passion for books. Last (but not least), I would like to thank my friends, Timo, Yara, Gina and Claudio. I am just very lucky to have you in my life.

Merci enfin à ma famille, mes parents et bien sûr, à ma soeur, ma jumelle, Maud.

Abstract

This thesis aims to identify and characterise the most distant galaxy clusters by targeting red sequence galaxies and active galactic nuclei in the wide area environment of distant radio galaxies. This study complements both the lower redshift cluster searches which have identified clusters out to $z = 1.45$ using optical and X-ray selections and the work on protoclusters around $z > 2$ radio galaxies using the Lyα emitters and Lyman break techniques. The new aspects of the work presented in this thesis are: *(i)* the study of the missing link between clusters and protoclusters known to date by the investigation of the less studied redshift range $1.4 < z < 2$ *(ii)* the selection of the more massive components of galaxy clusters i.e., the red passively evolving galaxy population using pertinent optical/near-infrared colour cuts *(iii)* the use of wide field observations to study possible large scale galaxy structures associated with high redshift galaxy clusters *(iv)* the study of the diversity of radio galaxy environment with the analysis of several radio galaxy fields *(v)* the more specific study of the population of active galactic nuclei in galaxy clusters and its evolution with cosmic time. Such studies are now possible thanks to the advent of new wide field near-infrared cameras such as CFHT/WIRCam or VLT/HAWK-I which permit to extend to higher redshift and larger scale the study of galaxy clusters.

We studied the fields around five radio galaxies at $1.4 < z \lesssim 2$. Using a combination of stellar evolution modeling and published spectroscopy, we designed appropriate optical + near-infrared colour selection criteria adapted from popular selection techniques (e.g. the *BzK* selection for galaxies at $z > 1.4$) to select both red passively evolved and blue star-forming galaxy cluster candidates. The spatial distribution of the red galaxies is clearly non homogeneous and often present a filamentary structure containing the radio galaxies. We found that two of our studied fields, 7C 1756+6520 at $z = 1.42$ and MRC 0156-252 at $z = 2.02$, show overdensities of a factor of $2 - 4$ in red sources compared to control fields. The first field shows a high concentration of red galaxies around the radio galaxy and several other aligned clumps forming a large scale filamentary structure of several Mpc. The second field demonstrates a more compact system of both blue and red galaxies concentrated within 1 Mpc of the radio galaxy. A spectroscopy campaign confirmed that our suspected structure around 7C 1756-6520 is indeed a galaxy cluster with 20 galaxies found with redshifts consistent with the radio galaxy. We therefore conclude that although not all radio galaxies are found in overdense regions —at least as far as the red population is concerned — they are however a very efficient tool to search for high redshift galaxy clusters with the discovery in this thesis of the second most distant galaxy cluster to date at = 1.42 and a galaxy cluster candidate at $z \sim 2$.

Résumé

Cette thèse est consacrée à l'identification et l'étude des amas de galaxies à grand redshift. Nous concentrons notre analyse sur l'environnement à grand échelle de radiogalaxies lumineuses et à l'étude des galaxies de la séquence rouge et des noyaux actifs de galaxies détectés dans leur voisinage. Le travail présenté dans ce manuscrit étend d'une part les études des amas de galaxies à $z < 1.5$ sélectionnés dans le visible et les rayons X et d'autre part celles des proto-amas détectés dans le voisinage des radiogalaxies à $z > 2$ grâce aux surdensités d'émetteurs Lyα ou de galaxies à discontinuité de Lyman. Cette thèse a permis d'explorer sous de nouveaux angles, la recherche des amas à grand redshift: *(i)* l'étude du chaînon manquant entre $z = 1.4$ et $z = 2$ i.e., entre les proto-amas et amas connus à ce jour *(ii)* la sélection des galaxies les plus massives, membres d'un amas (i.e. les galaxies rouges de type primitif) grâce à des critères de couleur adaptés *(iii)* l'utilisation d'observations grand champ nécessaires à l'étude sur une plus large échelle de structures de galaxies associées aux radiogalaxies *(iv)* l'étude de la diversité des environnements de radiogalaxies grâce à l'analyse de plusieurs champs *(v)* l'étude plus spécifique de la population des noyaux actifs de galaxies dans les amas de galaxies et de son évolution en fonction du redshift. De telles études ont été rendues possible grâce à la mise en place de nouveaux instruments comme WIRCam au CFHT et HAWK-I au VLT qui permettent d'étendre l'étude des amas de galaxies à plus grand redshift et sur une plus large échelle.

Nous avons étudié les champs de cinq radiogalaxies à $1.4 < z \lesssim 2$. Nous avons associé des modèles d'évolution stellaire à des échantillons de galaxies ayant un redshift spectroscopique dans la littérature et développé des critères de sélection dans le visible et l'infrarouge proche adaptés de techniques de sélection classiques (e.g. la sélection BzK pour les galaxies à $z > 1.4$). Ces critères nous ont permis de sélectionner à la fois les galaxies rouges de type primitif et les galaxies plus bleues formant des étoiles. La distribution spatiale des galaxies rouges n'est pas homogène et présente souvent une structure filamentaire qui contient la radiogalaxie. Deux champs, 7C 1756+6520 ($z = 1.42$) et MRC 0156-252 ($z = 2.02$) sont surdenses en galaxies rouges, d'un factor $2-4$ comparé à des champs de référence. Le premier champ présente une grande concentration de galaxies rouges autour de la radiogalaxie ainsi que plusieurs autres groupes alignés formant une structure filamentaire étendue sur plusieurs Mpc. Le deuxième champ présente un système plus compact de galaxies rouges et bleues concentrées à moins de 1 Mpc de la radiogalaxie. Une campagnie de spectroscopie a permis de confirmer que notre structure associée à 7C 1756+6520 est en effet un amas de galaxies. 20 galaxies ont été trouvées à un redshift consistent avec celui de la radiogalaxie. Nous avons ainsi montré que, bien que toutes les radiogalaxies ne se situent pas dans des champs surdenses — au moins en ce qui concerne les galaxies rouges — elles ont été toutefois un outil efficace pour la recherche d'amas de galaxies à grand redshift avec la découverte du deuxième amas le plus distant à ce jour à $z = 1.42$ et la mise en évidence d'un possible amas de galaxies à $z \sim 2$.

Contents

List of Figures

List of Tables

Chapter 1

Introduction

1.1 Environment of distant radio galaxies

1.1.1 Clusters of galaxies

Clusters of galaxies are the most massive and extended gravitationally bound systems in the universe with typical masses of 10^{14-15} $M_{\odot}$ and contain hundreds of galaxies over regions of several Mpc. According to the current hierarchical models e.g., the Cold Dark Matter ('ΛCDM') model, the smallest and primordial components such as stars appear through the gravitational merging of gas in large CDM halos (White & Rees 1978). As these halos collapse, matter gets distributed along filaments composed of a mixture of gas, young galaxies and other stellar systems. The galaxy clusters are found in the regions of highest galaxy density, at the intersection of these filaments.

Clusters contain a large number of galaxies at the same cosmic time making them a unique laboratory to study the formation and evolution of galaxies. In particular, studies of clusters show that their galaxy populations strongly differ at high and low redshift. It has been proven that clusters in the local universe have a core dominated by massive red early type galaxies forming a tight (scatter < 1 mag) 'red sequence' in colour magnitude diagrams that appears to have the same slope and scatter in most systems (Bower et al. 1992; Terlevich et al. 2001). For example, the colour-magnitude relation for red galaxies was investigated by Sandage (1972) in the Virgo and the Coma clusters and shown to extend over 8 magnitudes. The relation was found consistent in both systems with a single colour-magnitude relation shifted by the effect of distance. Similar results were also found for low-redshifts clusters (e.g., Barrientos et al. 2004). The Coma cluster is traditionally adopted as an example of low-redshift cluster to compare properties of early-type members of higher redshift galaxy clusters (see Fig. 1.1).

The galaxy distribution within clusters is clearly bi-modal with distinct populations of massive early type galaxies, and late-type star formation dominated galaxies. The massive early type galaxies show redder colours and form the red sequence. The classical picture for the formation of these galaxies proposes a single 'monolithic collapse' (Eggen et al. 1962) with stars being formed in a single burst and then, evolving passively (Sandage et al. 1970) with little or no recent star-formation. The late-type star formation dominated galaxies show a more spread out distribution forming the 'blue cloud' (Hogg et al. 2002; Bell et al. 2004). At higher redshifts ($0.1 < z < 0.5$), Butcher & Oemler (1984) showed that clusters contain much more blue late type galaxies, their fraction increasing as a function of redshift, the 'Butcher-Oemler' effect. The origin of this segregation is still an open question. The current hierarchical formation scenario suggests that elliptical galaxies can be built from the merger of massive disc galaxies (Farouki & Shapiro 1982), such a formation process being also expected in cosmologies dominated by cold dark matter. In recent

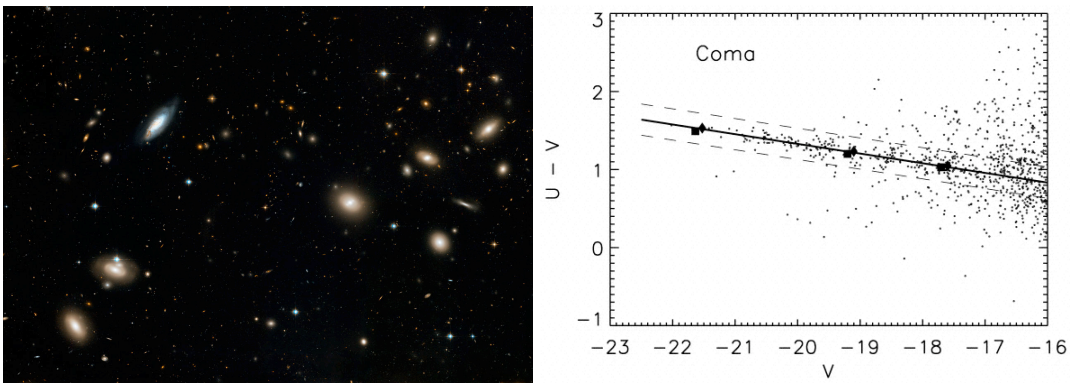

Figure 1.1. The Coma cluster. *Left:* From the Space Telescope website. *Hubble*/ACS view of the Coma cluster. *Right:* From De Lucia et al. 2004. Colour-magnitude relation of the Coma cluster for all the galaxies in the catalogue by Terlevich et al. 2001. A red sequence is clearly visible together with a significant population of blue galaxies. The thick solid line represents the best-fit relation of the sequence with a fixed slope of -0.085. The dashed line corresponds to 3σ from the best fit.

years, observational studies have shown that interaction and mergers indeed represent a common phenomenon at high redshift and also found numerous signs of merging in early-type galaxies (Tran et al. 2005) supporting the idea of a 'bottom-up' sense as massive galaxies formed later by mergers. But despite these numerous evidences, it is still challenging to quantify the importance of mergers in the formation and evolution of early-type galaxies. Numerous observational studies have been suggesting a rather different formation scenario with star formation evolving in a 'top-down' sense i.e., the more massive galaxies having been more star-forming in the past and the bulk of star formation having migrated towards less massive galaxies. This 'downsizing' scenario appears to be supported in galaxy clusters by the ages of red sequence galaxies as a function of mass with a deficit of faint red galaxies in clusters at high redshift ($z \sim 0.8$) relative to local ones (Tanaka et al. 2005; De Lucia et al. 2004, 2006; Gilbank et al. 2008). Tanaka et al. (2007) thus studied the colour magnitude relation of red galaxies in several clumps associated with a cluster at $z = 1.24$ and found that few faint red galaxies are populating the red sequence of these less dense sub-structures. They suggest an 'environment-dependent-downsizing' evolution with the massive galaxies in high density environments stopping their star-formation earlier that less massive ones in less dense regions. Other studies have brought additional support for an anti-hierarchical scenario. For example, Poggianti et al. (2009) recently looked at the evolution of the fraction of spirals and S0 population with cosmic time. They found that spirals are proportionally more common and S0 galaxies rarer in high redshift galaxy clusters compared to nearby ones suggesting that many of the high redshift blue star-forming galaxies in clusters had evolved in time into the S0 galaxies we observe in the local galaxy cluster cores (see also Postman et al. 2005). The contribution of mergers versus passive evolution to explain the present day number of early-type galaxies is still under intense study on both the theoretical and observational sides.

Red elliptical galaxies are still dominating the cluster cores up to very high redshift ($z \sim 1.5$; Stanford, Eisenhardt, & Dickinson 1998; Lidman et al. 2004, 2008; Mei et al. 2009) forming a tight red sequence of massive early type galaxies, comparable in scatter and slope to that observed in the red sequence of the local universe clusters (e.g. the Coma cluster). Fig. 1.2 shows examples from the literature of colour-magnitude diagrams of several high redshift galaxy clusters. All of them present a clear red sequence of elliptical galaxies. The red sequence has a slope such as

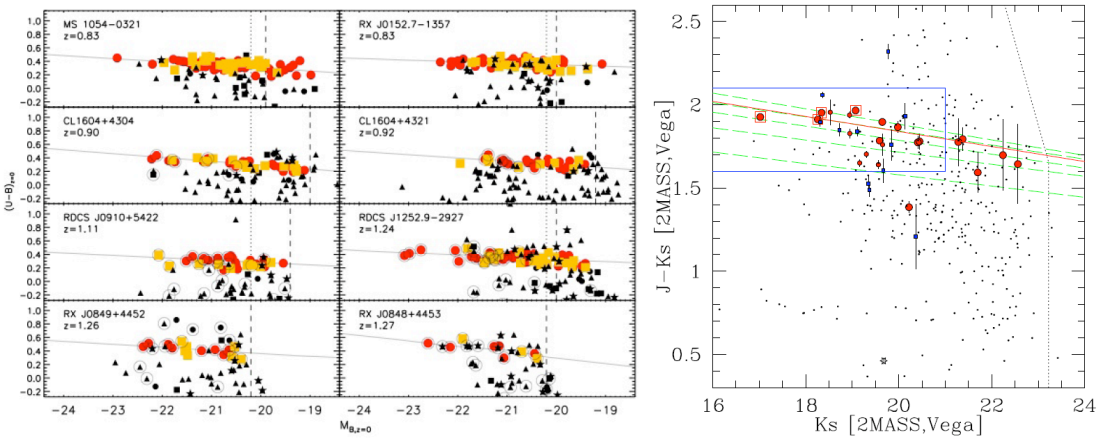

Figure 1.2. Example of colour-magnitude diagrams for high redshift galaxy clusters and their red sequence. *Left:* From Mei et al. 2009. Colour-magnitude in the restframe $(U-B)_{z=0}$ vs absolute restframe magnitude $M_{B,z=0}$ for the eight clusters of the ACS Intermediate Cluster Survey (z = 0.83 to 1.27). Galaxies are indicated by red circles for ellipticals and yellow squares for S0s. Black stars and triangles account for S0/a and spirals respectively. *Right:* From Lidman et al. 2008. Colour-magnitude diagram of XMMU J2235.3-2557 (z = 1.39). Galaxies within 180 kpc from the cluster center are plotted as large red circles. The four open squares are the spectroscopically confirmed cluster members. The continuous red line is a fit to the large red symbols that lie within the blue box. Clusters members outside the core are plotted as small red circles (for those that have no detectable [OII] emission) or small blue squares (for those that have [OII]).

the fainter galaxies are bluer than the bright ones. The origin of this slope has been controversial as early studies suggested it could be well explained by a decrease in either the metallicity or the stellar age of the red population. Works like Kodama et al. (1998) have been comparing colour-magnitude simulations to observations of distant clusters and favor the mass-metallicity relation. The origin of this mass-metallicity relation could be explained by the heating of the interstellar medium by supernovae which would trigger the formation of a galactic 'wind'. In this scenario, this wind would eject the gas more efficiently in smaller galaxies due to their shallower potential wells, resulting in the trend of increasing metallicity with mass. More massive galaxies — more metal-rich — would therefore appear redder than the less massive ones (Carlberg 1984). Red sequences for clusters at the same redshifts are found to have consistent slopes. However, a potential evolution of this slope with redshift is still under question. A significant evolution in the slope of the red sequence was found by Stott et al. (2009) in rich galaxy clusters between $z \sim 0.5$ and $z \sim 1$ (see also Gladders et al. 1998). Other studies of the slope have however found little or no evolution favoring the scenario of a monolithic collapse at very high redshifts ($z \sim 2$).

Identifying the epoch at which the red sequence appears is important since it can place constraints on models (e.g., models of the CDM universe) that predict the formation epoch of galaxies. It is indeed a serious challenge to hierarchical models to predict such a substantial population of passive galaxies of red sequences at such high redshifts. De Lucia et al. (2006) shows for example that the main progenitors (having more than 50% of their final mass) of massive early type galaxies with present-day M> 10^{11} M$\odot$ formed at $z < 1.5$, a result difficult to reconcile with the observations of red sequence at high redshift.

Looking at higher and higher redshifts i.e., further back in time, studies have attempted to identify the first appearance of the red sequence and witness the birth of the counterparts of the

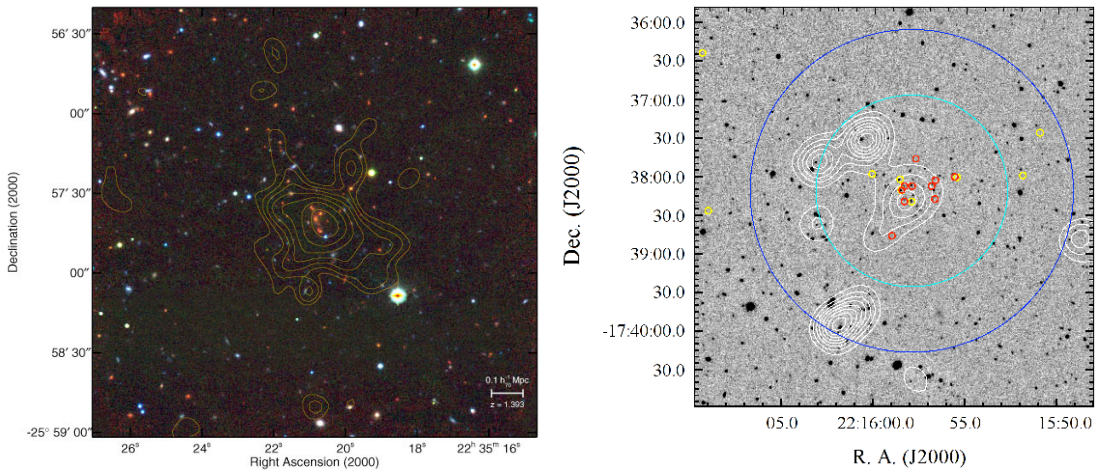

Figure 1.3. Example of galaxy clusters at $z > 1.3$ discovered thanks to the emission of the hot gas in their intracluster medium. *Left:* From Mullis et al. 2005. Three colours image of XMMU J2235.3-2557 (Ks, z, R) at $z = 1.39$ overlaid with its X-ray contours. *Right:* From Hilton et al. 2007. $5.2' \times 5.2'$ Ks-band image of XMMXCS J2215.9-1738 at $z = 1.457$ with X-ray contours overlaid in white. Objects spectroscopically identified as cluster members and with $z < 1.457$ ($z > 1.457$) are highlighted in red (yellow). The external (dark blue) circle marks the cluster virial radius of 1.05 Mpc, the internal (light blue) one, $R_{200} = 0.63$ Mpc.

massive galaxies found at the cores of local galaxy clusters. Despite its obvious scientific importance, such study has been limited by the small number of high redshift galaxy clusters currently known. We describe in the next section the different methods used in the last decade to probe high redshift galaxy clusters.

1.1.2 Searches for galaxy clusters at high redshift

One method to look for galaxy clusters has been to look at overdensities of red sources in optical imaging data using the 'red sequence algorithms'. Gladders & Yee (2000) showed that two-filter-imaging is sufficient to find clusters through the detection of their red sequence of early-type galaxies. The colours of galaxies are strongly related to a strong break in their spectrum: the 4000Å break, caused by the complete absorption of high energy radiation from metals in stellar atmospheres and by a deficiency of hot, blue stars. The early type galaxies are the brightest and reddest sources if the two filters are placed on either side of this spectral feature. As the 4000Å break shifts towards the near-infrared at $z > 1.5$, the cluster selection using the red sequence algorithms becomes more and more challenging. This technique has however recently been pushed to higher redshifts thanks to the mid-infrared *Spitzer* Space Telescope with the discovery of one cluster at $z = 1.34$ in the *Spitzer* Adaptation of the Red-Sequence Cluster Survey (SpARCS; Wilson et al. 2009). Also using *Spitzer* and the IRAC Shallow Survey (Eisenhardt et al. 2008; Stanford et al. 2005), Eisenhardt and his collaborators have been chasing 3D concentrations of objects with consistent photometric redshifts in the 8.5 square degree Boötes field of the NOAO Deep Wide-Field Survey. This project lead to the discoveries of three clusters at $z > 1.3$. See chapter 5 for details on this project.

Another efficient detection method has been to observe the extended X-ray emission of the intracluster medium (ICM). Compression and shocks, occurring when the cluster gravitational potential becomes settled, warm up the gas present in the intra-cluster environment. Observations of

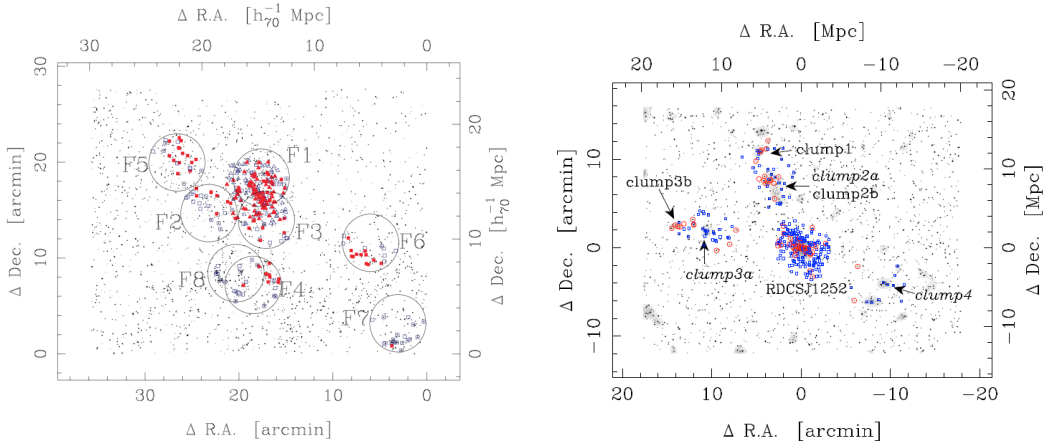

Figure 1.4. Large scale structures associated with high redshift galaxy clusters. *Left:* From Tanaka et al. 2006. Large scale structure associated with RX J0152.7-1352 at $z = 0.83$. Targeted fields are designated by F1 to F8. Points show photo-z selected galaxies with $0.76 < z_{phot} < 0.88$. Squares (triangles) are objects with spectroscopic redshifts from Tanaka et al. 2006 (previous studies). Red (blue) symbols account for structure members (fore/background objects). *Right:* From Tanaka et al. 2009. Large scale structure surrounding RDCS J1252.9-2927 at $z = 1.237$. The spectroscopically confirmed bound systems are indicated with labels (italic ones for foreground systems). Red circles are galaxies at $1.22 < z < 1.25$ and blue squares are those outside the redshift range.

galaxy clusters in X-rays have revealed that about 15−20% of the cluster mass is in the form of hot diffuse gas (while about 4% of the mass is coming from stars and galaxies and the rest from dark matter). This gas, reaching temperature of several 10^7K for typical cluster mass of 10^{14-15} $M_\odot$, becomes fully ionized and emits via thermal bremsstrahlung in X-rays (see Rosati et al. 2002; Sarazin 1988 for detailed reviews on X-ray galaxy clusters). With such high temperatures, the gas is almost fully ionized. The hot gas in the cluster is in an hydrostatic equilibrium and temperature, gas pressure and density are therefore related by simple equation: $dp/dR = -(GM(< R)\rho_{gas}(R))/R^2$. The pressure is directly proportional to both temperature and density by the equation of state for a perfect gas ($p = nk_BT$). Such relations show how quantities, such as ρ_{gas} and T, which can be measured from X-rays observations, are directly related to the cluster mass. Thus, in addition to providing an efficient method to detect clusters, X-rays studies of the ICM permit to measure the total gravitating cluster mass. X-rays selection of clusters has been crucial to find clusters, isolating already gravitationally bound systems, not only simple overdensities of galaxies (see Rosati et al. 2002). Observations conducted by the *ROSAT* satellite and later by *XMM-Newton* have detected galaxy clusters up to $z \sim 1.5$ with two clusters at $z > 1.3$ to date (see Fig. 1.3): XMMU J2235.3-2557 at $z = 1.39$ (Mullis et al. 2005; Lidman et al. 2008; Rosati et al. 2009) and XMMXCS J2215.9-1738 at $z = 1.46$ (Stanford et al. 2006; Hilton et al. 2007, 2009). However, searching for higher redshift clusters rapidly becomes difficult as the surface brightness of the X-ray emission fades as $(1 + z)^4$. XMMXCS J2215.9-1738 is still the highest redshift galaxy cluster spectroscopically confirmed to date with 17 members so far (Hilton et al. 2007), a large fraction of which are consistent with massive elliptical galaxies (Stanford et al. 2006). The velocity dispersion of the cluster obtained from the 17 high confidence members is 580 ± 140 km s^{-1}. Its bolometric X-ray luminosity is $L_x = 4.4^{+0.8}_{-0.6} \times 10^{44}$ ergs s^{-1} within a 2 Mpc region.

Several studies have been led beyond the immediate vicinity of high redshift X-ray galaxy

clusters to investigate possible associated filamentary structures at larger scales. Kodama et al. (2005) exploited the wide-field ($34' \times 27'$) of Suprime-Cam on Subaru to unravel possible large scale structures in the environments of known clusters at $z > 0.5$. One of the clusters RX J0152.7-1357 at $z = 0.83$, intensively studied at various wavelengths e.g., X-rays, SZ effect (see later in the section), near-infrared imaging and weak lensing analysis, was found to lie in a large-scale structure of several galaxy clumps (see Fig. 1.4, left panel). Tanaka et al. (2006) present a spectroscopic follow-up of the large scale structure confirming two large sheets of galaxies (one at $z = 0.837$ hosting the main body of the cluster in the direction N/S and another at $z = 0.844$ in the direction NE/SSW) likely in the process of interaction. They investigate the environmental dependence of their star formation histories looking at the red galaxies in three representative environments — cluster, group and field. They derived composite spectra of red galaxies from a number of red galaxies on the red sequence for each environment. They found that when 'cluster' red galaxies do not show sign of on-going or recent star formation, 'group' and 'field' ones tend to show remaining and/or recent star formation activities. They suggested that star formation is quenched in a short-time scale in group as compared to the more relaxed main cluster and that galaxy-galaxy interaction could be a viable mechanism. Similar analysis has been done in the surroundings of the X-ray galaxy cluster RDCS J1252.9-2927 at $z = 1.237$. A large scale structure of three galaxy groups was reported in Tanaka et al. (2009) to lie at the same redshift as the cluster with two groups embedded in a filamentary structure at the NE of the cluster core and one forming a second clump eastwards of the cluster (see Fig. 1.4, right panel). We note that their preliminary analysis of the field based on photometric redshifts had detected more potentially associated clumps which are in fact foreground systems, showing the importance of spectroscopy in order to confirm the real association of clusters members and reject random alignment along the line of sight.

The discovery of C1 0332-2742 is a more isolated example. Several works have made use of the unique multiwavelength data set available in the Chandra Deep Field South and found in this field a galaxy overdensity at $z \sim 1.6$. The Galaxy Mass Assembly Ultra-deep Spectroscopic Survey (GMASS, Kurk et al. in preparation) team has conducted an intense spectroscopy follow-up of objects with photometric redshifts $z_{phot} > 1.4$ with VLT/FORS2 in the GOODS-South field where several overdensities at diverse redshifts were discovered including the suspected overdensity at $z = 1.6$, the C1 0332-2742. Kurk et al. (2009) present a detailed study of this structure with 42 spectroscopic members so far. Seven of them have spectra consistent with being passively evolving galaxies. Fig. 1.5 show the spatial distribution of the members of C1 0332-2742 on top of the density map of all sources with $1.43 < z_{phot} < 1.77$ in the GOODS-South field. Kurk et al. (2009) derive an approximate cluster mass of $6 - 60 \times 10^{13}$ $M_{\odot}$. The distribution of the members in redshift space is bimodal with a main peak at $z = 1.610$ and a secondary peak at $z = 1.602$ suggesting that the structure is not yet virialized. The fact that no X-ray extended emission is detected (X-ray luminosity $< 3.5 \times 10^{43}$ erg s^{-1}; expected for a cluster with the same characteristics) reinforces this hypothesis. They conclude that C1 0332-2742 represents *'a sheet-like structure that will evolve into a cluster of galaxies at a later epoch'*.

In the near future, the study of high redshift galaxy clusters is likely to take a significant step forward through deep and large scale surveys targeting the Sunyaev-Zel'dovich (SZ). The SZ effect is the signature of the inverse-Compton scattering of the incident Cosmic Microwave Background (CMD) photons by the hot intracluster gas of galaxy clusters which results in a distortion of the CMD blackbody spectrum (Sunyaev & Zeldovich 1970, 1972; Birkinshaw 1999). The spectrum of the SZ effect has a null at about 217 GHz, where there is no net distortion and the intensity remains unchanged. At lower frequencies, a decrement in the CMB intensity is observed in the direction

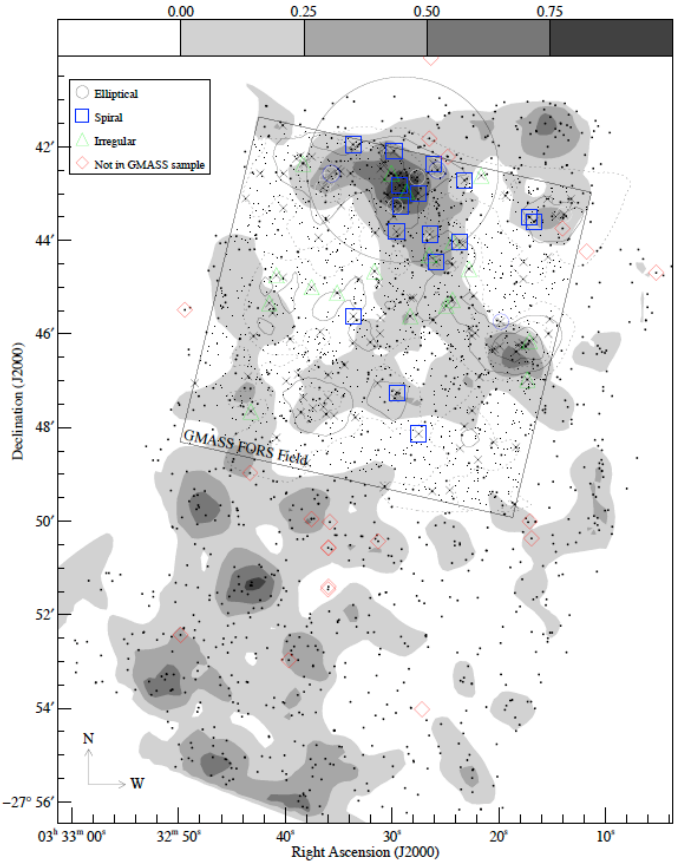

Figure 1.5. From Kurk et al. 2009. Density maps of galaxies at $z = 1.6$ in the GOODS-South field. Field (solid and dashed) contours indicate the density for $1.43 < z_{phot} < 1.77$ galaxies based on the GOODS-MUSIC (GMASS) catalogue photometric (spectroscopic) redshifts. Sources with spectroscopic redshifts are indicated by additional symbols according to their morphology: circles, squares and triangles for ellipticals, spirals and irregulars galaxies respectively. Red diamonds indicate galaxies with redshifts confirmed by ESO GOODS spectroscopy to be in the range $1.600 < z_{spec} < 1.622$ but are not in the GMASS sample.

of the galaxy cluster. As it is a distortion of the CMB spectrum, the surface brightness of the SZ effect does not depend on the cluster distance. Observations of the SZ effect permit the detection of clusters with a selection function that is nearly redshift-independent and therefore especially well-suited for chasing high redshift galaxy clusters ($z > 1$). The SZ effect is best known for allowing the determination of cosmological parameters when combined with other observational wavelength data such as X-rays. For example, studies have used both SZ and X-rays observations to provide estimates of the Hubble constant. The SZ/X-rays determinations of H_0 bridge the gap between observations of nearby objects and expansion values derived from CMD anisotropy and supernova measurements (Bonamente et al. 2006). Furthermore, the SZ effect measurements of galaxy clusters provide us with constraints typically derived from X-ray observations such as the central electron density, the core radius of the intracluster medium, the cluster gas mass or the fraction of the total cluster mass in gas. Significant SZ detections of previously known clusters have been reported in tens of X-ray and optically selected galaxy clusters (e.g., Joy et al. 2001; Bonamente et al. 2006; Halverson et al. 2009). Despite the promise of SZ surveys for high redshift galaxy clusters discoveries, few galaxy clusters candidates have been found using the SZ effect,

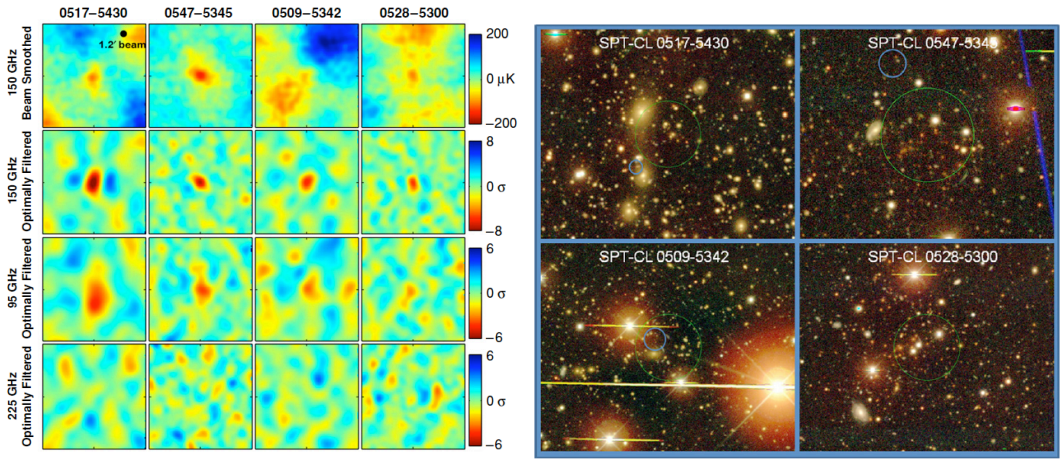

Figure 1.6. From Staniszewski et al. 2009. Examples of the four most significant galaxy clusters found by the South Pole Telescope Sunyaev-Zel'dovich survey. North is Up, East Left. CL 0517-5430 was previously identified at $z \sim 0.3$ in the REFLEX X-ray cluster survey. The other three are new detections. *Left:* $20' \times 20'$ box centered on the cluster. The top row shows the beam-smoothed 150 GHz map. The three lower rows show the 150, 95 and 225 GHz maps. The detections at 95 GHz (2.5 to 3.9σ detections) provide supporting evidence for the 150 GHz cluster detections. *Right:* Pseudo-colour optical images of the galaxy distributions towards the SPT clusters. Green circles are $1'$ diameter centered on the SPT position. Early-type galaxies with similar colours and central giant elliptical galaxies are found to lie within $0.5'$ of the SPT position. Gravitational lensing arcs are apparent near the central galaxy of CL 0509-5342 and in the southwest of the cluster core of CL 0547-5345.

this mainly due to the lack of instruments that demonstrate the requisite combination of resolution, mapping speed, and observing time to carry out a large scale search for distant galaxy clusters. But new instruments e.g. the South Pole Telescope (SPT), will permit large-area surveys aiming to find new clusters rather than study of known clusters. Recently, Staniszewski et al. (2009) report the detection of four SPT candidate SZ clusters only one of them having previously been identified in X-rays (see Fig. 1.6). Using photometric redshifts, they estimate that two of their cluster candidates lie at moderate redshifts ($z \sim 0.4$) while the two other were potentially lying at $z > 0.8$.

Over the past decade, numerous searches for high redshift galaxy clusters have also been conducted in the surroundings of powerful radio galaxies and radio-loud quasars at high redshifts ($z > 1.5$) that are known to inhabit rich environments. Best et al. (2003) studied the environments of six radio loud AGN at $z \sim 1.6$. Excesses of red galaxies were detected in most of the fields on two different scales: a central concentration on radial scales within $\sim$ 150 kpc and weaker large scale excesses detected between 1 and 1.5 Mpc radius. They see a large diversity in the concentrations found in different fields, some presenting excesses on both the smaller and larger scales, some showing excesses on only the smaller or larger scale, and in one case, no excess was detected. They deduced from the angular cross-correlation function that on average, the environment of the targeted AGN was consistent with Abell cluster richness classes 0 and 1. The next section will describe recent studies that were conducted more specifically on the environments of high redshift radio galaxies.

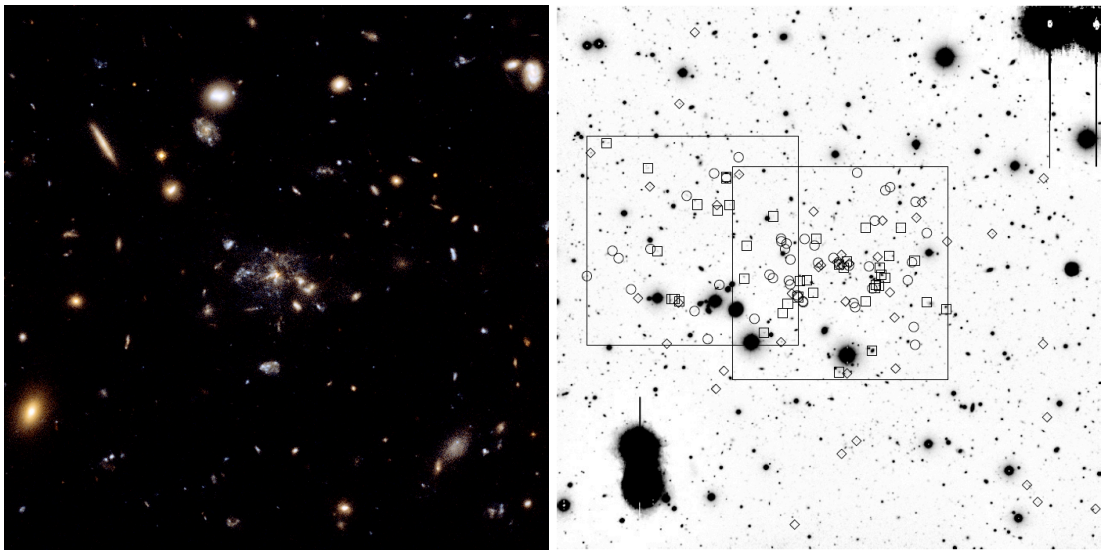

Figure 1.7. The Spiderweb galaxy. *Left:* From the ESA website. Close view of PKS 1138-262 with a composite image of different filters from the Advanced Camera for Surveys (ACS) on board *Hubble*. *Right:* From Kurk et al. 2004a. A $6.8' \times 6.8'$ I-band image of the field around PKS 1138-262 with its cluster members candidates (diamonds for Lyα emitters, squares for Hα emitters and circles for Extremely Red Objects).

1.1.3 Distant radio galaxies as tracers of high redshift galaxy clusters

It is now well established that the host galaxies of powerful radio sources are some of the most massive galaxies in the Universe (e.g., Seymour et al. 2007) and are likely to be the progenitors of Brightest Cluster Galaxies (Miley and De Breuck 2008). Because they are so massive, high redshift radio galaxies (HzRGs hereafter) are excellent signposts to pinpoint the densest regions of the Universe out to very high redshifts (e.g. Stern et al. 2003) and therefore provide a unique tool for studying cluster formation in the early universe.

Most of the past studies searching for companion galaxies in the vicinity of radio galaxies have been targeting HzRGs at $z > 2$. At these redshifts, the overdense systems of galaxies are probably still forming and cannot be already virialized and bound. The term 'protoclusters' seems therefore to be a more appropriate designation for those structures as they are probably the progenitors of local bounded clusters. We also note however that not all of the studied radio galaxy fields reside in overdense environments. The advantage of searching for these protoclusters using radio galaxies is that the redshift of the possible clusters is known. One search technique, extensively used by George Miley's team in Leiden has been to use narrow-band imaging to detect emission line objects around HzRG, in particular using bands that correspond to the redshifted Hα and Lyα emission lines. Extensive works have been done in the field of PKS 1138-262, a radio galaxy at $z = 2.16$ also called the 'Spiderweb' galaxy with a very massive central galaxy sitting at the center of its companions, similar to flies in a spider's web; see Fig. 1.7 (Pentericci et al. 2000; Kurk et al. 2004b,a; Croft et al. 2005; Zirm et al. 2008). Two overdense fields of Lyα emitters have even been detected around $z > 4$ HzRGs: TN J1338-1942 at $z = 4.1$ (Venemans et al. 2002) and TN J0924-2201 at $z = 5.2$, the most distant radio galaxy known to date (Venemans et al. 2004). Overdensities of Lyα emitters with densities $3 - 5$ times larger that the field density have been found by this method (Venemans et al. 2005, 2007).

However, Lyα and Hα emitters found in these environments are small, faint, blue objects likely to be young star-forming galaxies. Based on a Ks-stacking analysis of Lyα emitters, Overzier et al. (2008) found that they seem to have masses of only a few 10^8 $M_\odot$. These $Ly\alpha$ and $H\alpha$ emitters therefore probably constitute only a small fraction of the number of cluster galaxies, and represent only a small fraction of the total mass of the cluster.

Recent studies have tried an alternative approach and looked at the evolved more massive population in the surroundings of HzRGs at $z > 2$. Most of the information about this population comes from the rest-frame optical light that moves to near-infrared (NIR) wavelengths at high redshifts. Recently, the advent of new wide-field NIR cameras e.g., the Wide-field Infra-Red Camera (WIRCam) on the Canada France Hawaii Telescope (CFHT), the High Acuity Wide field K-band Imager (HAWK-I) on the Very Large Telescope (VLT) and the Multi-Object Infra-Red Camera (MOIRCS) on Subaru has permitted to extend the search of large scale structures, clusters and protoclusters to these high redshifts. For example, Kajisawa et al. (2006) developed purely near-infrared colour cuts to isolate the red passive evolving and blue star-forming populations of protoclusters associated with HzRGs at $z > 2$. A simple colour cut $(J - K)_{vega} > 2.3$ allows the selection of distant red galaxies (DRGs) at $z > 2$. Such red colours can only be reproduced by either the 4000Å break of galaxies with old populations or galaxies with heavy dust extinction. In order to select the possible members associated with their targeted HzRGs field at $z \sim 2.5$, a second refined criterion based on GALAXEV models ($J - K > 2(H - K) + 0.5 \cap J - K > 1.5$; Vega system) was used to select galaxies exclusively at $2 < z < 3$. The 4000Å break in this redshift range falls between J and H and the use of this additional H-band allows the additional selection of star-forming galaxies at $z > 2$ that have bluer $J - K$ colours. It also allows a more efficient removal of fore/backgroud galaxies. Two out of their 6 HzRGs fields show overdensities of red galaxies by a factor up to 5 compared to control fields suggesting that these assembling protoclusters already have many evolved red-sequence like galaxies. Applying this same JHK criterion, Kodama et al. (2007) recently explored the surroundings of four HzRGs using MOIRCS. They also found excesses of red galaxies in some of their targeted fields reaching a factor of 2 to 3 compared to the field and show that the massive brighter end of the red sequence ($M_{stars} > 10^{11}$ $M_\odot$) in their two lowest redshift targets ($2 < z < 2.6$) is already well populated but did not find any trace of a red sequence in their two fields at $z > 2.9$ (see Fig. 1.8 for near-infrared colour magnitude diagrams of the four HzRGs fields).

1.2 This thesis

This thesis presents the results of complementary works that made use of and studied the population of AGN (in particular, radio galaxies) in galaxy clusters. As shown by the numerous overdensities discovered in the surroundings of high redshift radio galaxies, these sources are excellent tracers to the densest structures in the early Universe (i.e., clusters and protoclusters). In chapter 2, we first present the study of the surroundings of two radio galaxies at $z = 1.4 - 1.5$, isolating galaxy cluster member candidates and highlighting potential galaxy structures associated with the targeted HzRGs. A large scale structure of galaxies was found in one of the studied field and has since been confirmed to be associated with the radio galaxy thanks to optical spectroscopy (see chapter 3). We then push the study of the vicinity of radio galaxies to higher redshifts with chapter 4 describing the observations and analysis of the fields of two high redshift radio galaxies (at $z = 1.77$ and $z = 2.02$). Finally, chapter 5 presents a reverse approach to these studies. We do not try to find high redshift galaxy structures by targeting AGN. We rather used a defined sample of galaxy clusters from $z = 0$ to $z = 1.5$ to study the AGN population of the clusters.

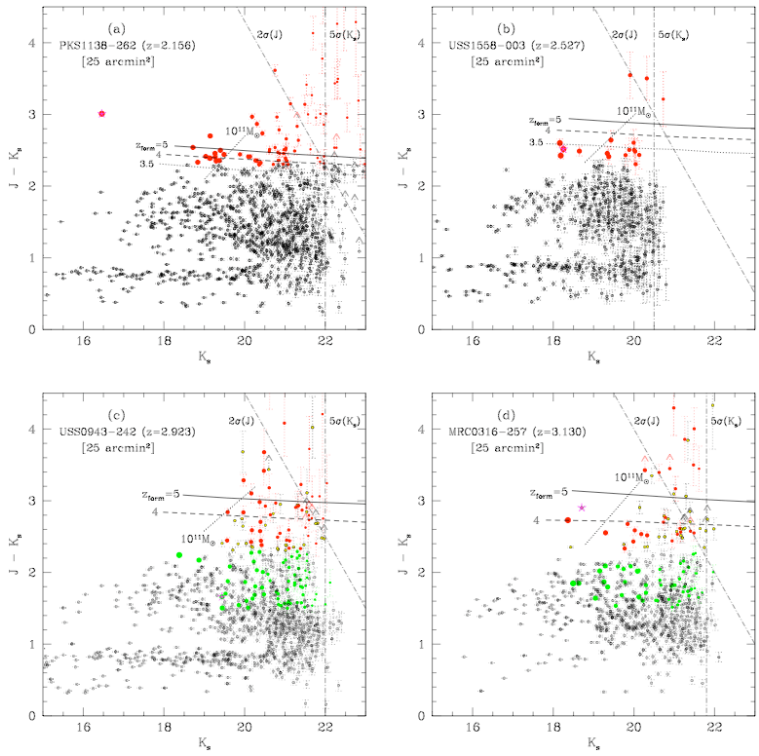

Figure 1.8. From Kodama et al. 2007. Colour-magnitude diagrams of four protoclusters at $2 < z < 3.2$. Protocluster member candidates are highlighted by filled circles. The expected locations of colour-magnitude relations at the redshift of the radio galaxies in the case of passive evolution are indicated by the nearly horizontal lines for $z_f = 4$ and 5 (3.5 also for the two first panels). *Top panels:* Fields around PKS 1138+262 and USS 1558-003. Early type galaxies candidates were selected by a single colour $(J - K)_{Vega} > 2.3$ (red circles). *Bottom panels:* Fields around USS 0943-242 and MRC 0316-257. Early type (red) and star-forming galaxies (green) were selected by the *JHK* colour-colour selection technique of Kajisawa et al. (2006).

A more detailed description of each chapter is provided below, highlighting the context in which this work has been done, and introducing the various teams, collaborations and observing campaigns associated with this work.

Chapter 2:

At the origin of the study presented in chapter 2 was the *Spitzer* High Redshift Radio Galaxies project (SHzRG, hereafter). SHzRG was based on the Cycle 1 *Spitzer*, program, "A comprehensive Spitzer Survey of High-Redshift Radio Galaxies" lead by Daniel Stern and Carlos De Breuck (for details on the project, see Seymour et al. 2007). The SHzRG sample was drawn from high redshift radio galaxy surveys executed during the last 45 years (3C, 6CE, MG, MRC, USS etc.). A HzRG is defined as a radio galaxy with $z > 1$ and a rest-frame 3 GHz luminosity greater than 10^{26} WHz^{-1} to ensure that we included only objects with very powerful obscured AGNs. To examine how *Spitzer*-derived quantities depend on redshift and radio luminosity, we selected a representative subset of 70 targets which span the full range of redshifts from $z \sim 1$ to the redshift of the most distant known radio galaxy, TN J0924-2201 at $z = 5.19$ (see Fig. 1.9). Most sources were observed

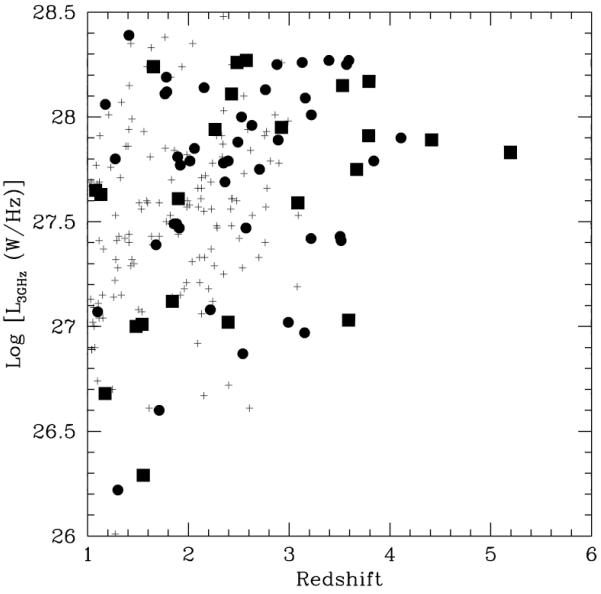

Figure 1.9. From Seymour et al. 2007. Radio luminosity at rest-frame 3 GHz plotted against redshift for 263 $z > 1$ radio galaxies from the literature (pluses). Filled symbols indicate sources in our *Spitzer* program, carefully chosen to uniformly cover $1.5 - 2$ orders of magnitude in radio power at each redshift $1 < z < 4$. The entire *Spitzer* sample was observed with IRAC, IRS and MIPS.

as part of the *Spitzer* Cycle 1 project; a few observations derive from guaranteed time observations by *Spitzer* instrument teams (see Seymour et al. 2007 for the list and properties of our targets).

Many people have contributed to the success of SHzRG, including among others[1]: Daniel Stern (JPL, Pasadena, CA, USA), Carlos De Breuck (ESO, Garching, Germany), Joël Vernet (ESO), Nick Seymour (MSSL, London, UK), S. Adam Stanford (Lawrence Livermore National Laboratory, Livermore, CA, USA), Alessandro Rettura (University of California, Riverside, CA, USA), Brigitte Rocca-Volmerange (IAP, Paris, France), Andrew Zirm (Dark Cosmology Center, Copenhagen, Denmark), Arjun Dey (NOAO, Tucson, AZ, USA), Mark Dickinson (STScI, Baltimore, MD, USA), Bob Fosbury (ESO), Mark Lacy (Spitzer Science Center, Caltech, CA, USA), Patrick McCarthy (Observatories of the Carnegies, Pasadena, CA, USA), George Miley (Leiden Observatory, the Netherlands), Harry Teplitz (IPAC, Pasadena, CA, USA), Wil van Breugel (Livermore) and myself.

An intense observing campaign has been made to complete this unique *Spitzer* dataset with multi-wavelength data in the 'bluer' optical and near-infrared bands. We decided to make use of the new (at that time) near infrared wide-field imager of CFHT, WIRCam, in operation since November 2005 which covers a $20' \times 20'$ field of view. Two SHzRG targets available in the Northern Hemisphere were selected for observations in J and Ks-band: 7C 1756+6520 (z = 1.42) and 7C 1751+6809 (z = 1.54) for which we already had optical supporting data. Chapter 2 describes the analysis of these two fields. We applied colour cuts combining our multi-wavelength data and selected cluster member candidates around our two targets. No evidence of a source overdensity was found in the surroundings of 7C 1751+6809. A significant excess of red galaxies is, on the contrary, found in the surroundings of 7C 1756+6520. This overdensity is even more pronounced within 2 Mpc of the HzRG, this area being overdense by a factor of 3 compared to a blank field.

[1] Affiliations are given at the time of writing.

These red galaxies form in an appropriate colour-magnitude diagram, a clear red sequence. Other concentrations of red galaxies are also found forming a large-scale structure of evolved galaxies in the field of 7C 1756+6520 which moreover shows an excess of mid-infrared selected AGN.

Chapter 3:

We present in this chapter the spectroscopic follow-up of the overdensity found in the field of 7C 1756+6520 and described in chapter 2. Using the DEep Imaging Multi-Object Spectrograph (DEIMOS) on the Keck Telescope, we observed 141 targets (82 blue galaxies, 47 red galaxies, 11 mid-infrared selected AGN candidates and the radio galaxy) and obtained redshifts for 56 of them. A new more accurate redshift of 1.4156 was assigned to the radio galaxy. We confirmed that there is indeed a galaxy structure associated with 7C 1756+6520 with 20 galaxies found with redshifts consistent with the radio galaxy. 7 galaxies are found with peculiar velocities $\Delta V < 1000$km/s relative to the velocity of the radio galaxy and within 2 Mpc from it, confirming that there is a galaxy cluster associated with 7C 1756+6520. A second compact clump of galaxies (4 objects) is found at $z \sim 1.437$, forming a very compact sub-clump of galaxies, 1.5′ east of 7C 1756+6520.

Chapter 4:

The data exploited in the work presented in chapter 4 were obtained as part of a larger project, effectively a collaboration between leading teams in the area of high redshift galaxy clusters including: George Miley, Nina Hatch (University of Nottingham, UK), Carlos De Breuck, Joël Vernet, Bram Venemans (ESO), Jaron Kurk (MPE, Garching), Roderik Overzier (MPA, Garching), Alessandro Rettura, Tadayuki Kodama (National Astronomical Observatory of Japan, Tokyo, Japan) and myself.

Overdensities of galaxies, especially overdensities of narrow lines emitters, are known around radio galaxies with $z > 2$ and up to $z = 5.2$, the so-called protoclusters. But no overdensities of red massive galaxies have been spectroscopically confirmed to date. Clear and tight red sequences are observed in clusters up to $z \sim 1.4$ and the study of PKS 1138-262 at $z = 2.2$ has shown evidence of an emergent red sequence with two red galaxies confirmed at the redshift of the HzRG (Doherty et al. 2010). The redshift range $1.7 < z < 2.5$ is crucial to study the epoch of appearance of the red sequence, the main tool used to set lower limits to the redshift at which the stellar populations formed. The immediate purpose of our HAWK-I project was to build the first statistically significant sample of protoclusters around high redshift radio galaxies and investigate the epoch of formation of high redshift galaxy clusters through the study of their old population. In 2008, we built a unique well-defined sample of 8 HzRGs with $1.7 < z < 2.5$: MRC 1017-220 ($z = 1.77$), MRC 0156-252 ($z = 2.02$), MRC 1324-262 ($z = 2.28$), USS 1425-148 ($z = 2.35$), MRC 0406-244 ($z = 2.43$), MG 2308+0336 ($z = 2.46$), MRC 2104-242 ($z = 2.49$) and MRC 2139-292 ($z = 2.55$). We observed these targets with HAWK-I on VLT bracketing the 4000Å break using a set of three near-infrared broad-band filters (either $YHKs$ or $JHKs$ depending of the position of the 4000Å break at the redshift of the studied radio galaxy).

In this chapter, we push the study of the environments of high redshift radio galaxies started in chapter 2 and 3 to higher redshifts. One project is currently focussing on the $z > 2$ targets of our sample (see Hatch et al. in preparation). In this chapter, we concentrate our analysis on the fields of the two lowest redshift radio galaxies of our HAWK-I sample: MRC 1017-220 ($z = 1.77$) and MRC 0156-252 ($z = 2.02$). These fields and additional control fields were observed in the Y, H and Ks bands. We designed a purely $YHKs$ near-infrared colour criterion to isolate galaxies at

$z > 1.6$, classifying the selected objects into passively evolving or star-forming candidates. We intensively tested this new selection technique on the GOODS-South field using the imaging and spectroscopy available on this field. We observed large field-to-field variations between our targeted fields and found in particular a clear excess (by a factor of $2-4$ depending on the comparison field) of red objects in the close vicinity of our higher redshift radio galaxy: MRC 0156-252. Both targets show a small excess of blue galaxies. One clump of blue objects is seen in the close vicinity of MRC 0156-252 and another group is also suspected in the south-east part of the field about 2 Mpc away from the HzRG. This chapter also presents the first Y-band galaxy number counts.

Chapter 5:

In this chapter we present a different and complementary approach to the study of galaxy cluster. The earlier chapters of this thesis have made use of radio galaxies to discover high redshift galaxy clusters. Radio galaxies are however only a small part of the population of AGN in clusters. This chapter includes a detailed review of studies of the AGN population residing in galaxy clusters, noting the limiting redshift range and cluster sample size of those studies.

The work presented in this chapter uses a very large sample of galaxy clusters (310) discovered thanks to the Irac Shallow Survey Cluster Search (ISSCS) project including among others: Peter R. M. Eisenhardt (JPL), Daniel Stern, Mark Brodwin (NOAO, Tucson, AZ, USA), Anthony H. Gonzalez (University of Florida, FL, USA), S. Adam Stanford, Michael J. I. Brown (School of Physics, Victoria, Australia), Arjun Dey, Buell T. Jannuzi (NOAO), C. S. Kochanek (Department of Astronomy, Columbus, OH, USA), Leonidas A. Moustakas (JPL) and myself.

Eisenhardt et al. (2008) present a sample of 335 galaxy clusters identified in the Boötes field of the NOAO Deep Wide-Field Survey (NDWFS; Jannuzi & Dey 1999). The clusters, reaching out to redshift $z \sim 2$, were identified by combining the IRAC Shallow Survey (ISS; Eisenhardt et al. 2004) with B_wRI imaging from the NDWFS and JKs imaging from the FLAMINGOS Extragalactic Survey (FLAMEX; Elston et al. 2006). Brodwin et al. (2006) calculated photometric redshifts for 4.5μm-selected sources in the ISS. Clusters were then identified using a wavelet algorithm which detected three-dimensional overdensities of galaxies (in 2 angular dimensions) with comparable photometric redshifts. The AGN and Galaxy Evolution Survey (AGES; Kochanek et al. in preparation) in Boötes provides spectroscopic confirmation for dozens of clusters at $z \leq 0.5$. At higher redshift, a Keck spectroscopic campaign has to date confirmed 10 $z > 1$ clusters (see Fig.1.10 and Eisenhardt et al. 2008; Stanford et al. 2005; Elston et al. 2006; Brodwin et al. 2006).

Using this unique sample of galaxy clusters at $0 < z < 2$ and the multiwavelength data available on the Boötes field, we derived the surface density of luminous AGN. AGN were selected using three different selection techniques: mid-infrared colours (using *Spitzer*/IRAC data), radio luminosity and X-ray luminosity. We found an excess of the number of AGN within 0.5 Mpc of the clusters centers for clusters at $z > 0.5$. The amplitude also increases with redshift. We thus confirmed the existence of a 'Butcher-Oemler' type effect for AGN in galaxy clusters.

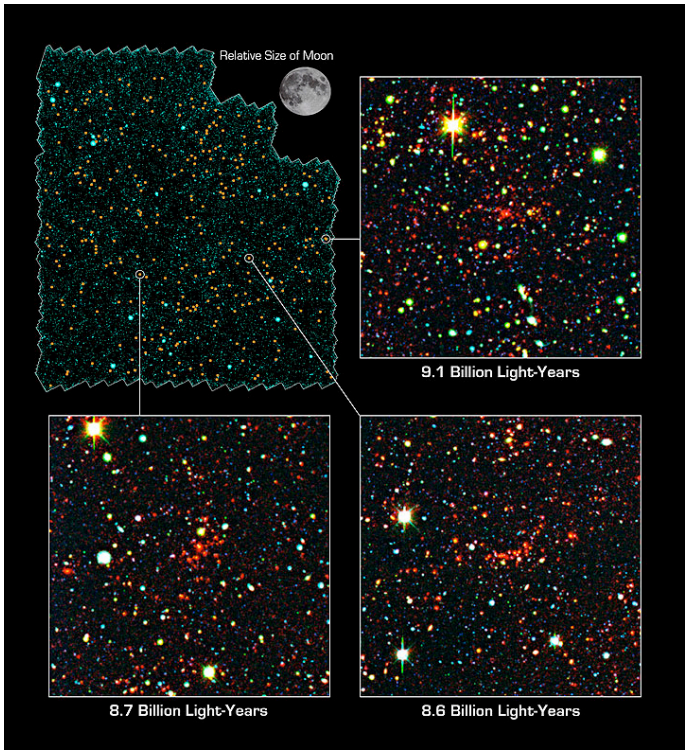

Figure 1.10. Composite 3-colour images (B_w, I, [4.5]; $5' \times 5'$) of three clusters at $z > 1$ presented in Eisenhardt et al. (2008) and their location in the Boötes field (Top Left). *Top Right:* ISCS J1438.1+3414 ($z = 1.413$). *Bottom Left:* ISCS J1429.3+3437 ($z = 1.258$). *Bottom Right:* ISCS J1434.5+3427 ($z = 1.243$). Courtesy of Mark Brodwin.

Chapter 2

Large Scale Structures around Radio Galaxies at $z \sim 1.5$

Abstract.

We explore the environments of two radio galaxies at $z \sim 1.5$, 7C 1751+6809 and 7C 1756+6520, using deep optical and near-infrared imaging. Our data cover 15×15 arcmin^2 fields around the radio galaxies. We develop and apply *BzK* colour criteria to select cluster member candidates around the radio galaxies and find no evidence of an overdensity of red galaxies within 2 Mpc of 7C 1751+6809. In contrast, 7C 1756+6520 shows a significant overdensity of red galaxies within 2 Mpc of the radio galaxy, by a factor of 3.1 ± 0.8 relative to the four MUSYC fields. At small separation ($r < 6''$), this radio galaxy also has one $z > 1.4$ evolved galaxy candidate, one $z > 1.4$ star-forming galaxy candidate, and an AGN candidate (at indeterminate redshift). This is suggestive of several close-by companions. Several concentrations of red galaxies are also noticed in the full 7C 1756+6520 field, forming a possible large-scale structure of evolved galaxies with a NW-SE orientation. We construct the colour-magnitude diagram of red galaxies found near 7C 1756+6520 ($r < 2$ Mpc), and find a clear red sequence that is truncated at $K_s \sim 21.5$ (AB). We also find an overdensity of mid-infrared selected AGN in the surroundings of 7C 1756+6520. These results are suggestive of a protocluster at high redshift.

Audrey Galametz, Carlos De Breuck, Joël Vernet,
Daniel Stern, Alessandro Rettura, Chiara Marmo,
Alain Omont, Mark Allen & Nick Seymour

Astronomy & Astrophysics, **507**, 131 (2009)

2.1 Introduction

Galaxy clusters are the most massive collapsed structures in the universe, which make them an excellent tool for investigating fundamental questions in astronomy. For example, the evolution of cluster number density depends sensitively upon Ω_0, but only weakly upon Λ and the initial power spectrum (e.g., Eke et al. 1998), and thus provides strong constraints on cosmology. Moderate-redshift clusters from well-defined samples such as the *ROSAT* Deep Cluster Survey have been used to constrain Ω_M and σ_8 (Borgani et al. 2001), while Stern et al. (2009) use the ages of cluster ellipticals to constrain the equation of state of dark energy. Distant X-ray luminous clusters provide the best lever arm for such studies, yet few have been found to date. Because galaxy clusters supply large numbers of galaxies at the same redshift, they also provide unique resources to study the formation and evolution of galaxies.

Due to the sensitivity limits of current surveys, it remains challenging to identify a large sample of high redshift galaxy clusters using classical optical and X-ray selection techniques. During the past decade, a new technique for detecting galaxy clusters at $z > 1$ has been to look at the immediate surroundings of high-redshift radio galaxies (HzRGs hereafter; Best et al. 2003; Venemans et al. 2005; Kodama et al. 2007). Indeed, it is now well established that the host galaxies of powerful radio sources are among the most massive galaxies in the universe (Seymour et al. 2007). At low redshift, radio galaxies are associated with giant ellipticals (cD and gE galaxies; Matthews et al. 1964), which are preferentially located in rich environments. Because they are so massive, radio galaxies are excellent signposts to pinpoint the densest regions of the universe out to very high redshifts (e.g., Stern et al. 2003). For example, this has been shown by the strong (5σ) overdensities of Lyα and Hα emitters around HzRGs at $2.1 < z \leq 5.2$ (Kurk et al. 2004b; Miley et al. 2004; Venemans et al. 2005, 2007), believed to be the progenitors of rich, local clusters. However, Lyα and Hα emitters found in these environments are small, faint, blue objects likely to be young star-forming galaxies and probably constitute a small fraction of both the number of cluster galaxies and the total mass of the cluster.

Interestingly, overdensities at the highest redshifts often have a filamentary nature and extend beyond ~ 2 Mpc (Croft et al. 2005). Carilli et al. (2002), in a detailed study of filaments in the field of PKS 1138-262, an HzRG at $z = 2.1$, do not detect any extended X-ray emission, indicating that this structure has not yet had sufficient time to virialize. However, Kurk et al. (2004a) show that some segregation has occured, with the Hα emitters, tracing the more evolved population, more centrally concentrated than the younger Lyα emitters. Therefore, the missing link between these protoclusters and the classical X-ray confirmed clusters found out to $z \sim 1.4$ (e.g., Mullis et al. 2005; Stanford et al. 2006) apparently occurs in the redshift range $1.4 < z \leq 2$. This redshift range is therefore particularly interesting for identifying clusters at a redshift beyond where the classical selection techniques are sensitive, but at a redshift where clusters are already partly virialized with a core of older, massive galaxies in place.

In this chapter, we present the study of the surroundings of two radio galaxies at $z \sim 1.5$. The next section describes the targets and the multi-wavelength data available for the two fields as well as how we derive the multi-band source catalogues. The third section describes the colour criteria we derive to select candidate massive cluster members and the results of this selection. The properties of the cluster member candidates are discussed in §2.4. A study of the AGN candidates found in the two fields is also presented in §2.5. Section 2.6 describes possible close-by companions of one of our targeted radio galaxies, 7C 1756+6520. We discuss the results in §2.7. We assume a ΛCDM cosmology with $H_0 = 70$ km s^{-1} Mpc^{-1}, $\Omega_m = 0.3$ and $\Omega_\Lambda = 0.7$. The magnitudes are expressed in the AB photometric system unless stated otherwise.

Table 2.1. Observations

Instrument	Pix Scale (arcs/pix)	Band	λ (nm)	Bd.width (nm)	FoV (arcmin^2)	Exp.[a] (min)	Seeing[b] (arcsec)
Palomar/LFC	0.18	*B*	440	100	588/566	345/360	∼ 1
-	-	*z*	900	180	556/442	60/135	∼ 1
CFHT/WIRCam	0.3	*J*	1252	158	477/482	182/219	0.7-1
-	-	*Ks*	2146	325	477/482	53/64	0.7-1
Spitzer/IRAC	0.61	IRAC1	3560	750	42/42	2/2	1.66
-	-	IRAC2	4520	1010	42/42	2/2	1.72
-	-	IRAC3	5730	1420	42/42	2/2	1.88
-	-	IRAC4	7910	2930	42/42	2/2	1.98

[a] FoV and exposure time for 7C 1751+6809 and 7C 1756+6520 respectively.

[b] Values of the mean FWHM for *Spitzer*/IRAC four bands.

2.2 The data

2.2.1 Target selection

This work follows on the SHzRG project (*Spitzer* High-Redshift Radio Galaxy; Seymour et al. 2007), which was designed to study a representative sample of 70 radio galaxies at $1 < z \leq 5.2$ and their surroundings. SHzRG obtained rest-frame near- to mid-infrared photometry for this sample using all three cameras on board *Spitzer*. From this sample, we selected radio galaxies with $z \sim 1.5$ for further study. From the seven such sources available in the Spring semester of the Northern hemisphere, we selected the two radio galaxies with the most supporting data, 7C 1756+6520 (z = 1.42; R.A.: 17:57:05.44, Dec.: +65:19:53.11) and 7C 1751+6809 (z = 1.54; R.A.: 17:50:49.87, Dec.: +68:08:25.93). These two radio galaxies were first published in Lacy et al. (1992) as part of a sample of 57 radio sources selected at 38 MHz. That paper presents high resolution radio maps of both objects. Their redshifts were first presented in Lacy et al. (1999). Lacy et al. (1999) had first tentatively given a z = 1.48 to 7C 1756+6520 assigning a very doubtful emission line of the spectrum to [NeIV]. A recent spectrum obtained with Keck/DEIMOS shows that the radio galaxy is in fact at z = 1.4156 (see chapter 3).

2.2.2 Observations and data reduction

Palomar/LFC *B*-band data

We imaged the two targets using the Bessel *B*-band filter of the Large Format Camera (LFC; Simcoe et al. 2000) on the Palomar 5m Hale Telescope (see Table 3.1). LFC is a prime focus, wide-field optical imager with a well-sampled 24.6 arcmin diameter field, imaged by an array of six 2048 × 4096 pixel back-side illuminated SITe CCDs. We observed each target for 6 hours in September 2007. The nights were photometric with an average 1″seeing.

The LFC data were reduced using the `MSCRED` package of IRAF, a suite of tasks designed to process multi-extension, large-format images from the new generation of optical cameras. Processing followed standard optical procedures. A distortion correction was applied to each chip, first using the default solution for LFC, then matching the stars of the USNO-B1.0 catalogue (Monet et al. 2003). The final stacked image was therefore astrometrized to the USNO-B1.0 ref-

erence frame. For photometry, we calibrated the images using observations of standard stars from Landolt (1992). We then converted to AB magnitudes using: $B_{\rm AB} = B_{\rm Vega} - 0.1$. We derived the 3σ (5σ) detection limits using $1.5''$ diameter apertures uniformly distributed over the images and found limiting magnitudes of ~ 27.1 (~ 26.6).

Palomar/LFC z-band data

We imaged the radio galaxy fields using the z-band filter of Palomar/LFC (see Table 3.1). In February 2005, we observed 7C 1751+6809 for 60 min under photometric conditions. In August 2005, we observed 7C 1756+6520 for 135 min but in non-photometric conditions. The LFC data were reduced using the `MSCRED` package of IRAF. The standard reduction process included an iterative removal of a z-band fringe pattern derived from the supersky flat as well as the same correction of distortion process used for the B-band data. The final, stacked images were astrometrically registered to the USNO-B1.0 catalogue. The FWHM of the final images is $\sim 1''.0$ for both fields. Because these data were not all obtained in photometric conditions, nor were these fields covered by the Sloan Digital Sky Survey (SDSS; York et al. 2000), photometric calibration of the z-band imaging relied on empirically derived optical through near-IR colour relations for Galactic stars. Matching a portion of SDSS imaging data with the Two Micron All Sky Survey (2MASS; Skrutskie et al. 1997), Finlator et al. (2000) show that stars have a well-defined optical/near-infrared colour locus, mainly determined by spectral type. We created a 2MASS/SDSS matched catalogue of 530 stars with $z < 18$ selected in three random extragalactic fields imaged by both SDSS and 2MASS. Following recent results from the SDSS collaboration[1], SDSS z band magnitudes are shifted by 0.02 relative to the AB system in the sense $z_{\rm AB} = z_{SDSS} + 0.02$. We apply this systematic shift to the SDSS photometry and convert the J and K magnitudes from 2MASS to AB magnitudes using the following corrections: $J_{\rm AB} = J_{\rm Vega} + 0.90$ and $K_{\rm AB} = K_{\rm Vega} + 1.86$. Using the criteria defined in Finlator et al. (2000) and optical photometry from SDSS (g, r and i-band) to separate stars into spectral classes, we plot their location in a $J - K$ vs $z - K$ colour-colour diagram (Fig. 2.1, left panel). Stars with spectral type K5 and earlier have $J - K < -0.26$ and a colour-colour relation well fit by a simple linear function: $J - K = 0.61 \times (z - K) - 0.2$. Galaxies and cooler stars have redder $J - K$ colours.

Using 2MASS photometry, we identified stars with a spectral type earlier than K5 in our two radio galaxies fields assuming a $J - K \leq -0.26$ colour. We selected 72 and 40 stars, respectively, for 7C 1756+6520 and 7C 1751+6809. Using the above colour-colour relation, we thus derived the z-band photometric zeropoints for the Palomar data. The colour-colour diagram for stars in our fields is given in Fig. 2.1 (right panel). Measuring the dispersion of the empirical colour-colour relation, we estimate a 0.1 mag uncertainty in the z-band photometric zeropoints. The 3σ (5σ) limiting magnitude determined from random $1.5''$ diameter apertures is 25.0 (24.5) for 7C 1756+6520 and 24.8 (24.3) for 7C 1751+6809.

CFHT/WIRCam data

In order to sample the red side of the 4000 Å break at the redshift of the targets, the radio galaxies fields were observed in the J and Ks bands using the new Wide-field Infrared Camera (WIRCam; Puget et al. 2004) of the Canada-France-Hawaii Telescope (CFHT; see Table 3.1). WIRCam contains four 2048×2048 pixel HAWAII2-RG detectors with a gap of $45''$ between arrays, and covers a $20' \times 20'$ field of view (FoV) with a sampling of $0.3''$ per pixel. The imaging observations

[1] See http://www.sdss.org/DR2/algorithms/fluxcal.html.

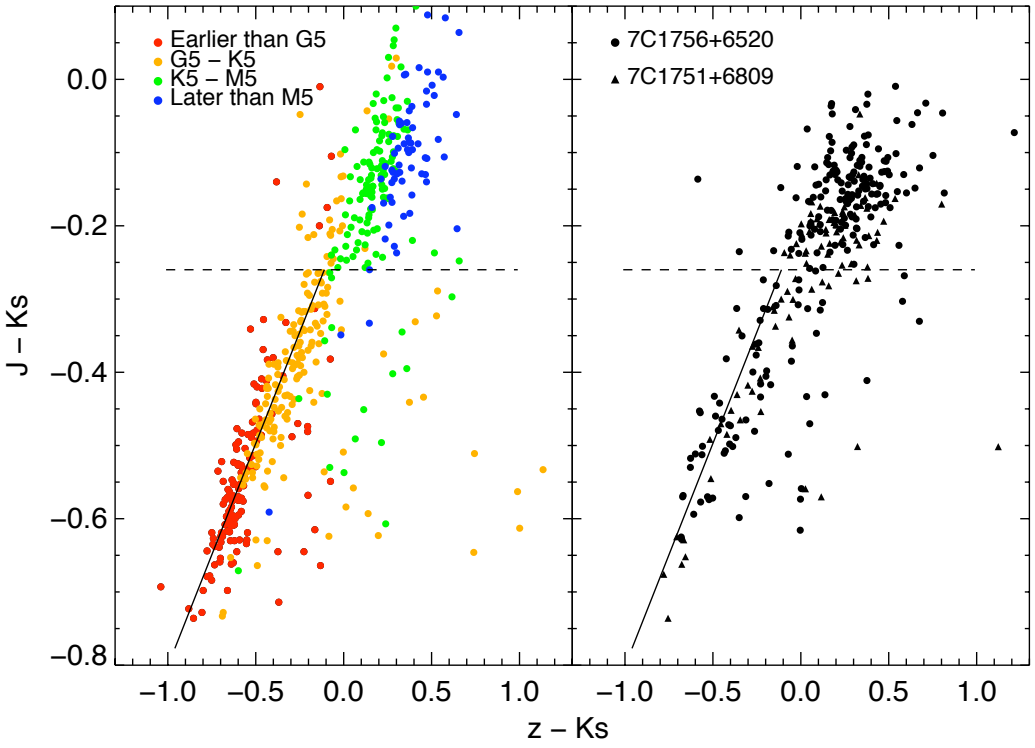

Figure 2.1. Colour-colour diagrams for stars from the matched 2MASS/SDSS catalogue (left) and for stars in the two radio galaxy fields (right). The spectral types of stars in the left panel were deduced from optical SDSS colours using Finlator et al. (2000) criteria. As illustrated by the solid line, stars with a spectral type earlier than K5 ($J - Ks < -0.26$) are well fit by an empirical colour-colour relation, $J - Ks = 0.61(z - Ks) - 0.2$, which was used to calibrate the optical images of the 7C fields using 2MASS stars in each 7C field. The right panel shows the final colour-colour diagram of the 2MASS stars of our two fields after calibration.

were obtained in April, May and July 2006 (Projects 06AF38 and 06AF99; P.I. Omont). The seeing varied between 0.7 and 1″ during the observations and the nights were photometric.

The WIRCam data suffer from serious crosstalk, which echoes all bright objects in the 32 amplifiers of each chip. Although our HzRGs are at high Galactic latitude ($b > 30°$), our images contain numerous bright stars due to the wide field of view of WIRCam. The crosstalk has different profiles and thus proves especially challenging to correct. Several techniques were attempted to correct crosstalk but none of them were fully satisfactory. For our total exposure time of approximately 3h30 in the J band, the crosstalk is clearly visible for all objects brighter than magnitude 16. In the end, we processed the WIRCam data without any crosstalk correction and instead flagged the most seriously affected regions (see §2.3). The remaining processing followed standard near-infrared data reduction strategies. We subtracted the dark and performed flatfielding with a super flat created from science frames. The images were then sky subtracted and stacked using the reduction pipeline developed by the Terapix team[2] (Marmo 2007). The images were photometrically calibrated to 2MASS J and K bands using ~ 60 stars per field. The 3σ (5σ) limiting magnitudes determined from random 1.5″ radius apertures in the J and Ks bands are ~ 24.4

[2]http://terapix.iap.fr.

(∼ 23.9) and ∼ 23.4 (∼ 22.9), respectively.

Spitzer/IRAC data

Observations with the *Spitzer* Infrared Array Camera (IRAC; Fazio et al. 2004) were performed as part of the GO-1 *Spitzer* program "The Most Massive Galaxies at Every Epoch: A Comprehensive *Spitzer* Survey of High-Redshift Radio Galaxies" (Seymour et al. 2007). These data consisted of four dithered 30s exposures in each of the four IRAC channels (see Table 3.1). The size of the final IRAC mosaic is about $13' \times 7'$. Due to the configuration of the camera, only a $6.5' \times 6.5'$ region is covered with all four bands. The data were processed and mosaiced using the MOPEX package (Makovoz & Khan 2005) from the *Spitzer* Science Center and re-sampled by a factor of two. The final pixel scale is $0.61''$ (see Seymour et al. 2007 for further details on the *Spitzer* data and processing). The 5σ limiting magnitudes determined from random $1.5'$ radius apertures are 22.1, 21.7, 19.8 and 19.7 for the 3.6, 4.5, 5.8 and 8.0μm channels, respectively.

2.2.3 Catalogue extraction

For the WIRCam data, we identified crosstalk-affected pixels in the J band image, the deeper of our WIRCam bands. A map was created to flag crosstalk contaminated pixels as well as the zones contaminated by bright star artifacts, which accounted for approximately 8% of the final mosaic pixels (see Fig. 2.2). The J and Ks images were smoothed to the $1''$ seeing of the B and z band data. We used SExtractor (Bertin & Arnouts 1996) to extract source catalogues with SExtractor dual mode for J and Ks using the unsmoothed images for object detection and the smoothed one for photometry. For B, z, J and Ks bands, we derived colours using a fixed $2.''5$ diameter aperture. For total magnitudes, we used the Kron automatic aperture photometry given by the SExtractor MAG_AUTO parameter. All magnitudes were corrected for Galactic extinction using the dust maps of Schlegel et al. (1998) assuming the $R_V = A_V/E(B-V) = 3.1$ extinction law of Cardelli et al. (1989). Since both fields are at high Galactic latitude, their extinction maps are very uniform. For both fields, the applied corrections were 0.18 in B-band, 0.06 in z, 0.04 in J and 0.02 in Ks.

The point source function (PSF) of IRAC is well defined (Lacy et al. 2005), providing consistent and readily tabulated aperture corrections to determine total magnitudes from aperture photometry. For both magnitudes and colours, we chose an aperture of $2''.5$ diameter and corrected the measured flux by the corresponding multiplicative correction factors — i.e., 1.68, 1.81, 2.04 and 2.45 for the 3.6, 4.5, 5.8 and 8.0μm channels, respectively.

Combining all of these catalogues, we built a master catalogue which provides multiwavelength data for all sources detected in at least one of the eight bands observed. The final surface covered by B, z, J and Ks and not affected by the WIRCam crosstalk is ∼ 0.1 square degrees. Fig. 4.3 shows the galaxy number counts for the different bands compared with previous counts from the literature. The galaxies were first isolated from the stars based on SExtractor parameter CLASS_STAR. The 1σ error on the number counts is overplotted on Fig. 4.3, assuming a Poisonnian error. No incompleteness correction was applied to the counts.

The galaxy counts determined from B, J and Ks were compared to previous works: Williams et al. (1996); Metcalfe et al. (1995, 1991) for B, Maihara et al. (2001); Teplitz et al. (1999) for J and Elston et al. (2006); Maihara et al. (2001) for Ks. For the z-band, we derive number counts from zBoötes (Cool 2007), a z-band survey of the Boötes field that covers 7.62 square degrees and reaches a 50% completeness limit of 23.4[3]. We also derive z-band number counts from the

[3]The final catalogues and images are available at http://archive.noao.edu/nsa/zbootes.html.

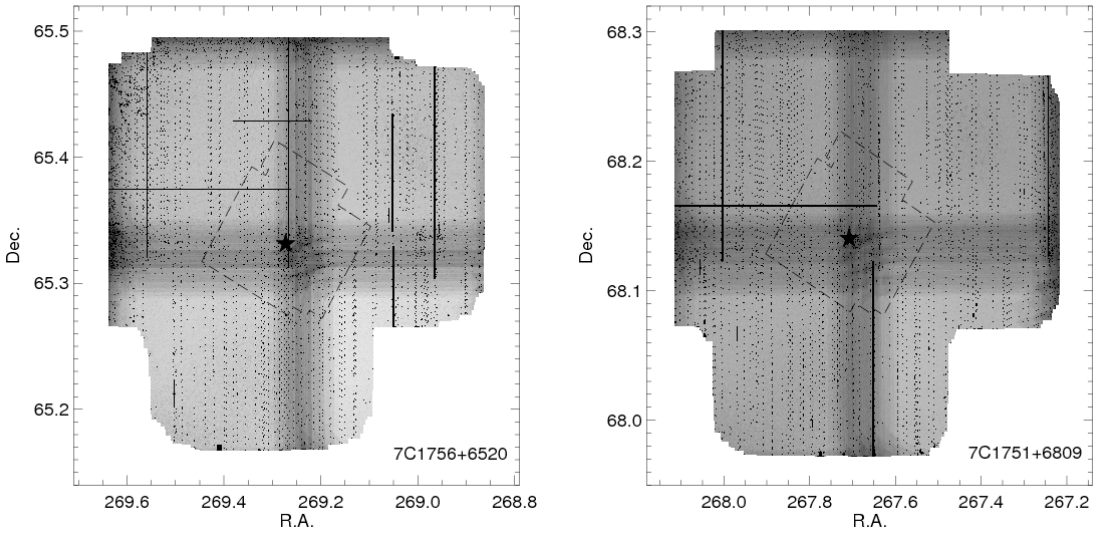

Figure 2.2. Combined field covered by our B, z, J and Ks-band data showing both the weight map of the WIRCam data (J) and the crosstalk flag map. We also flag regions contaminated by bright stars. The dashed lines outline the regions covered by the four IRAC bands. The positions of the HzRGs in the fields are indicated by stars.

GOODS-MUSIC catalogue, a multiwavelength catalogue of *Chandra* Deep Field South (CDFS) in the GOODS South field (Grazian et al. 2006bsee §3.1 for details on this catalogue).

The B, z and J-band counts are found in good agreement with the literature. The Ks-band counts are also found in agreement with previous studies for the field around 7C 1751+6809. The field around 7C 1756+6520 however shows an excess of sources with $17 < Ks < 20.5$; at the faint limit, Ks number counts drop due to incompleteness. This overdensity is the first evidence of an overdensity of very red objects around this radio galaxy.

2.2.4 Completeness

In order to assess the completeness limit of our images, artificial galaxies of different types were added to our images using the IRAF `artdata` package (`gallist` and `mkobjects` routines). We first consider the completeness limit for elliptical galaxies. For half magnitude intervals of brightness, we created catalogues of 5000 elliptical galaxies which were randomly added to the B, z, J and Ks images, including Poisson noise. We adopted a de Vaucouleurs surface brightness law, a minimum galaxy axial ratio b/a of 0.8 and a maximum half flux radius of $1\farcs0$. Running SExtractor with the same configuration files used for the unadulterated data, we determined the fraction of artificial sources detected. For ellipticals, the derived 90% completeness limits for our images are 25.0, 23.2, 22.8, and 22.2 in the B, z, J and Ks bands, respectively. We then determined the completeness limit for spiral galaxies by creating catalogues of 5000 spirals galaxies assuming an exponential disk surface brightness law with a minimum b/a of 0.8 and a maximum half flux radius of $1\farcs0$. The derived 90% completeness limits are 24.8, 22.9, 22.6 and 21.7 in the B, z, J and Ks bands, respectively. As expected, the completeness limit for exponential profile galaxies is slightly worse than for ellipticals due to the less compact nature of their morphologies.

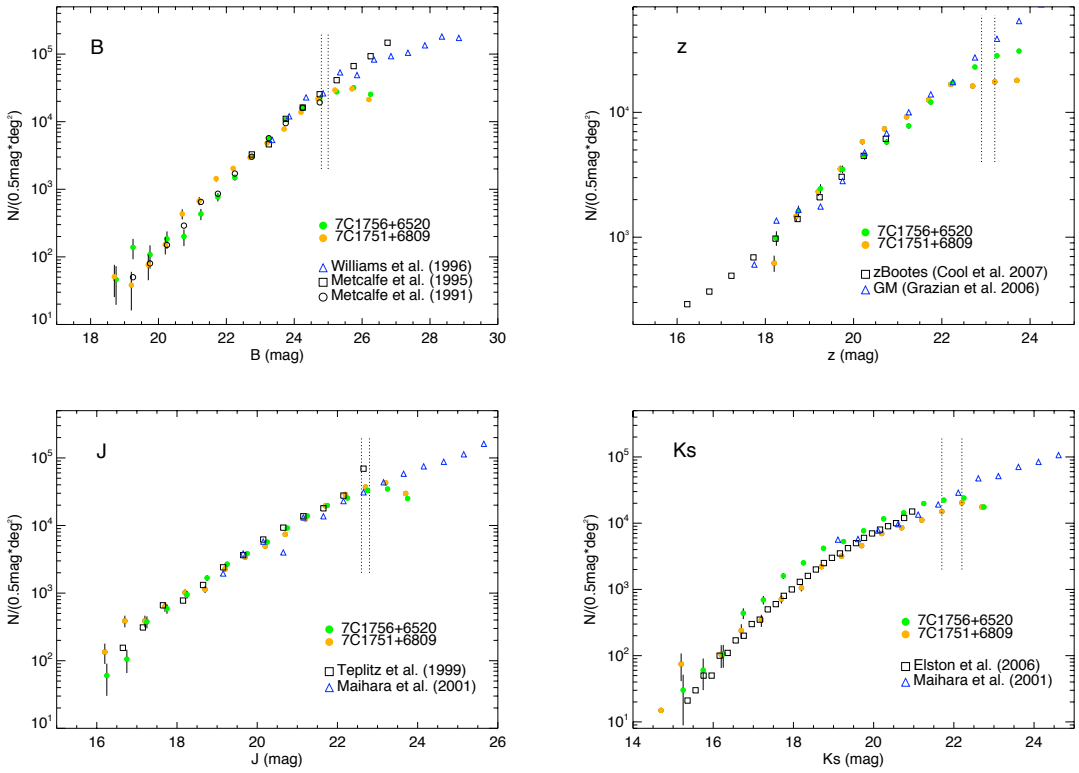

Figure 2.3. Galaxy number counts for our B, z, J and Ks data. We use the stellar index determined by SExtractor (CLASS_STAR) to separate galaxies from stars. No completeness correction was applied. The 90% completeness limits of our images for elliptical and spiral galaxies are indicated by the two vertical dotted lines. We plot number counts from the literature (see legends for symbols; GM: GOODS-MUSIC). The counts in B, z and J are found in good agreement with the literature. However, the 7C 1756+6520 field shows an excess of sources with $17 < Ks < 20.5$, the first evidence of an overdensity of very red objects in this field.

2.3 Candidate massive cluster members at $z \sim 1.5$

We now consider the environments of 7C 1756+6520 and 7C 1751+6809. We first introduce a colour criterion to select candidate cluster members based on the BzK selection technique of Daddi et al. (2004). We then discuss the selection of candidates selected using the full multiwavelength master catalogue (§2.3) and finally present the results on the properties and clustering of these sources.

2.3.1 Colour selection of evolved galaxies at $z \sim 1.5$

Substantial effort has gone into identifying colour criteria to select galaxies and galaxy cluster members at high redshift. Selecting extremely red objects (EROs; $R - K \geq 4$), Stern et al. (2003) and Best et al. (2003) successfully identified evolved galaxy overdensities around HzRGs at $z \approx 1.1 - 1.6$. It has been shown that near-IR colour criteria can be used to robustly identify passively evolving galaxies at $z \gtrsim 2$. These criteria are mainly based on the position of the 4000 Å break at a given redshift. Thus, the criterion $(J - Ks)_{\rm Vega} > 2.3$, which was first exploited by the FIRES team (Franx et al. 2003), is now well established and has been used to select cluster members at $z > 2$

(Distant Red Galaxies, hereafter DRGs; Kajisawa et al. 2006; Tanaka et al. 2007). The galaxies selected by this criterion are mainly massive, evolved galaxies with old stellar populations. The goal of the current study is devise colour criteria that are optimized for identifying evolved galaxies at $z \gtrsim 1.4$, sampling slightly higher redshifts than the ERO selection criteria, but not as high redshift as the DRG or Lyman break selection criteria.

Based on the K20 survey (Cimatti et al. 2002), Daddi et al. (2004) proposed a simple two-colour criterion based on BzK-band photometry for identifying galaxies at $1.4 \leq z \leq 2.5$ and classifying them as either star-forming galaxies, selected by $BzK \equiv (z - K) - (B - z) > -0.2$ (hereafter sBzK galaxies) or passive evolving systems, selected by $BzK < -0.2 \cap (z - K) > 2.5$ (hereafter pBzK galaxies). The BzK selection is largely insensitive to dust extinction since $E(B - V)$ is parallel to $BzK = -0.2$ criterion (Daddi et al. 2004). This 2 colour selection is therefore particularly efficient at isolating the red massive component of galaxy clusters at $z \geq 1.4$.

We consider first the colours of different stellar populations at $z \sim 1.5$ obtained from the Bruzual & Charlot (2003) models (Fig. 2.4). The different curves show the various dust-free τ models predictions (from left to right, $\tau = 5, 3, 1, 0.7, 0.5$ Gyr), assuming solar metallicity and a Salpeter (1955) initial mass function. For each model, four different population ages are indicated ($t = 2.5, 3, 3.5$ and 4 Gyr). As previously stated, the BzK criterion is relatively insensitive to dust extinction since the reddening vector for an extinction of $E(B - V) = 0.2$ is almost parallel to the $BzK = -0.2$ line (see black arrow in Fig. 2.4).

The model colours are consistent with the BzK selection criterion, with models covering first the sBzK zone and then the pBzK zone of the BzK diagram as τ decreases. We note however that the criterion is most likely missing early-type galaxies at $z > 1.4$, in particular those with the youngest stellar populations (models with small τ and large t values). We overplot a sample of the (rare) examples of early-type galaxies at $1.4 < z < 2$ and spectroscopically confirmed in the literature. Daddi et al. (2004) report five high redshift early-type galaxies from the K20 survey, classified as such on the basis of continuum breaks and absorption lines in their spectra. Four are in the GOODS area and one is in the Q0055 area. Cimatti et al. (2008) used the Galaxy Mass Assembly ultra-deep Spectroscopic Survey (GMASS; Kurk et al. 2008b) to find passive galaxies at $z > 1.4$. They used the UV properties of passive galaxies and derived a colour index of the UV continuum for galaxies with spectroscopic redshift $z > 1$ (see Cimatti et al. 2008 for details). Thirteen passively evolving galaxies at $1.390 < z < 1.981$ were found in GMASS, seven of which are members of an overdensity at $z \sim 1.6$ (Kurk et al. 2008a). The Gemini Deep Deep Survey (GDDS; Abraham et al. 2004) obtained spectroscopy for 309 objects attempting to target galaxies in the 'redshift desert' ($1 < z < 2$)[4]. Fifty of these sources have BzK photometry (SA12 and SA15 fields) and $z \geq 1.4$, of which five have $BzK < -0.2$. One of these sources is at $z > 2$ and has a $z - K$ which is far too blue to be considered as a passively evolving galaxy ($z - K < 1$). We therefore find only four strong candidates for passively evolving galaxies in GDDS. The location of all these passive galaxies in the BzK diagram is given in Fig. 2.4. Nine out of 22 are found to have $z - K < 2.5$. We thus confirm what we had already suspected from the models, i.e. the BzK criterion for the pBzK selection is missing a significant fraction ($\sim 40\%$) of old galaxies at $z > 1.4$.

We revise the pBzK criterion and adopt $z - Ks > 2.2$ rather than $z - Ks > 2.5$, coupled with $BzK < -0.2$, to select passively evolving galaxies at $z > 1.4$ (hereafter pBzK* galaxies). This colour cut has been chosen as a compromise between following the elliptical model colour predictions as well as selecting the majority (91%) of spectroscopically confirmed passive systems

[4]The GDDS catalogue is publicly available at http://lcirs.ociw.edu/public/GDDSSummary-dist.txt. Targeted magnitudes are in the Vega system. We convert from Vega to the AB photometric system using the corrections adopted earlier in this work.

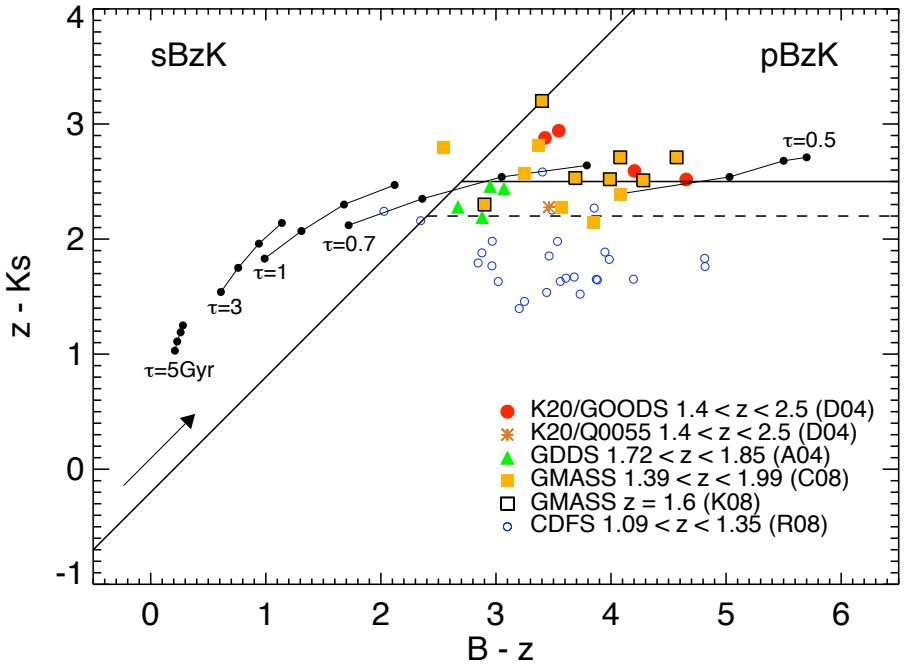

Figure 2.4. *BzK* colour-colour plot of stellar population models at $z = 1.5$. The curves account for star formation histories with various τ models (respectively from left to right $\tau = 5, 3, 1, 0.7$ and 0.5 Gyr). For each model, black points indicate four different ages of the population ($t = 2.5, 3, 3.5$ and 4 Gyr). The black arrow indicates a dust extinction of E(B-V) = 0.2 as parameterized with the reddening curve of Cardelli et al. (1989). The models are consistent with the *BzK* criteria of Daddi et al. (2004; solid lines). However, the *BzK* colour selection for p*BzK* galaxies is relatively strict and omits some passive elliptical galaxies at $z \sim 1.5$. We plot the early-type galaxies with a spectroscopic redshift $1.4 < z < 2.5$ found in the literature (K20 - Daddi et al. 2004 - D04; GDDS - Abraham et al. 2004 - A04; GMASS - Cimatti et al. 2008 - C08; Kurk et al. 2008 - K08). We revise the p*BzK* criterion and adopt $z - Ks > 2.2 \cap BzK < -0.2$ to select passive candidates at $z > 1.4$ (dashed line). This criterion has been chosen as a compromise between selecting the majority of the passive galaxies candidates and avoiding contamination by lower redshift red objects. Contamination is expected to be small, though, as shown by the location of a sample of spectroscopically confirmed elliptical galaxies at lower redshift ($1.09 < z < 1.35$ - CDFS - Rettura et al. 2008 - R08) with only 15% of them selected by our extended *BzK* criteria.

at $z > 1.4$ to date and minimizing contamination from very red galaxies at lower redshift. Rettura et al. (2008) study a sample of 27 early-type galaxies found in the CDFS with $1.09 < z < 1.35$. Out of 27, only four (all with $z > 1.3$) are selected with our extended *BzK* criteria (see Fig. 2.4, open circles; *BzK* photometry from A.Rettura, private communication). We are therefore confident that the contamination of lower redshift red objects is small. Indeed, since the 4000Å break is at the red end of the z-band at $z \sim 1.4$, the $z - Ks$ colour increases rapidly with redshift for $z \sim 1.4$ making this simple colour criteria an efficient redshift indicator, especially for passive systems.

Grazian et al. (2006b) presents the GOODS MUlticolor Southern Infrared Catalog (GOODS-MUSIC), a multiwavelength catalogue of the GOODS South field, combining imaging ACS (optical), VLT (near-infrared), and *Spitzer* (mid-infrared) data with available spectroscopic data. Grazian et al. (2006b) applied a photometric redshift code to this multiwavelength dataset[5]. For

[5]The full catalogue, including photometric redshifts, is publicly available at http://lbc.mporzio.astro.it/goods/goods.php.

this study, we used an updated version of the GOODS-MUSIC catalogue (version 2) recently presented in Santini et al. (2009). The new catalogue contains, among other things, additional spectroscopic redshifts and new MIPS 24μm photometry. The total area covered by the GOODS-MUSIC catalogue is 143.2 square arcmin. We check the revised BzK selection technique using the photometric redshifts (z_{phot} hereafter) of the pBzK (65), pBzK* (116) and sBzK (4727) galaxies found in the GOODS-MUSIC catalogue. Of the pBzK galaxies, 56% (78%) are found with $z_{phot} > 1.4$ ($z_{phot} > 1.2$). The corresponding percentages are 49% (74%) for the pBzK* galaxies and 82% (88%) of the sBzK galaxies. Using the same photometric redshift code as used for GOODS-MUSIC z_{phot}, Grazian et al. (2006a) estimate an accuracy of $\sigma_z = 0.05 \times (1+z)$ for red galaxies ($J-K > 0.7$) and $\sigma_z = 0.03 \times (1+z)$ for their full sample. Fig. 2 of the same paper shows that, at all redshifts, the photometric redshifts systematically underestimate the spectroscopic redshifts. Similar results were also found in Mobasher et al. (2004) whose photometric redshifts in the GOODS Southern Field at $z > 1.3$ were also underestimated. The percentages presented above are thus likely lower limits. The revised BzK selection is therefore very efficient at isolating red galaxies at $z > 1.4$, with some inevitable contamination by lower redshift reddened galaxies.

2.3.2 Candidate cluster members

The combination of filters used during the observations were checked for consistency with the one used by Daddi et al. (2004). Comparing the shape of the filter transmission curves, we deduce that the B-band filters are equivalent. The z-band filter of Palomar/LFC is consistent with the Gunn z-band of VLT/FORS1 though it is shorter at long wavelength by $\sim$ 400Å. Finally, the CFHT/WIRCam Ks-band filter is slightly more extended at bluer wavelength (by $\sim$ 300Å) compared to the one used at VLT/ISAAC by Daddi et al. (2004). We use a library of galaxy templates generated with PÉGASE2 (Projet d'Étude des Galaxies par Synthèse Évolutive; Fioc & Rocca Volmerange 1997) and compare the colours obtained with the different filter sets. We conclude that the correction to the $B-z$ colour is negligible, especially for galaxies at intermediate to high redshift ($z \geq 1.4$ - less than 0.02) and the correction to $z-Ks$ colour is not systematic (i.e., depending on the galaxy type and age) and are generally smaller than the calibration error of our z-band photometry (e.g. ≤ 0.1 mag on average; see §2.2.2).

We next verify that the depth of our data is sufficient to select passively evolving systems at $z > 1.4$. The magnitudes of early-type galaxies at $z > 1.4$ and confirmed spectroscopically are, unfortunately, rarely given in the literature. Furthermore, the selection of such objects itself is strongly biased to the brightest objects. We look at the expected magnitudes of $pBzK$* galaxies in the GOODS-MUSIC catalogue (see §3.1). 57 objects have $z_{\rm phot} > 1.4$ and BzK magnitudes fitting the pBzK* criteria (hereafter the "GM sample"). These sources have $24.8 < B < 29.7$ ($\langle B \rangle \sim 28.2$), $22.2 < z < 26.2$ ($\langle z \rangle \sim 24.4$) and $19.7 < Ks < 24.4$ ($\langle Ks \rangle \sim 21.8$). Considering the 3σ limits of our imaging, our Ks data would detect 98% of the GM sample, our z data would detect 75% of the GM sample, but our B data would detect only 11% of the GM sample. Therefore, we treat the z-band as the limiting band for this work and consider sources with upper limits in B. However, at a given B magnitude, fainter objects in z will have a bluer $B-z$ colour, corresponding to bluer objects. We are therefore confident that the majority of very red passive members of the clusters will be selected in our dataset.

We select the sBzK, pBzK and pBzK* galaxies around 7C 1756+6520 and 7C 1751+6809 using our multi-wavelength catalogue. The coordinates and B, z, J and Ks magnitudes of the pBzK* and sBzK galaxies found in each field are given in Appendix 2, Tables B.1, B.2, B.3 and B.4. We assume Poisson errors for source density determinations. Fig. 2.5 shows the BzK colour diagram of all the objects with a 3σ detection in B, z and Ks. We also plot the sources that have a

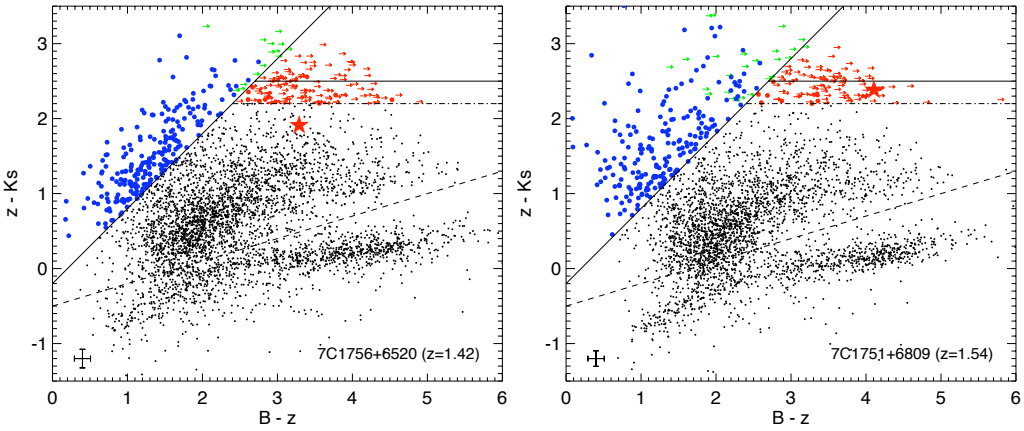

Figure 2.5. Colour-colour BzK diagram of 7C 1756+6520 at $z = 1.42$ (left) and 7C 1751+6809 at $z = 1.54$ (right). The sBzK and pBzK selection regions defined by Daddi et al. (2004) are shown by the solid lines. Our new pBzK* selection is shown by the dot-dashed line. The dashed line separates stars and galaxies. All sources with a 3σ detection in B, z and Ks are plotted. Also plotted are the sources with a $z - Ks > 2.2$ but no (or $< 3\sigma$) detection in the B-band (arrows). In order to place those sources in the plot, we assign them the 3σ detection limit for the B magnitude ($B = 27.1$). Typical uncertainties on colours are indicated in the lower left corner of each plot. HzRGs are marked as red stars (7C 1751+6809 has only an upper limit in the B-band).

$z - Ks > 2.2$ but no (or $< 3\sigma$) detection in the B-band (arrows). In order to place those sources in Fig. 2.5, we assign them the 3σ detection limit for the B magnitude ($B = 27.1$). For 7C 1756+6520 (7C 1751+6809), we found 129 (106) pBzK* galaxies including 42 (42) pBzK galaxies (with a 3σ detection in z and Ks). This gives a surface density of 0.39 ± 0.03 (0.32 ± 0.03) arcmin^{-2} for pBzK* galaxies and 0.13 ± 0.02 (0.12 ± 0.02) arcmin^{-2} for pBzK galaxies. We extract the star-forming candidates with a 3σ detection in B, z and Ks and found 218 (200) sBzK galaxies, i.e., a surface density of 0.65 ± 0.05 (0.59 ± 0.04) arcmin^{-2}. 14 (26) sources have $z - Ks > 2.2$ and no (or $< 3\sigma$) detection in B (green arrows) and can not be reliably distinguished as star-forming or passive systems.

Considering the $J - Ks$ colour of the BzK sources, there is a clear difference between sBzK and pBzK galaxies, with pBzK galaxies having a redder and narrower distribution centered around $\langle J - Ks \rangle \simeq 1.07$ (0.93) for the 7C 1756+6520 (7C 1751+6809) field. sBzK galaxies have a $\langle J - Ks \rangle \simeq 0.71$ (0.57). We note that the pBzK* galaxies found around 7C 1756+6520 are, on average, redder that those found in the 7C 1751+6809 field.

2.3.3 Surface density of BzK-selected galaxies

We now compare the densities found in our HzRG fields to blank fields. Grazian et al. (2007) study the properties of various classes of high redshift galaxies, including pBzK and sBzK sample in the GOODS-MUSIC sample. They compare their number densities of sBzK and pBzK galaxies with the literature (Daddi et al. 2004; Kong et al. 2006; Reddy et al. 2006) and conclude that the GOODS-South field is representative of the distant universe. We therefore use the GOODS-South as a first comparison field for our HzRG field. We cut the GOODS-MUSIC catalogue at the same completeness limit as our data, i.e., we select pBzK and pBzK* galaxies to our 90% completeness limits of $Ks < 22.2$ and $z < 23.2$, and we select sBzK galaxies to $Ks < 21.7$ and $z < 22.9$. The number densities of sBzK, pBzK and pBzK* galaxies in the GOODS-MUSIC catalogue are given

Table 2.2. Surface densities of *BzK* galaxies (to the completeness limits; degrees^{-2})

Field	GOODS	MUSYC				All	7C 1756+6520		7C 1751+6809	
	MUSIC	ECDFS	EHDFS	SDSS1030	CW1255	MUSYC	Full	$r < 2$ Mpc	Full	$r < 2$ Mpc
Area[a]	143.2	969.6	201.1	106.7	101.9	1379.3	333.4	47.9	336.2	47.7
(1)	(2)	(3)	(4)	(5)	(6)	(7)	(8)	(9)	(10)	(11)
p*BzK*	130 ± 60	70 ± 20	70 ± 40	170 ± 80	35 ± 35	70 ± 10	190 ± 45	330 ± 160	140 ± 40	no detection
p*BzK**	430 ± 100	370 ± 40	320 ± 80	640 ± 150	210 ± 90	370 ± 30	620 ± 80	1160 ± 295	510 ± 70	250 ± 140
s*BzK*	500 ± 110	505 ± 40	480 ± 90	300 ± 100	490 ± 130	485 ± 40	490 ± 70	990 ± 270	350 ± 60	500 ± 190

[a] Area are given in square arcmin.

in Table 2.2 (column 2) assuming Poisson errors on the numbers. The corresponding densities in our two fields (corrected for incompleteness) are given in columns 8 and 10.

We also compare our results to the MUSYC survey. The MUSYC survey (Gawiser et al. 2006; Quadri et al. 2007) consists of four fields: an extended Hubble Deep Field South (E-HDFS), an extended Chandra Deep Field South (E-CDFS) and two fields called SDSS 1030 and CW 1255. We note that the region covered by GOODS-MUSIC is included in the E-CDFS. Optical and near-infrared imaging of $30' \times 30'$ were obtained for all the fields. Deeper near-infared imaging of $10' \times 10'$ were obtained for subfields of SDSS 1030 and CW 1255 as well as for two adjacent subfields of E-HDFS (resulting in a deeper subfield of $20' \times 10'$ for E-HDFS). The MUSYC team did not obtain additional data for E-CDFS since the region had already been observed extensively by the GOODS team. All images and photometric catalogues are available on the MUSYC website[6]. We use four *UBVRIzJHK* catalogues of the MUSYC fields i.e., the multiwavelength catalogues of the deepest subfields in E-HDFS (201.1 sq. arcmin), SDSS 1030 (106.7 sq. arcmin) and CW 1255 (101.9 sq. arcmin) presented in Quadri et al. (2007) and the catalogue of the full E-CDFS (969.6 sq. arcmin; Taylor et al. 2009 in preparation). For each field, we select the p*BzK*, p*BzK** and s*BzK* galaxies to the 90% completeness limit of our data. Surface densities of the MUSYC fields are given in Table 2.2 (columns 3 – 6). The surface densities derived from the four MUSYC fields is given in column 7. Since GOODS-MUSIC is in E-CDFS, the surface densities for those two fields are not independent; see Table 2.2, columns 2 – 3.

Whereas the star-forming s*BzK* galaxies only vary by up to 70% from field to field, the red p*BzK* and p*BzK** galaxies show significant field to field variations. The surface densities of both p*BzK* and p*BzK** galaxies around 7C 1756+6520 are comparable to the MUSYC SDSS 1030 field, the denser control field as far as the red galaxies are concerned. We find an excess of p*BzK* and p*BzK** galaxies by a factor of 2.4 ± 1.2 and 1.7 ± 0.4 relative to the average density derived from the four MUSYC fields. The density of s*BzK* in the full 7C 1756+6520 field is, on the contrary consistent with the control fields. We find that *BzK* densities in 7C 1751+6809 are all in good agreement with MUSYC and GOODS-MUSIC.

Overdensities of narrow-band emitters and EROs have been found out to 1.75—2 Mpc in protoclusters around HzRGs at $2 < z < 3$ (Kurk et al. 2004a; Venemans et al. 2007). Best et al. (2003) studied the radial distribution of EROs around powerful radio-loud AGN at lower redshifts ($z \sim 1.6$) and found overdensities on scales of at least 1 Mpc for four fields out of the six in their sample. We therefore also compute the density of sources found within 2 Mpc ($\sim 4'$) of the radio galaxies (Table 2.2, columns 9 and 11). The corresponding region is also outlined by dashed lines in Fig. 2.8. No excess of *BzK* galaxies is found in the close surroundings of 7C 1751+6809. This region is actually under-dense for elliptical candidates by a factor of two compared to the

[6] http://www.astro.yale.edu/MUSYC/

full field. A concentration of galaxies is found in the 2 Mpc surroundings of 7C 1756+6520 for pBzK, pBzK* and sBzK galaxies not only compared to the control fields (by a factor of 4.7 ± 2.4, 3.1 ± 0.8 and 2.0 ± 0.6 respectively) but also compared to the full 7C 1756+6520 field (by a factor of 1.7 ± 0.9, 1.9 ± 0.5 and 2.0 ± 0.6 respectively). We note that the full field 7C 1756-6520 is biased towards higher densities since it contains the excess of sources near the HzRG. If we compute the surface density of pBzK* in the rest of the field removing the 2 Mpc surroundings of the HzRG, the surface density reduces to 480 ± 80 sources per sq. degrees implying that the inner 2 Mpc region is denser by a factor of 2.4 ± 0.7 compared to the rest of the field.

In order to further quantify the probability to find an overdensity of pBzK* and sBzK galaxies in a 2 Mpc radius region, we now work out the counts-in-cells fluctuations of E-CDFS, the largest field of MUSYC. We measure the number of pBzK* and sBzK galaxies (in the limits of completeness) found in 10000 randomly placed circular cells of 4′ radius (corresponding to 2 Mpc radius at $z = 1.42$) in the E-CDFS 969.6 sq. arcmin field of view. Edges were avoided by forcing the cells centers to be at least 4′ distant from the edges of the E-CDFS field. We chose a large number of cells (allowing some overlapping) to fully sample the counts fluctuations. We do not consider counts-in-cell of pBzK in this analysis due to the very small number of these galaxies in E-CDFS (18). Fig. 2.6 shows the histogram of counts-in-cells. sBzK are more common than pBzK*. In order to be able to directly compare those two populations, we subtract from our counts the expected average density in E-CDFS scaled to the cell size. Counts are given in percentage of the total number of cells. We also mark with arrows the galaxies counts within 2 Mpc of our two HzRGs (also corrected from the average E-CDFS density). The histogram has a right-skewed distribution. We note that the tail of the distribution of red galaxies is longer that the one for blue galaxies confirming that red galaxies are more clustered than blue ones (see Daddi et al. 2000; Kong et al. 2006). Counts in 7C 1751+6908 are consistent, if anything slightly lower, than the average of E-CDFS. The counts of pBzK* and sBzK galaxies around 7C 1756+6520 on the contrary fall way beyond the average density in E-CDFS, near the end of the tail of the distribution with only 0.26% of the cells having similar densities, confirming the result that the HzRG is found in an exceptionally overdense region.

2.3.4 Number counts

We derive the Ks-band number counts in 0.5 mag bins for pBzK, pBzK* and sBzK galaxies in our two fields (Fig. 2.7). We adopt Poissonian errors for the counts and use the Gehrels (1986) small numbers approximation for Poisson distributions. We overplot the findings of Kong et al. (2006; K06 hereafter) as a dotted line for comparison (see also Lane et al. 2007; Imai et al. 2008; Hartley et al. 2008). The number counts become incomplete at $Ks > 21$ when we start reaching the completeness limit of our z-band.

The number counts of pBzK and sBzK galaxies are in good agreement with Kong et al. (2006). We find the number of sBzK galaxies increasing steeply with decreasing magnitude, with the slope for the 7C 1756+6520 field similar to K06. 7C 1751+6809, however, shows a small excess (2σ) of sBzK galaxies at bright Ks magnitudes ($19.5 < Ks < 20.5$). The slope of the number counts for pBzK galaxies is similar for both of our radio galaxy fields and Kong et al. (2006). A small excess of Ks-bright pBzK galaxies is suggested in both fields (1.5σ). Such excesses of Ks-bright galaxies have also been noticed around other HzRGs (Kodama et al. 2007). If these Ks-bright sources were associated with the HzRGs, they would be very massive ($M > 10^{11} M_{\odot}$) and would represent the massive, evolved galaxy population of a young galaxy cluster around the HzRG. However, the number of sources considered here is too small to reach any firm conclusion since we detect only five pBzK galaxies with $19.5 < Ks < 20.5$. Previous work (K06; Lane et al. 2007; Hartley et al.

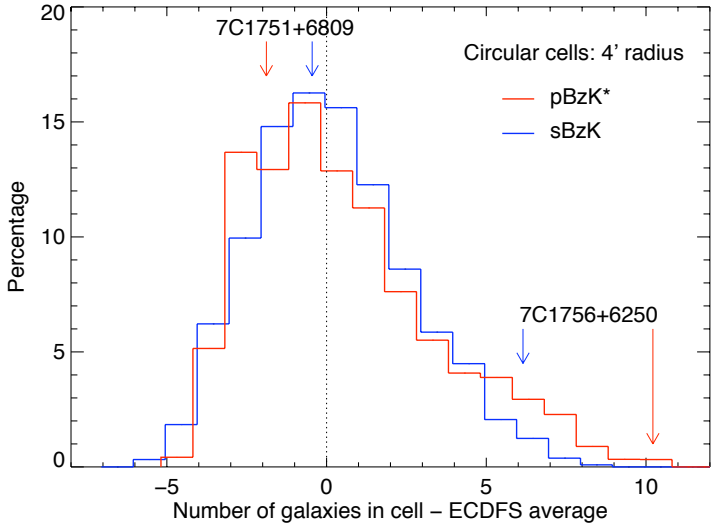

Figure 2.6. Histogram of the number of pBzK* (red) and sBzK (blue) galaxies in the MUSYC E-CDFS field in circular cells of 4′ radius (equivalent to 2 Mpc at z=1.42). We subtract from our counts the number of galaxies expected in such a cell corresponding to the E-CDFS average density (7.05 for sBzK and 5.18 for pBzK*). Cells below (above) 0 are therefore underdense (overdense) compared to the full field. Arrows indicate the number of galaxies found within 2 Mpc of our two HzRGs. We first note that the tail of the red galaxies distribution falls further than the blue galaxies one, confirming that red galaxies are more clustered than blue ones. 7C 1751+6809 is found in a slightly underdense region for both blue and red BzK galaxies. The number of pBzK* for 7C 1756+6520 falls at the very end of the tail of the distribution with only 0.26% of the cells containing such a high number of red objects.

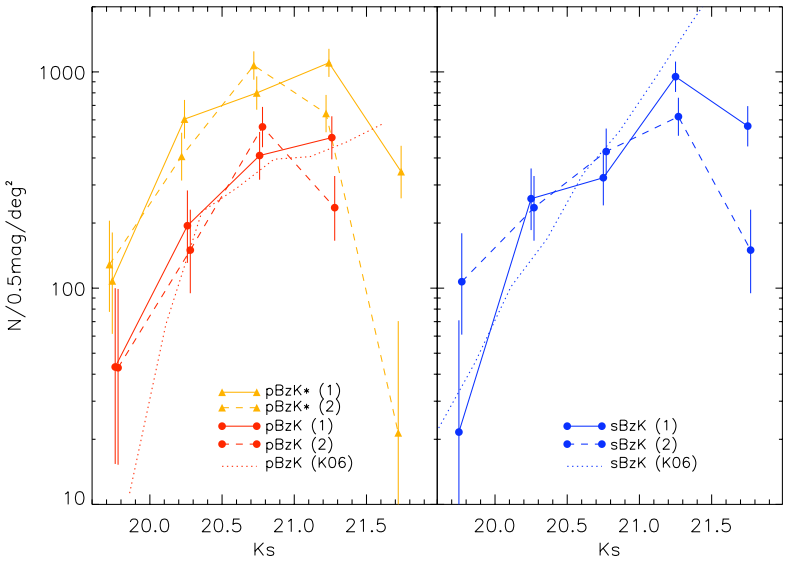

Figure 2.7. Ks number counts for pBzK (red), pBzK* (orange) and sBzK galaxies (blue) compared with counts from Kong et al. (2006; K06). The solid and dashed lines correspond to 7C 1756+6520 (1) and 7C 1751+6809 (2), respectively.

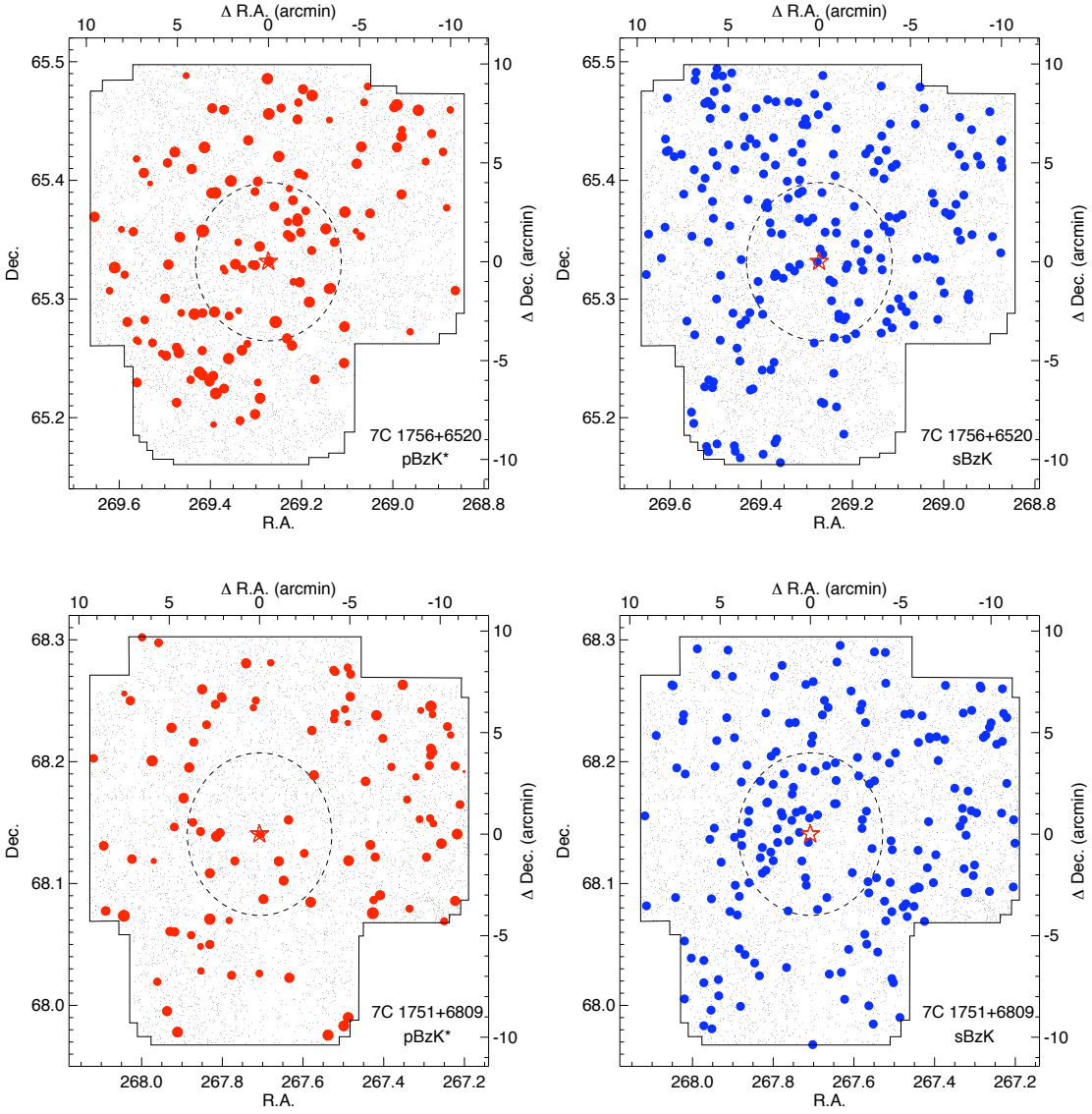

Figure 2.8. Spatial distribution of the BzK-selected galaxies in the two fields: left panels, pBzK* galaxies in red with the size of the symbol scaled according to the Ks-magnitude; right panels, sBzK galaxies in blue. The radio galaxies are marked by the red stars. The area simultaneously covered by the BzK bands is outlined and all sources detected in all three bands (3σ) are indicated by black points. The coordinates are also given relative to the radio galaxy in arcmin (right and top axes). The 2 Mpc radius region around the HzRG is marked by the dashed line.

2008) has shown that the pBzK number counts show a turn over at $K > 21$ with the counts slope flattening at fainter sources. We also strongly suspect this flattening in our counts although our BzK selection rapidly becomes incomplete at $Ks \geq 21$. A possible explanation for this turn-over is that pBzK galaxies are selected in a small redshift range and consist of very massive, passively evolving galaxies. Due to downsizing, their number decrease at lower luminosities (Hartley et al. 2008). The slope of the counts and the range of Ks magnitudes sampled by the pBzK* galaxies are also consistent with the pBzK galaxies, suggesting that our extended selection criteria is also

likely to be selecting galaxies in the same redshift range.

2.4 Properties of candidate massive cluster members

2.4.1 Spatial distribution

Fig. 2.8 displays the spatial distribution of the candidates around the radio galaxies. We also plot all the sources detected (3σ) in B, z and Ks (black dots) in order to visualize the zones of the field affected by our crosstalk flag (see Fig. 2.2) and very bright stars. In both fields, the BzK source distribution is clearly inhomogenous. In the 7C 1756+6520 field, the passive candidates (Fig. 2.8; top left panel) are more numerous in the surroundings of the radio galaxy than in the rest of the field. This was also seen in §3.3 and Table 2.2. Eight pBzK* galaxies are roughly aligned with the HzRG in a small E/W structure ∼ 2.5′ in length. Two other excesses are also observed in the field, one ∼ 3′ SE of the HzRG and another one at ∼ 6.5′ NW of the HzRG. These excesses appear to be aligned with a global overdensity of pBzK* galaxies along a large structure in a NW-SE direction. In contrast, no clear excess of pBzK* galaxies is detected in the 7C 1751+6809 field (Fig. 2.8; bottom left panel) even though they show a relatively non-uniform distribution. We note that one pBzK* galaxy is found near the line of sight to both HzRGs (at 2.4′ for 7C 1756+6520 and 6.3′′ for 7C 1751+6809), suggesting that both HzRGs may have close companions.

The sBzK galaxies also have an inhomogenous distribution though it is less well defined than the pBzK* galaxies. In particular, 7C 1756+6520 has nine sBzK galaxies along the same elongated structure near the HzRG. One sBzK galaxy is also found near the line of sight of the HzRG (at ∼ 5.5′′, Fig. 2.12). The sBzK galaxies in the 7C 1751+6809 field show an excess near the center of the field with an elongation in the direction NW-SE with no obvious correlation with the pBzK* spatial distribution. This overdensity was not seen with the density counts in Table 2.2, most probably due to the fact that the HzRG is at the "edge" of the elongated structure of sBzK galaxies. If associated with the HzRG, this structure would have a ∼ 4 Mpc extent.

Fig. 2.9 presents the radial distribution of pBzK* and sBzK galaxies around both HzRGs i.e., the number of candidates found per radius bin (binsize = 1′) divided by the corresponding ring area. The large error bars are due to the small number of sources used to derive the radial profiles, e.g., only 5 pBzK* and 1 sBzK galaxies are found within 1′ of 7C 1756+6520. The distribution of candidates near 7C 1756+6520 forms an elongated structure, not centered around the HzRG. The radial profile in Fig. 2.9 is therefore a lower limit to the true concentration of BzK around the HzRG as it does not fully reflect the complex spatial distribution of the sources. However, we note that a clear peak of pBzK* galaxies is seen near the HzRG. The pBzK* density decreases with radius and asymptotes to the full field density (red dashed line) at ∼ 5′ from the radio galaxy. Variations are also observed in the profile of the sBzK galaxies with a deficit of sources near the HzRG (< 1′) and a "bump" in the profile between 2′ and 4′, suggestive of some segregation in the properties of the galaxies in the large scale structure. We note however that the significance of those variations is less that 1σ. As seen previously, no significant variation of the pBzK* density is seen around 7C 1751+6809 but a small overdensity of sBzK is observed within 5′ of the HzRG (1σ significant though).

2.4.2 Colour-magnitude diagram

Colour-magnitude diagrams (CMD) are an efficient method to study the formation and evolution of galaxies. At $z < 1$, galaxy cluster cores are dominated by massive, passively-evolving elliptical galaxies that trace a clear red sequence on the colour-magnitude diagram. In the last decade,

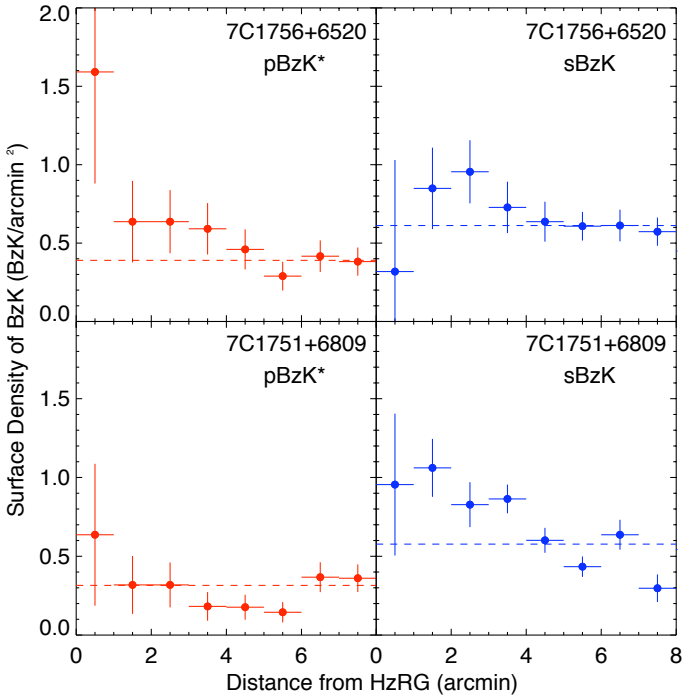

Figure 2.9. Radial density profile of BzK selected galaxies around 7C1756+6520 (upper panels) and 7C 1751+6809 (lower panels) for pBzK* galaxies (left panels) and sBzK galaxies (right panels). The full field density is shown by the horizontal dashed lines. The profiles and surface densities were derived from the entire sample of candidates. The values obtained are therefore higher than in Table 3.1 where the study was restricted to the completeness limit. The error bars indicate the 1σ errors on the counts assuming Poissonian errors.

studies have shown that this red sequence of early-type galaxies is also found in galaxy clusters out to $z \sim 1.5$ (e.g. Mei et al. 2006; Stanford et al. 2006; Tanaka et al. 2007; Lidman et al. 2008). Recent work at even higher redshifts have studied the evolved galaxy population in $z \sim 2$ galaxy clusters and conclude that the red sequence may appear between $z = 3$ and 2 (Kodama et al. 2007; Zirm et al. 2008). We have investigated the CMD of the sources in the region surrounding the HzRGs. Their CMDs are shown in Fig. 2.10. Sources within $3'$ of the HzRGs and with a 3σ detection in all BzK bands are plotted as black dots. The size of the studied region was chosen as a compromise between selecting sources close to the HzRG and including the majority of the candidates in the apparent central overdensity. We note that the region of the CMD at faint Ks magnitude starts to be empty well before the magnitude limit of our Ks-band data due to the non detection of faint Ks sources in the optical bands. pBzK* and sBzK galaxies within $3'$ (~ 1.5 Mpc at $z = 1.5$) are plotted as red points and blue triangles, respectively. All pBzK* galaxies found near the HzRGs have a $> 3\sigma$ detection in the J-band; sBzK galaxies with lower limits in J are marked as blue arrows. The two pBzK* galaxies found near both HzRGs and the sBzK galaxy found near 7C 1756+6520 are marked as squares. We overplot models of the expected location of the red sequence at $z = 1.5$, i.e., the predicted $J - K$ colour of a passively evolving galaxy with different formation redshifts ($z_f = 3, 4, 5$; provided by T.Kodama). The models reproduce the red sequence of passively evolving galaxies in the Coma cluster at $z = 0$ and include a metallicity-magnitude dependance which causes the red sequence slope (Kodama et al. 1998).

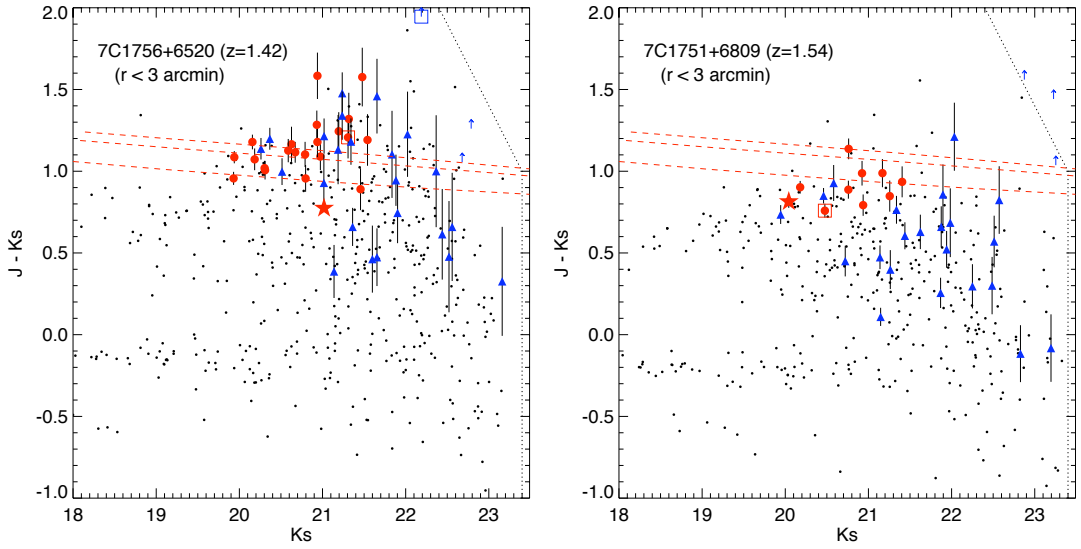

Figure 2.10. Colour-magnitude diagram ($J - Ks$ vs Ks) of the regions surrounding the HzRGs (within 3 ′). The pBzK* and sBzK galaxies are plotted as red circles and blue triangles respectively. sBzK galaxies not detected in J are shown as blue arrows. Also plotted are all sources in this same region detected in the three BzK bands (black dots). The radio galaxies are shown as red stars. The dotted lines represent the 3σ detection limits in J and Ks reported in §2.2.3. The two pBzK galaxies found near the line of sight of both HzRGs and the sBzK galaxy found near 7C 1756+6520 are indicated by the red and blue squares, respectively. The dashed lines indicate the expected locations of the red sequence at $z = 1.5$ corresponding to the predicted colour of a passively evolving stellar population with $z_f = 3, 4$ and 5 (from lower to upper curve; see text for details).

The pBzK* galaxies in the inner 3′ region around 7C 1756+6520 have colours consistent with passively evolving galaxies with $z_f \geq 2$ in contrast to the pBzK* galaxies around 7C 1751+6809 which have bluer $J - Ks$ colours. Some elliptical candidates have slightly redder colours ($J - Ks > 1.2$) and may be background objects since the BzK criteria is designed to select objects at $1.4 < z < 2.5$. Two of the pBzK* and three of the sBzK galaxies have $(J - K)_{\rm Vega} > 2.3$ and would be classified as DRGs, i.e., they are likely to be either passive elliptical or dusty star-forming galaxies at $z > 2$.

Recent observations of some high redshift galaxy clusters have shown a deficit of red galaxies at the faint end of the red sequence compared to local clusters (Kajisawa et al. 2000; De Lucia et al. 2007; Tanaka et al. 2005, 2007). It has been suggested that the red sequence appears at bright magnitudes and progressively extends to fainter magnitudes with time. Tanaka et al. (2007) studied a possible large-scale structure around a galaxy cluster at $z = 1.24$ and found that a deficit of faint red galaxies is noted in the clumps surrounding the central cluster but not in the CMD of the cluster itself, suggesting that the build-up of the red sequence is dependent on environment, progressing more rapidly in higher density environments. Considering the potential cluster around 7C 1756+6520, we note a clear deficit of Ks-faint pBzK* galaxies. No pBzK* galaxy is found with $Ks > 21.5$ near the HzRG. At these faint Ks magnitudes, we surely reach the combined incompleteness of our z and Ks bands data. But, as described in §3.2, we are more than 60% complete at our magnitude limits. For example, 29 pBzK* galaxies with $Ks > 21.5$ are found in the full field and sBzK galaxies are found with $Ks > 21.5$ within 3′ of the HzRG. We therefore conclude that the truncation at faint magnitudes is real. This would imply that this is another

example of downsizing (Cowie et al. 1996); i.e., the more massive cluster members stopped their star-formation earlier than the less massive cluster members. A similar study of the CMD of red galaxies in the field of the X-ray galaxy cluster XMMUJ2235.3-2557 at $z = 1.39$ is presented in Lidman et al. (2008). They do not observe evidence of a truncation of the red sequence at fainter magnitudes, suggesting that they are looking at a richer or more evolved system. The scatter of the pBzK* galaxies relative to the red sequence model at $z_f = 5$ ($z_f = 4$) is 0.089 ± 0.067 (0.095 ± 0.061) magnitudes for non-DRG galaxies. This scatter is large and most probably inflated by non-cluster members. Studies of the intrinsic scatter of the red sequence in galaxy clusters at $1.2 < z < 1.5$ have however shown that the scatter in $J - K$ can be up to ~ 0.06 (Lidman et al. 2004, 2008).

We stress that the pBzK* galaxies selected in this work are only candidate cluster members and that spectroscopic follow-up will be necessary to confirm their physical association to the HzRGs.

2.5 AGN candidates

Recent studies suggest that AGN companions are often found around radio galaxies. Croft et al. (2005) spectroscopically confirmed three QSOs in the surroundings of PKS 1138-262 at $z = 2.16$ and suggested that the QSOs were triggered by the protocluster formation (see also Pentericci et al. 2000). Venemans et al. (2007) also detected QSOs near radio-galaxies at $z > 3$. Recently, Galametz et al. (2009) (see chapter 5) studied the AGN population in a large sample of galaxy clusters at $z < 1.5$ and found an excess of AGN within 0.5 Mpc of the cluster centers, with the number of AGN in clusters increasing with redshift (see also Eastman et al. 2007). Powerful AGN provide an alternative way to look for relatively massive host galaxies in a complementary technique to the near-IR colour selection.

Stern et al. (2005) presents a robust technique for identifying active galaxies from mid-infrared colour criteria (see also Lacy et al. 2004). While the continuum emission of stellar populations peaks at approximately 1.6μm, the continuum of AGN is dominated by a power law throughout the mid-infrared. Stern et al. (2005) adopt the following (Vega system) criteria[7] to isolate AGN from other sources: $([5.8]-[8.0]) > 0.6 \cap ([3.6]-[4.5]) > 0.2 \times ([5.8]-[8.0]) + 0.18 \cap ([3.6]-[4.5]) > 2.5 \times ([5.8]-[8.0]) - 3.5$ Since the criterion is designed to identify power-law spectra, they do not preferentially select AGN in any specific redshift range. We apply this selection criteria to all sources with a 5σ detection in all four IRAC bands. The coordinates of the selected AGN for 7C 1756+6520 (12 candidates) and 7C 1751+6809 (5 candidates) are given in Table 2.3 and Table 2.4, respectively. Fig. 2.11 shows their distributions in the [3.6]-[4.5] vs [5.8]-[8.0] colour-colour diagram. We note that although neither HzRG is detected at a 5σ level in the 5.8μm-band, their IRAC magnitudes and position in the IRAC colour-colour diagram are presented in the tables and in Fig. 2.11. Both are undeniably classified as AGN by the Stern et al. (2005) criterion.

As a comparison field, we use the IRAC Shallow Survey (ISS; Eisenhardt et al. 2004), which includes four IRAC bands and covers 8 square degrees in the Boötes field with at least 90s exposure time per position. 2262 sources in ISS are found in the Stern et al. (2005) AGN selection wedge, where we require a 5σ detections in all four IRAC bands (Galametz et al. 2009 and chapter 5). The 5.8μm band is the least sensitive with a 5σ limiting depth of 15.9 (Vega, in an aperture-corrected 3″ diameter aperture; equivalent to 51μJy). Whereas we would expect three to four AGN candidates in the HzRG fields, we find 8 AGN candidates near 7C 1756+6520 and four near 7C 1751+6809 at the depth of ISS. We therefore observe an overdensity of AGN candidates in

[7] We use the following conversions between the Vega and AB photometric systems: $[3.6]_{AB} = [3.6]_{Vega} + 2.792$, $[4.5]_{AB} = [4.5]_{Vega} + 3.265$, $[5.8]_{AB} = [5.8]_{Vega} + 3.733$ and $[8.0]_{AB} = [8.0]_{Vega} + 4.399$.

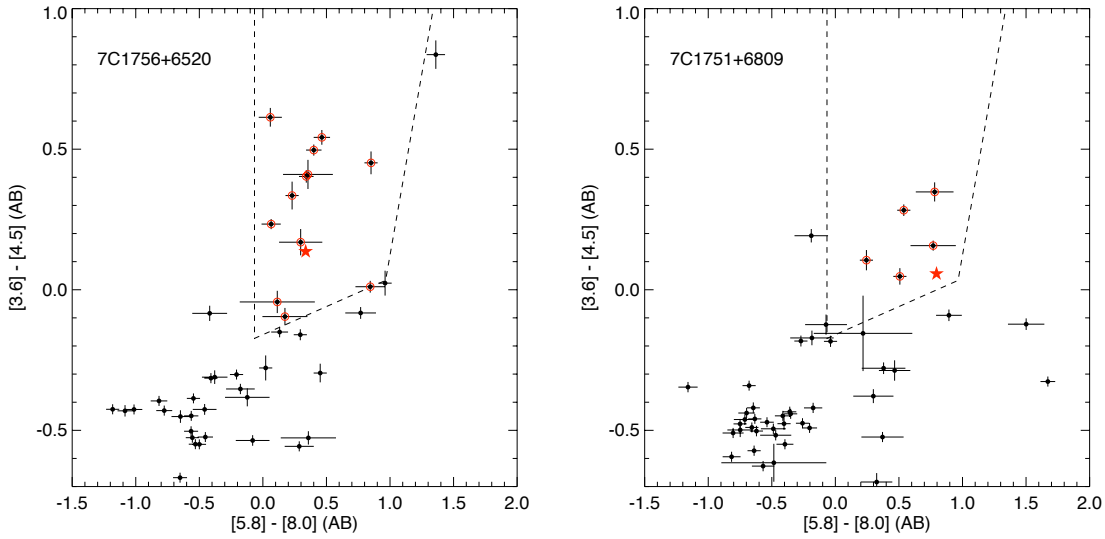

Figure 2.11. Mid-IR colour-colour diagram for 7C 1756+6520 (top) and 7C 1751+6809 (bottom). All sources with a 5σ detection in all four IRAC bands are plotted. We overplot the Stern et al. (2005) wedge for AGN selection. Sources circled in red are identified as AGN candidates by this criterion. HzRGs are indicated by the red stars and are both found in the selection wedge, as expected.

the field of 7C 1756+6520 by a factor of two compared to the 7C 1751+6809 and ISS fields. One AGN candidate is found only 5″ offset from 7C 1756+6520 (Fig. 2.12, §6) and two additional candidates are found within 1.5′ of the HzRG. However, the 12 AGN candidates do not show any particular spatial distribution as was seen for both the pBzK* and sBzK galaxies (see §2.4.1). No AGN candidate is found within 1.5′ of 7C 1751+6809.

2.6 Candidate close companions to 7C 1756+6520

An elliptical, a star-forming and an AGN candidate are found near the line of sight to 7C 1756+6520 (within 6″), suggestive of several close companions. Fig. 2.12 shows the immediate surroundings of 7C 1756+6520 in our imaging bands; arrows indicate the pBzK* galaxies, sBzK galaxies and the AGN candidate. Using the density of BzK galaxies found in the full field, we find that the probability of finding a pBzK* galaxy within 6′ of the HzRG is ~ 0.44%, and the probability of finding a sBzK galaxy is ~ 0.54%. At the depth of our IRAC data, the probability of finding an AGN candidate in the same area is ~ 0.57%. The probability of finding the three candidates in this small area around the HzRG is therefore extremely small, strongly suggesting that these candidates are associated with the HzRG and form a very unique and diverse system of bound galaxies.

2.7 Conclusions

We study the surroundings of two radio galaxies at $z \sim 1.5$ using deep multiwavelength imaging. We select candidate cluster members using colour selection techniques designed to select galaxies at the redshift of the targeted HzRG. This technique has been proven to identify clusters and protoclusters at high redshift ($z > 2$; Kajisawa et al. 2006; Tanaka et al. 2007). An excess of

Table 2.3. AGN candidates in the field of 7C 1756+6520

ID[a]	R.A. h:m:s	Dec. d:m:s	[3.6] (AB)	[4.5] (AB)	[5.8] (AB)	[8.0] (AB)
HzRG	17:57:06.00	+65:19:53.9	20.01	19.87	20.08	19.74
1005	17:57:13.15	+65:17:06.4	19.41	19.51	19.64	19.46
1110	17:56:52.53	+65:16:56.7	20.12	19.67	19.78	18.93
1164	17:56:59.06	+65:17:55.0	19.82	19.48	19.43	19.20
1206	17:57:13.19	+65:19:08.4	19.77	19.15	18.51	18.45
1213	17:57:33.29	+65:20:25.6	18.77	18.76	18.95	18.10
1317	17:56:55.86	+65:19:06.6	18.32	17.82	17.56	17.16
1340	17:57:30.88	+65:21:21.8	18.98	18.57	17.98	17.64
1352	17:57:30.46	+65:21:21.8	19.12	18.58	17.97	17.50
1354	17:57:04.98	+65:19:51.0	20.02	19.61	19.69	19.34
1748	17:57:20.16	+65:21:56.8	20.16	19.99	19.63	19.33
1767	17:57:15.44	+65:21:56.0	19.13	19.17	19.73	19.62
1814	17:56:41.15	+65:22:59.1	17.48	17.24	18.42	18.36

[a] The ID corresponds to the identification number in our 3.6μm catalogue. The radio galaxy is identified by 'HzRG'.

Table 2.4. AGN candidates in the field of 7C 1751+6809

ID[a]	R.A. h:m:s	Dec. d:m:s	[3.6] (AB)	[4.5] (AB)	[5.8] (AB)	[8.0] (AB)
HzRG	17:50:50.02	+68:08:26.5	19.68	19.63	20.78	19.99
1201	17:50:51.44	+68:06:06.6	18.52	18.23	18.56	18.02
1290	17:51:24.88	+68:08:34.1	19.99	19.88	19.72	19.47
1400	17:50:39.18	+68:06:47.6	19.41	19.36	19.23	18.72
1872	17:50:34.24	+68:10:23.6	19.50	19.15	19.14	18.36
1912	17:50:51.76	+68:10:57.7	17.40	17.24	19.59	18.82

[a] The ID corresponds to the identification number in our 3.6μm catalogue. The radio galaxy is identified by 'HzRG'.

candidate passive elliptical candidates is found in the field of one of our two targets, 7C 1756+6520 by a factor of 3.1 ± 0.8 compared to control fields. A study of the counts-in-cells fluctuations in our larger control field shows that the probability to find such an overdensity in the field is very low (0.26%). These results may be compared to previous studies that have been made at similar or higher redshifts. The Best et al. (2003) study of the environments of six radio-loud AGN at $z \sim 1.6$ finds an excess by a factor of 1.5 to 4 of EROs within radial distances of $\sim$ 1 Mpc of the AGN. Similarly, Kodama et al. (2007) select passive evolving and star forming cluster member candidates in the surroundings of four HzRGs with $2 < z < 3$ applying colour cuts in $JHKs$ and found excesses by a factor of two to three compared to the field. Clusters were already suspected around those HzRGs in previous studies that were concentrated on overdensities of narrow-band (Hα, Lyα) emitters also by a factor of two to five larger than in the field (Kurk et al. 2004b; Venemans et al. 2005, 2007). Looking at narrow-band emitters has been very efficient at finding overdensities around HzRGs. However, such clusters members, dominated by young stellar populations, are likely not the most massive members of the galaxy clusters. Indeed, recent studies show that Lyα emitters have rather small stellar masses. Finkelstein et al. (2007) found

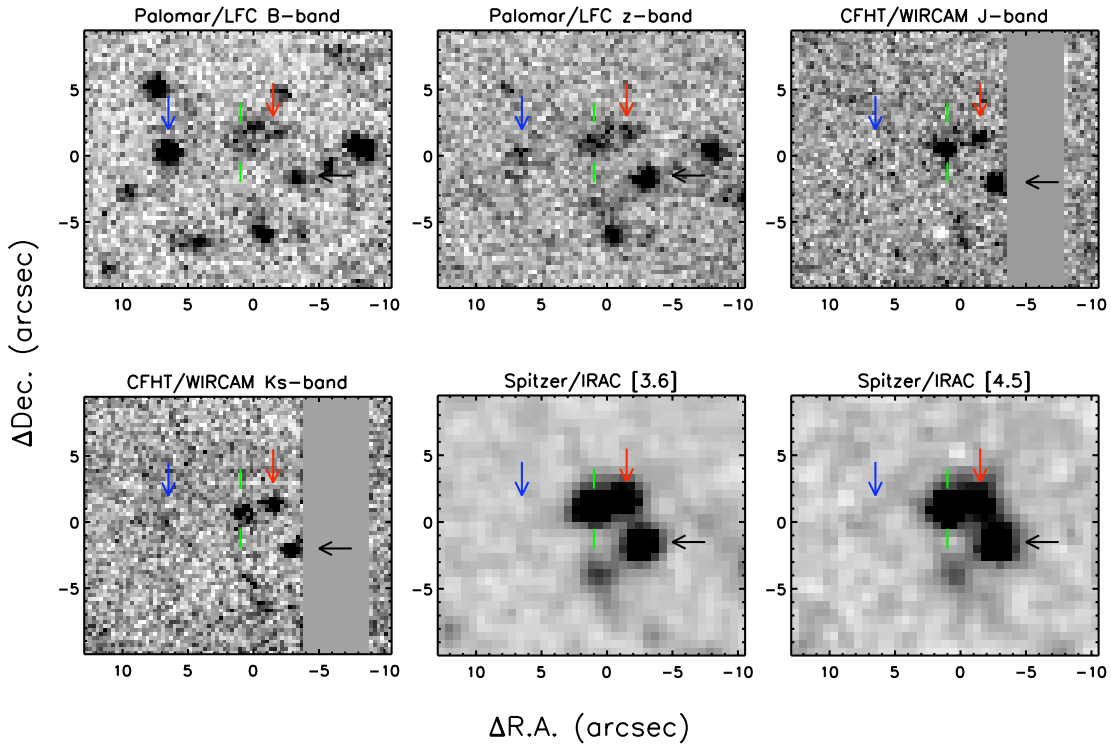

Figure 2.12. 7C 1756+6520 and its immediate surroundings in our Palomar/LFC B and z-bands, CFHT/WIRCam J and Ks-bands, and Spitzer/IRAC 3.6 μm and 4.5 μm images. North is up and East is to the left. 7C 1756+6520 is indicated by the green marks. The sBzK galaxy, pBzK galaxy and AGN candidate found near the HzRG are marked by the blue, red and black arrows, respectively.

masses ranging from 2×10^7 to $2 \times 10^9 M_\odot$ for a sample of 98 Lyα emitters at $z \sim 4.5$. Similar masses were deduced from Lyα emitters in Gawiser et al. (2007) who found stellar masses of $10^9 M_\odot$ for lower redshift objects ($z \sim 3.1$). Looking at the properties of Lyα emitters, members of a protocluster at $z = 4.1$, Overzier et al. (2008) derived a mean stellar mass of $\sim 10^{8-9} M_\odot$ based on stacked Ks-band images, indicating that Lyα emitters in the field and in protoclusters at high redshift have similar masses. Kurk et al. (2004a) used near infrared magnitudes to derive the stellar masses of Hα emitters found in the overdensity surrounding PKS 1138-262, a well known protocluster at $z = 2.16$, and found that Hα emitters are more massive than Lyα emitters, with a stellar mass $\sim 2 \times 10^{10} M_\odot$. The total stellar mass derived from both Lyα and Hα emitters around PKS 1138-262 (40 sources) is $\sim 10^{12} M_\odot$ (Kurk et al. 2004a). The mass function of galaxy clusters is in fact dominated by the evolved galaxy population, known to be rarer but much more massive than the narrow-band emitters (e.g., for $Ks < 21.5$, $M_{stars} > 10^{11} M_\odot$; Kodama et al. 2007). If at $z \sim 1.5$, the two objects with $Ks = 20$ found within 3′ of 7C 1756+6520 would each have a stellar mass of $5 \times 10^{11} M_\odot$ and would therefore already have a mass equivalent to all the narrow-band emitters found near PKS 1138-262. It is therefore essential to search for this population of red elliptical galaxies to fully understand the earliest phases of cluster formation.

Our study makes use of wide-field optical and near-infrared cameras and permits the investigation of the spatial distribution of potential cluster members over a large area around the HzRG. Indeed, the small field of view of the previous generation of near-infrared instruments limited

the study of large-scale structures, clusters and protoclusters. Recently, Tanaka et al. (2007) presented a study of a large-scale structure around a galaxy cluster at $z = 1.24$ with a possible large (20 Mpc) filamentary structure formed by the main cluster and four possible associated clumps of red galaxies, illustrating the necessity to look at galaxy clusters on larger scales than the cluster itself. The 7C 1756+6520 field presents several overdensities of red objects separated by several arcmin, as well as one nearby the HzRG. However, spectroscopic confirmation of these extended structures being associated and at high redshift is challenging due of the required large field of view on a multi-object spectrograph, and the high redshift which places the main spectral features (emission lines for star-forming and breaks for elliptical galaxies) out of the optical bands. This will hopefully be achieved with the new generation of multi-object, near-infrared spectrographs (e.g. MOIRCS on Subaru).

Acknowledgements: We are very grateful to S. Adam Stanford for useful discussions and Tadayuki Kodama for having provided the models of red sequences presented in this work. We thank Brigitte Rocca-Volmerange for her support of this project. We would also like to thank Andrea Grazian (and the GOODS-MUSIC team) and Ryan Quadri (and the MUSYC survey team) for useful emails exchanges on their online catalogues. This work is based in part on data products produced at the TERAPIX data center located at the Institut d'Astrophysique de Paris and generated from observations obtained at the Canada-France-Hawaii Telescope (CFHT) which is operated by the National Research Council of Canada, the Institut National des Sciences de l'Univers of the Centre National de la Recherche Scientifique of France, and the University of Hawaii. It is also based on observations obtained at the Hale 200 inch telescope at Palomar Observatory and on observations made with the *Spitzer Space Telescope*, which is operated by the Jet Propulsion Laboratory, California Institute of Technology under a contract with NASA.

2.8 Appendix: Complementary study of 7C 1805+6332 (z = 1.84)

This appendix presents the study of the surroundings of 7C 1805+6332 (z = 1.84). This target was observed along with 7C 1756+6520 and 7C 1751+6809 as part of our CFHT/WIRCam program, described at the beginning of this chapter. They were all observed in J and Ks by WIRCam and in z by Palomar/LFC. As described earlier in the chapter, we also obtained B-band data for the two lowest redshift targets. As the results presented earlier in this chapter show, it is crucial to have a B-band to separate high redshift star-forming galaxies from low to moderate redshift ones. As we lack a B-band image of 7C 1805+6332, the analysis on this source could not be done as thoroughly as for the other two lowest redshift targets. In order to keep the uniformity of our selection criteria, we decided to keep the analysis of these two targets separately, but we here describe what we can learn using the z, J and Ks-band data only on 7C 1805+6332. We designed colour criteria relevant at the redshift of this target to isolate the passively evolving cluster members candidates. No clear excess of galaxies was found in the field bringing additional evidence that not all radio galaxies are systematically lying in overdense regions. The next sections describe the data and the colour selection we designed to select the red cluster member candidates in this particular HzRG field.

2.8.1 Target and data

We obtained J (192min) and Ks-band (53min) data of the surroundings of 7C 1805+6332 (z = 1.84; R.A.=18:05:56.88, Dec.=+63:33:13.14). The seeing was 1″ during the observations and the night was photometric. We reduced the data using the same method as for 7C 1756+6520 and 7C 1751+6809. A flag map was created to flag the crosstalk present in our data and the area of the field affected by bright stars artifacts. 7% of our field was flagged. The 3σ (5σ) limiting magnitudes determined from random 1.5″ radius apertures are 24.2 (23.6) and 23.1 (22.6) for J and Ks respectively.

This target was also observed in August 2005 using the z-band filter of Palomar/LFC for 45min under non-photometric conditions and a seeing of 1″. The image was reduced the same way as the Palomar/LFC z-band data of 7C 1756+6520 and 7C 1751+6809. As for the calibration of these two other fields, we selected 66 stars with $J-K \leq -0.26$ (i.e., with a spectral type earlier than K5) and used the relation $J - K = 0.61 \times (z - K) - 0.2$ derived in §2.2.2 to find the adequate z-band photometric zeropoint (with 0.1mag uncertainty). The 3σ (5σ) limiting magnitude is 24.9 (24.4) - determined from random 1.5″ radius aperture as for the near-infrared data.

We used SExtractor to extract the source catalogues. Magnitudes in z, J and Ks were derived using the Kron aperture photometry (SExtractor MAG_AUTO parameter). For colours, we also derived photometry using a fixed 2.5″ diameter aperture. All magnitudes were corrected for Galactic Extinction (−0.04, −0.03 and −0.01 for z, J and Ks respectively) using the dust maps of Schlegel et al. (1998) assuming the extinction law of Cardelli et al. (1989). We then combined the three source catalogues. The final area covered by all three bands is 0.097 deg^2. Galaxy counts for each band are shown in Fig.2.13 compared with counts from the literature. The same counts have been used for comparison with our counts in the fields of 7C 1756+6520 and 7C 1751+6809 in §2.2.3. We therefore refer to this section for references. Counts in the field of 7C 1805+6332 are found in good agreement with the literature for the three bands.

2.8.2 Colour criteria

The 4000Å break at the redshift of our target falls between the z filter and the J filter. Such colours as $z - J$ or $z - Ks$ will therefore be efficient at isolating the more evolved 'red' population at high

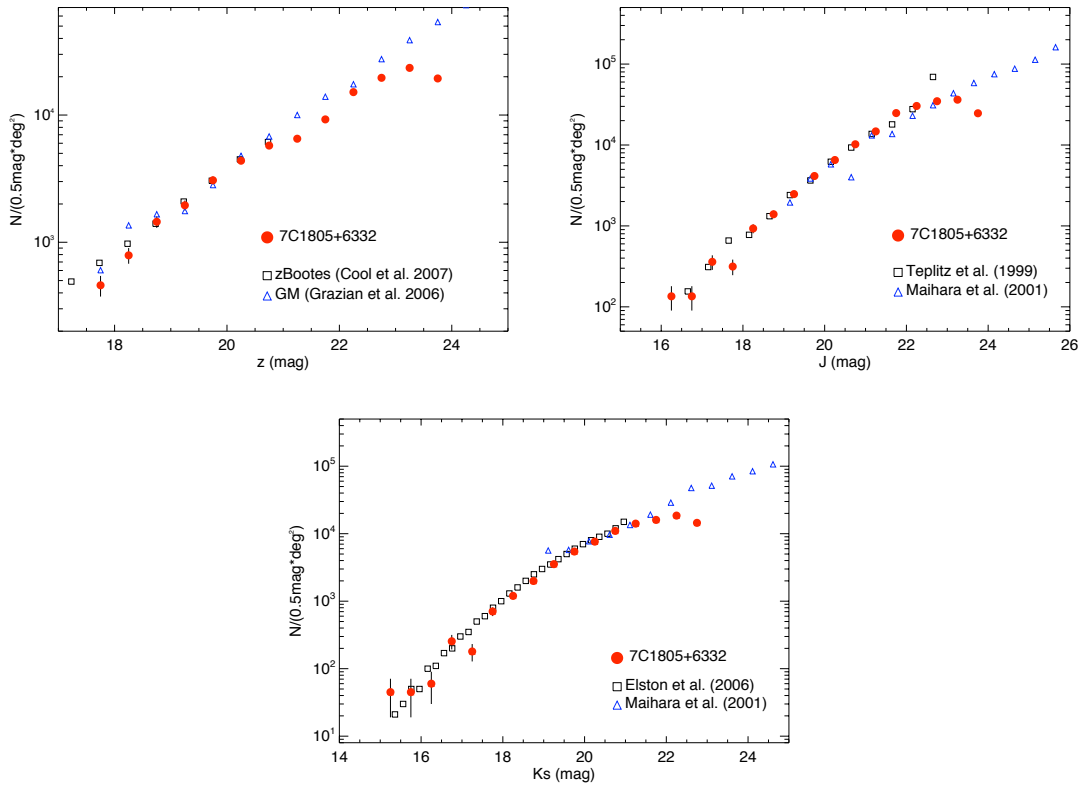

Figure 2.13. Galaxy number counts for our z, J and Ks-band data of the field around 7C1805+6332. We use the stellar index determined by SExtractor (CLASS_STAR) to separate galaxies from stars. No completeness correction was applied. We overplot number counts from the literature (see legends for symbols; GM: GOODS-MUSIC). Counts in the three bands are found consistent with results from the literature.

redshift. In the analysis of our two first targets, we combined a'red' ($z-K>2.2$) colour cut with a 'bluer' band, B, in order to select the $z>1.4$ star-forming dominated population. We unfortunately lake blue data for 7C 1805+6332. We therefore focus only on the colour selection of red passively evolving galaxies at high redshift.

We consider colours of different stellar populations using Bruzual & Charlot (2003) models. We assume a solar metallicity, and a Chabrier (2003) initial mass function. We only consider dust-free models. Fig. 2.14 shows the predictions for an exponentially declining star formation history for $\tau = 0.1$, 0.3, 0.5, 0.7, 1 and 5 Gyr for $z = 0$ to $z = 4$ in a colour-colour $z-Ks$ vs $z-J$ diagram. A constant population age of 2 Gyr was assumed. Models with very short period of star-formation history ($\tau < 0.5$), at $z > 1.5$ are found at the top right corner of the colour-colour diagram with both red $z-K$ and red $z-J$. At $z > 2.5$, the 4000Å break leaves the J-band and the colour $z-J$ starts getting bluer again. We define a 2 colour selection criterion to select red galaxies at $1.5 < z < 3$:

$$z-K \geq 2.2 \cap z-J \geq 1.4 \tag{2.1}$$

The selected zone is shown in Fig. 2.14 by the two dashed lines. We refer to this red population of galaxies as the zJK galaxies. We test this colour criterion on a sample of passive elliptical galaxies at $z > 1.4$. Cimatti et al. (2008) study the physical properties of a sample of old, passive

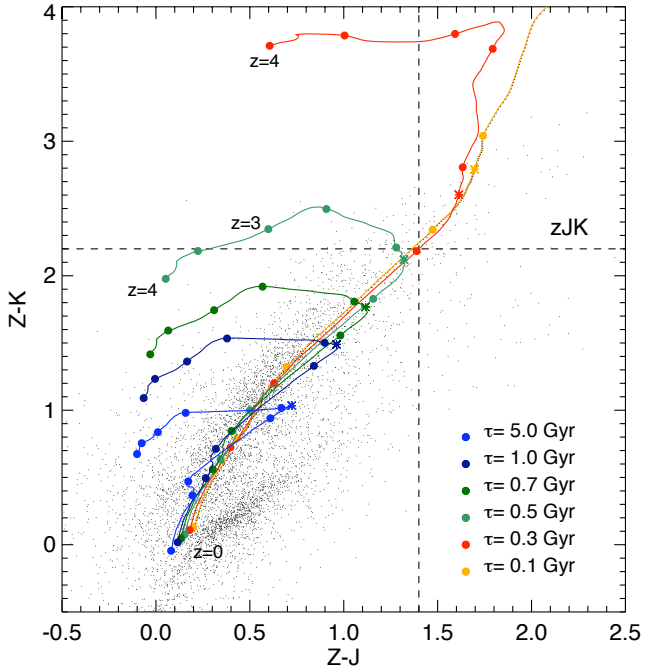

Figure 2.14. Bruzual & Charlot (2003) models predictions of different stellar populations in a $z-K$ vs $z-J$ colour-colour diagram. The dashed lines account for the 2 colour selection ($z-K \geq 2.2 \cap z-J \geq 1.4$) designed to isolate red passively evolving galaxies at $z > 1.5$. We assume an exponential declining star formation history with τ = 0.1, 0.3, 0.5, 0.7, 1 and 5 Gyr assuming a constant age of 2 Gyr. Colours at $z = 0$ to $z = 4$ by bins of 0.5 are indicated by the points along the curves. Colours at $z = 1.84$ are indicated by the stars. Sources in the field of 7C1805+6332 are overplotted in small dots for indication

galaxies with $1.39 \leq z < 2$. These galaxies were found in the Galaxy Mass Assembly ultra-deep Spectroscopic Survey (GMASS; Kurk et al. in preparation), a spectroscopic survey conducted in the GOODS-South with VLT/FORS2. They were classified as elliptical galaxies based on prominent breaks and metal absorptions present in their spectra and typical from galaxies in a passively evolving stage (e.g. B2640Å, B2900Å, MgIλ2852, MgIIλ2800, FeI and FeII lines). The $z-Ks$ colour for each galaxy is provided in Table 1 of Cimatti et al. (2008). We also cross-correlate this sample with the GOODS-MUSIC catalogue (see §2.3.1) to find their J-band magnitude. $z-J$ and $z-Ks$ colours for each source is provided in Table 2.5. All targets with $z_{spec} > 1.5$ are selected by our two-colour criterion thus proving the efficiency of this criterion.

2.8.3 Results

We apply the zJK criterion to our multiwavelength catalogue, only considering sources detected at a 3σ level in all three bands. Fig. 2.15 shows these zJK galaxies. The left panel shows how they were selected in the colour-colour $z-K$ vs $z-J$ diagram. Early-type galaxies with $z > 1.5$ from Cimatti et al 2008 are also overplotted in red squares. The right panel shows their spatial distribution around the radio galaxy. We note three large 'empty' (without small black dots) zones in this right panel of Fig. 2.15. They correspond to three extremely bright stars (2 with $J_{Vega} \sim 7$ and one 'monster' with $J_{Vega} \sim 5$ at the top left corner) that completely dominate their

Table 2.5. *zJK* colours of passive galaxies from Cimatti et al. (2008)

ID	R.A.	Dec.	z_{spec}	$z-J$	$z-Ks$
472	53.1588440	-27.7971249	1.921	1.80	2.57
996	53.1538162	-27.7745972	1.390	1.29	2.27
1498	53.1746445	-27.7533722	1.848	2.00	2.80
2111	53.1164055	-27.7126999	1.610	1.61	2.52
2148	53.1512375	-27.7137375	1.609	1.83	2.71
2196	53.1527710	-27.7162437	1.614	1.64	2.51
2239	53.1304817	-27.7211590	1.415	1.56	2.39
2286	53.1249580	-27.7229443	1.604	1.51	2.53
2355	53.0596466	-27.7258034	1.610	1.74	2.30
2361	53.1085548	-27.7101574	1.609	1.81	2.71
2470	53.1421547	-27.7112675	1.416	1.45	2.14
2543	53.1496468	-27.7113838	1.612	1.97	3.20
2559	53.1764069	-27.7011585	1.981	1.77	2.81

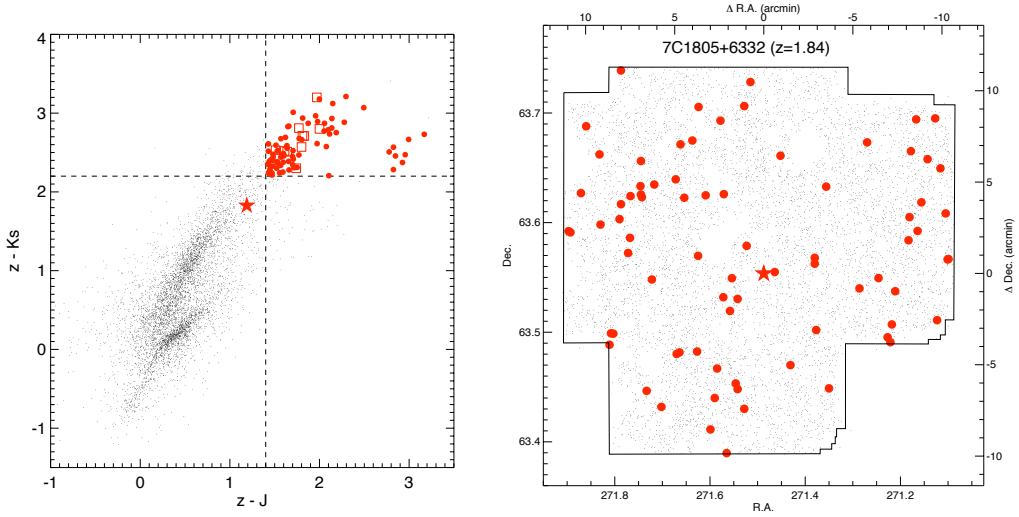

Figure 2.15. *zJK*-selected galaxies in the field of 7C 1805+6332. *Left:* Colour-colour diagram for 7C 1805+6332. *zJK* galaxies are shown in red points. Passive galaxies from Cimatti et al. 2008 are overplotted as red squares. The radio galaxy position is shown by the red star. *Right:* Spatial distribution of the *zJK* galaxies around the radio galaxy (red star). All sources detected at a 3σ level in all three bands are marked in small black dots.

surroundings. Coordinates and magnitudes of the zJK selected galaxies are provided in Appendix B, Table B.5. The spatial distribution of the red selected galaxies is non homogeneous with a higher density of sources detected in the North-East region of the field of view. However, the radio galaxy does not seem to lie in a specifically overdense region.

At the limit of 90% completeness of our data (i.e., 23.2, 22.8, and 22.2 in z, J and K respectively), the density of zJK galaxies is 18165 ± 430 deg^{-2}. We find densities of 24280 ± 490 deg^{-2} and 10300 ± 320 deg^{-2} for the fields around 7C 1756+6520 and 7C 1751+6809 respectively. Recent studies have shown that the red population of high redshift galaxies — pBzK galaxies (Kong et al. 2006; Hartley et al. 2008), EROs (Kong et al. 2006), DRGs (Quadri et al. 2008) — is strongly clustered. As expected for a strongly clustered population, a large field-to-field variation is observed in our three studied fields.

2.8.4 Summary

We studied the surroundings of 7C 1805+6332. We designed a two-colour criterion in order to select passively evolving galaxies at $1.5 < z < 3$ and therefore isolate the red population of a potential structure associated with the radio galaxy. However, no evidence of overdensity has been detected and we conclude that 7C 1805+6332 is not lying in an overdense region, at least as far as red sources are concerned. This result prove once more that not all radio galaxies are found in overdense regions.

Chapter 3

Spectroscopic confirmation of a galaxy cluster associated with 7C 1756+6520 at $z = 1.416$

Abstract.

We present spectroscopic follow-up, obtained with the DEIMOS optical multi-object spectrograph on the Keck 2 telescope, of an overdensity of galaxies photometrically selected to be at $1.4 < z < 2.5$ found in the vicinity of the radio galaxy 7C 1756+6520 at $z = 1.4156$. We observed a total of 129 *BzK*-selected sources, comprised of 82 blue, star-forming galaxy candidates (s*BzK*) and 47 red, passively-evolving galaxy candidates (p*BzK**), as well as 11 mid-infrared selected AGN candidates. We derive spectroscopic redshifts for 36 blue galaxies, 7 red galaxies and 9 AGN candidates. Assuming we identified redshifts for all of the foreground interlopers, we find that only 16% (9%) of the s*BzK* (p*BzK**) galaxies are at $z < 1.4$. Therefore, the *BzK* criteria are shown to be relatively robust at identifying galaxies at moderate redshifts. Twenty-one galaxies, including the radio galaxy, four additional AGN candidates and three red galaxy candidates, are found with 1.4156 ± 0.025, forming a large scale structure at the redshift of the radio galaxy. Of these, eight have projected offsets < 2 Mpc relative to the radio galaxy position and have velocity offsets < 1000 km s^{-1} relative to the radio galaxy redshift. This confirms that 7C 1756+6520 is indeed associated with a high-redshift galaxy cluster. A second compact group of four galaxies is found at $z \sim 1.437$, forming a sub-group offset by $\Delta v \sim 3000$ km/s and approximately 1.5 east of the radio galaxy.

Audrey Galametz, Daniel Stern, S. Adam Stanford
Carlos De Breuck, Joël Vernet
Roger Griffith, Fiona Harrison

To be submitted to A&A.

3.1 Introduction

Galaxy clusters provide an important tool for studying both the formation of galaxies and for deriving cosmological parameters. Out to furthest redshifts studied thus far, the oldest, most massive galaxies reside within clusters, and thus clusters provide ideal probes of the formation and evolution of galaxies. Relatedly, as the largest collapsed structures in the universe, the cosmic history of galaxy clusters is sensitive to key cosmological parameters (e.g., Vikhlinin et al. 2009; Stern et al. 2009). Significant work has been done to discover more and more distant galaxy clusters. However, the number of clusters currently confirmed at $z > 1$ remains low. Two of the most distant confirmed galaxy clusters were identified from the extended X-ray emission of their intracluster medium: XMMU J2235.3-2557 at $z = 1.39$ (Mullis et al. 2005; Lidman et al. 2008; Rosati et al. 2009) and XMMXCS J2215.9-1738 at $z = 1.46$ (Stanford et al. 2006; Hilton et al. 2007). However, the X-ray identification of higher redshift systems becomes difficult at $z > 1.3$ since the surface brightness of the extended X-ray emission fades as $(1 + z)^4$.

Another method to find galaxy clusters has been to detect overdensities of red sources in optical imaging data using the so-called 'red sequence method'. Gladders & Yee (2000) showed that two filter imaging is sufficient to perform a cluster search through the detection of the red sequence of early-type galaxies. The colours of such galaxies are quite distinct due to the strong 4000Å break (D4000) in their spectra. However, this break shifts into the near-infrared at $z > 1.5$. Using sensitive mid-infrared data obtained with the *Spitzer Space Telescope*, the *Spitzer* Adaptation of the Red-Sequence Cluster Survey (SpARCS; Wilson et al. 2009) team have recently pushed the technique to higher redshift and confirmed one galaxy cluster at $z = 1.34$. Relatedly, but using photometric redshifts for effectively a mass-selected galaxy sample, (Eisenhardt et al. 2008) have identified 106 galaxy cluster candidates at $z > 1$, 12 of which have been spectroscopically confirmed to date. This technique, which does not restrict their sensitivity to only the oldest galaxies, has confirmed three galaxy clusters at $z > 1.3$, with the most distant at $z = 1.41$ (Stanford et al. 2005).

An alternative method to find high-redshift galaxy clusters is to look in the surroundings of powerful, high-redshift radio galaxies (HzRGs). HzRGs are among the most massive galaxies in the Universe ($M_{\rm star} > 10^{11}\ M_{\odot}$; Seymour et al. 2007) and therefore are likely to inhabit dense regions. Narrow-band imaging surveys have been intensively conducted in the surroundings of HzRGs, mostly at $z > 2$ to search for overdensities of Lyα and/or Hα emitters. Numerous overdensities have been detected and spectroscopically confirmed around radio galaxies at $z > 2$, reaching even to $z = 5.2$ (TN J0924-2201; Venemans et al. 2007). However, Lyα emitters are small, faint, young star-forming galaxies with masses of a few $\times\ 10^8$ $M_{\odot}$ (Overzier et al. 2008) and probably represent only a small fraction of the total mass of these clusters. Furthermore, at such high redshifts, these overdensities are suspected to still be forming and not yet bound. The term 'protoclusters' is commonly used to describe such systems. A complementary approach is to isolate the evolved, massive galaxy population near HzRGs using purely near-infrared colour selection (Kajisawa et al. 2006; Kodama et al. 2007). Though this method has successfully found overdensities of red galaxies at $z \sim 2$, it has been challenging to spectroscopically confirm their association with the HzRGs (e.g., Doherty et al. 2010). A few studies have also applied related methods to slightly lower redshift HzRGs — e.g., Stern et al. (2003) and Best et al. (2003) found overdensities of extremely red galaxies in the environments of radio-loud active galactic nuclei (AGN) at $z \sim 1.5$.

Chapter 2 (Galametz et al. 2009) presented an overdensity of galaxy candidates at $z > 1.4$ in the field of the radio galaxy 7C 1756+6520. The radio galaxy was initially reported to be at

$z = 1.48$ by Lacy et al. (1999) based on the tentative identification of a single, uncertain emission feature. Based on deeper Keck spectroscopy, we find that the radio galaxy is, in fact, at $z = 1.4156$ (see §3.3.1). In chapter 2, we made use of a revised version of the so called 'BzK criteria', a two-colour selection technique based on BzK photometry (Daddi et al. 2004) to isolate galaxies at $1.4 \leq z \leq 2.5$ and classify them as either red, passively evolving (pBzK) or blue, star-forming (sBzK) systems. The star-forming candidates are selected by $BzK \equiv (z - K) - (B - z) > -0.2$. The original Daddi et al. (2004) criterion selected passive (pBzK) systems by $BzK < -0.2 \cap (z - K) > 2.5$, but was empirically shown in chapter 2 to have a low success rate at $z \sim 1.4$. In chapter 2, we therefore extended the selection criteria to reliably idenfify galaxies at the low-redshift end of the BzK criteria by defining pBzK* galaxies to have $BzK < -0.2 \cap (z - K) > 2.2$.

In chapter 2, we selected sBzK and pBzK* galaxies in the field around 7C 1756+6520 using deep, multiwavelength data: B-band and z-band images from the Large Format Camera (LFC; Simcoe et al. 2000) on the Palomar 5m Hale telescope and a Ks-band (hereafter K) image from the Wide-field Infrared Camera (WIRCAM; Puget et al. 2004) on the Canada-France-Hawaii telescope (see chapter 2, Table 3.1 for details of the dataset).

Relative to the four deep MUSYC blank fields (Gawiser et al. 2006; Quadri et al. 2007), chapter 2 reports an overdensity of cluster member candidates around 7C 1756+6520 for both sBzK and pBzK* galaxies — by a factor of 2 and 4.7, respectively. Using the *Spitzer*/IRAC colour-colour selection of Stern et al. (2005), we also isolated 12 mid-infrared selected AGN candidates around 7C 1756+6520, which represents an overdensity by a factor of two compared to the IRAC Shallow Survey (Eisenhardt et al. 2004).

We describe in this chapter the results of our spectroscopic follow-up of the overdensity found in the surroundings of 7C 1756+6520. The next section presents the selected targets, observations and data reduction. Section 3.3 describes the results of our spectroscopy and presents the redshift distribution of the observed sources. Section 3.4 reports the discovery of a concentration of 20 galaxies whose redshifts are close to that of the radio galaxy. We assume a ΛCDM cosmology with $H_0 = 70$ km s^{-1} Mpc^{-1}, $\Omega_m = 0.3$ and $\Omega_\Lambda = 0.7$. The magnitudes are expressed in the AB photometric system unless otherwise stated.

3.2 Keck/DEIMOS Spectroscopy

In order to examine whether the detected overdensities were indeed associated with 7C 1756+6520, we started a spectroscopic follow up campaign at the Keck 2 telescope using the Deep Imaging Multi-Object Spectrograph (DEIMOS; Faber et al. 2003).

We observed one slit mask on UT 2008 August 31 using the 600ZD grating which is blazed at 7500 Å, covers a typical wavelength range of 5000 − 10000 Å, and has a spectral resolution of 3.7 Å (FWHM). This slitmask targeted 47 sources, including one AGN candidate, 22 sBzK galaxies and 24 pBzK* galaxies. Eight 1800s exposures were obtained over the course of three nights using the same mask; conditions were clear with 0.″8 seeing on average.

Two additional slit masks were observed in September 2009, again with DEIMOS and the 600ZD grating. The first mask, observed for a total of 2.5 hr on UT 2009 September 16, contained 54 objects: the radio galaxy itself, five AGN candidates, 34 sBzK galaxies and 14 pBzK* galaxies. This slit mask was orientated so that a pBzK* galaxy 3″ south-west of 7C 1756+6520 was on the same slitlet as the radio galaxy itself (e.g., PA= −61.57°). The second slit mask, observed for a total of 1.75 hr on UT 2009 September 17, contained 56 sources: seven AGN candidates, 36 sBzK galaxies and 13 pBzK* galaxies. Both nights were exceptional, with photometric conditions and 0.″5 seeing.

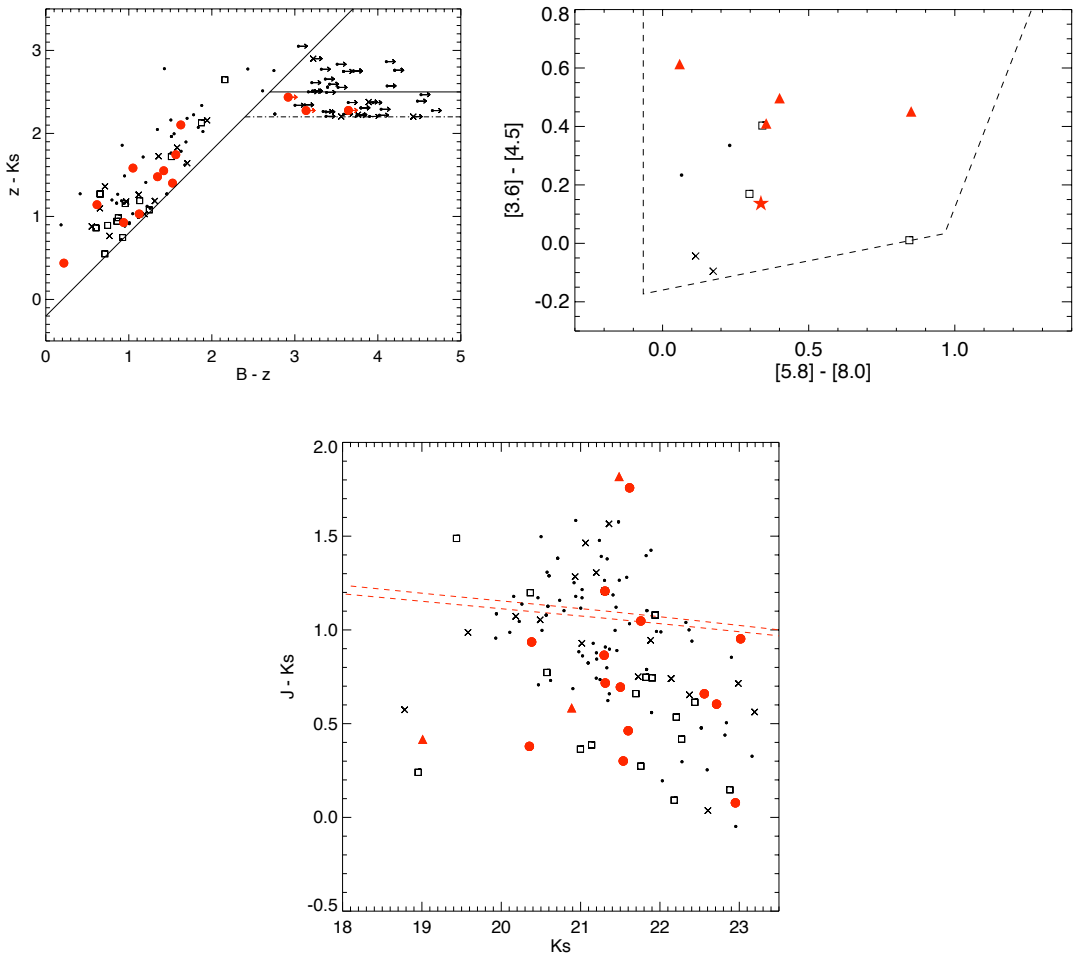

Figure 3.1. Keck/DEIMOS spectroscopic targets. *Top Left:* Distribution of targeted *BzK* galaxies in the modified Daddi et al. (2004) '*BzK*' diagram. *Top Right:* Distribution of targeted AGN candidates and 7C 1756+6520 (red star) in the IRAC colour-colour diagram from Stern et al. (2005). *Bottom:* Colour-magnitude diagram ($J - K$ vs. K) of spectroscopic targets with reliable J and/or K photometry. We also plot the expected locations of the red sequence at $z = 1.42$ (dashed line) for a formation redshifts of $z_f = 4$ (lower curve) and $z_f = 5$ (upper curve). For the three panels, small dots indicate all sources observed but not yielding a redshift. Spectroscopically confirmed members of the structure around 7C 1756+6520 (e.g., with $| z - z_{\rm HzRG} | < 0.03$) are indicated by red symbols (points for *BzK*-selected galaxies and triangles for AGN candidates). Other sources with spectroscopic redshifts are indicated by crosses and squares for background and foreground sources, respectively.

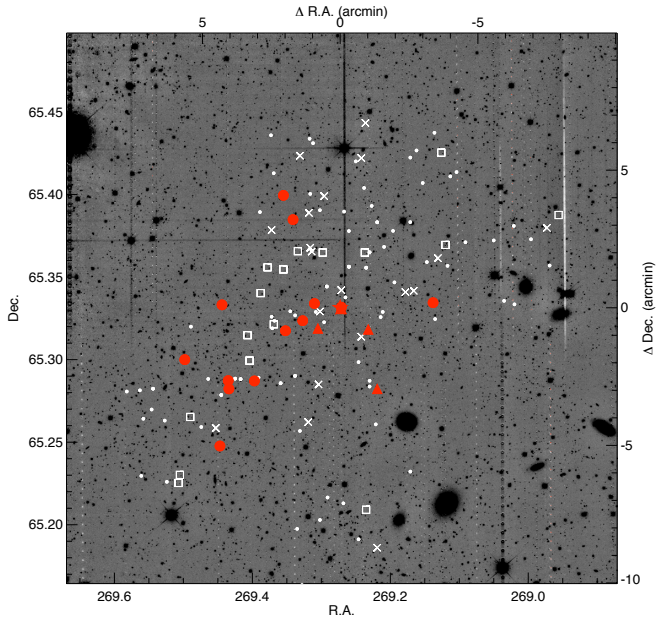

Figure 3.2. *J*-band image of 7C1756+6520 (red star) illustrating the spatial distribution of our targets. See Fig. 3.1 for description of symbols. Left and bottom axes are in J2000 coordinate system; right and top axes indicate distances relative to the radio galaxy. Image is $20' \times 20'$ and was obtained with WIRCAM on CFHT.

Fourteen *BzK* galaxies and two AGN were observed multiple times across these three slit masks. Thus, the total number of distinct targets was 129 *BzK*-selected targets — including 82 (47) s*BzK* (p*BzK**) galaxies — as well as 11 AGN candidates and the radio galaxy itself. Fig. 3.1 shows the distribution of the targets in the two colour-colour diagrams used in chapter 2 to select candidate cluster members: the '*BzK*' diagram for the *BzK*-selected galaxies and the IRAC [3.6] – [4.5] vs. [5.8] – [8.0] diagram for the mid-infrared selected AGN. We refer to chapter 2 for details on the selection techniques. The last panel of Fig. 3.1 shows the distribution of our targets in a $J-K$ vs. K colour-magnitude diagram. Fig. 3.2 shows the spatial distribution of these targets around the radio galaxy. The targeted sources have optical magnitudes in the range $20.8 < z < 24.5$ with $\langle z \rangle \sim 23.6$ and near-infrared magnitudes in the range $20.2 < K < 23.3$ with $\langle K \rangle \sim 21.6$.

All data were processed using a slightly modified version of the pipeline developed by the DEEP2 team at UC-Berkeley, and data were flux calibrated using archival sensitivity functions for the same instrument configuration derived using standard stars from Massey & Gronwall (1990).

3.3 Results

3.3.1 Spectrum of 7C 1756+6520

Lacy et al. (1999) tentatively assigned $z = 1.48$ to the radio galaxy based on an uncertain emission line at 6005 Å assumed to be [NeIV]λ2425Å. This redshift was assigned a quality 'γ', indicating an 'uncertain' redshift. We obtained a quick (10 min) spectrum of the radio galaxy during twilight on UT 2009 April 27 using the Low Resolution Imaging Spectrometer (LRIS; Oke et al. 1995) on the Keck 1 telescope. These data detected only a single, faint emission line at 6759 Å from

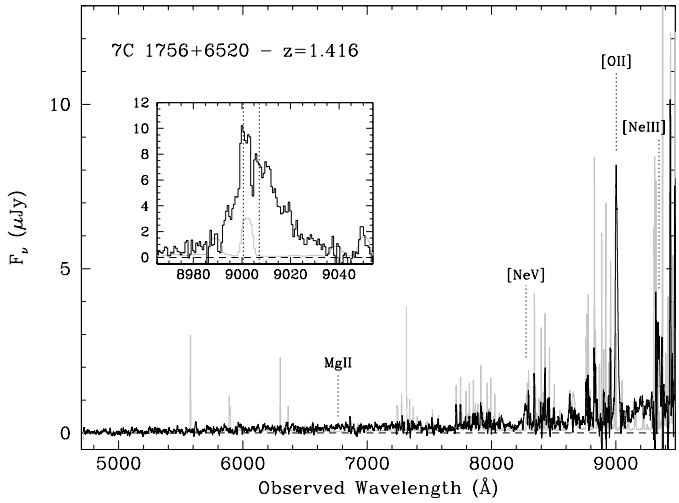

Figure 3.3. Keck/DEIMOS spectrum of 7C 1756+6520 obtained on UT September 16 (black, with a smoothing box of 13 Å applied for clarity in the large panel; the inset, detailing the [OII] doublet, was not smoothed). The sky spectrum, in grey, has been scaled down by a factor of 10. The locations of prominent lines are labeled (MgII is not detected in these data).

which no reliable redshift could be assigned. The deeper Keck/DEIMOS spectrum obtained in September 2009 (Fig. 3.3) yielded a redshift of 1.4156 based on three clearly detected emission lines: [NeV]λ3426Å, [OII]λ3727Å and [NeIII]λ3869Å. The [OII] line (Fig. 3.3, inset) is clearly split in these data. In retrospect (and as we hypothesized earlier, albeit uncertainly), the faint emission line in the LRIS spectrum in fact corresponds to MgIIλ2800Å. We note that the emission line in Lacy et al. (1999), from which their redshift identification was based, is not detected in either of our deeper Keck spectra. It would correspond to restframe 2486 Å at the redshift of the radio galaxy and was therefore most likely a spurious detection.

3.3.2 Spectroscopy of candidate cluster members

The redshift range $1.4 < z < 2.5$ is often described as the 'redshift desert' because optical spectroscopic confirmation of targets in that redshift range is challenging since most of the strongest classical spectral features used to identify redshifts (e.g., [OII]λ3727Å, D4000, H$\beta\lambda$4861Å, [OIII]λ5007Å, H$\alpha\lambda$6563Å) are redshifted longward of the wavelength range where CCDs are most sensitive (e.g., 4000 – 9000 Å). DEIMOS uses a modern, red-sensitive CCD detector which, combined with the grating we had installed for these observations, provides data out to $\sim 1\ \mu$m and would, in principle, detect the [OII] emission line to $z \sim 1.7$. However, the sensitivity of the spectrograph detectors rapidly decreases at the longest wavelengths and telluric OH emission becomes progressively problematic, especially at $\lambda > 9300$ Å (corresponding to $z > 1.5$ for the [OII] line).

A visual inspection of the reduced spectra permitted us to assign spectroscopic redshifts ($z_{\rm spec}$) to 43 *BzK* galaxies, 9 AGN candidates and the radio galaxy (see §3.3.1). Due to the design of the masks and the length of the slits, we also obtained additional spectroscopic redshifts of several serendipitous sources. All measured redshifts were assigned a quality flag 'A' or 'B': 'A' indicates a highly certain $z_{\rm spec}$ based on at least two spectral features or [OII]λ3727Å being clearly identified as a doublet; 'B' indicates high-level confidence in the $z_{\rm spec}$ based on one well-detected

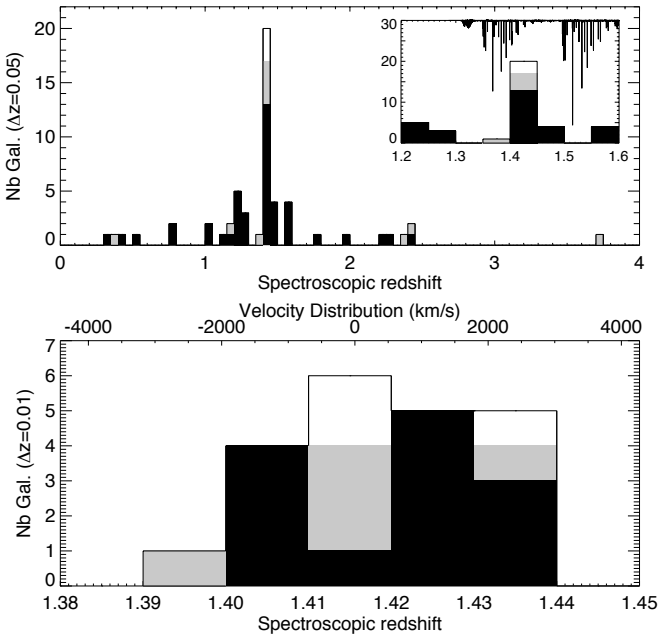

Figure 3.4. Histogram of the 52 spectroscopic redshifts, including the 43 *BzK*-selected objects (black), the nine mid-infrared selected AGNs and the radio galaxy (the AGN are all shown in grey). We also include the spectroscopic redshifts of the three serendipitous objects detected in our slits with $| z - z_{\rm HzRG} | < 0.025$ (white; see §3.4.2). The inset shows the $1.2 < z < 1.6$ redshift range with sky lines overlaid from the top axis. The bottom panel shows the spectroscopic redshift distribution near the redshift of 7C 1756+6520, with the corresponding velocity distribution relative to $z = 1.4156$ on the top axis.

spectral feature. (Lower confidence quality flags were recorded during our data analysis, but are not reported here.)

Fig. 3.4 presents the distribution of our spectroscopic redshifts. Coordinates, $z_{\rm spec}$, redshift, quality flags ('Q'), magnitudes and the target selection criteria of all confirmed sources are provided in Table 3.1 (for members of the HzRG large-scale structure) and Table 3.2 (for the foreground/background sources). The final column of these tables lists the spectral features used to determine redshifts.

BzK-selected sources

We obtained spectroscopic redshifts for 43 (33%) of the targeted *BzK*-selected sources, including 36 (44%) of the s*BzK* targets and seven (15%) of the p*BzK** targets. The majority (79%) of the redshifts were calculated from the [OII]λ3727Å doublet, which is resolved at the spectral resolution of the DEIMOS data. Other features, such as MgIIλ2798Å (either in absorption or emission) or the D4000 break, were also present in several of the spectra, permitting us to unambiguously confirm our redshift identifications.

Of the sources for which we derived successful spectroscopic redshifts, 64% (43%) of the s*BzK* (p*BzK**) galaxies are at $z_{\rm spec} > 1.4$. Based on these spectroscopic results, it is challenging to derive definitive conclusions regarding the reliability of the *BzK* criterion to select high-redshift galaxies. At $z > 1.3$, bright and numerous sky lines (see Fig. 3.4, sub-panel) coupled with de-

creasing detector sensitivity at longer wavelengths limits our ability to measure redshifts based on the [OII] doublet. Furthermore, our redshift coverage does not permit detection of [OII] at $z > 1.7$ (and at slightly lower redshifts for many sources since the spectral coverage of any given source will depend on where it is located on the slitmask). With these caveats in mind, we now briefly discuss the efficiency of the two *BzK* criteria to identify galaxies at $z > 1.4$.

sBzK galaxies: Assuming that the s*BzK* criterion successfully identifies sources with strong signatures of star formation — e.g., strong [OII], [OIII] and Hα emission lines — then our Keck/DEIMOS data should have yielded robust spectroscopic redshifts for the vast majority of s*BzK* galaxies at $z < 1.4$. Indeed, all but four of the successfully identified s*BzK* sources show these emission lines. The last four are at $1.6 < z < 2.4$ where the [OII] line had shifted beyond the spectroscopic coverage of our instrument; their redshifts were instead identified on the basis of absorption lines such as CIVλ1549 and AlIIλ1670 which are commonly seen in the UV spectra of star-forming galaxies. If we thus assume that our data identified all of the interlopers and that the failed sources are all at $z > 1.4$, then we find that the s*BzK* criterion is quite robust, with only 16% of such targets at $z < 1.4$.

pBzK galaxies:* As expected, the p*BzK** galaxies often presented very red optical continuum with no clear features (e.g., spectral breaks or emission lines) — indeed, all seven of the p*BzK** galaxies for which we did derive spectroscopic redshifts had [OII] emission features. For evolved galaxies, the D4000 break is generally the strongest spectral signature. However, assuming that a spectrum must cover out to restframe 4100 Å to robustly identify this feature, then the 1 μm cut-off of the DEIMOS data implies that we can only identify D4000 out to $z = 1.44$; we are thus forced to rely on weaker spectroscopic features such as B2640 to identify evolved galaxies at $z \sim 1.5$ and beyond. This makes redshift determinations quite challenging, and is presumably the reason for our low success rate for the p*BzK** sources. Assuming that our data identified all of the foreground interlopers and that the failed sources are all at $z > 1.4$, then we find that the p*BzK** criteria are also quite robust, with only 9% of such targets at $z < 1.4$. We note, however, that this assumption is less robust than the similar assumption for the s*BzK* galaxies.

In the colour-magnitude diagram in Fig. 3.1 (bottom panel), we show the expected location of the red sequence at $z = 1.42$ for a formation redshift $z_f = 4-5$ (T. Kodama, private communication; see also Kodama et al. 1998). We targeted numerous p*BzK** galaxies with colours consistent with the red sequence for which we unfortunately could not determine a redshift. We note however that the three p*BzK** galaxies that were confirmed to be at $z_{\rm spec} > 1.4$ all have $2.2 < z - K < 2.5$ and would have been missed by the standard Daddi et al. (2004) criterion for p*BzK* galaxies (see §3.1). Our modified p*BzK** criterion presented in chapter 2 increases the completeness of galaxies at $z > 1.4$. On the other hand, our selection is also contaminated by lower redshift (albeit still relatively distant) objects. The other four p*BzK** with $z_{\rm spec}$ are foreground interlopers with $1.18 < z < 1.26$.

Mid-infrared selected AGN candidates

Eleven of the 12 AGN candidates presented in chapter 2 were observed and we were able to assign spectroscopic redshifts for 9 of them. The AGN selection criterion of Stern et al. (2005) does not preferentially select AGN in any specific redshift range (other than an inefficiency at selecting sources at $z \sim 4$ where Hα shifts into the IRAC channel 1 and produces blue [3.6]−[4.5] colours; see Assef et al. 2010). The mid-infrared selection criteria are also sensitive to both obscured and unobscured AGN (e.g., Eckart et al. 2010). Unsurpringly, therefore, we identified AGN at a range of redshifts ($0.37 < z < 3.70$) and with a range of properties.

The three AGN at $z > 2$ are all classical (e.g., unobscured or type 1) quasars showing broad CIVλ1549Å and CIII]λ1909Å emission lines. Two AGN candidates (Table 3.1, sources 1 and 18)

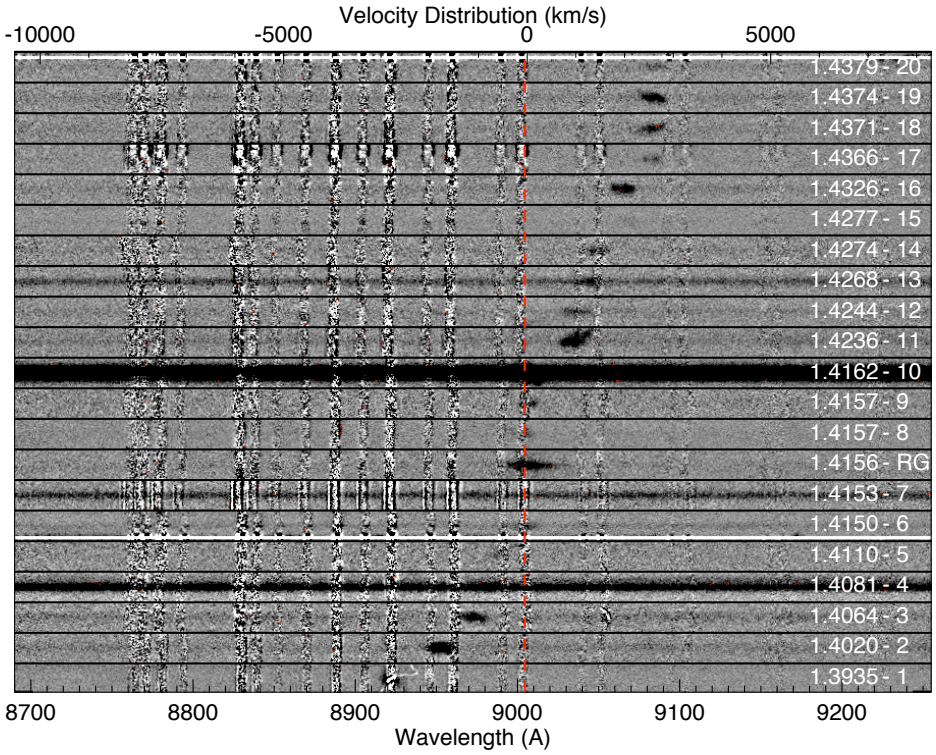

Figure 3.5. Two-dimensional spectra of the spectroscopically confirmed members of the structure, centered near the [OII] emission line. The position of the [OII] doublet at $z = 1.4156$ is indicated by the vertical red dashed line. The redshift and ID number of each source is provided on the right end side. The top axis indicates the corresponding velocity distribution relative to the redshift of the radio galaxy.

do not show any classical AGN features. The first was assigned a quality B spectroscopic redshift of 1.3935 based on a single emission line (which falls on a sky line) attributed to [OII]. Note, however, that this source also shows hints of spectral breaks at restframe 2900 Å and 3260 Å, making the inferred redshift quite likely. The second source shows a resolved [OII] doublet at $z = 1.4371$. Two AGN candidates at $z_{\rm spec} > 1$ show both the narrow [OII] doublet (which could be due to AGN activity and/or star formation) as well as broad MgII emission, which clearly indicates an AGN. Four of the mid-infrared selected AGN candidates sources are at redshifts close to the radio galaxy and are discussed more in §3.4.2 (see Table 3.1).

3.4 A structure of galaxies associated with 7C 1756+6520

3.4.1 Companions close to the radio galaxy

In chapter 2, we noted that an sBzK galaxy, a pBzK* galaxy and an AGN candidate are all found within 6″ of 7C 1756+6520. For $z = 1.4156$, this corresponds to a projected separation of 50 kpc. The probability of finding three candidates in such a small area is less than 0.2%, suggesting that these sources are all associated with the radio galaxy. Both the pBzK* and the AGN candidates were observed with DEIMOS. The pBzK* source shows a clear, resolved [OII] doublet at $z = 1.4244$, and is thus associated with the radio galaxy (Table 3.1, ID 12; quality A). The AGN candidate shows a single, broad emission line which we interpret to be MgII at $z = 1.4153$ (Table 3.1, ID 7; quality B). The sBzK galaxy was not observed. We therefore believe that the radio

galaxy has at least one, most probably two, and perhaps three close-by companions.

3.4.2 Two compact sub-groups in a large scale structure

A clear peak is seen in the spectroscopic redshift distribution near the radio galaxy redshift (Fig. 3.4). Not including the HzRG, 20 galaxies are found with $|z - z_{\rm HzRG}| < 0.025$, corresponding to peculiar velocities $\lesssim 3000$ km s^{-1} with respect to the radio galaxy. Table 3.1 reports the coordinates and BzK magnitudes of these 20 galaxies (21 including the HzRG), comprised of four mid-infrared AGN candidates, three pBzK* galaxies, 10 sBzK galaxies and three serendipitous galaxies. The first serendipitous galaxy, Cl1756.6 (or serendip.1), is blended in all of our imaging bands with an object at $z = 0.76$. The foreground object, whose photometry is contaminated in all three bands by its projected neighbor, was one of our targeted sBzK galaxies. The second (Cl1756.8, or serendip.2) was observed in the same slit as Cl1756.9, one of the sBzK targets. The two sources are close both on the plane of the sky and in redshift, and are therefore close-by companions. Cl1756.8 is very faint at K (detected at $< 2\sigma$) and was not considered by our BzK criteria. The last serendipitous object (Cl1756.20, or serendip.3) was not selected by any of our criteria. Coordinates and magnitudes of pBzK* galaxies, sBzK galaxies and AGN are also reported in Table B.1, Table B.2 and Table 2.3 respectively. They are identified by the same ID number in both these tables and Table 3.1, column 2 i.e. Ks-band (3.6μm) ID number in our SExtractor source catalogues for BzK galaxies (AGN candidates).

The two dimensional spectra of the 20 galaxies associated with 7C 1756+6520 are shown in Fig. 3.5, centered near the [OII] line used to determine their redshifts. As expected, the pBzK* galaxies (sources 5, 12 and 15) show fainter [OII] emission lines than most of the AGN or star-forming (sBzK) candidates.

There is still no clear and agreed upon definition of what comprises a galaxy cluster. Eisenhardt et al. (2008) considers a $z > 1$ cluster spectroscopically confirmed if five galaxies are robustly identified within a radius of 2 Mpc and $\pm 2000\,(1 + \langle z_{\rm spec}\rangle)$ km s^{-1}. According to this definition, 14 objects (including the radio galaxy) would therefore be part of our galaxy cluster. However, the spectroscopically-confirmed, high-redshift galaxy clusters in Eisenhardt et al. (2008) and elsewhere usually show much narrower velocity distributions. The spectroscopically confirmed members of XMMXCS J2215.9-1738 at $z = 1.457$ all have peculiar velocities offset by less than 1000 km s^{-1} with respect to the cluster redshift (Hilton et al. 2007). Recently, Hayashi et al. (2009) presented an [OII] emission survey of this same cluster. They identified 44 [OII] emitters in the cluster with $\Delta v < 2000$ km s^{-1} with respect to the cluster redshift.

The spatial distribution of the 20 objects is shown in Fig. 3.6 (the 17 red symbols in Fig. 3.2 and the three additional serendipitous objects). Seven galaxies (IDs 6 – 12) have velocities within 1000 km s^{-1} of the radio galaxy redshift (i.e., the assumed cluster redshift) and are found within 2 Mpc of the HzRG (yellow circles; $1.415 \leq z \leq 1.424$). The lowest redshift sources (IDs 1 – 5; blue circles; $z < 1.415$) are found with projected separations more than 1 Mpc with respect to the radio galaxy (3/5 beyond 2 Mpc). Objects with $1.424 < z < 1.436$ (IDs 13 – 16; green circles) are all more than 2 Mpc distant from the radio galaxy. In contrast, the highest redshift sources (IDs 17 – 20; orange circles; $z \geq 1.436$) are found within 1′ from each other and appear to form a compact sub-structure. We therefore confirm that 7C 1756+6520 is part of a large scale structure of galaxies composed of (at least) two main galaxy groups — the galaxy cluster centered on the radio galaxy redshift ($z = 1.4156$) and a compact galaxy sub-group at $z \sim 1.437$, 1.5 east of the radio galaxy.

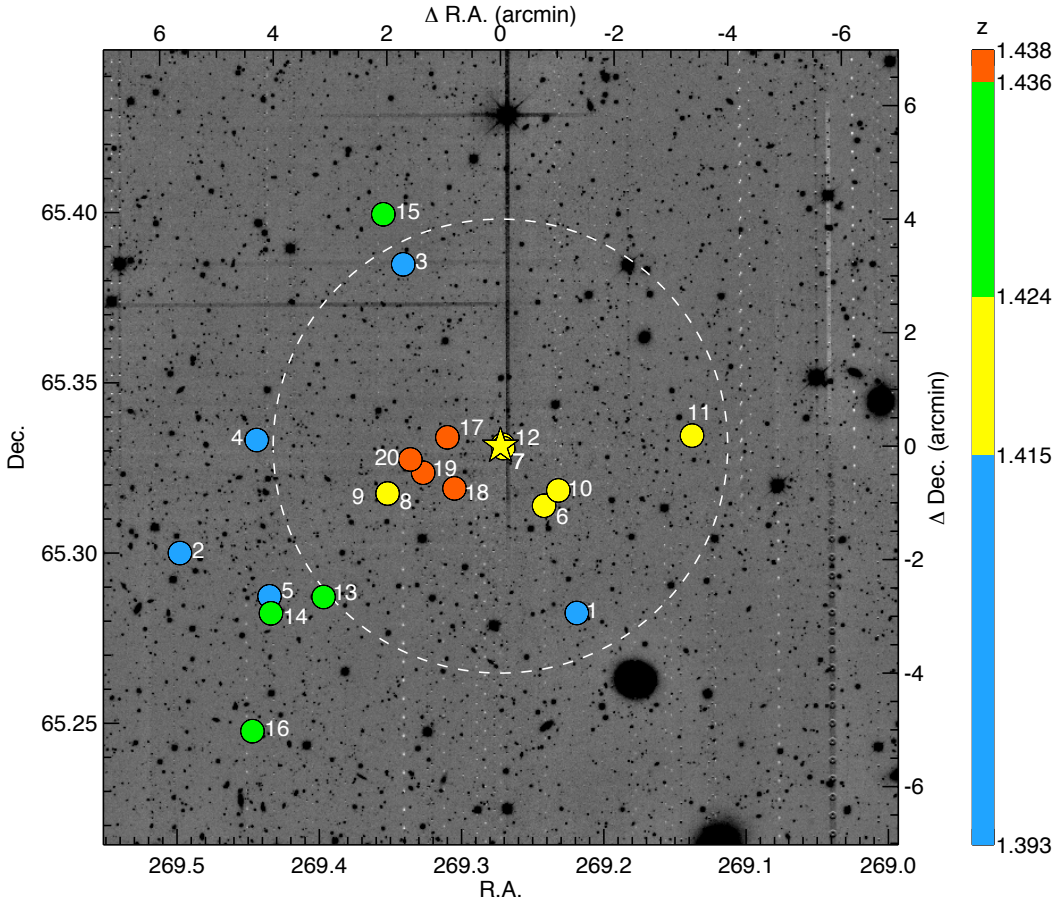

Figure 3.6. The 20 spectroscopically confirmed members of the structure around 7C 1756+6520 (plotted on our J-band data in filled symbols). The four colours (blue, yellow, green and orange, see redshift scale on the right) indicate different ranges of redshifts: $z < 1.415$, $1.415 \leq z \leq 1.424$, $1.424 < z < 1.436$ and $z \geq 1.436$ respectively. ID numbers from Table 3.1 are also provided for each source. The dashed circle indicates a distance of 2 Mpc from the radio galaxy.

3.4.3 A high fraction of AGN cluster members

Four mid-infrared AGN candidates have been confirmed to be associated with 7C1756+6520 (IDs 1, 7, 10 and 18). Galaxies 4 and 13, both targeted as sBzK galaxies, also show AGN signatures in their spectra with strong, broad MgII emission lines. Assuming that the mid-infrared selected sources are indeed all active, six active galaxies (seven with the radio galaxy) have therefore been spectroscopically confirmed in close proximity both spatially and in redshift space. Three of them are found within 1.5′ of the radio galaxy. Studying the surface density of luminous AGN associated with a sample of 330 galaxy clusters at $0 < z < 1.5$, Galametz et al. (2009) (see chapter 5) have found an excess of AGN within 0.5 Mpc of the center of clusters at $z > 0.5$. They identify AGN using three different selection methods including the Stern et al. (2005) mid-infrared selection. Our spectroscopy brings additional evidence that galaxy clusters at $z > 1$ have a significant fraction of members being AGN and that they lie preferentially near the cluster center.

3.5 Conclusions

The observations presented here confirm the existence of a large scale structure of galaxies associated with 7C 1756+6520. A new reliable redshift of $z = 1.4156$ has been assigned to the radio galaxy. Our optical spectroscopy demonstrates the efficiency of the BzK selection technique of Daddi et al. (2004) at finding galaxies at $z > 1.4$. It also shows that the modified pBzK* criterion presented in chapter 2 increases the completeness of galaxies at $z > 1.4$. Twenty galaxies are found with spectroscopic redshifts consistent with the redshift of 7C 1756+6520. Seven of these galaxies have velocity offsets $\Delta v < 1000$ km s^{-1} relative to the redshift of the radio galaxy (assumed here to be the galaxy structure mean redshift) and found within 2 Mpc of the radio galaxy. A second compact group of four galaxies (all within 1′ of each other) lies at $z \sim 1.437$ and forms an associated sub-group of galaxies, offset by about 1.5′ to the east of the radio galaxy. 7C 1756+6520 is therefore part of a large scale galaxy structure composed of (at least) two main groups — a galaxy cluster centered on the radio galaxy at $z = 1.4156$ (with 8 spectroscopically confirmed members including the radio galaxy) and a compact group at $z \sim 1.437$ (i.e., offset by $\Delta v \sim 3000$ km/s), 1.5′ east of the radio galaxy (with 4 confirmed members so far).

Acknowledgements: This work is based on a spectroscopic campaign at the W. M. Keck Observatory, a scientific partnership between the University of California and the California Institute of Technology, made possible by a generous gift of the W. M. Keck Foundation. We are very grateful to Tadayuki Kodama for having provided the models of red sequence presented in this work. The work of DS and RLG was carried out at Jet Propulsion Laboratory, California Institute of Technology, under a contract with NASA. SAS's work was performed under the auspices of the U.S. Department of Energy, National Nuclear Security Administration by the University of California, Lawrence Livermore National Laboratory under contract No. W-7405-Eng-48.

Table 3.1. Spectroscopic members of the structure around 7C 1756+6520

ID	Name[a]	R.A. (J2000)	Dec. (J2000)	z_{spec}	Q[b]	B[c] (AB)	z[c] (AB)	K[c] (AB)	Notes
Cl1756.1	AGN.1110	17:56:52.56	65:16:56.65	1.3935	B	23.21	22.14	20.89	B2900, B3260, [OII]
Cl1756.2	sBzK.6355	17:57:59.55	65:18:00.64	1.4020	A	24.36	23.34	21.54	[OII]
Cl1756.3	sBzK.9622	17:57:21.75	65:23:05.04	1.4064	A	24.00	22.78	20.38	[OII]
Cl1756.4	sBzK.7556	17:57:46.54	65:20:00.48	1.4081	A	20.97	20.77	20.35	AGN: broad MgII, [OII]
Cl1756.5	pBzK.5858	17:57:44.40	65:17:14.30	1.4110	B	> 27.1	23.80	21.62	[OII]
Cl1756.6	serendip.1	17:56:57.67	65:18:49.45	1.4150	A	-	-	-	[OII]
Cl1756.7[d]	AGN.1354	17:57:04.98	65:19:51.00	1.4153	B	26.34	22.03	-	AGN: broad MgII
HzRG	7C 1756+6520	17:57:05.48	65:19:53.75	1.4156	A	> 27.1	21.40	20.17	AGN: [NeV], [OII], [NeIII]
Cl1756.8	serendip.2	17:57:25.00	65:19:04.83	1.4157	A	26.32	24.34	> 23.4	[OII]
Cl1756.9	sBzK.6997	17:57:24.43	65:19:03.87	1.4157	A	25.21	24.21	22.56	[OII]
Cl1756.10	AGN.1317	17:56:55.75	65:19:07.00	1.4162	A	20.16	19.46	19.01	AGN: broad MgII, [NeV], [OII]
Cl1756.11	sBzK.7624	17:56:33.16	65:20:04.46	1.4236	A	22.51	22.39	21.30	FeII+MgII absn, [OII]
Cl1756.12[e]	pBzK.7523	17:57:05.04	65:19:54.50	1.4244	A	> 27.1	23.47	21.31	[OII]
Cl1756.13	sBzK.5860	17:57:35.34	65:17:14.39	1.4268	A	22.96	22.35	21.31	AGN: broad MgII, [OII]
Cl1756.14	sBzK.5699	17:57:44.06	65:16:57.11	1.4274	A	25.89	24.20	22.71	[OII]
Cl1756.15	pBzK.10235	17:57:25.20	65:23:58.19	1.4277	B	> 27.1	23.45	21.76	[OII]
Cl1756.16	sBzK.4449	17:57:47.40	65:14:52.17	1.4326	A	24.93	23.89	23.02	[OII]
Cl1756.17	sBzK.7625	17:57:14.41	65:20:02.40	1.4366	A	> 27.1	24.46	22.95	[OII]
Cl1756.18	AGN.1206	17:57:13.08	65:19:08.37	1.4371	A	> 27.1	> 25.0	21.49	[OII]
Cl1756.19	sBzK.7208	17:57:18.31	65:19:24.94	1.4374	A	24.93	23.46	22.00	[OII]
Cl1756.20	serendip.3	17:57:20.76	65:19:39.14	1.4379	A	25.29	23.18	21.50	[OII]

[a] The names are composed of the selection technique for the source — AGN, sBzK or pBzK (≡ pBzK* here) — followed by the identification number in our K-band (3.6μm) catalogue for BzK (AGN) targets. Sources serendipitously identified are given a simple 'serendip.#' designation.

[b] Q indicates the quality of the redshift, either 'A' indicating a highly certain redshift, or 'B' indicating a high level of confidence (see §3.3.2).

[c] Magnitudes were derived using SExtractor MAG_AUTO and are therefore slightly different from the aperture magnitudes used to derive colours for candidate selection.

[d] AGN found within 6″ of 7C 1756+6520. No accurate magnitude is available in K due to artifact due to a bright star in the near-infrared data. See Fig. 2.12.

[e] pBzK* galaxy found within 3″ of 7C 1756+6520.

Table 3.2. Other spectroscopic redshifts

Name[a]	R.A. (J2000)	Dec. (J2000)	z_{spec}	Q[b]	B[c] (AB)	z[c] (AB)	K[c] (AB)	Notes
sBzK.8902	17:57:15.84	65:22:04.07	0.335	B	24.28	22.93	21.88	[OIII]
AGN.1005	17:57:05.48	65:19:53.75	0.366	A	22.25	19.51	18.78	CaHK, Hβ, Hα, [NII]
sBzK.4858	17:57:48.87	65:15:31.59	0.427	A	24.18	22.85	22.14	[OII], Hβ, [OIII], Hα
sBzK.9364	17:57:29.28	65:22:42.61	0.530	B	> 27.1	23.62	21.06	[OIII]
sBzK.7895	17:57:05.04	65:20:31.57	0.753	A	22.70	21.75	20.94	[OII], Hβ
sBzK.6858	17:56:58.08	65:18:50.05	0.760	B	23.06	23.11	21.02	[OII]
sBzK.7921	17:56:39.84	65:20:30.52	1.020	A	22.73	23.67	22.79	[OII], [NeIII]
sBzK.11226	17:57:19.44	65:25:24.60	1.050	A	24.45	23.83	23.19	[OII], [NeIII], Hβ
sBzK.9844	17:57:16.38	65:23:19.85	1.122	A	26.00	24.18	21.99	[OII]
pBzK.7866	17:56:42.72	65:20:27.97	1.181	B	> 27.1	23.11	20.93	[OII]
AGN.1767	17:57:15.33	65:21:56.14	1.183	A	> 27.1	> 25.0	19.58	MgII, [OII]
sBzK.9430	17:55:53.37	65:22:48.02	1.208	A	23.44	22.79	21.73	AGN: MgII absn, [OII], [NeIII], Hζ, Hδ
pBzK.7359	17:57:12.44	65:19:45.10	1.212	A	26.65	22.63	20.18	[OII]
pBzK.4948	17:57:16.54	65:15:44.17	1.213	A	> 27.1	22.79	20.49	[OII]
sBzK.11168	17:56:57.97	65:25:20.26	1.236	A	25.46	23.93	22.37	[OII]
sBzK.12407	17:56:56.58	65:26:36.42	1.247	A	25.02	24.33	22.99	[OII]
sBzK.8631	17:56:31.31	65:21:41.17	1.259	A	23.90	23.06	21.36	[OII]
pBzK.10254	17:57:11.04	65:23:56.76	1.260	A	> 27.1	23.40	21.20	[NeV], [OII], [NeIII]
sBzK.2137	17:56:52.56	65:11:09.95	1.283	A	24.09	23.96	22.61	Hβ, [OIII], [NII]
sBzK.8410	17:57:25.15	65:21:18.01	1.456	A	25.37	23.75	21.90	[OII]
sBzK.7159	17:57:28.56	65:19:17.93	1.458	A	24.70	23.05	22.44	[OII]
sBzK.6886	17:57:37.75	65:18:53.95	1.466	A	25.82	23.25	21.70	[OII]
sBzK.8761	17:56:57.03	65:21:53.86	1.477	A	23.35	22.83	20.37	[OII]
sBzK.8799	17:57:11.43	65:21:53.94	1.559	A	23.59	22.26	21.14	CIII], MgII abns, [OII]
sBzK.2998	17:56:56.40	65:12:32.76	1.560	A	24.19	23.79	22.88	[OII]
sBzK.9006	17:56:28.73	65:22:10.94	1.594	A	22.95	22.84	22.27	[OII]
sBzK.9788	17:55:49.35	65:23:16.14	1.595	A	23.93	22.98	22.18	FeII+MgII absn
sBzK.11725	17:56:30.31	65:25:31.69	1.762	B	22.35	21.78	21.00	AGN: MgII
sBzK.5102	17:57:57.61	65:15:55.59	1.985	A	23.59	22.84	22.21	AlII, MgII
sBzK.6330	17:57:37.08	65:17:58.83	2.217	A	23.82	23.23	21.94	AGN: CIV, CIII], MgII
sBzK.3534	17:58:01.74	65:13:31.73	2.264	A	23.73	22.84	21.82	CIV+AlII absn
AGN.1748	17:57:20.07	65:21:56.96	2.399	A	23.06	21.39	20.58	Quasar: CIV, CIII]
AGN.1340	17:57:30.88	65:21:22.32	2.401	A	24.05	21.80	19.44	Quasar: CIV, CIII]
sBzK.3718	17:58:01.19	65:13:49.25	2.402	A	22.65	21.75	21.76	CIV+AlII absn
AGN.1213	17:57:33.22	65:20:26.24	3.702	A	22.73	19.72	18.95	Quasar: Lyα, CIV, CIII]

[a] The names are composed of the selection technique for the source — AGN, sBzK or pBzK (≡ pBzK* here) — followed by the identification number in our K-band (3.6μm) catalogue for BzK (AGN) targets. Sources serendipitously identified are given a simple 'serendip.#' designation.

[b] Q indicates the quality of the redshift, either 'A' indicating a highly certain redshift, or 'B' indicating a high level of confidence (see §3.3.2).

[c] Magnitudes were derived using SExtractor MAG_AUTO and are therefore slightly different from the aperture magnitudes used to derive colours for candidate selection.

Chapter 4

Galaxy cluster candidates at $1.6 < z \lesssim 2$

Abstract.

We present a study of the surroundings of two high redshift radio galaxies, MRC 1017-220 (z = 1.77) and MRC 0156-252 (z = 2.02). The two fields were imaged using the near-infrared wide-field ($7.5' \times 7.5'$) imager VLT/HAWK-I in Y, H and Ks. We develop a purely near-infrared colour selection technique using $YHKs$ photometry to isolate galaxies (both red passively evolving and blue star-forming dominated) at $1.6 < z < 3$ and thus possibly associated with our two targets. We first test our selection technique combining $YHKs$ imaging, photometric redshifts and spectroscopy available in GOODS-S. Applying the selection to our radio galaxy fields, we then find a significant overdensity of red sources around MRC 0156-252 — by a factor of two to three compared to our control fields. This overdensity is more pronounced in the close vicinity of the radio galaxy (within 1 Mpc; factor of three to four). Both our targeted fields show a small excess of blue galaxies. The spatial distribution of $YHKs$-selected galaxies is not uniform with a clear and compact concentration of red objects in the immediate surroundings of MRC 0156-252. The field around MRC 1017-220, although less dense than average, shows traces of a filamentary distribution of the red galaxies. In this work, we also present the first Y-band galaxies number counts determined from all our reference fields (about 200 arcmin^2).

Audrey Galametz, Joël Vernet, Carlos De Breuck
Nina Hatch, George Miley, Bram Venemans, Tadayuki Kodama
Jaron Kurk, Alessandro Rettura, Roderik Overzier, Nick Seymour

To be submitted.

4.1 Introduction

It is now well established that the evolution of galaxies is strongly dependent on their environment. Locally, the higher density regions (e.g., core of local galaxy clusters) are dominated by red early-type galaxies, the portion of blue galaxies with on-going star-formation being significantly smaller than in the field. The spectrum of these red passive evolving galaxies shows a characteristic 4000Å break i.e., the light of the old stellar population dominates that emitted by the population of younger stars. These galaxies also form a clear red sequence in a colour-magnitude diagram of galaxy clusters. Studies have shown that this red sequence is already present in cluster of galaxies out to very high redshifts ($z \sim 1.5$; Stanford et al. 2005, 2006; Mei et al. 2006, 2009; Lidman et al. 2008; Kurk et al. 2009). But in order to understand when this red sequence actually appeared i.e., when the segregation between passive and star-forming galaxies occurred in clusters, one needs to go to higher redshifts.

However, the number of known galaxy clusters at high redshifts ($z > 1$) is still small since it becomes challenging to find them using the classical methods e.g., the detection of extended X-ray emission of the interstellar medium in clusters (Stanford et al. 2006; Rosati et al. 2004, 2009) or the use of red-sequence algorithms to point at overdense regions of red objects (Gladders & Yee 2000; Andreon et al. 2008). The two highest redshifts and most studied galaxy clusters to date were discovered through their extended X-ray emission: XMMXCS J2215.9-1738 at $z = 1.457$ (the most distant spectroscopically confirmed cluster with 17 members found within the cluster virial radius; Stanford et al. 2006; Hilton et al. 2007) and XMMU J2235.3-2557 at $z = 1.39$ whose galaxies in the core form a well defined red sequence (e.g. scatter, slope and location studied in Lidman et al. 2008). Most of the galaxy overdensities currently known at $z > 1.5$ were found in the vicinity of high-redshift radio galaxies (HzRGs hereafter). HzRGs are in fact among the most massive galaxies in the universe ($M > 10^{11} M_{\odot}$; Seymour et al. 2007) and known to be excellent markers of the highest density regions in the early universe (see Miley & De Breuck 2008 for a review on HzRGs and their surroundings). Numerous studies have been conducted in the surroundings of radio galaxies. Narrow-band surveys of emitters for $2 < z < 5$ showed that HzRGs are often found in overdense regions of narrow line emitters, the so-called 'protoclusters' likely to be the progenitors of the present day massive groups and clusters (e.g., Lyα and Hα; Venemans et al. 2002, 2005, 2007; Pentericci et al. 2000; Kurk et al. 2004b). However, these narrow line emitters are faint star-forming galaxies and do not constitute the major fraction of the total cluster mass. Based on a Ks-stacking analysis of Lyα emitters, Overzier et al. (2008) found that they seem to have masses of only a few 10^8 M$\odot$. Several studies have targeted directly the most massive evolved population of high redshift clusters at $z > 1.4$. Best et al. (2003) looked at the environment of powerful radio-loud sources at $z \sim 1.6$ and found overdensities of red galaxies ($R - K > 4$) on two scales around the AGN: a pronounced central peak (within 150 kpc) and/or weaker excesses between 1 and 1.5 Mpc radius. More recently, Galametz et al. (2009) (chapter 2) studied the surroundings of 7C 1756+6520, a radio galaxy at $z = 1.416$ and found an excess by a factor of 3 of red sources (passive elliptical candidates at $z > 1.4$) within 2 Mpc of the HzRG.

At higher redshifts ($z > 2$), studies have chased red evolved galaxies by bracketing with filters the position of the 4000Å break (shifted in the near-infrared wavelengths). Kajisawa et al. (2006) explored the surroundings of six HzRGs at $z \sim 2.5$ and isolated the evolved populations at $z > 2$, using purely near-infrared ($JHKs$) colour cuts. Kodama et al. (2007) used the same near-infrared criteria to select protocluster member candidates in the field of HzRGs at $2 < z \lesssim 3$ (see also Zirm et al. 2008 for a near-infrared study of a forming red sequence in a protocluster at $z = 2.16$). They both found overdensities in some of their targeted fields that reach a factor of 2 to 3 compared to

blank fields. Recent spectroscopy follow-up has been conducted in two of Kodama et al. (2007) protocluster fields. Doherty et al. (2010) confirm two red galaxies associated with PKS 1138-262 at $z = 2.16$ (the so-called SpiderWeb galaxy), one being a star-forming dusty galaxy and the other, evolved with only little ongoing star formation. These HzRG companions have an estimated mass of $4 - 6 \times 10^{11}$ M$\odot$. Their results also confirm that their two-colour pure near-infrared criteria is efficient at selecting galaxies at $z > 2$. However, the low success rate of their spectroscopic campaign confirms the difficulty (especially at such high redshifts) of deriving redshifts for the passively evolving population that have no characteristic features (e.g. emission lines) in their spectra.

We are carrying out a large project in order to detect and study the evolved population in clusters and protoclusters associated with high redshift radio galaxies. We built a unique well-defined sample of 10 HzRGs fields at $1.7 < z < 2.6$ that were observed with the High Acuity Wide field K-band Imager (HAWK-I) on the Very Large Telescope (VLT) in 2008 and 2009. Our sample was observed in a set of three filters ($YHKs$ or $JHKs$ depending on the redshift of the targeted radio galaxy). This first analysis will deal with the results for our two lowest redshift targets. A subsequent paper will describe the results for the higher redshifts targets (Hatch et al. in preparation).

In this work, we design a new purely near-infrared criterion to isolate galaxies at $1.6 < z < 3$. We apply this selection technique to study the galaxy population in the vicinity of the lowest redshift radio galaxies of our HAWK-I sample: MRC 1017-220 ($z = 1.77$) and MRC 0156-252 ($z = 2.02$). We first describe in §4.2 the multi-wavelength data available for the targets and four control fields (including two sub-fields of GOODS South). The extraction of the source catalogues is described in §4.3. §4.4 presents the colour-colour selection we developed and applied to isolate cluster member candidates at $z > 1.6$ as well as the sample of selected galaxies in our studied fields. Their properties (overdensities compared to control fields, spatial distribution etc.) are detailed in §4.5. §4.6 is a summary of our results.

We assume a ΛCDM cosmology with $H_0 = 70$ km s^{-1} Mpc^{-1}, $\Omega_m = 0.3$ and $\Omega_\Lambda = 0.7$. The magnitudes are expressed in the AB photometric system unless stated otherwise.

4.2 The data

4.2.1 The targets

We present a study of the two lowest redshifts targets of our HAWK-I sample: MRC 1017-220 and MRC 0156-252 (McCarthy et al. 1996), observed with HAWK-I in Y, H and Ks. MRC 1017-220 ($z = 1.768$; R.A.: 10:19:49.05, Dec.: -22:19:58.03, J2000) is our lowest redshift HzRG. We note that this HzRG is a broad line radio galaxy (Kapahi et al. 1998) and unresolved both in near-infrared and radio (Pentericci et al. 2001). Investigating extremely red objects (EROs; $R - K > 6$) around high-z AGN, Cimatti et al. (2000) found an excess of EROs in the close vicinity of MRC 1017-220 compared to the field. We also targeted the field around MRC 0156-252 ($z = 2.016$; R.A.: 01:58:33.63, Dec.: -24:59:31.10). This HzRG has been reported to be a quasar obscured by dust (Eales & Rawlings 1996; McCarthy et al. 1992). Two smaller objects were also found, aligned in the direction North-East less than 5″ from the HzRG (Pentericci et al. 2001).

Table 4.1. Observations

Field	R.A. J2000	Dec. J2000	Band	Exp.Time min	Limit 2σ (3σ)
MRC 1017-220	10:19:49.05	-22:19:58.03	Y	122	25.91 (25.47)
			H	53	24.89 (24.45)
			K	33	24.36 (23.92)
MRC 0156-252	01:58:33.63	-24:59:31.10	Y	200	26.42 (25.98)
			H	47	24.91 (24.47)
			K	33	24.42 (23.98)
CF1	11:39:59.66	-11:24:29.50	Y	122	25.80 (25.36)
			H	53	24.18 (23.74)
CF2	16:02:06.80	-17:25:31.70	Y	122	25.78 (25.34)
			H	53	24.90 (24.46)
			K	33	24.35 (23.91)

4.2.2 Observations and data reduction

New VLT/HAWK-I data

Our fields were imaged in 2008/09 in service mode with VLT/HAWK-I. HAWK-I (Casali et al. 2006) is a wide-field imager on UT4 with a field of view of $7.5' \times 7.5'$ composed of four 2048×2048 pixel detectors separated by a gap of $15''$. The pixel scale is $0.1064''$. The field of MRC 1017-220 was observed in Spring 2008 for 122min in Y (λ_C = 10210Å), 53min in H (λ_C = 16200Å) and 33min in Ks (λ_C = 21460Å; hereafter K). MRC 0156-252 was also observed in the same set of filters: 200min in Y (Autumn 2008), 47min in H and 33min in K (August 2009). In order to avoid the gaps between the chips and to have a deeper coverage of the immediate surrounding of the HzRGs, MRC 1017-220 and MRC 0156-252 were placed near the center of one of the chips. Part of each Y-band observation was done during a photometric night when a standard star selected from the United Kingdom Infrared Telescope (UKIRT) faint standards list (Hawarden et al. 2001) was also observed immediately after the science data to calibrate the final Y image and derive its zeropoint.

Two control fields, hereafter CF1 and CF2 respectively centered on R.A.: 11:39:59.66, Dec.: -11:24:29.5 and R.A.: 16:02:06.80, Dec.: -17:25:31.7 were also observed from May to September 2008 in Y, H and K. For calibration, part of the observations in Y were done during photometric nights and sources with photometry provided by UKIRT were also observed the same nights for calibration.

Between January and March 2008, the entrance window of HAWK-I suffered a degradation. As a consequence, the shadow of the camera spider became visible on the data. The data thus contain the convolution of the spider shadow with the rotating pupil image resulting in a cross pattern which repeats the spider symmetry in the background[1]. As advised by the HAWK-I team, we reduced the DIT*NDIT of our observations to attenuate the cross pattern. However, some HAWK-I data taken between April and August 2008 show an increase in the sky noise independently of the configuration of the observations and the cross pattern is therefore very hard to subtract. This has been the case for the H and K-bands of CF1. During the data reduction, we optimize the subtraction of the cross pattern when removing the background. Unfortunately, the cross pattern in the

[1]See http://www.eso.org/sci/facilities/paranal/instruments/hawki/doc/HAWKI-NEWS-2008-07-11.pdf for details on the HAWK-I entrance window problem

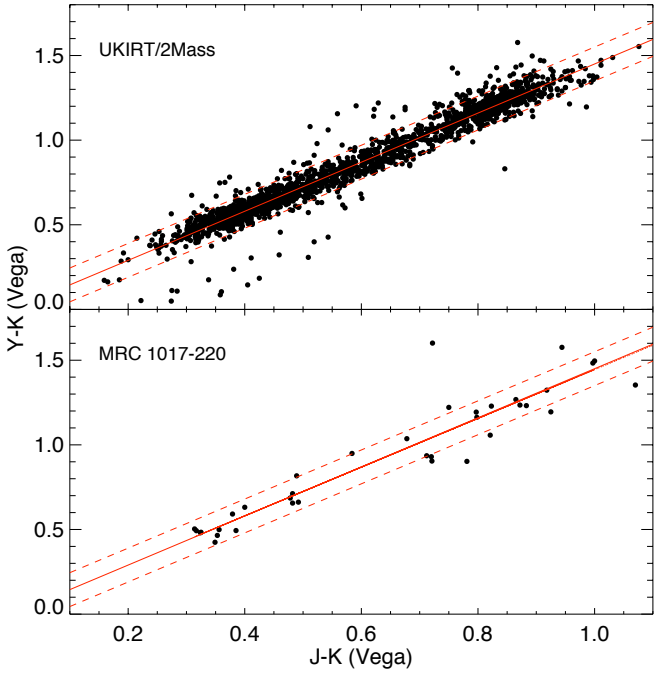

Figure 4.1. Colour-colour diagram ($Y - K$vs $J - K$) for the stars from a combined UKIDSS/2MASS catalogue (upper panel) and for the 2MASS stars of our MRC 1017-220 field (lower panel), shown as an example for the calibration of the Y-band HAWK-I data. The stars are well fitted by an empirical colour-colour relation, $(Y - K)_{Vega} = 1.45 \times (J - K)_{Vega}$ (solid line). 0.1 magnitude errors are shown by the dotted line, for information.

K-band of CF1 could not be properly subtracted and the image is unusable.

The data were reduced using the ESO/MVM (or 'alambic') reduction pipeline[2] (see Appendix A, section A.1). The image processing follows standard near-infrared reduction steps : dark subtraction, division by normalized sky flats, subtraction of the background, fringing correction and harmonization of the four chip gains. A distortion correction was applied to each chip using stars from the USNO-B1.0 (Monet et al. 2003) catalogue. The images were finally stacked using the same astrometric catalogue (for full details on the pipeline, see Vandame 2004).

The photometry of the H and K-bands was done using 2MASS point source catalogue (Skrutskie et al. 2006) for objects with $11 \leq K \leq 14.5$ (22 stars for MRC 1017-220, 13 for MRC 0156-252, 9 for CF1 and 37 for CF2). The derived zeropoints are accurate to 0.06 magnitudes. The 2σ (3σ) detection limits determined using $1.5''$ diameter apertures uniformly distributed over the images are reported in Table 4.1.

A first zeropoint of the Y-band was derived using the standard stars observations and was then refined using empirically derived near-infrared colour relations for stars. Using the Wide Field Infrared Camera (WFCAM) Science Archive[3] which holds images and catalogues of the UKIRT Infrared Deep Sky Surveys (UKIDSS), we retrieved stars from a sky portion of 1.5×1.5 square degrees (centered around R.A.: 14:00:00, Dec.: 10:00:00) and matched the Y-photometry of UKIDSS (data release 5) with 2MASS J and K-photometry. We extracted stars with accurate

[2]http://archive.eso.org/cms/eso-data/data-packages/eso-mvm-software-package
[3]http://surveys.roe.ac.uk/wsa/

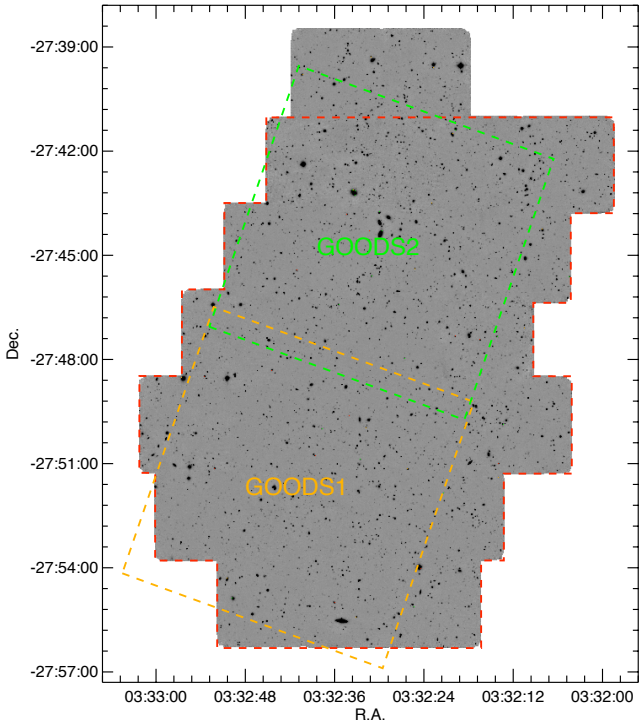

Figure 4.2. K-band combined mosaic of the 26 tiles observed by VLT/ISAAC in GOODS-S. The 24 fields also observed in H are highlighted by the red dashed line. The two VLT/HAWK-I Y-band observed as part of the science verification of the instrument are overlaid (orange: GOODS1, green: GOODS2).

photometry in Y, J and K (less than 0.05 magnitude errors; 1707 stars). Fig. 4.1 (upper panel) show their location in a $(Y-K)_{Vega}$ vs $(J-K)_{Vega}$ colour-colour diagram. Both UKIDSS and 2MASS use Vega photometric systems. Vega magnitudes were therefore used in this analysis for consistency. The colour-colour relation for stars is well fit by a simple linear function $(Y-K)_{Vega} = 1.45\times(J-K)_{Vega}$. We extracted the 2MASS stars from our HzRGs data and our two control fields and refined the zeropoints previously derived from the standard stars observations using the above colour-colour relation (Fig. 4.1; lower panel; example of the calibration method for MRC 1017-220). The offsets applied to the previous zeropoint were less than 0.03 mag. We estimated an average 0.06 mag uncertainty in the Y-band photometry of MRC 1017-220, CF1 and CF2 and 0.07 mag for MRC 0156-262. This last field indeed contains fewer stars and thus photometry is slightly less accurate. See Table 4.1 for the 2σ (3σ) limiting magnitudes of our Y-band data in random 1.5″ diameter aperture.

Archival GOODS-S data

The Southern field of the Great Observatories Origins Deep Survey (GOODS-S) was observed in J, H and Ks (hereafter K) using VLT/ISAAC from October 1999 to January 2007. The data were also reduced with the ESO/MVM pipeline by the GOODS team (Retzlaff 2009). The final data release, available since September 2007 includes 24 ISAAC fields in H and 26 ISAAC fields in K

as well as the final H and K combined mosaics[4] covering respectively 159.6 and 173.1 arcmin^2.

The GOODS-MUlticolor Southern Infrared Catalog[5] (GOODS-MUSIC; Grazian et al. 2006b; Santini et al. 2009) is a multiwavelength catalogue of GOODS-S, covering 143.2 arcmin^2 and cross-correlated optical (u, b, v, i, z from Hubble/ACS and VLT/VIMOS), near-infrared (see above), mid-infrared (*Spitzer*/Irac [3.6], [4.5], [5.8], [8.0] and *Spitzer*/MIPS 24μm) with available spectroscopic redshifts (12%). GOODS-MUSIC provides photometry for 12 of the 24 fields in H and 22 of the 26 fields in Ks. We use the GOODS-MUSIC photometry to calibrate the complete GOODS-S mosaics. The 2σ (3σ) limiting magnitudes in random $1.5''$ diameter aperture are 25.36 (24.92) and 25.20 (24.76) for H and K.

As part of the VLT/HAWK-I Science Verification programs, two sub-fields of GOODS-S were observed in Y in December 2007, centered respectively on R.A.: 03 : 32 : 40.92, Dec.: −27 : 51 : 41.6 (355min; PI: Fontana et al., GOODS1, hereafter) and R.A.: 03 : 32 : 29.71, Dec.: −27 : 44 : 38.6 (145min; PI: Venemans et al., GOODS2, hereafter). Fig. 4.2 shows the K-band mosaic of GOODS-S with the H-band (red) and the two Y-band fields, GOODS1 (orange) and GOODS2 (green) overlaid. We reduced the data using ESO/MVM pipeline. The images were astrometrically calibrated using a source catalogue extracted from the GOODS K-band mosaic. To flux calibrate the images we selected all objects in the field classified as stellar in the NASA/IPAC Extragalactic Database (NED). Broad band photometry for these stars was taken from the Multiwavelength Survey by Yale-Chile (MUSYC) catalogues (Gawiser et al. 2006). The broadband SED of the stars were fit using stellar templates from the BPGS spectrophotometric atlas (Hewett et al. 2006). For each star, the best fitting SED provided the Y magnitude of the star and, combined with the flux measured in the image, a zeropoint. The average of the individual zeropoints gave us the image zeropoint, which had an uncertainty of 0.05 magnitudes. The Y-band 2σ (3σ) limiting magnitudes in random $1.5''$ diameter aperture are 26.94 (26.50) and 26.41 (25.97) for GOODS1 and GOODS2 respectively.

4.3 Source extraction

HAWK-I data, especially those taken prior to May 2009, also present crosstalk between the amplifiers of the chips i.e., all the sources are repeating on some of the other 32 amplifiers producing a series of crater-like artifacts arrayed horizontally (see Appendix A, section A.2.1 and Finger et al. 2008). Due to its intensity, only crosstalk produced by the brightest objects is observed out of the background, e.g., in our image, all sources with $K_{2MASS,Vega} < 15.5$. Regions affected by crosstalk were masked before extracting the source catalogues. The crosstalk of the HAWK-I data is more important in the Y-band since the image is the deepest and stars are brighter in bluer bands. We therefore first identified the crosstalk in our Y-band. A map was created to flag the crosstalk-affected pixels by $4'' \times 4''$ squared masks. The flag area accounted for less than 2% of the final Y images for MRC 1017-220 and CF1 and less than 1% for GOODS-S. Our CF2 field contained numerous bright stars and $\sim 4\%$ of the final mosaic was flagged.

Source detection was performed using SExtractor (Bertin & Arnouts 1996). We derived total magnitudes for the HAWK-I data as well as for the GOODS-S ISAAC H and K mosaics using SExtractor MAG_AUTO parameter (DETECT_MINAREA=5 pixels; DETECT_THRESH=2σ). We also used aperture magnitudes (SExtractor MAG_APER) with a fixed $2.5''$ diameter aperture for colours measurements. All magnitudes were corrected for Galactic extinction (worked out for

[4]The reduced single field images and final mosaics are publicly available at http://archive.eso.org/archive/adp/GOODS/ISAAC_imaging_v2.0/goodsreq.html

[5]Publicly available at http://lbc.mporzio.astro.it/goods/goods.php

Table 4.2. Galaxy number counts in Y-band (N/(0.5mag.deg^{-2}))

Mag. (1)	1017 (2)	0156 (3)	CFs+GOODS-S (4)	GOODS-S (5)
17.75	747	485	470	-
18.25	896	1213	759	-
18.75	1792	1940	1228	-
19.25	1792	3881	2131	-
19.75	3286	3759	3468	-
20.25	5377	6913	6141	-
20.75	8812	7276	9464	-
21.25	15682	13461	13293	-
21.75	18818	17585	18531	-
22.25	24494	26801	24816	-
22.75	33156	36746	36845	-
23.25	31066	47054	46742	44807
23.75	35397	58817	54652	54695
24.25	-	78948	-	74609
24.75	-	-	-	76683

HAWK-I filters) according to the dust maps of Schlegel et al. (1998) assuming $R_V = A_V/E(B-V) = 3.1$ extinction law of Cardelli et al. (1989). All our fields are at high galactic latitude ($b > 20$). Corrections were small for our MRC 1017-220 field (0.054, 0.029, 0.019), our MRC 0156-252 field (0.012, 0.007, 0.004) and CF1 (0.033, 0.018, 0.011) in Y, H and K respectively. Due to a lot of dust along the line of sight, corrections for CF2 were, on the contrary rather big (0.344, 0.187, 0.118). We did not apply the negligible (< 0.01 in Y and < 0.005 for H and Ks) extinction corrections for the GOODS-S field.

We evaluated the completeness limits of our images using a IRAF `gallist` and `mkobjects` routines (`artdata` package) to simulate artificial galaxies (both elliptical and spiral galaxies). We chose a minimum galaxy axial ratio b/a of 0.8 and a maximum half flux radius of 1″.0. We adopted a de Vaucouleurs and an exponential disk surface brightness law for ellipticals and spirals respectively. For both types of galaxies, we generated catalogues of 5000 objects and added them on our Y, H and K images including Poisson noise. We determined how many artificial sources were recovered using the same SExtractor configuration files. The 90% completeness limits for elliptical (spiral) galaxies are 24.0 (23.3), 22.9 (22.2) and 22.4 (21.7) in Y, H and K respectively for MRC 1017-220, 24.4 (23.8), 23.2 (22.5) and 22.4 (21.8) for MRC 0156-252.

We derived the differential galaxy counts in our HzRG fields for each band (see Fig. 4.3). We only consider the deepest regions of the final images, i.e., we did not take into account the edges and the shallower regions resulting from the gap between chips (central 'cross'). We compared our galaxy counts with results from the literature: Yan et al. (1998); Chen et al. (2002); Moy et al. (2003); Metcalfe et al. (2006) for H and Maihara et al. (2001); Kümmel & Wagner (2001); Saracco et al. (2001); Huang et al. (2001); Elston et al. (2006) for K. No attempt was made to correct for the imcompleteness, neither to correct for differences in the filters (e.g., K or Ks). For the Y-band, we combined the counts from our two control fields: CF1, CF2 and the two GOODS-S Y bands. Table 4.2 reported, for the first time, Y-band galaxy counts. Counts for our two HzRGs fields are indicated up to the 90% completeness limit. Due to the completeness limits of CF1 and CF2, we first derived counts for $Y < 24$ from the four fields i.e., a total area of about 200 arcmin^2 (see

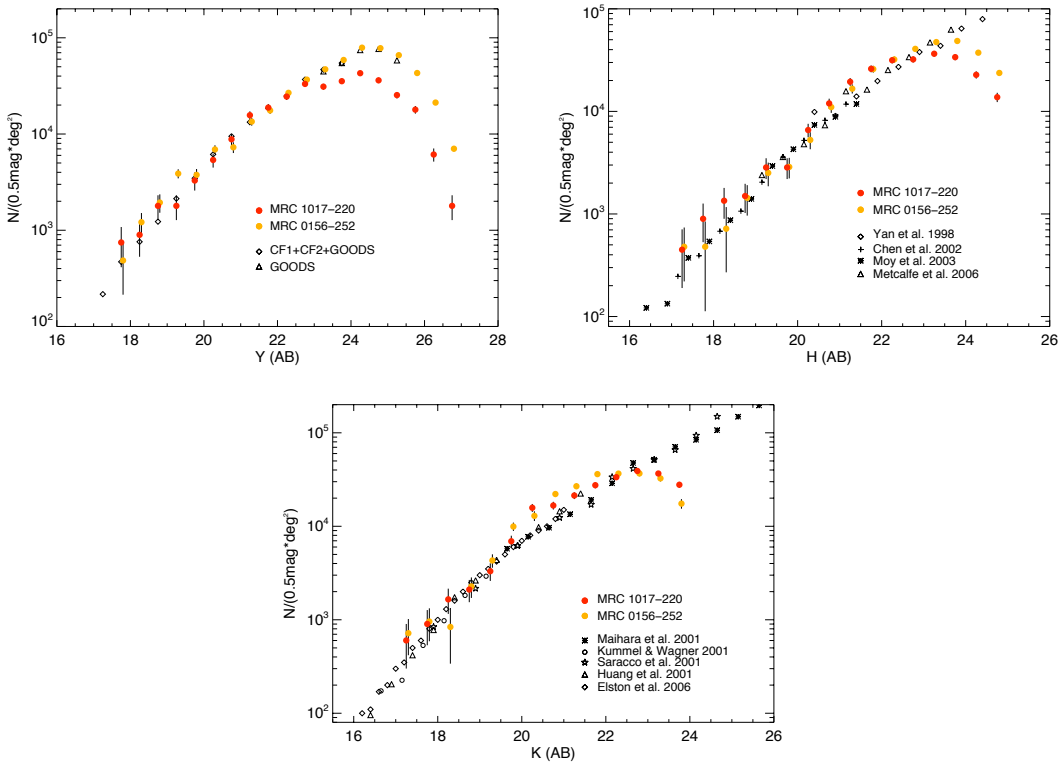

Figure 4.3. Galaxy number counts in Y, H and K for MRC 1017-220 (red dots) and MRC 0156-252 (orange). No completeness correction was applied. We remove stars from the galaxies using the stellar index CLASS_STAR in SExtractor. Counts from the literature are overplotted for H and K. For the Y-band, we derive counts from the two GOODS-S Y field and our two control fields (CF1 and CF2) until $Y < 24$. For $23 < Y < 25.5$, galaxy counts were also derived from GOODS-S only.

Table 4.2, column 4). We also derived the counts for $23 < Y < 25.5$ from GOODS-S only (column 5). As shown in Fig. 4.3 (first panel), Y counts in our HzRG fields are in good agreement with counts derived from our control fields. We note, on the contrary, that the galaxy counts of our targeted HzRG fields show an excess of galaxies in H ($20.5 < H < 22.5$) and K ($19.5 < K < 22$) compared to results from the literature suggesting that both fields might have an excess of red galaxies.

4.4 Candidate cluster members

4.4.1 YHK colour selection of galaxies at $z > 1.6$

Colour criteria have been efficient at selecting objects at a precise redshift range and isolating potential clusters members associated with HzRGs, e.g., at intermediate redshifts ($z \sim 1.4 - 1.7$), looking for overdensities of Extremely Red Objects (EROs; $R - K \geq 4$; Best et al. 2003). At high redshifts ($z \geq 2 - 3$), the position of the 4000Å break of galaxies falls between the J and H-band. Pure near-infrared colours have thus been used to isolate candidate protocluster members at this redshift range, e.g. the well known $(J - K)_{Vega} > 2.3$, designed by the FIRES team (Franx et al. 2003) which permits to select the so-called Distant Red Galaxies (DRGs). However, these single

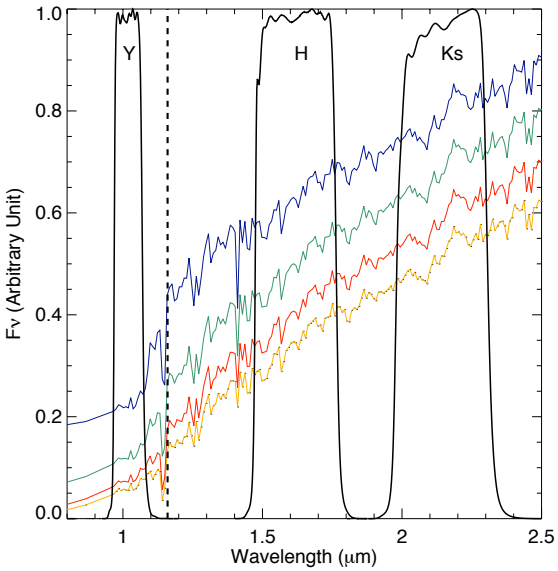

Figure 4.4. Redshifted (here at $z = 1.9$) spectral energy distribution of models of 2 Gyr-old galaxies assuming an exponential declining star formation history with $\tau = 0.1, 0.3, 0.5$ and 1 (from yellow to blue; see Fig. 4.5 for colours). The transmission curves of the HAWK-I filters Y, H and K and the position of the restframe 4000Å break (dashed line) are overlaid.

colour cuts mostly pick out red passive or dusty galaxies. Kajisawa et al. (2006) define a new two-colour selection technique combining JHK to select both red passive and blue star-forming galaxies at $z > 2$. This criterion ($J-K > 2\times(H-K)+0.5$ & $J-K > 1.5$; Vega system) is almost insensitive to dust extinction with the reddening vector ($E(B-V)$) parallel to the colour-colour selection technique.

At the redshift of our targeted HzRGs, the 4000Å break is between the Y and the J-band. One can therefore use the Y-band instead of the J-band in a Kajisawa-like two-colour YHK selection in order to isolate clusters members around MRC 1017-220 and MRC 0156-252. We use Bruzual & Charlot (2003) models to determine the colours of different stellar populations at $z = 1.77$ and $z = 2.02$. We assume for the models a solar metallicity and a Chabrier (2003) initial mass function. Fig. 4.4 shows dust-free model predictions for an exponentially declining star formation history (see Bruzual & Charlot 2003) for $\tau = 0.1$ to $\tau = 5$ at $z = 1.9$ with the HAWK-I transmission filters (black curves) and the position of the 4000Å break at $z = 1.9$ (dashed line) overlaid. We note that the Y and H filters encompass the *restframe* 4000Å. The Y filter is very narrow (width=0.1μm, about 3 times narrower than H and K) making $Y-H$ a very sensitive colour at the targeted redshifts. Fig. 4.5 shows the same models in a $Y-H$ vs $H-K$ colour-colour diagram: at various redshifts with constant population age of 2 Gyr (top panel) or at various population ages ($t = 1.5$ to 2.75Gyr) at $z = 1.77$ and $z = 2.02$ (bottom panel). Model predictions of galaxies at the targeted redshifts are found at the top-left corner of the colour-colour diagram. From $z \sim 1.4$, the $Y-H$ colour is getting redder with the 4000Å break entering the Y-band. The $H-K$ colour stays almost constant until $z \sim 2.5$ when the 4000Å break enters the H band. According to the models, galaxies at higher redshifts ($z > 3$) have their $Y-H$ ($H-K$) colour getting rapidly bluer (redder) than those of galaxies at $1.5 < z < 3$.

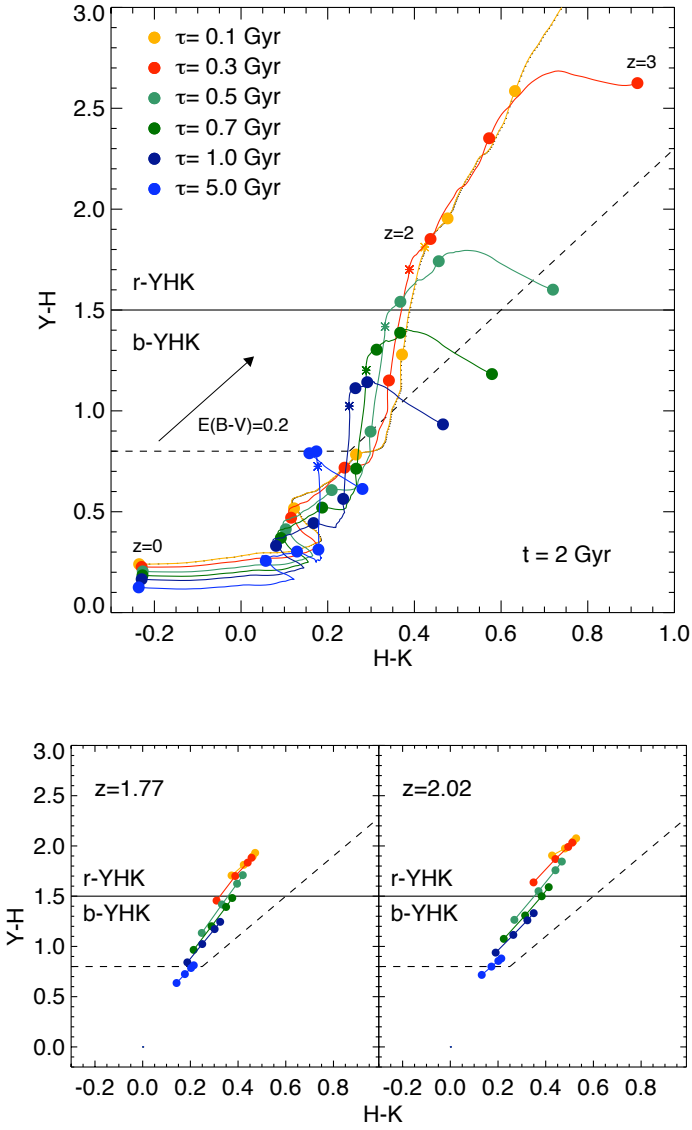

Figure 4.5. Bruzual & Charlot (2003) model predictions of different stellar populations in a $Y-H$ vs $H-K$ colour-colour diagram (see text for details on the models). The dashed line accounts for the two-colour selection designed to isolate galaxies at $z > 1.6$. The horizontal line ($Y - H > 1.5$) shows the single-colour selection to separate red passively evolving galaxies (r-YHK galaxies) from star-forming ones (b-YHK galaxies). We assume an exponential declining star formation history with τ = 0.1, 0.3, 0.5, 0.7, 1 and 5 Gyr (see legend). *Top:* for increasing redshifts (z = 0 to z = 3, each 0.5 bins marked by colored points) and a constant age of 2 Gyr, the star corresponding to z = 1.77. The black arrow indicates the reddening vector $E(B - V)$ = 0.2 as parameterized by Cardelli et al. (1989). *Bottom:* for various population ages (t = 1.5, 2, 2.5, 2.75 Gyr, colored points with $Y - H$ getting redder with ages) at z = 1.77 and z = 2.02.

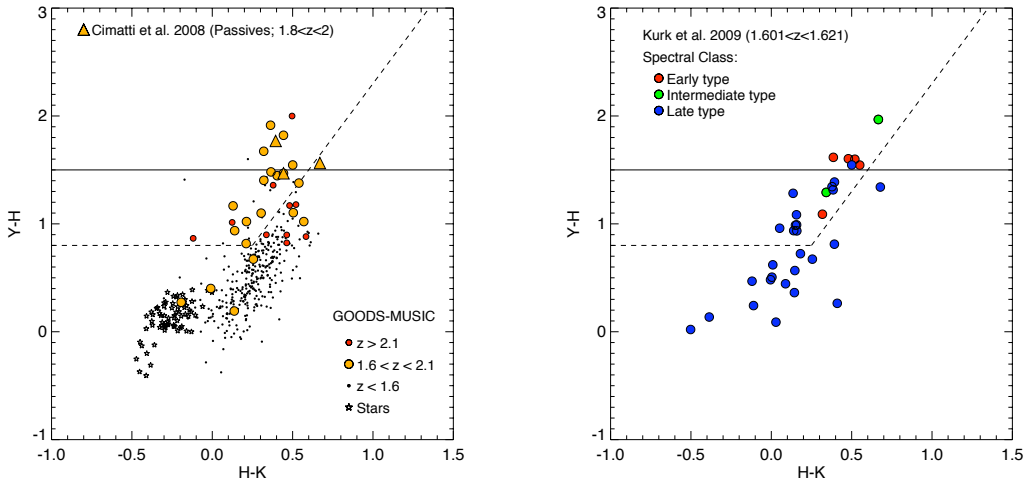

Figure 4.6. *YHK* colour-colour diagrams of sources with spectroscopic redshifts from the literature (GOODS-S field). The selection criteria (4.1) and (4.2) are shown by the dashed and solid horizontal lines respectively. *Left:* Sources with spectroscopic redshifts from the GOODS-MUSIC catalogue (see legend for symbols). We overplot the three passive galaxies at $z > 1.8$ from Cimatti et al. (2008) (triangles). *Right:* Members of the overdensity at $z \sim 1.6$ found in GOODS-S (Kurk et al. 2009). Colours of the symbols account for the spectral class of the group members: red, green and blue for early-type, early-type with signs of star formation and late type galaxies respectively.

We define a new colour criterion, analogous to the Kajisawa et al. (2006) two-colour *JHK* selection technique to select galaxies with $1.6 < z < 3$ (Fig. 4.5, dashed line):

$$Y - H \geq 0.8 \cap Y - H \geq 2 \times (H - K) + 0.3 \tag{4.1}$$

A single-colour criterion is defined to separate red galaxies with old stellar population from blue star-forming galaxies:

$$Y - H \geq 1.5 \tag{4.2}$$

similar to the single-colour criterion $(J - K)_{Vega} > 2.3$ that select DRGs at $z > 2$ and shown in Fig. 4.5 with the horizontal solid line.

The *YHK* criterion is insensitive to dust extinction since it has been defined parallel to the reddening vector $E(B - V)$ (see Fig. 4.5; black arrow). By analogy with Kodama et al. (2007) notations (r-*JHK* and b-*JHK*) for galaxies selected by Kajisawa et al. (2006) near-infrared criteria, galaxies selected by (4.1+4.2) are referred as r-*YHK* galaxies when galaxies selected by (4.1) with $Y - H < 1.5$ are referred as b-*YHK* galaxies.

We look at the *YHK* colours of galaxies in GOODS-S with spectroscopic redshifts available in the GOODS-MUSIC catalogue (see §2.2.2), combining the two archival *Y*-band (GOODS1 and GOODS2) photometry and the two *H* and *K* GOODS-S mosaics. We select sources with a reliable photometry in *H* and *K* (less than 0.1 magnitude errors), detected (2σ) in the two *Y*-band images and have a reliable spectroscopic redshift (flag 0: very good or 1: good). Fig. 4.6 (left panel) shows the distribution of these sources in the *YHK* colour-colour diagram i.e., 72 stars (empty stars), 316 galaxies at $z < 1.6$ (black dots), 20 with $1.6 < z < 2.1$ (orange circles) and 12 with $z > 2.1$ (red circles). AGN (defined as BLAGN or NLAGN in GOODS-MUSIC) are not

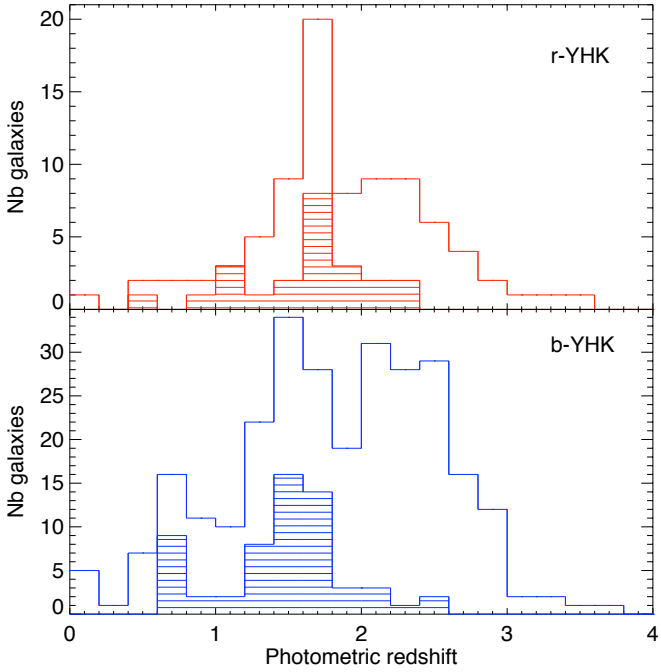

Figure 4.7. (Photometric) redshift distribution of the YHK-selected sources for r-YHK galaxies (upper panel) and b-YHK galaxies (lower panel) in GOODS1+GOODS2 for both the 2σ detection limits (solid histogram) and the limit of completeness of our HAWK-I data (filled histogram).

considered here. We note that 13/20 (65%) galaxies at $1.6 < z < 2.1$ are selected by our criteria. The criterion is really efficient at removing foreground and background objects with only 4/10 (40%) of galaxies with $z > 2.1$ and 12/316 (3.8%) galaxies with $z < 1.6$ found in the YHK-selected region. Cimatti et al. (2008) study a sample of 13 old, passive galaxies at $z > 1.4$ found in the northern part of GOODS-S covered by the Galaxy Mass Assembly ultra-deep Spectroscopic Survey (GMASS; Kurk et al. 2008b). 10 have $z > 1.6$ including three at $z > 1.8$, the seven others being part of an overdensity at $z \sim 1.6$ described in Kurk et al. (2009; see later in the text). The three passive galaxies at $z > 1.8$ are well detected in Y (in the GOODS2 field), H and K. They are shown by orange triangles in Fig. 4.6 (upper panel). Two of them have a $Y - H > 1.5$. The third one is a b-YHK galaxy but has however a red $Y - H$ colour close to the selection limit ($Y - H > 1.4$). We also test the limitation of our selection technique at the lowest redshift end with a sample of galaxies spectroscopically confirmed at $z \sim 1.6$. Kurk et al. (2009) present a galaxy overdensity at $z = 1.6$ with 42 spectroscopically confirmed members in the GMASS area: five galaxies with a spectral class early-type, two galaxies at an intermediate stage (early-type but with sign of star formation; intermediate type, hereafter) and 35 late type galaxies. All 42 members are covered and detected in the GOODS2 Y-band. Eight late type galaxies have magnitude errors larger than 0.1 mag in either Y, H or K and will not longer be consider in our analysis. Fig. 4.6 (right panel) shows the colours of the 34 remaining sources in the YHK colour-colour diagram, the colours of the symbols accounting for their spectral class. The five early-type galaxies and the two 'intermediate type' galaxies are also reported in Cimatti et al. (2008) as passive galaxies. These seven sources are selected by our YHK criterion. Four early-type and one 'intermediate type' are r-YHK galaxies. The last two sources are b-YHK galaxies. 11/27 (41%) late type galaxies are

selected by our criteria showing the limitation of our YHK criterion for star-forming dominated sources at $z \sim 1.6$.

We also test the YHK criteria using the photometric redshifts (z_{phot}; hereafter) available in the GOODS-MUSIC catalogue. Using the multiwavelength photometry of the GOODS-S field, Grazian et al. (2006b) applied a photometric redshift code on their catalogue, testing their code with the available spectroscopic redshifts and found an accuracy of $\sigma_z = 0.03 \times (1 + z)$ (Grazian et al. 2006a). We select the YHK galaxies in GOODS1 and GOODS2 (detected at 2σ). We also isolate the subsample of YHK galaxies detected in the limits of completeness of our HAWK-I data i.e., the completeness of passive red ellipticals for the r-YHK galaxies and the one of spiral galaxies for the b-YHK galaxies. Fig. 4.7 shows the photometric redshift distribution of the r-YHK galaxies (upper panel) and the b-YHK galaxies (lower panel). We find that 76.7% (2σ; 70.8% in the completeness limits) of the r-YHK galaxies and 68.1% (51.7%) of the b-YHK have $z_{phot} > 1.6$ confirming the efficiency of our selection criteria. The r-YHK criterion is extremely efficient at selecting galaxies at the targeted redshift with 41.7% (50.0%) of the sources with $1.6 < z_{phot} < 2.1$. We note that if indeed an overdensity of red galaxies exists in the surroundings of our HzRGs, the sample of YHK-selected galaxies in these fields would contain a higher fraction of sources at the targeted redshift. The percentages given earlier are therefore expected to be lower limits.

4.4.2 The YHK-selected galaxies

We apply the YHK selection technique to our five fields with YHK coverage i.e., MRC 1017-220, MRC 0156-252, CF2, GOODS1 and GOODS2. We consider sources with a 2σ detection in all three bands. The $Y - H$ vs $H - K$ colour-colour diagrams for the five fields are shown in Fig. 4.8. Red and blue circles account for r-YHK and b-YHK galaxies respectively. Sources with $Y - H >$ 1.5 but that are not selected by our r-YHK selection criterion are shown by the small red dots for information. We find 28 r-YHK galaxies (116 b-YHK galaxies) in MRC 1017-220, 105 (169) in MRC 0156-252, 38 (70) in CF2, 47 (158) in GOODS1 and 48 (145) in GOODS2. We precise that the numbers given here are not directly comparable to one another since the 2σ magnitude limits and the area considered slightly vary from field to field. Coordinates and magnitudes of b-YHK and r-YHK galaxies found in the MRC 1017-220 and MRC 0156-252 fields are reported in the Appendix B, Tables B.6, B.7, B.8 and B.9.

Cimatti et al. (2000) observed 14 fields around radio-loud AGN at $z > 1.5$ including MRC 1017-220 to look at the populations of EROs ($(R-K)_{Vega} > 6$). They find an excess of EROs in the field of MRC 1017-220 comparing to average with three EROs found down to their limiting magnitudes in an area within $\sim 2.5'$ of the HzRG. Two of the three have been observed in spectroscopy with VLT/ISAAC in the H-band (Cimatti et al. 1999). A 'spectro-photometric' redshift (z_{sphot}) was derived for both sources combining the ISAAC spectrum continuum and broad-band photometry. The two sources, J101948-2219.8 (R.A.: 10:19:47.79, Dec.: -22:19:46.6, $K_{Vega} = 18.7$, $z_{sphot} = 1.52 \pm 0.12$) and J101950-2220.9 (R.A.: 10:19:49.76, Dec.: -22:20:53.9, $K_{Vega} = 18.6$, $z_{sphot} = 1.50 \pm 0.25$), were both classified as an elliptical due to their SEDs consistent with no dust extinction We look at the colours of these two objects and their location in our colour-colour diagram (see black squares, Fig. 4.8, middle right panel). The first is selected as a b-YHK galaxy, the second is not selected by our criterion. However, it lies very close to the YHK selection limit. Only deeper spectroscopy over a wider wavelength range however would tell if those two targets are at the redshift of the MRC 1017-220.

Pentericci et al. (2001) present near-infrared NICMOS imaging of MRC 0156-252 and note that two small objects are seen aligned with the HzRG (within $5''$) in the direction of the radio axis. Fig. 4.10 is a three-colour image of the close vicinity of MRC 0156-252. Four small components

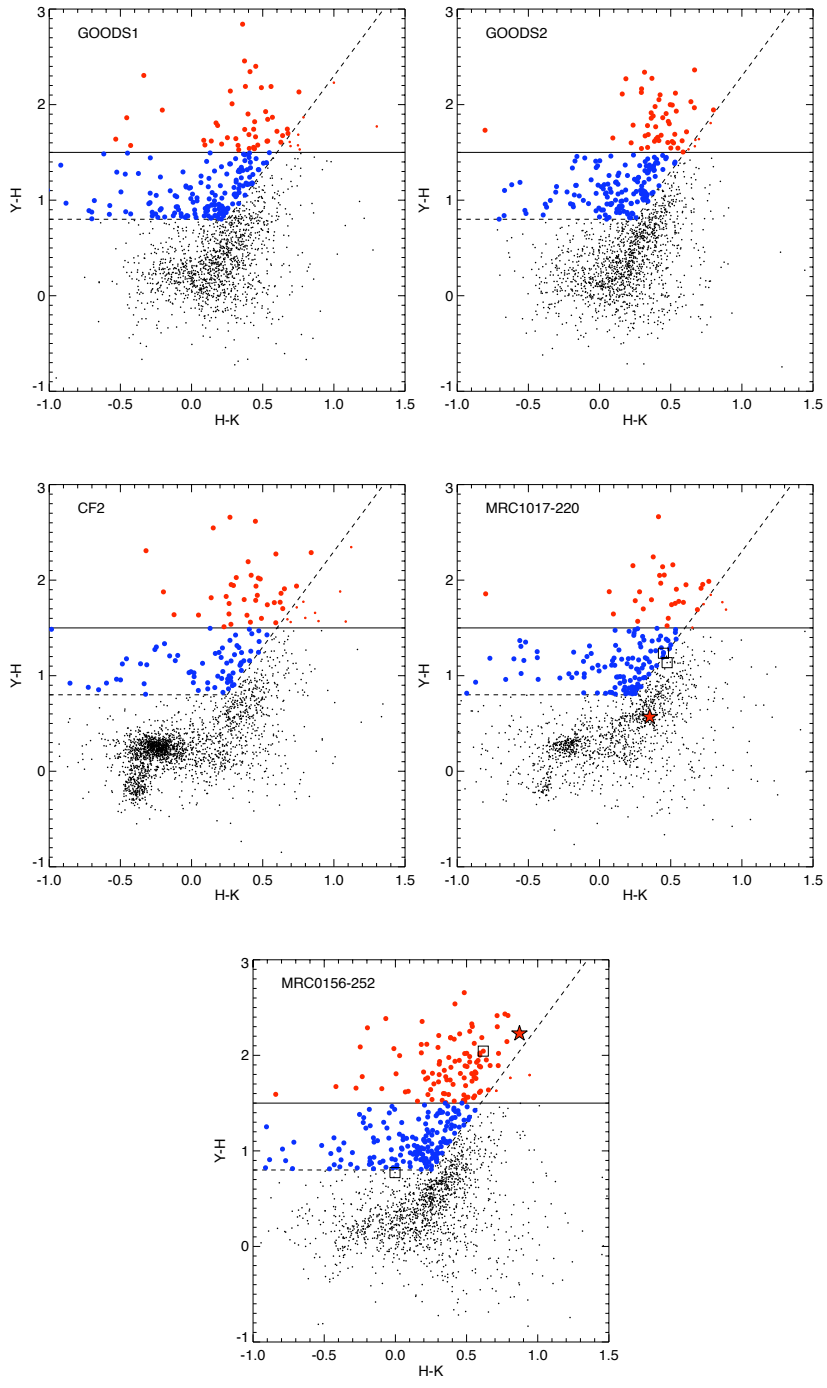

Figure 4.8. Colour-colour diagrams $Y - H$ vs $H - K$ for all the fields : *Upper panels:* Control fields: GOODS1 (left), GOODS2 (right). *Middle panels:* CF2 (left) and MRC 1017-220 (right). *Lower panel:* MRC 0156-252. We plot galaxies down to the 2σ detection limits in Y, H and K (black dots). r-YHK and b-YHK galaxies are designed by red and blue circles. Small red circles show the galaxies with $Y - H > 1.5$ but are not selected by our YHK criteria. The radio galaxies are marked by the red stars in the lower panels. We also indicate the two EROs found in the field of MRC 1017-220 (Cimatti et al. 1999) and the two sources found within 5″ of MRC 0156-252 (Pentericci et al. 2001) by black open squares

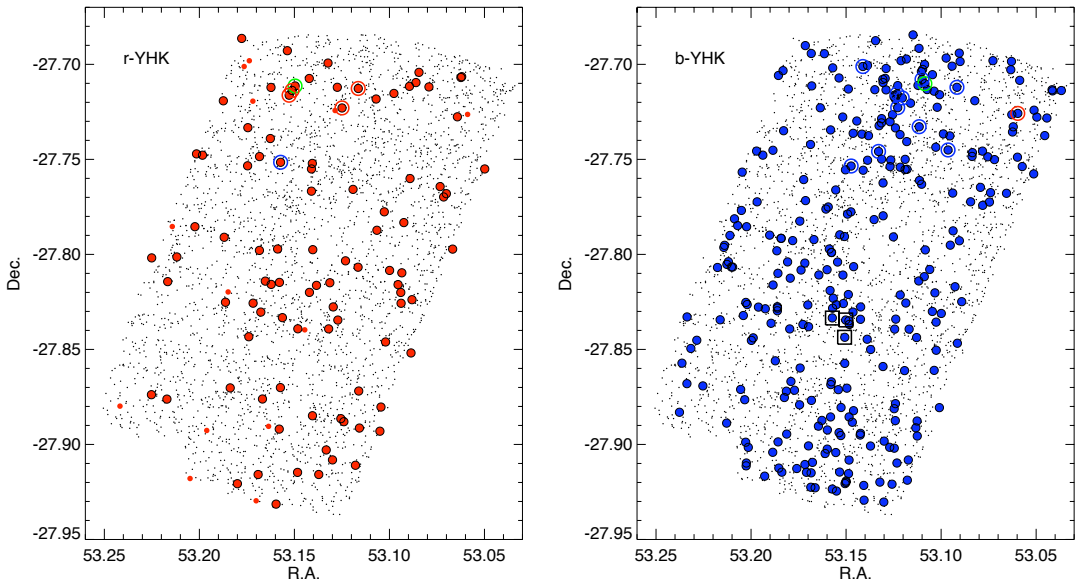

Figure 4.9. Spatial distribution of the YHK-selected galaxies in the GOODS fields (GOODS1+GOODS2; see Fig. 4.8 for symbols). We also indicate with open circles the 6 r-YHK and 12 b-YHK galaxies, spectroscopically confirmed members of the overdensity at $z \sim 1.6$ reported by Kurk et al. (2009), symbols colours accounting for the object spectral class (see Fig. 4.6, right panel). Three b-YHK galaxies confirmed at $z \sim 1.6$ from the ESO GOODS spectroscopy are also indicated by black squares.

are actually seen near MRC 0156-252. We label the components using the same notation (A for MRC 0156-252, B and C for the two eastern components) as Pentericci et al. (2001) adding 'D' for the fourth faint component on the west of the HzRG. As previously noticed in Pentericci et al. (2001), component C is much redder than component B. C is actually selected by our r-YHK criteria; B is too blue in $Y - H$ to be selected. B and C are indicated by black squares in Fig. 4.8, bottom panel. D is detected but very faint in K ($< 2\sigma$ level) and therefore was not considered in our candidate selection process. Spectroscopy will be needed in order to prove the association of these objects with the radio galaxy. However, the alignment of these three sources with the radio galaxy (as well as with the radio axis) strongly suggests that MRC 0156-252 has close-by companions. The scale for this system is similar to the one of the structure associated with PKS 1138-262 i.e., about 15″ (see Miley et al. 2006; Fig. 2). We suggest we may only be detecting the brightest clumps of a merging system at $z \sim 2$ similar to the SpiderWeb galaxy.

4.5 Candidates properties

4.5.1 Surface densities of YHK-selected galaxies

We compare the densities of YHK-selected galaxies in our four fields to assess a possible overdensity of sources around our targeted HzRGs. We cut all our catalogues at the completeness limits of our (shallowest) HAWK-I data (see §4.3) in order to directly make a field to field comparison. Table 4.3 summarizes the densities for both the r-YHK and b-YHK galaxies in our five fields assuming Poisson errors for the source densities. As far as the r-YHK galaxies are concerned, the fields around MRC 1017-220, CF2 and GOODS1 show similar densities. As expected, GOODS2

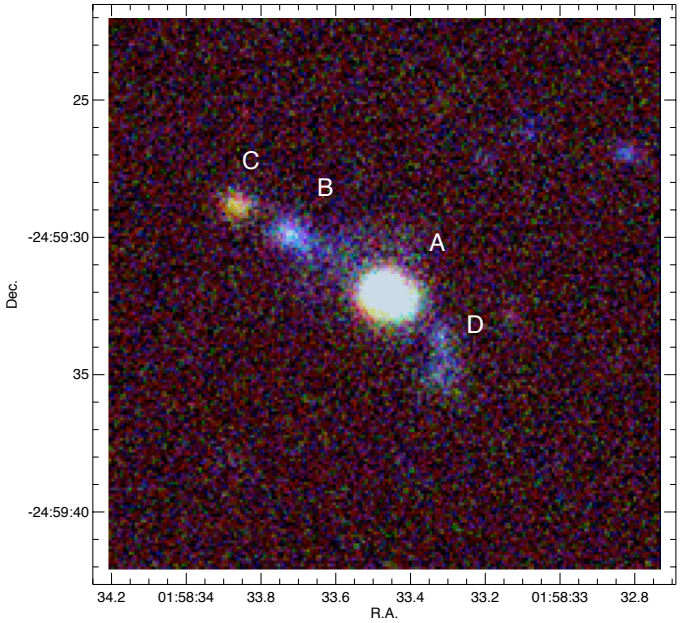

Figure 4.10. 3-colour image (R, G, B for K, H, Y) of the $20'' \times 20''$ field of view around MRC 0156-252 (North is Up, East Left). A is the radio galaxy. C is a r-YHK galaxy.

Table 4.3. Densities of YHK-selected galaxies

Field	Area (arcmin^2)	r-YHK[a] (deg^2)	b-YHK[a] (deg^2)
MRC1017-220	54.9	650 ± 205	2090 ± 370
MRC1017-220 (< 1Mpc)	11.0	1080 ± 590	1440 ± 685
MRC0156-252	59.0	2080 ± 355	1880 ± 340
MRC0156-252 (< 1Mpc)	11.0	2515 ± 905	2160 ± 840
CF2	54.3	795 ± 230	1390 ± 305
GOODS1	50.3	570 ± 200	1000 ± 270
GOODS2	50.3	1290 ± 305	1645 ± 345

[a] Densities were rounded for clarity.

which contains the overdensity at $z = 1.6$ described in Kurk et al. (2009) is denser than average, by a factor of 2.3 ± 0.9 compared to GOODS1 despite the two fields being neighbors. The field around MRC 0156-252 is clearly overdense compared to all fields by a factor of 3.2 ± 1.1 compared to MRC 1017-220 and by a factor of 1.6 ± 0.5 compared to GOODS2. We study the density within 1 Mpc of both HzRGs ($\sim 2'$, corresponding to an unflagged area of 11 sq arcmin; see second and fourth lines of Table 4.3). The r-YHK density in the vicinity of MRC 0156-252 is even higher, about 2 times denser than GOODS2 and 3.9 ± 1.8 denser than the field of MRC 1017-220[6]. This observed overdensity suggests that the field of MRC 0156-252 may contain a structure of evolved galaxies at $z > 1.6$ possibly associated with the HzRG. The b-YHK galaxies densities are more similar from field to field. We note however that the HzRGs fields are 1.5 to 2 times denser than our blank fields, CF2 and GOODS1.

4.5.2 Spatial distribution of the candidate cluster members

The spatial distribution of the YHK-selected galaxies in the two GOODS fields is shown in Fig. 4.9 for r-YHK and b-YHK galaxies in red and blue large circles. Sources detected in Y, H and K (2σ) are marked with black dots. We also overplot on the first plot, the sources with $Y - H > 1.5$ that are not passing the r-YHK selection criterion (in small red dots as for Fig. 4.8). As far as the northern part of the field (GOODS2) is concerned, we observe as expected a clear inhomogeneity in the distribution of both r-YHK and b-YHK galaxies. The red sources are found in majority in the upper part of the field without showing any specific spatial arrangement. The b-YHK galaxies show more segregation in their distribution forming one big clump of objects also in the northern part of GOODS2. We note that the northern part of GOODS1 (the southern part of the GOODS field) is more populated with r-YHK galaxies than the rest of GOODS1. The spatial distribution of b-YHK galaxies is more homogenous but we also observe a 'clump' of b-YHK galaxies at the same position as the excess of r-YHK galaxies (at R.A.$\sim$ 53.15 and Dec.~ -27.83). Several studies of the full GOODS field involving among others 2D distribution of photometric redshifts have shown that the overdensity found in GMASS spreads towards the south (see Kurk et al. 2009, Fig. 2 and Castellano et al. 2007, Fig. 1). The concentration of YHK-selected galaxies found in the northern part of GOODS1 is a direct confirmation. Three of the b-YHK-selected galaxies have a spectroscopically confirmed redshift of ~ 1.6 from the ESO GOODS spectroscopy (reported in the GOODS-MUSIC catalogue; see the three black squares).

The spatial distribution of the YHK-selected galaxies around MRC 1017-220, MRC 0156-252 and in CF2 is shown in Fig. 4.11 for r-YHK and b-YHK galaxies in red and blue large circles, first and second column respectively (see Fig. 4.9 for the symbols). Distances from both HzRGs (marked by the red star) are indicated on the top and right axis of the four first panels. We do not see any specific distribution of YHK-selected galaxies in CF2 (Fig. 4.11, bottom row). For MRC 1017-220, we indicate the two EROs with spectro-photometric redshift from Cimatti et al. (1999) by black squares. As noted before, one of the EROs with z_{sphot} (J101948-2219.8, situed at $\sim 20''$ NW of the HzRG) is also a b-YHK galaxy. A second b-YHK galaxy is detected in its vicinity ($< 2''$). We also note that a b-YHK galaxy is also found close ($\sim 5''$) to the second ERO with z_{sphot} (J101950-2220.9, not selected by our YHK criterion, situated at $\sim 1'$ SE of the HzRG). The r-YHK-selected galaxies are clearly non uniformly distributed over the field, with a hint of a filamentary distribution of the r-YHK galaxies in the direction NW-SE. But, the spatial distribution confirms that the field seems to be underdense compared to the other fields as far as

[6]We note that the YHK colour selection is very sensitive to the calibration of our images including our Y-band zeropoint with relatively large error bars (0.07). We precise however that even if the zeropoint was offset by -0.07, the field would still be overdense by a factor of 2.8 comparing to MRC 1017-220 and 1.5 comparing to GOODS2.

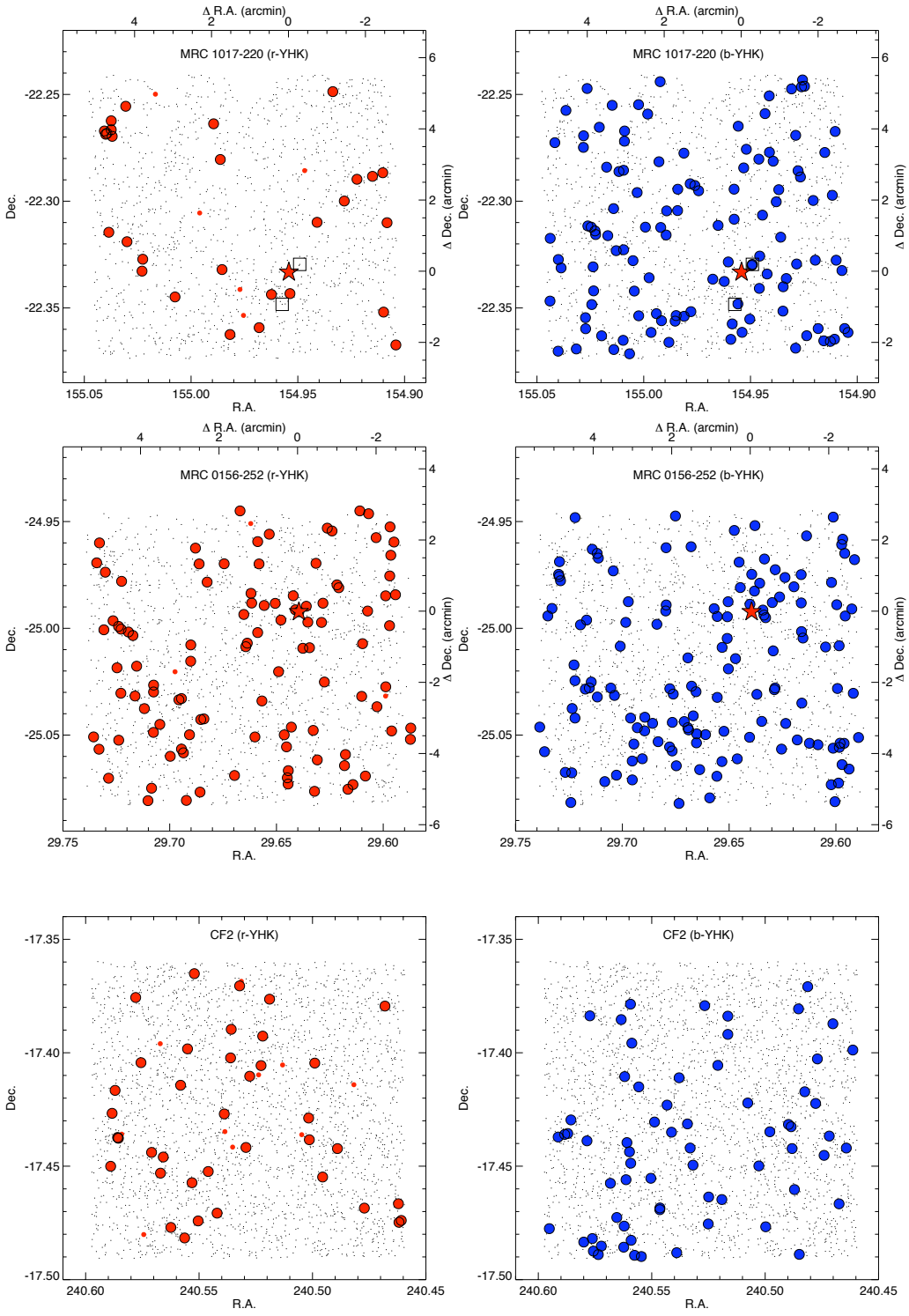

Figure 4.11. Spatial distribution of the *YHK*-selected galaxies in the fields around MRC 1017-220 and MRC 0156-252 and our control field CF2 (see Fig. 4.8 for symbols).

the red sources are concerned. A very compact group ($< 20''$ radius) of five red passive evolving candidates is also found at the extrem NE of the field about $6'$ away from the HzRG. (see §5.3 for details). No clear spatial segregation is seen for the b-YHK galaxies. The visual inspection of the field around MRC 0156-252 confirms that there is an overdensity of red objects around the HzRG. The red sources look concentrated around the HzRG and a second high concentration of sources is suggested in the South-East part of the field. A concentration of b-YHK galaxies is also seen in the North-West of the HzRG. A second concentration of blue galaxies is also suggested in the South-East part of the field with no clear counterpart in the r-YHK galaxies distribution.

4.5.3 A compact clump of red galaxies in the field of MRC 1017-220

As seen in §4.5.2, we find a clump of five r-YHK galaxies in the NE part of the MRC 1017-220 field, about $6'$ away from the HzRG. The two more distant of them (in projection) are only separated by $15''$. Fig 4.12 shows a 3-colour image of the concerned region. We note that this clump is exclusively formed by red sources. No indication of an overdensity of blue sources is observed in that region of the field. Several studies have been reporting such clumpy structures of red galaxies associated with galaxy clusters. In chapter 2, we selected pBzK galaxies in the field of the radio galaxy 7C 1756+6520 at $z = 1.42$ and found several clumps of red galaxies in the field whose association with the cluster around the HzRG still needs to be confirmed. Tanaka et al. (2009) reported three galaxy groups associated with the X-ray luminous cluster RDCS J1252.9-2927 at $z = 1.24$ and as distant of the main cluster as 12 Mpc (transverse distance). The spectroscopic follow-up of these regions showed a population of star-forming galaxies with strong [OII] emission but with red colours. Such red colours are not seen in the galaxies of the main cluster. For lack of near-infrared spectroscopy or observations in the mid-infrared, the authors suggested that those star-forming galaxies are reddened by dust. However, no analogy between the large scale structure around RDCS J1252.9-2927 and our field can be derived for now. Spectroscopy of our clump of candidates will be necessary to confirm both the association of the clump with MRC 1017-220 and the nature of its members.

4.5.4 The colour-magnitude diagram

We look at the distribution of our candidates in a colour-magnitude diagram ($Y - H$ vs K; see Fig. 4.13). Red and blue filled circles indicate r-YHK and b-YHK galaxies respectively. Candidates in the close vicinity of the HzRGs ($r < 1$ Mpc $\sim 2'$) are also shown by open circles. The five r-YHK that form the red clump in the NE of the field of MRC 1017-220 (see §4.5.3) are indicated by red squares (left panel). Both HzRGs are marked by a red star. We overplot the expected location of a sequence of passively evolving galaxies (taken from the Coma cluster at $z = 0$) at $z = 1.77$ and $z = 2.02$ for three different formation redshifts ($z_f = 3$, 4 and 5). The observed slope is caused by a dependance in metallicity-magnitude (Kodama et al. 1998). We observed that a large majority of our r-YHK selected galaxies — and more particularly the ones found within 1 Mpc of the HzRG — have colours consistent with the predictions of the red sequence models. Half of the red sources within 1 Mpc have $21 < K < 21.5$ suggesting that the cluster candidate contain very massive members. This is consistent with results found in the PKS 1138-262 field at $z = 2.16$ where the majority of the red near-infrared selected sources ($(J - K)_{Vega} > 2.3$) which lie on the red sequence models similarly had $21 < K_{Vega} < 21.5$ (Kodama et al. 2007).

The right insets of each panel give the histogram of the $Y - H$ colours of the candidates cluster members. It is now well known that galaxies in clusters show a strong bimodality in their colour distribution with star-forming non dusty galaxies being on the bluer side and passively evolving

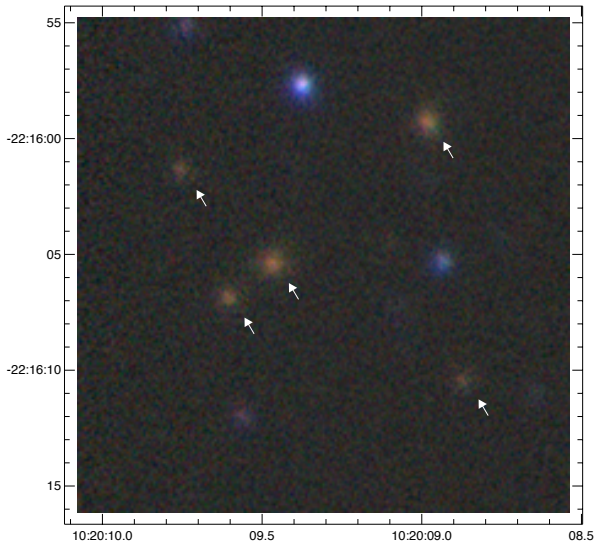

Figure 4.12. 3-colour image (R, G, B for K, H, Y) of the clump of five r-YHK galaxies found $6'$ NE of MRC 1017-220 (North up, East right). Arrows indicate the r-YHK galaxies.

one on the redder side (corresponding to the location of the red sequence) separated by a 'green valley' of intermediate type objects. A bimodal repartition can be seen in the histogram with two peaks on both sides of $Y - H \sim 1.5$ corresponding to the separation criteria that was designed to isolate passively evolving galaxies from star-forming blue ones.

4.6 Conclusions

We developed a new purely near-infrared YHK colour-colour selection technique to isolate galaxies at $z > 1.6$ and classify them between passively evolving galaxies and star-forming dominated ones. We tested the method in the GOODS-South field which has been observed in Y, H and K and for which large amount of spectroscopic data is available. GOODS-S contains a structure of galaxies at $z \sim 1.6$ (42 spectroscopic members so far). Applying our near-infrared criteria on the field, we recovered this structure confirming the efficiency of our new selection technique. We targeted the surroundings of two high redshift radio galaxies, MRC 1017-220 ($z = 1.77$) and MRC 0156-252 ($z = 2.02$) and a control field using VLT/HAWK-I. The field of MRC 1017-220 is underdense compared to the other targeted fields. However, the red galaxies show a non-homogeneous filamentary-like spatial arrangement around the radio galaxy. We found that MRC 0156-252 lies in an overdense region of red galaxies, by a factor of $2 - 3$ denser compared to our other studied fields. The red galaxies are found more clustered around the HzRG (< 1 Mpc). Three galaxies including one r-YHK-selected galaxy are found aligned with the HzRG and within $5''$ suggesting that the radio galaxy may has close-by companions. We also present for the first time, Y-band galaxies number counts derived from a total area of about 200 arcmin^2.

At the considered redshift, the 4000Å break enters the J-band. J-band spectroscopy is thus necessary to prove that the detected overdensity of red galaxies is not just a line of sight projection effect and is indeed associated with MRC 0156-252. Kriek et al. (2008) present a near-infrared

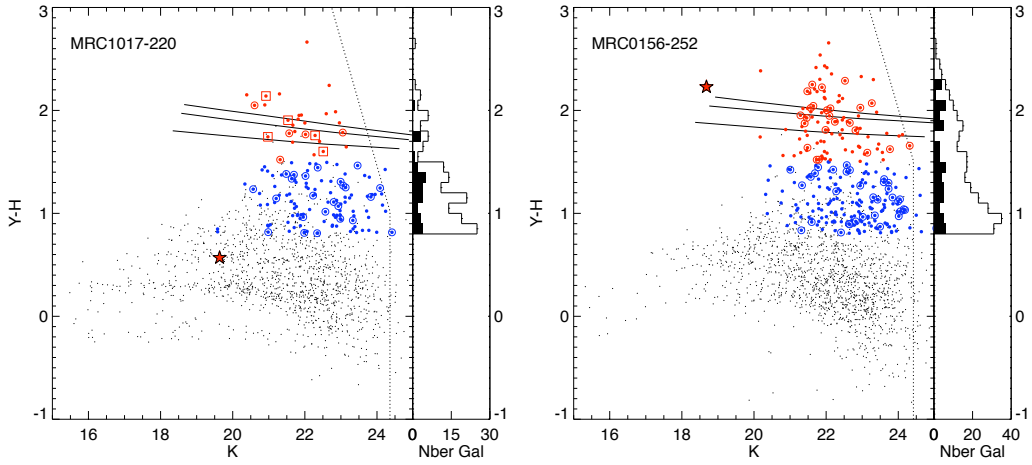

Figure 4.13. Colour-magnitude diagrams ($Y - H$ vs K) of the surroundings of our two HzRGs. The r-YHK and b-YHK galaxies are marked by red and blue dots. YHK galaxies within 1 Mpc of the HzRGs are highlighted by open circles. The five galaxies of the clump in the NE of the field of MRC 1017-220 (left panel) are pointed out by open squares. The red stars indicate the radio galaxies. The 2σ detection limits of our Y, H and K bands are shown by the dotted lines. Models of a red sequence at $z = 1.77$ and $z = 2.02$ are shown by the dashed lines. They indicate the predicted colours of a passively evolving stellar population ($z_f = 3$, 4 and 5 from bottom to top). We also show on the right side of each plot, the histogram of the $Y - H$ colours of all our candidate cluster members (red + blue) for both the full field (open histogram) and within 1 Mpc (filled) of the HzRG.

spectroscopic survey of 36 K-bright galaxies ($K < 19.7$) at $z_{phot} > 2$ selected from the MUlti-wavelength Survey by Yale-Chile (MUSYC; Gawiser et al. 2006; Quadri et al. 2007). They derive spectroscopic redshifts ($1.6 < z_{spec} < 2.73$) for their full sample of 36 galaxies and used the high spectral resolution and reduced redshift uncertainty to improve constraints on their stellar population parameters. Such a spectroscopic campaign could be conducted similarly in the field of MRC 0156-252 since it contains 26 r-YHK (25%) and 23 b-YHK (14%) galaxies which have $K < 19.7$. Doherty et al. (2010) present an example of such a spectroscopic follow-up campaign. Several works have shown that a protocluster is surrounding the radio galaxy PKS 1138-262 (the SpiderWeb at $z = 2.16$). Overdensities of both narrow-line emitters (spectroscopically confirmed) and DRGs have been found in the surroundings of the radio galaxy. Doherty et al. (2010) describe a spectroscopic campaign in the PKS 1138-262 field to follow-up the red massive galaxies. Two DRGs (out of 33 targeted sources) were confirmed at the redshift of the radio galaxy (thanks to their Hα emission line). One is actually a dust-obscured star-forming red galaxy when the other is an evolved galaxy with little on-going star formation. These are the first spectroscopically confirmed red galaxies associated with a protocluster at $z > 2$. This is very encouraging for a prospected follow-up we hope to lead in the field of MRC 0156-252 at $z = 2.02$.

Chapter 5

The Cosmic Evolution of AGN in Galaxy Clusters

Abstract.

We present the surface density of luminous active galactic nuclei (AGN) associated with a uniformly selected galaxy cluster sample identified in the 8.5 square degree Boötes field of the NOAO Deep Wide-Field Survey. The clusters are distributed over a large range of redshift ($0 < z < 1.5$) and we identify AGN using three different selection criteria: mid-IR colour, radio luminosity, and X-ray luminosity. Relative to the field, we note a clear overdensity of the number of AGN within 0.5 Mpc of the cluster centers at $z > 0.5$. The amplitude of this AGN overdensity increases with redshift. Although there are significant differences between the AGN populations probed by each selection technique, the rise in cluster AGN surface density generally increases more steeply than that of field quasars. In particular, X-ray selected AGN are at least three times more prevalent in clusters at $1 < z < 1.5$ compared to clusters at $0.5 < z < 1$. This effect is stronger than can be explained by the evolving median richness of our cluster sample. We thus confirm the existence of a Butcher-Oemler type effect for AGN in galaxy clusters, with the number of AGN in clusters increasing with redshift.

Audrey Galametz, Daniel Stern, Peter R. M. Eisenhardt,
Mark Brodwin, Michael J. I. Brown, Arjun Dey,
Anthony H. Gonzalez, Buell T. Jannuzi,
Leonidas A. Moustakas & S. Adam Stanford

Astrophysical Journal, **694**, 1309 (2009)

5.1 Introduction

In the local universe, AGN are known to be much less common in rich galaxy cluster environments as compared to the field. Optical observations dating back more than three decades show that while 5% of massive field galaxies show spectroscopic signatures of nuclear activity, only 1% of the corresponding population in local galaxy clusters show such signatures (Dressler et al. 1985). Assuming that the $M_\bullet - \sigma$ relation (e.g., Magorrian et al. 1998) holds in rich environments, this suggests that the supermassive black holes hosted by massive cluster galaxies are currently quiescent or their nuclear activity is optically obscured. In addition, the intracluster plasma in rich galaxy clusters is maintained at high temperatures; AGN feedback has been suggested as the most natural heat source by numerous authors (e.g., McNamara et al. 2000; Bîrzan et al. 2004). This suggests that the activity level of AGN in cluster galaxies, and their influence on the formation and evolution of clusters, may have been higher in the past.

Early studies of AGN in clusters largely relied on optical spectroscopy (e.g., Bahcall et al. 1969), a technique which is notoriously insensitive to both obscured and low luminosity AGN. In contrast, multi-wavelength approaches provide a significantly more thorough census of AGN. For example, Compton-thick, luminous AGN will be faint at the relatively low (< 10 keV) energies probed by *Chandra* and *XMM/Newton* and would be unlikely to show a UV-excess or spectroscopic signatures of nuclear activity at cosmological distances. Such sources would be easier to identify at radio or mid-IR energies, though only a $\sim$ 10% of AGN are radio-loud. We briefly review selection of AGN at non-optical wavelengths, summarizing previous work using these techniques to study the cosmic evolution of AGN in galaxy clusters.

X-Ray Selected AGN. In the past decade, sensitive X-ray observatories have provided an efficient method to identify AGN. Several studies conducted on individual clusters or small cluster samples have shown an excess of X-ray point sources in galaxy clusters (Cappi et al. 2001; Eckart et al. 2006). Martini et al. (2002, 2006, 2007) study samples of X-ray sources near low-redshift galaxy clusters with spectroscopic follow-up to confirm cluster membership. Similar to field X-ray source studies, this work has shown that X-ray emitting galaxies in clusters often do not show AGN signatures in their optical spectra, implying that a significant fraction of cluster nuclear activity is optically obscured. Considering a sample of four galaxy clusters at $z \sim 0.6$, Eastman et al. (2007) show that the X-ray AGN are more common at $z \sim 0.6$ than at $z \sim 0.2$, implying that the cluster AGN fraction increases rapidly with redshift.

Other groups have foregone spectroscopic observations and have looked for enhancements in the radial distribution of X-ray sources around clusters. For example, Ruderman & Ebeling (2005) derive the surface density profile of X-ray sources around a sample of 51 galaxy clusters at $0.3 < z < 0.7$ from the *Chandra* MAssive Cluster Survey (MACS; Ebeling et al. 2001). They find that X-ray sources show a very pronounced central spike ($r < 0.5$ Mpc) and a second excess at ~ 2.5 Mpc relative to the cluster centers. They suggest the former is from nuclear activity triggered by infalling galaxies approaching the central giant elliptical galaxy, while the second peak, which is most pronounced in virialized clusters, is due to galaxy mergers at the cluster-field interface. Bignamini et al. (2008) find an excess of X-ray point sources near the centers of optically-selected clusters at $0.6 < z < 1.2$.

Radio Selected AGN. Over the past 50 years there have been numerous studies of the environments of powerful radio galaxies which are now well known to often be associated with the central member of galaxy clusters, not only at low redshifts (Matthews et al. 1964) but also at high redshifts (Dickinson 1993; Stern et al. 2003; Miley et al. 2004; Venemans et al. 2005, 2007; Galametz et al., in prep.). Correlating the Sloan Digital Sky Survey (SDSS; Gunn & Weinberg

1995) with the Faint Images of the Radio Sky at Twenty cm survey (FIRST; Becker et al. 1995), Best et al. (2005) show that there is a strong tendency for low-redshift radio-loud galaxies to be found in rich environments. Lin & Mohr (2007) derive the radio-loud AGN density profile from a sample of 573 nearby ($z \leq 0.2$) X-ray selected galaxy clusters and find a clear excess of AGN in the center of the galaxy clusters. Croft et al. (2007), studying brightest clusters galaxies (BCGs) at $z < 0.3$ from a sample of 13,240 galaxy clusters, report that 19.7% of BCGs are detected in the radio, with the majority of these (92.8%) being radio-loud ($L_{1.4\mathrm{GHz}} \geq 10^{23}$ W Hz^{-1}). In contrast to these studies of X-ray and radio-selected AGN in galaxy clusters, optically-selected, luminous quasars exhibit clustering comparable to that of local field galaxies, and therefore primarily reside in lower mass dark matter halos (e.g., Croom et al. 2005; Coil et al. 2007).

Mid-IR Selected AGN. AGN can also be efficiently identified using mid-infrared colours (Lacy et al. 2004; Stern et al. 2005). While the optical to mid-infrared ($\lambda \leq 5\mu$m) continuum of normal galaxies is dominated by the composite stellar black body emission and peaks at approximately 1.6μm, the optical to mid-infrared continuum of active galaxies is dominated by a power law. Consequently, with sufficient wavelength baseline, one can easily distinguish AGN from stellar populations. Little work has been done to date on the prevalence of mid-IR selected AGN in clusters, though Hickox et al. (submitted) shows that low redshift ($z < 0.8$) mid-IR selected AGN have weaker clustering properties (e.g., smaller correlation lengths) than either X-ray or radio-selected AGN. At high redshift ($z \sim 2$), however, various mid-infrared AGN samples show strong clustering, suggesting that they are preferentially associated with clusters (Brodwin et al. 2008; Dey et al. 2008; Magliocchetti et al. 2008).

Previous studies of AGN activity in galaxy clusters have typically focussed on a single selection technique, generally over a limited redshift range and with a limited cluster sample size. Combining the IRAC Shallow Survey (ISS; Eisenhardt et al. 2004) and the *Chandra* XBoötes Survey (Murray et al. 2005), Gorjian et al. (2008) compare mid-IR and X-ray AGN selection and find that only 28% of XBoötes sources are selected by the Stern et al. (2005) mid-infrared criteria. On the other hand, a significant number (43%) of AGN selected in mid-infrared have an X-ray counterpart in XBoötes (V.Gorjian, private communication). Furthermore, only $\sim$ 10% of optically-selected luminous quasars are radio-loud (e.g., Stern et al. 2000). These results imply that to obtain the fullest census of nuclear activity, multiple AGN selection techniques are required.

In this work, we present the surface density of AGN selected by three techniques (mid-infrared colour, radio luminosity, and X-ray luminosity) in a large sample of uniformly-selected galaxy clusters identified in the Boötes field (Eisenhardt et al. 2008). The next section (§2) describes the galaxy cluster and AGN samples. We describe the radial surface density profile of AGN in galaxy clusters in §3 and discuss the results in §4. We assume a ΛCDM cosmology with $H_0 = 70$ km s^{-1} Mpc^{-1}, $\Omega_m = 0.3$ and $\Omega_\Lambda = 0.7$.

5.2 The Galaxy Cluster and AGN Samples

The galaxy cluster sample we analyze has been uniformly selected from the 8.5 square degree ISS field in Boötes survey, which has been observed by a wide array of facilities at multiple wavelengths. The following sections describe first the cluster sample and then AGN samples identified in the Boötes field at mid-infrared, radio and X-ray energies. Note that in the later analysis (§3), we will use these AGN samples, generally from flux-limited catalogues, to study the cosmic evolution of AGN in galaxy clusters. To ensure uniformity in the analysis, this will entail creating luminosity-selected sub-samples (§3).

5.2.1 The IRAC Shallow Survey cluster sample

Eisenhardt et al. (2008) present a sample of 335 galaxy clusters identified in the Boötes field of the NOAO Deep Wide-Field Survey (NDWFS; Jannuzi & Dey 1999). The clusters, reaching out to redshift $z = 2$, were identified by combining ISS with $B_W RI$ imaging from the NDWFS and JK_s imaging from the FLAMINGOS Extragalactic Survey (FLAMEX; Elston et al. 2006). Brodwin et al. (2006) calculated photometric redshifts for 4.5μm-selected sources in the ISS. Clusters were then identified using a wavelet algorithm which identified three-dimensional overdensities of galaxies (in 2 angular dimensions) with comparable photometric redshifts. The clusters have average halo masses of $\sim 10^{14}\ M_\odot$ (Brodwin et al. 2007). The cluster centers were determined from their peaks in the wavelet detection map. Since this map is based on the positions of a limited number of galaxies per cluster, the cluster center accuracy is expected to be comparable to the 1$'$2 resolution of the wavelet map.

An estimate of the cluster redshifts was obtained from the photometric redshift probability distribution of candidate cluster members. At $z < 0.5$, 67 of the 91 clusters candidates are confirmed by the AGN and Galaxy Evolution Survey (AGES; Kochanek et al., in prep.), which provides spectroscopic redshifts for $\sim$ 17000 objects in the ISS. To date, 12 of the $z > 1$ cluster candidates have been confirmed spectroscopically (Stanford et al. 2005; Elston et al. 2006; Brodwin et al. 2006; Eisenhardt et al. 2008). Where available, we use the spectroscopically determined cluster redshifts. For the remaining cluster sample, we use the best fit photometric redshift which includes a small, empirically-determined offset relative to the mean photometric redshift of the candidate cluster members. This large, uniformly selected galaxy cluster sample is spread over a large range of cosmic time and thus provides a powerful tool for studying the dependence of the AGN distribution on both redshift and environment.

5.2.2 Mid-IR selected AGN

Using mid-infrared colours, provided by the ISS, of nearly 10,000 spectroscopically identified sources from AGES, Stern et al. (2005) show that AGN can robustly be identified from their IRAC colours (see also Lacy et al. 2004; Donley et al. 2008). Simple mid-infrared colour criteria select over 90% of the spectroscopically identified type 1 AGN and 40% of the type 2 AGN. The selection relies on the fact that while stellar populations fade longward of their 1.6μm peak, luminous AGN exhibit red power-law emission throughout the mid-infrared. Notably, this power-law long wavelength emission is relatively immune to gas and dust absorption, making mid-infrared AGN selection sensitive to both obscured and unobscured luminous AGN, relatively independent of redshift. We note however that this selection fails for low-luminosity AGN where the host galaxies contributes much of the mid-IR flux (Eckart et al., in prep.). We extract all 2262 sources selected by the Stern et al. (2005) criteria that are well detected (5σ) in all four IRAC bands. For a typical AGN spectral energy distribution, the 5.8μm band is the least sensitive, with a 5σ limiting depth of 51μJy (3$''$ diameter aperture). We find a mean surface density of 283 mid-infrared selected AGN candidates per square degree in the Boötes field.

5.2.3 Radio selected AGN

Several shallow ($\geq$ 1mJy) radio surveys have covered the ISS field at 1.4 GHz, including the NRAO VLA Sky Survey (NVSS; Condon et al. 1998) and FIRST. More recently, the Westerbork Synthesis Radio Telescope (WSRT) has covered approximately 6.68 square degrees of Boötes, reaching a 1σ limit of 28μJy at 1.4 GHz (de Vries et al. 2002). The final catalogue of 5σ detected

sources contains 3172 objects[1], corresponding to a surface density of 453 radio sources per square degree.

The brightest radio sources in the sky tend to be AGN, with their radio emission dominated by synchrotron radiation. However, sufficiently deep radio surveys are also able to detect radio emission associated with stellar processes such as supernova explosions and compact stellar remnants, abundant in star-forming galaxies. Condon (1992) shows that for these star forming galaxies, the star formation rate (SFR) is proportional to the radio emission. Following Condon et al. (1992), Serjeant, Gruppioni & Oliver (2002) obtain $L_{1.4\mathrm{GHz}}(\mathrm{erg\ s^{-1}\ Hz^{-1}}) = 8.2 \times 10^{27} \times \mathrm{SFR}(M_\odot\ \mathrm{yr}^{-1})$. Submillimeter galaxies correspond to the objects with the highest known SFR, reaching SFR $\sim 1000 M_\odot\ \mathrm{yr}^{-1}$ (Pope et al. 2006). We conservatively assume that no galaxy has a SFR greater than $3000 M_\odot\ \mathrm{yr}^{-1}$ and thus any radio source with a 1.4 GHz luminosity density greater than 2.46×10^{31} erg s^{-1} Hz^{-1} must host an AGN (see §3). Given the depth of the WSRT observations, all radio-loud AGN in the Boötes field should be detected out to redshift $z \sim 3.7$.

5.2.4 X-ray selected AGN

XBoötes is the largest contiguous survey with the *Chandra X-Ray Observatory*. It consists of 9 square degrees of imaging of the NDWFS Boötes field, comprised of 126 5 ks pointings, with a corresponding depth of $\sim 7.8 \times 10^{-15}$ ergs cm^{-2} s^{-1} in the 0.5-7 keV band. The X-ray catalogue consists of 3293 point sources with four or more X-ray counts (366 sources per square degree; Kenter et al. 2005; Brand et al. 2006) and is publicly available[2]. At the shallow depth of these data, the majority of the X-ray sources are expected to be AGN. Indeed, based on AGES optical spectra for 892 XBoötes sources (Kenter et al. 2005), AGN represent at least 69% of the sources with spectra. Only 3% of the sources are identified as stars. The remaining 28% lack obvious AGN features in their optical spectra but are suspected to be AGN based on their X-ray luminosities. XBoötes is only sensitive to starbursts out to $z = 0.12$ (e.g., see Gorjian et al. 2008). Since only one of the galaxy clusters in the ISS sample is at $z \leq 0.12$, we consider the possible influence of X-ray detected starbursts negligible in this work.

5.3 Radial Surface Density Profile of AGN

In order to study the cosmic evolution of AGN in galaxy clusters, we opt for a simple empirical approach: we calculate the radial distribution of AGN around galaxy clusters as a function of cluster redshift, with AGN identified using the three selection criteria described above. We separate the ISS clusters into three redshift bins: $0 < z \leq 0.5$, $0.5 < z \leq 1$ and $1 < z \leq 1.5$, resulting in 91, 140 and 79 clusters per bin, respectively, for the mid-IR and X-Ray techniques. The remaining 25 clusters are at $z > 1.5$, and are thus ignored in this work. The area covered by the WSRT radio data is smaller than the ISS and thus only 285 clusters have deep coverage at radio wavelengths. Of these 285 clusters, 77, 121 and 69 are found at $0 < z \leq 0.5$, $0.5 < z \leq 1$ and $1 < z \leq 1.5$, respectively.

In order to ensure that similar populations are plotted in each cluster redshift bin, we apply uniform luminosity cuts to the data. In detail, since most of the sources considered here lack spectroscopic redshifts, for a given cluster at redshift z, we only consider sources brighter than some evolving flux density such that their luminosity would be equal to or above our luminosity limit assuming that the source were in the cluster. For the very sensitive radio survey, we apply the

[1]The catalogue as well as the mosaic can be obtained through anonymous ftp to ftp://ftp.nfra.nl/pub/Bootes.
[2]http://heasarc.nasa.gov/W3Browse/all/xbootes.html

Table 5.1. Number and surface density of Boötes AGN candidates after luminosity cuts.

Selection	Luminosity limit (ergs s^{-1})	Area (deg^2)	Total number N (Σ, $arcmin^{-2}$)	$0 < z \leq 0.5$ N_{AGN} (Σ_{AGN})	$0.5 < z \leq 1$ N_{AGN} (Σ_{AGN})	$1 < z \leq 1.5$ N_{AGN} (Σ_{AGN})
Mid-IR	$S_{5.8\mu m} > 2.2 \times 10^{44}$	8.0	2262 (0.079)	177 (0.006)	1570 (0.054)	2262 (0.079)
Radio	$S_{1.4GHz} > 2.5 \times 10^{40}$	6.68	3172 (0.132)	229 (0.009)	591 (0.025)	1394 (0.058)
X-ray	$S_{0.5-7keV} > 3.3 \times 10^{43}$	9.0	3293 (0.102)	205 (0.006)	2102 (0.065)	3293 (0.102)

luminosity cut $S_{1.4GHz} > 2.5 \times 10^{40}$ ergs s^{-1} (see §2.3) to isolate AGN from star-forming galaxies. For the mid-IR and X-ray selected AGN, we apply a luminosity cut corresponding to the flux limit of the corresponding surveys at $z = 1$ (see §3.1 and 3.3 for details). This redshift is selected as a compromise between obtaining sufficient numbers of AGN, large numbers of clusters, and sufficient leverage on the cosmic time probed. Table. 5.1 presents the number of sources that remain for each selection technique and redshift bin. These numbers are based on cuts (described in detail in the following subsections) corresponding to the median redshift of the clusters in each bin, e.g., $\langle z \rangle = 0.38$ (0.39), $\langle z \rangle = 0.74$ (0.74) and $\langle z \rangle = 1.19$ (1.18) for mid-IR and X-ray (radio) selections. Also tabulated are the field AGN surface densities for each technique and redshift bin, where we have simply divided the number of sources by the corresponding survey area. These field surface densities are shown as dashed horizontal lines in Fig. 5.1. Finally, we note that for the X-ray and mid-IR selected AGN in the highest redshift bin ($1 < z \leq 1.5$), this approach only provides a lower limit to the surface density of AGN down to the luminosity limit considered in the lower redshift bins.

The surface density distributions for AGN in the galaxy clusters are calculated as follows. We calculate the angular separation from each ISS cluster center to each mid-infrared, radio and X-ray selected AGN candidate, subject to the flux cuts discussed above. AGN candidates are identified out to $5'$ from the cluster centers, and we bin the radial distances to compute the surface density profiles of AGN ($0.5'$ bins), presented in Fig. 5.1. As expected, at large radii the derived surface densities asymptote to the field AGN surface densities. Throughout this chapter, we adopt Poissonian errors for AGN counts and use the Gehrels (1986) small numbers approximation for Poisson distributions. Fig. 5.1 presents the 1σ errors for both the AGN counts and the field surface densities for each technique and redshift bin.

As a check on this method, we also calculated the AGN surface density distribution at random locations in the field. We created 40 mock cluster samples by simply offsetting all of the cluster positions by medium-scale offsets — larger than the typical cluster size, but small enough that few clusters would fall outside of the survey region. Deriving the radial surface density profile around the mock cluster samples, we consistently find no significant variation relative to the field surface densities.

In contrast to the mock sample, an excess of AGN is found near the centers of clusters, most prominently at $z \geq 0.5$. The next sections detail the results obtained for each of the three AGN selection criteria considered. We note that we have verified that spatially proximate clusters are not biasing our results. Since the overdensities described below are only found at small radii (< 1 Mpc), the number of AGN counted as potential central members to more than one cluster is negligible (null for $r < 0.5$ Mpc, and $< 1\%$ for $0.5 < r < 1$ Mpc).

5.3.1 Density profile of mid-IR selected AGN

The radial surface density profile for mid-IR selected AGN is shown in Fig. 5.1 (top row), separated into the three redshift bins described above. The 5.8μm limiting flux density of the ISS is 51μJy (5σ). Assuming a pure power law spectrum for the AGN, the corresponding luminosity

density is $L_\nu = 4\pi d_L^2 S_\nu/(1+z)^{(1-\alpha)}$ where d_L is the luminosity distance and α is the spectral index ($S_\nu \propto \nu^\alpha$). This assumption of a power-law is born out by both the mid-IR colour-colour plots of broad-lined AGN used to develop the mid-IR AGN selection criteria (e.g., Lacy et al. 2004, Stern et al. 2005) and broad-band composite AGN spectral energy distributions (Richards et al. 2006). We adopt a mean spectral index of 0.73, as given by Stern et al. (2005). The depth of the ISS 5.8μm data corresponds to a 5.8μm luminosity of 2.2 x 10^{44} ergs s^{-1} at $z = 1$, which we adopt as our luminosity cut. Thus for any given cluster we only consider mid-IR selected AGN whose luminosity (and corresponding flux density) is above this value under the assumption that they are at the cluster redshift.

The $z \leq 0.5$ galaxy clusters do not show any significant enhancement of mid-IR selected AGN relative to the field. In the $0.5 < z \leq 1$ bin, however, a weak overdensity of mid-IR selected AGN is observed at the cluster center ($r < 0.3$ Mpc). Throughout the chapter, the significance of overdensities have been derived as follows. We first subtract the number of AGN in a given aperture by the field AGN population to a given (redshift-dependent) flux density limit. This field-corrected number of AGN is then referenced to the expected field counts using the Gehrels (1986) small numbers approximation for Poisson distributions. The central excess of $0.5 < z \leq 1$ mid-IR selected AGN is thus significant at the 2σ level. A small excess of AGN is suggested in the center of the $z > 1$ galaxy clusters, but is not significant relative to the field density. Recall that since the highest redshift bin considers more luminous AGN than the $z < 1$ bins, the resulting, weak overdensity is a lower limit to the number of AGN per cluster to the luminosity limit of the $z < 1$ clusters.

5.3.2 Density profile of radio selected AGN

The radial surface density profile for radio-selected AGN is shown in Fig. 5.1 (middle row), separated into three redshift bins. For each redshift bin, we apply the conservative uniform luminosity cut described in §2.3 to remove star-forming galaxies, adopting a mean radio spectral index of -0.75, as given in de Vries et al. (2002).

In the $z \leq 0.5$ bin, a weak overdensity (1.5σ) of radio sources is observed at the cluster center. The $0.5 < z \leq 1$ galaxy clusters show a very clear excess of AGN in the center ($r < 0.3$ Mpc), with no excess seen at larger radii. The central excess is significant at the 3σ level. The higher redshift galaxy clusters ($1 < z \leq 1.5$) also show a significant excess (2σ) at the cluster center, albeit weaker and on a larger scale ($r < 0.5$ Mpc) relative to the moderate redshift galaxy clusters.

5.3.3 Density profile of X-ray selected AGN

The radial surface density profile for X-ray selected AGN is shown in Fig. 5.1 (bottom row). The limiting flux of XBoötes in the 0.5 – 7.0 keV range is $\sim$ 7.8 x 10^{-15} ergs cm^{-2} s^{-1}, where the XBoötes flux values have been calculated from the counts assuming an X-ray AGN power-law spectrum with photon index $\Gamma = 1.7$ (Kenter et al. 2005). While the shallow depth of the XBoötes survey implies that any source detected at $z \geq 0.12$ must be an AGN (Gorjian et al. 2008), we only plot sources whose X-ray luminosity exceeds the limiting sensitivity of XBoötes at redshift unity. The same photon index value is adopted to calculate the X-ray luminosities. The luminosity cut applied for X-ray selection is therefore 3.3 x 10^{43} ergs s^{-1} in the 0.5 – 7.0 keV range. As emphasized for the mid-IR selected AGN, the lower, right panel of Fig. 5.1 is a lower limit to the surface density of X-ray selected AGN at the luminosities plotted in the first two panels.

No significant enhancement of the X-ray selected AGN is observed for the lowest redshift ($z \leq 0.5$) galaxy clusters. A small central overdensity is suggested for $0.5 < z \leq 1$ galaxy clusters

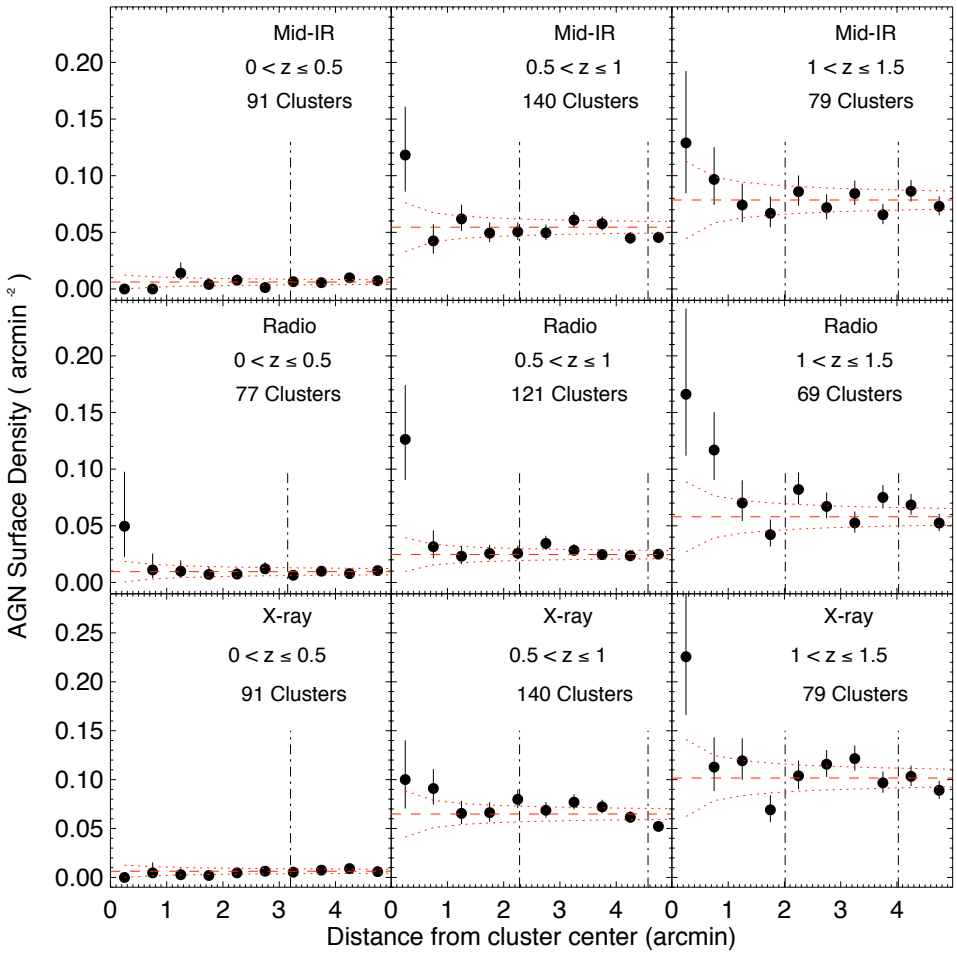

Figure 5.1. Radial density profile of mid-IR selected AGN (top row), radio-selected AGN (middle row) and X-ray selected AGN (bottom row). Galaxy clusters are divided into three redshift bins: $z \leq 0.5$ (left column), $0.5 < z \leq 1$ (middle column) and $1 < z \leq 1.5$ (right column). The global field density is shown by the red dashed line. The red dotted lines indicate the 1σ variations in the field densities and the error bars indicate the 1σ errors on the AGN counts; both assume Poissonian errors and Gehrels (1986) small numbers approximation. The 1 Mpc and 2 Mpc projected radii are indicated by vertical dot-dashed lines for the median redshift of the clusters plotted in each bin. The number of galaxy clusters used in the profile calculation is also indicated at the top right of each panel. An overdensity of AGN is observed in the centers of galaxy clusters at $z > 0.5$ while little or no variation relative to the field density is found at lower redshifts ($z \leq 0.5$).

(1.2σ level; $r < 0.5$ Mpc). On the other hand, the $1 < z \leq 1.5$ galaxy clusters show a modest excess (2σ) at the cluster center ($r < 0.25$ Mpc).

We note that, in principle, X-ray point sources are harder to identify in galaxy clusters with significant diffuse X-ray emission. The intergalactic medium in such clusters would tend to decrease the apparent AGN surface density for lower redshift clusters in a shallow survey such as XBoötes. XBoötes identifies 43 extended sources (Kenter et al. 2005) of which 38 are covered by ISS. The size of these extended sources, derived from Gaussian fits to their source profiles, is (except for one source) less than $0.5'$. The overdensity of X-ray point sources that we observe in

our galaxy cluster sample is clearly detected within 0.5 Mpc ($r \sim 1.5'$ at $z = 0.5$) of the cluster center. The brightness of an unresolved cluster member with an X-ray luminosity equivalent to our threshold would, on average, be five times brighter than that of the extended sources. Only in four clusters would a threshold source have a flux comparable to the extended source (e.g., brightness contrast < 2). Given these small numbers, we are confident that extended, diffuse X-ray emission from rich clusters is not strongly biasing our results.

5.4 Discussion

This chapter presents the first comprehensive study of the radial density profile of AGN for a uniformly-selected cluster sample distributed over a large fraction of cosmic time. Only the radio-selected AGN show a weak (1.5σ) overdensity in the lowest redshift ($z \leq 0.5$) bin. An excess of AGN is observed near the center ($r < 0.5$ Mpc) of galaxy clusters at $z > 0.5$, and all three AGN selection criteria show a pronounced enhancement in AGN activity at $0.5 < z \leq 1$ relative to $z \leq 0.5$. The excess is even observed for the highest redshift galaxy clusters ($1 < z \leq 1.5$), though we are only plotting to the flux limits of the input mid-IR and X-ray catalogues at these high redshifts, implying a less sensitive luminosity limit than in the $z \leq 1$ clusters. We therefore show that AGN activity in galaxy clusters increases with redshift.

We first compare the luminosity cuts applied for each selection criteria to see how the AGN samples relate to one another. The luminosity cut applied for the mid-infrared selection is 2.2 x 10^{44} ergs s^{-1} at 5.8μm. Elvis et al. (1994) provides a mean spectral energy distribution (SED) for quasars derived from broad-band photometry covering the full electromagnetic spectrum from radio to X-rays. Using this composite SED for radio-loud quasars, the luminosity cut at 5.8μm corresponds to a luminosity cut of $\sim 2.2\times10^{43}$ ergs s^{-1} in the 0.5−7 keV X-ray band and 2.2×10^{41} ergs s^{-1} at 1.4 GHz. Our X-ray luminosity cut is 3.3×10^{43} ergs s^{-1} which is comparable to the depth of the mid-infrared selection. A more recent determination of the mean quasar SED was performed by Richards et al. (2006) and gives an X-ray luminosity five times smaller at a given mid-infrared luminosity compared to the Elvis et al. (1994) template. This would imply that our X-ray selection only identifies AGN five times more powerful than the mid-infrared selection. Our radio luminosity cut is 2.5×10^{40} ergs s^{-1} at 1.4 GHz. Therefore, the AGN radio selection depth is reaching almost ten times the depth of the mid-infrared selection, and ten to fifty times the depth of the X-ray selection, depending on which quasar composite template is adopted. This deeper radio sensitivity is a plausible explanation for why only the radio-selected AGN show an overdensity in the lowest redshift galaxy clusters.

One concern is that due to the larger volumes accessible at higher redshifts, our sample of clusters becomes progressively richer with redshift. In this case, the rising number of AGN seen in the higher redshift clusters could simply trace the rising number of massive cluster members in the higher redshift clusters, with a constant, non-evolving fraction of massive galaxies being active. In order to study this effect, we use the photometric redshifts derived from the 4.5μm ISS sample (see §2.1) to determine the mean number of cluster members brighter than $0.5L^*$ as a function of cluster redshift. We consider the observed 3.6μm flux density, converted to 1.6μm rest-frame luminosity assuming a $z_f = 3$ formation redshift and passive evolution (e.g., see Eisenhardt et al. 2008). We only consider members brighter than $0.5L^*$ within the inner 0.5 Mpc of the clusters. As expected, we do indeed find clusters at $z \sim 0.3$ are, on average, slightly less rich than clusters at $z \sim 0.8$. Clusters at $0 < z \leq 0.5$ have an average of 6.5 members brighter than $0.5L^*$ while 10.0 members are found, on average, in clusters at $0.5 < z \leq 1$. At redshifts above 0.8, the number of cluster members in the inner 0.5 Mpc and brighter than $0.5L^*$ actually begins to decrease,

with 5.7 galaxies, on average, for clusters at $z > 1$. This is not a sensitivity issue since the 90 seconds of combined exposure of ISS provides sufficient sensitivity to detect evolving L^* galaxies to $z = 2$ (Eisenhardt et al. 2008). This decrease in cluster member numbers instead could reflect that clusters at $z > 0.8$ are still in the process of collapsing, that the clusters members are merging, or some combination thereof. However, the variation with redshift is only at the 50% level, while the cosmic evolution of AGN activity is a factor of several more significant (with some variation depending on which AGN selection criterion has been used). For the following discussion, we therefore omit the modest systematic dependence of cluster richness on redshift inherent to the Boötes cluster sample. We do note, however, that this trend would serve to make the fraction of active galaxies in the central regions of $z > 1$ clusters even higher relative to the fraction at $z < 0.8$, since the number of AGN is rising while the number of luminous cluster members is falling.

It is well known that AGN are more common at high redshift. Indeed, there is a strong increase in the quasar density with redshift from the local universe out to $z \sim 2$, a result that dates back four decades (Schmidt 1968). Since then, numerous studies have determined the quasar luminosity function (QLF) for radio (e.g., Dunlop & Peacock 1990), optical (e.g., Croom et al. 2004), infrared (e.g., Brown et al. 2006) and X-ray AGN samples (e.g., Ueda et al. 2003). Eastman et al. (2007) find that the cluster AGN fraction at $z \sim 0.6$ is approximately a factor of 20 greater than the cluster AGN fraction at $z \sim 0.2$. In comparison, this increase is only 1.5 (3.3) for the field sample of AGN more luminous than $L_x > 10^{42}$ (10^{43}) ergs s^{-1} over this redshift range. In order to compare the AGN overdensities associated with galaxy clusters, seen in Fig. 5.1, to the field AGN population, we derive average cluster AGN volume densities as follows. We count the number of sources projected within 0.25 Mpc of the cluster centers for the various redshift bins and selection criteria, and then field-correct this number by subtracting the expected number of sources over this same area based on the field surface density. We assume any identified overdensity is associated with the cluster (e.g., is neither foreground nor background). For the sake of simplicity, we assume a spherical distribution at the cluster redshift to derive a volume density from the measured (field-corrected) surface density. Fig. 5.2 presents this field-corrected volume density of AGN within 0.25 Mpc of the galaxy clusters in the three redshift intervals and for the three AGN selection criteria. We also plot the evolution of optically-selected quasars over this same redshift range using the QLF derived by Croom et al. (2004) from the 2dFQZ project[3]. At $z = 1$, Croom et al. (2004) find that $L^*_{\rm AGN} = 1.6 \times 10^{45}\,{\rm ergs\,s^{-1}}$, corresponding to $M_B = -24.5$. Using the Elvis et al. (1994) quasar template, the mid-IR and X-ray depth of our survey correspond to optical luminosities of $L^*_{\rm AGN} + 1$ ($M_B = -23.5$). Therefore, we plot in Fig. 5.2 the cosmic evolution of optically-selected field quasars brighter than $L^*_{\rm AGN} + 1$ ($M_B = -23.5$) and $L^*_{\rm AGN}$ ($M_B = -24.5$). We find a more pronounced cosmic evolution in the relative density of cluster AGN compared to the field from $z = 0$ to 1.5. In particular, the field-corrected X-ray selected AGN density in clusters evolves at least three times more rapidly than that of the field population.

This work shows that a higher surface density of AGN is observed in galaxy cluster centers than in the field and that this AGN overdensity increases with redshift out to $z \geq 1$. We therefore confirm a Butcher-Oemler type effect for AGN in galaxy clusters (e.g., Martini et al. 2007) as the number of AGN in clusters increases with redshift similar to the way that higher redshift galaxy clusters have larger numbers of blue, star-forming galaxies.

We find that up to ten percent of the galaxy clusters have at least one AGN near their center ($r < 0.25$ Mpc). Table. 5.2 summarizes the percentage of galaxy clusters with an AGN for each selection technique and redshift bin. These fractions are field-corrected. Considering the lumi-

[3]Croom et al. (2004) present various forms of the empirical QLF. We use the version which fits the QLF with a second-order polynomial to describe the luminosity evolution (Table 5 of that paper).

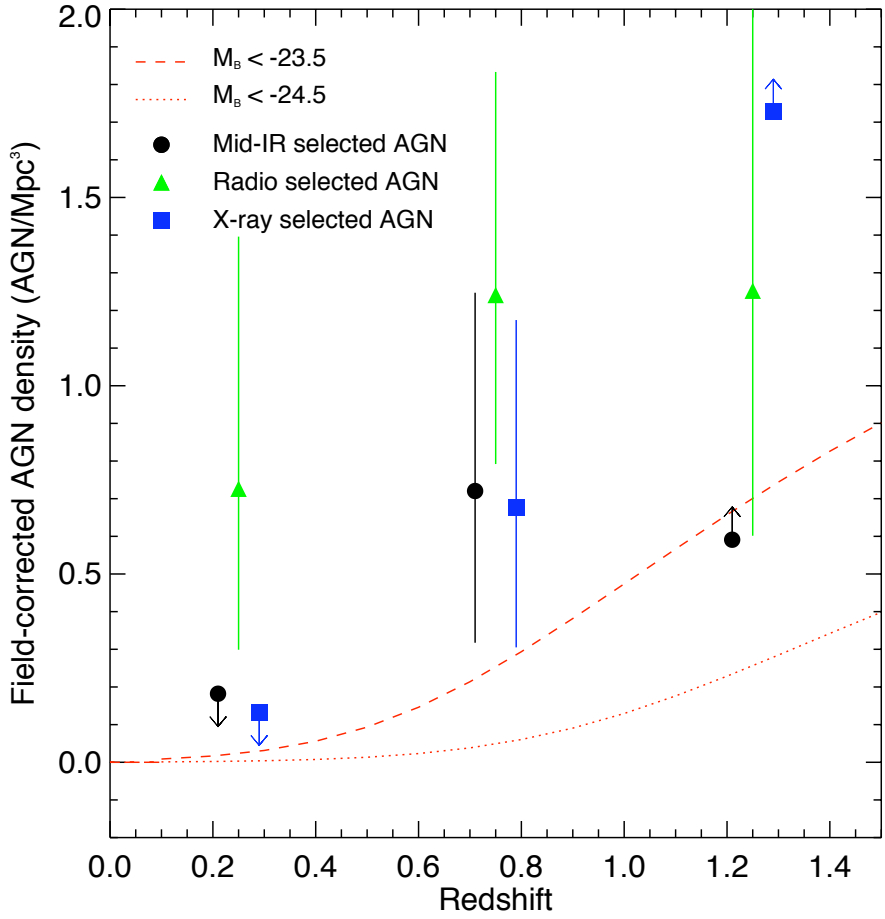

Figure 5.2. Field-corrected volume density of AGN in galaxy clusters and comparison of its evolution relative to an optical quasar luminosity function. Points show the field-corrected overdensity of AGN within 0.25 Mpc of the ISS cluster centers for the three AGN criteria: mid-infrared (black points), radio (green triangles) and X-ray (blue squares). No mid-IR or X-ray selected AGN are found within 0.25 Mpc for the galaxy clusters at $z < 0.5$. We plot the 1σ uncertainty of the field density as an upper limit. Lines show the relative evolution of quasars brighter than $L^*_{\rm AGN}$ ($M_B = -24.5$, dotted red line) and $L^*_{\rm AGN} + 1$ ($M_B = -23.5$, dashed red line) for the field, where $L^*_{\rm AGN}$ is calculated at $z = 1$. These models, which show a less dramatic evolution of AGN in the field relative to clusters, are calculated from the Croom et al. (2004) 2dFQZ QLF (see text for details).

nosity cuts applied for each selection, only 3% of galaxy clusters at $z < 0.5$ have a radio-selected AGN near their center ($r < 0.25$ Mpc) and neither mid-IR nor X-ray selected AGN are found. We find that the fraction of galaxy clusters hosting such an AGN evolves with redshift. By $z \sim 1.5$, up to 10% of our clusters sample host at least one X-ray emitting AGN near their center (9% for radio-selected AGN).

Finally, we note that the current analysis is rather simple, using only the apparent two dimensional distribution of sources across the sky to address the evolving role of AGN in clusters. In principle, a three dimensional analysis, accounting for source redshifts (either spectroscopic or photometric), would significantly lower the field counts in each redshift bin and provide a more

Table 5.2. Fraction of galaxy clusters with at least one AGN in the inner 0.25 Mpc

Selection	$0 < z \leq 0.5$	$0.5 < z \leq 1$	$1 < z \leq 1.5$
Mid-IR	$< 1\%$	$5 \pm 2\%$	$4 \pm 3\%$
Radio	$3 \pm 2\%$	$8 \pm 3\%$	$9 \pm 4\%$
X-ray	$< 1\%$	$3 \pm 2\%$	$10 \pm 4\%$

robust measurement of the AGN Butcher-Oemler effect. We have opted for the former analysis as it relies only on the simple observables of position and flux, and is thus model free. Brodwin et al. (2006) derive photometric redshifts for the Boötes field AGN with an accuracy $\sigma = 0.12(1+z)$, with a 5% outlier fraction. This is approximately half the precision that can be derived for normal galaxies. We are currently obtaining spectroscopic observations of candidate active members of clusters. Future work will use these results to better constrain the pronounced cosmic evolution of AGN activity in rich environments.

5.5 Summary

The spatial distribution of AGN has been derived for a well-defined sample of galaxy clusters at $0 < z \leq 1.5$. The AGN are selected using three different selection techniques (mid-IR colour, radio luminosity, and X-ray luminosity) that isolate distinct types of active galaxies to ensure the fullest selection of AGN in our galaxy cluster sample. An overdensity of AGN is found near the center ($r < 0.5$ Mpc) of galaxy clusters at $z > 0.5$ and this AGN excess increases with redshift. We confirm that the rising number of AGN is not simply due to the clusters becoming richer with redshift with a non-evolving fraction of cluster members being active. It is well known that AGN are also more common at high redshift. We therefore also confirm that the observed increase in redshift is more pronounced in the galaxy cluster sample than in the field. We thus find a Butcher-Oemler type effect for AGN in galaxy clusters.

Acknowlegments: We thank the anonymous referee whose comments significantly improved this work. We thank Joël Vernet and Carlos De Breuck for carefully reading the manuscript. This work is partly based on observations made with the *Spitzer Space Telescope*, which is operated by the Jet Propulsion Laboratory, California Institute of Technology under a contract with NASA. This work made use of data products provided by the NOAO Deep Wide-Field Survey, which is supported by the National Optical Astronomy Observatory (NOAO). NOAO is operated by AURA, Inc., under a cooperative agreement with the National Science Foundation. AHG acknowledges support from NSF grant AST-0708490. SAS's work was performed under the auspices of the U.S. Department of Energy, National Nuclear Security Administration by the University of California, Lawrence Livermore National Laboratory under contract No. W-7405-Eng-48.

Chapter 6

Conclusions & Perspectives

In the first chapters of this thesis, we investigated the surroundings of powerful radio galaxies known to often lie in overdense regions to chase galaxy clusters at high redshifts. Classical studies (optical, X-rays) have discovered galaxy clusters up to $z \sim 1.45$. Protoclusters have been found in the surroundings of radio galaxies at $z > 2$ and up to $z = 5.2$. We focussed our work in the less studied redshift range $1.4 < z < 2$ in order to unravel the nature of galaxy clusters in that transition period and study the missing link between protoclusters at $z > 2$ and relaxed bounded virialized systems at $z < 1.5$. We targeted in priority the passively evolving population in order to directly aim for the more massive components and study the presence and characteristics of a red sequence in these systems.

Four[1] fields around high redshift radio galaxies at $1.4 < z \lesssim 2$ are intensively studied in this thesis: 7C 1756+6520 ($z = 1.416$), 7C 1751+6809 ($z = 1.54$), MRC 1017-220 ($z = 1.77$) and MRC 0156-252 ($z = 2.02$). The targets were selected to be luminous radio galaxies ($L_{3GHz} > 10^{26}$ W/Hz) that do not show any divergent properties. The spatial arrangement of the red galaxies is always clearly non-homogeneous and often presents some filament-like distribution. However, a large field-to-field variation is observed. Half of our studied HzRGs reside in an overdense region of red sources (by a factor of $2 - 3$ compared to other fields). Venemans et al. (2007) studied the Lyα emitting galaxies population around 8 HzRGs at $2.0 < z < 5.2$ and found that 75% of their sample reside in protoclusters. Both these complementary methods show that powerful radio galaxies are an efficient tool to reveal high redshift galaxy systems.

A clump of both red passively evolved and blue star-forming galaxies is found in the close vicinity of 7C 1756+6520. Several other clumps of red sources are also detected, aligned in the direction NW/SE with this 'central' group, forming a large scale elongated structure of galaxies of about 5 Mpc. An overdensity of red and blue sources is also found around MRC 0156-252, although much more compact and concentrated within 1 Mpc of the radio galaxy. Although a second clump of blue galaxies is suggested in the South-East part of the field, no clear evidence of a large scale structure is observed in that field showing how different these two detected structures can be. In both cases, the red galaxies candidates have colours consistent with red-sequence-like objects with $z_f \geq 2$. We find that the bright end of the red sequence ($K_{AB} < 21.5$ corresponding to $M_{stars} > 10^{11}$ M$\odot$; Kodama et al. 2007) in 7C 1756+6520 is already well populated. A truncation of the red sequence is observed at $K > 21.5$ suggesting that the galaxy cluster may still be a young system in formation and that the fainter end of the red sequence will get populated with time. The red galaxies in the field of MRC 0156-252 are fainter by an order of magnitude in K. The majority of red sources with colours consistent with our red sequence models have $21 < K < 21.5$, a result

[1]The study of an additional fifth field around 7C 1805+6332 ($z = 1.84$) is also presented in an appendix of chapter 2.

consistent with what was found for the protocluster associated with PKS 1138-262, another radio galaxy at $z \sim 2$. This suggests that the structure around MRC 0156-252 contains less massive galaxies that the system associated with 7C 1756-6520.

Both radio galaxies have possible close-by companions. A star forming candidate at $z > 1.4$, a passively evolving candidate at $z > 1.4$ and an AGN candidate are found in the immediate surrounding of 7C 1756+6520 (within $6''$; see chapter 2). The red galaxy and the AGN candidate were observed in spectroscopy and are both found with spectroscopic redshifts consistent with the radio galaxy (chapter 3). MRC 0156-252 is also surrounded by three nearby sources (within $7''$ from the radio galaxy). All three sources are aligned with the radio axis of MRC 0156-252 which strongly suggests they are lying at the same redshift. We still require spectroscopic observations however, to confirm their association with the HzRG. The scale of the two groups around 7C 1756+6520 and MRC 0156-252 is consistent with the Spiderweb structure associated with PKS 1138-262 (see chapter 1) suggesting that radio galaxies may be often lying in very dense merging systems.

Spectroscopy is still to be performed in the field of MRC 0156-252 in order to prove the association of the excess of red sources with the radio galaxy. We confirmed on the other end that 7C 1756+6520 is indeed lying in a large scale structure of galaxies thanks to a successful spectroscopic campaign with Keck/DEIMOS (chapter 3). Optical spectroscopy in this field has permitted to confirm 20 galaxies at the redshift of the radio galaxy. Seven of these galaxies have velocity offsets $\Delta v < 1000$ km s^{-1} relative to the redshift of the radio galaxy and found within 2 Mpc of the radio galaxy. A second clump of four galaxies form a compact (within $1'$ from each other) sub-group at $z \sim 1.437$ (offset by $\Delta v \sim 3000$ km/s), associated with the galaxy structure and offset by about $1.5'$ to the east of 7C 1756+6520. We therefore confirm a large scale structure of galaxies associated with the radio galaxy composed of (at least) two main groups: a galaxy cluster centered on the radio galaxy at $z = 1.4156$ (8 spectroscopically confirmed members so far) and a background compact sub-group at $z \sim 1.437$. We note however that we obtained spectroscopic redshifts for only three of our red galaxies. Most of the confirmed members were either AGN or present a clear [OII] emission line, signature of on-going star-formation. Galaxies with no recent/on-going star-formation are characterized by breaks in their spectral energy distribution in particular the 4000Å break beyond 0.96μm at $z > 1.4$. Near-infrared spectroscopy is therefore required to prove the association of our red candidates with the large scale structure in the field of 7C1756+6520. It will permit to confirm the membership of the several clumps of red galaxies detected in the field (chapter 2) as well as derive more specific properties of the cluster itself through the analysis of its red sequence.

We also dedicated part of our work to study the population of AGN in galaxy clusters. Four AGN were spectroscopically confirmed to be associated with 7C1756+6520, two of them lying within 0.75 Mpc of the radio galaxy. In light of this result and of numerous recent multiwavelength studies of AGN in galaxy clusters, we extended this study to a large sample of 310 clusters at $0 < z < 1.5$ (chapter 5). We selected AGN using three different selection techniques: mid-infrared colours, radio luminosity and X-ray luminosity and found a clear overdensity of AGN within 0.5 Mpc of the cluster centers, the amplitude of the overdensity increasing with redshift. We confirmed the existence of a Butcher-Oemler type effect for AGN in galaxy clusters with the population of AGN being more prevalent in clusters at high redshifts than at the present time.

Many projects are now in progress to pursue the work that has been done in this thesis. Following is a non exhaustive list of on-going projects.

Studying the red sequence at $z = 1.9$:

As part of the HAWK-I project on which the analysis in chapter 4 was based, we obtained near-infrared data from a sample of 8 radio galaxies fields with $1.7 < z < 2.5$. We recall that the first goal of this project was to study the emergence of the red sequence in cluster/protoclusters at high redshifts through the study of their red evolved population. Our sample spreads over the redshift range $1.7 < z < 2.5$. The initial HzRG sample contained 10 targets but two HzRGs at $z \sim 1.9$ were not observed due to a confusion in the coordinates systems during the OBs design at VLT. A first study has been done on the $z > 2$ fields (Hatch et al. in preparation) and shows that these fields present a clear segregation of the galaxy populations with the red evolved systems being more centrally concentrated than the blue star-forming younger ones. These protoclusters are however dominated by young, blue galaxies and are therefore probably at an early stage of their evolution. For at least one of the lowest redshift fields, MRC 0156-252 at z=2.02 (chapter 4), our study showed a quite different population of cluster galaxies, with a prominent excess of red galaxies in the vicinity of the radio galaxy, with their colours consistent with what is expected from an old stellar population that has evolved passively from $z_f = 2 - 5$. These results show how important this redshift range is to look at the first 'clusters'. In December 2009, the ESO time allocation committee accepted our new proposal to re-observe our missing sources at $z \sim 1.9$: MRC 0324-228 ($z = 1.894$) and MRC 0350-279 ($z = 1.90$) in Y, H and Ks with VLT/HAWK-I. The analysis of these two new targets will be done the same way as in chapter 4 with a YHK selection of both the red and blue cluster populations. It will complete our original sample which will finally cover homogeneously the redshift range $1.7 < z < 2.5$.

Tracking the galaxy build-up in a protocluster around TNJ1338-1942 at $z = 4.1$:

In this thesis, we focused on the redshift range $1.4 < z < 2$ in order to look at the missing link between the clusters known to date at lower redshifts and the protoclusters that were found at $z > 2$ around HzRGs. Much attention has been given to the redshift range $2 < z < 3$. Spectroscopy of Lyα emitters in the field of HzRGs at $z > 2$ have revealed protoclusters up to $z \sim 5.2$. A complementary approach focussing on fields at $2 < z < 3$ has made use of wide near-infrared imaging and colour cuts with filters bracketing the 4000Å break to isolate more massive protoclusters members, the red evolved galaxies (with $M_{stars} > 10^{11}$ M$\odot$). Kodama et al. (2007) found overdensities of red galaxies in their fields at $z \sim 2$ with colours consistent with red-sequence like objects that will most likely evolve into present day cluster ellipticals. They also note that the massive end ($M_{stars} > 10^{11}$ M$\odot$) of the red sequence of their protoclusters at $z \sim 2$ is already well populated. On the contrary, only a few galaxies are found with colours consistent with red sequence models of an evolved population at $z \sim 3$. If these cluster candidates are confirmed to be at the redshift of the radio galaxy, these red objects would also be much less massive. Following this first and promising study, we aim to target even higher redshift radio galaxies to look further back in time and explore even earlier epoch of massive galaxies formation. Two protoclusters were confirmed in the surroundings of HzRGs at $z > 4$. The highest redshift radio galaxy to date, TN J0924-2201 at $z = 5.2$ is known to lie in an overdense region of 6 spectroscopically confirmed Lyα emitters (Venemans et al. 2004). Another protocluster is known in the field of TN J1338-1942, a radio galaxy at $z = 4.1$. 37 Lyα emitters are confirmed in this region to date (Venemans et al. 2002, 2007). Using deep optical multiwavelength observations with HST/ACS, Overzier et al. (2008) selected 66 Lyman Break Galaxies candidates (g_{475}-band dropouts), 6 of which are also Lyα emit-

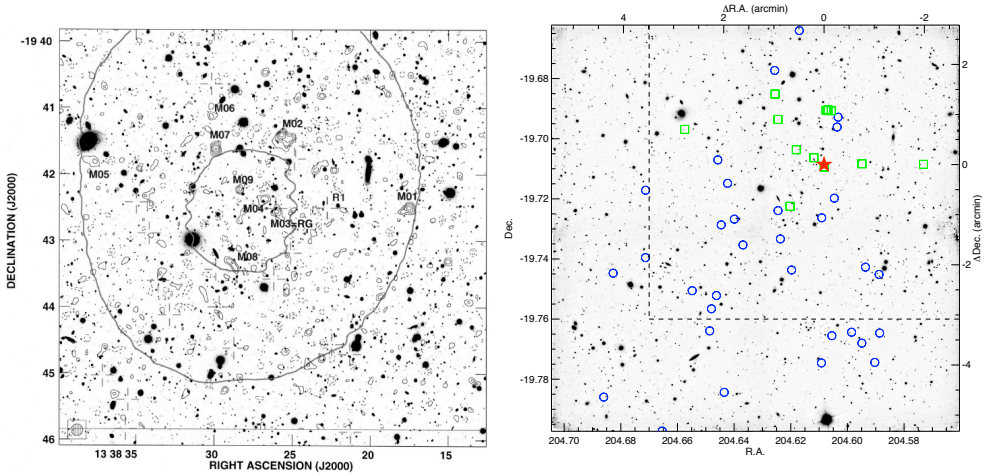

Figure 6.1. The TN J1338-1942 protocluster at $z = 4.1$. *Left:* From De Breuck et al. (2004): A FORS R-band image of the protocluster with the 1.2mm MAMBO contours overlaid. The nine objects (M01-M09) are clear mm detections. *Right:* Our new VLT/HAWK-I H-band of the field with Lyα emitters (MAMBO mm sources) overlaid in blue circles (green squares). TN J1338-1942 is shown as the red star. Right and upper axis indicate distances from the radio galaxy. The MAMBO field of view (left panel) is shown by the dashed line.

ters confirmed protocluster members. Overzier et al. (2008) estimate the TN J1338-1942 to be a $> 10^{14}$ M$\odot$ structure. The field also shows a significant overdensity of 1.2mm sources detected by MAMBO/IRAM (see Fig. 6.1, left panel, from De Breuck et al. 2004). If confirmed at $z = 4.1$, these sources would have SFRs > 1000 M$\odot$ yr^{-1} which would trace the bulk of star-formation of this protocluster. *Spitzer*/IRAC data are also available for our SHzRG project (see next section). To complete this unique dataset, we obtained H and Ks-band data with VLT/HAWK-I (Spring 2009). Data were reduced by the MVM pipeline and are now ready for analysis. They covered the entire MAMBO mm objects from De Breuck et al. (2004) as well as the 37 Lyα emitters from Venemans et al. (2007); see Fig. 6.1, right panel. The 4000Å break at $z = 4.1$ is at the blue end of the Ks-band. The colour combination H, Ks and 3.6μm at $z = 4$ will match nicely the JHK selection used to identify both red and blue population of protoclusters at $2 < z < 3$.

Statistical study of the environment of 70 **HzRGs using** *Spitzer***:**

All the radio galaxies whose surroundings have been studied in the first chapters of this manuscript (7C 1756+6520, 7C 1751+6809, 7C 1805+6332 in chapter 2, MRC 1017-220, MRC 0156-252 in chapter 4) as well as those that are planned to be observed by HAWK-I (MRC 0324-228 and MRC 0350-279 at $z \sim 1.9$, see earlier in the text) are part of the SHzRG sample, 70 high redshift radio galaxies from $1 < z \leq 5.2$ (see chapter 1). They were all observed in the four *Spitzer*/IRAC channels (3.6, 4.5, 5.8 and 8.0μm; channels 1, 2, 3 and 4 hereafter), most of them as part of our project consisting of four dithered 30s exposures. 8 observations were conducted during 'Guaranteed Time Observation' (GTO) programs and are deeper than our standard 120s observations (see Seymour et al. 2007for details on the dataset). Each image covers an area about 12′ by 8′ but the final area covered simultaneously by the four channels is about $6' \times 8'$. This is a unique sample of HzRGs observed homogeneously at the same wavelengths.

Chapter 5 presents a statistical study of the AGN population in galaxy clusters to $z = 1.5$. One of the method used in this chapter to select AGN was a purely mid-infrared colour selection technique introduced by Stern et al. (2005). This method was also described and applied in chapter 2 where a clear overdensity of mid-infrared selected AGN (now spectroscopically confirmed, see chapter 3) has been detected around 7C 1756+6520. We recall that active galaxies can robustly been identified using pure mid-infrared colour criteria (Stern et al. 2005). AGN are distinguished from normal galaxies by: $([5.8] - [8.0]) > 0.6 \cap ([3.6] - [4.5]) > 0.2 \times ([5.8] - [8.0]) + 0.18 \cap ([3.6] - [4.5]) > 2.5 \times ([5.8] - [8.0]) - 3.5$ (where [3.6], [4.5], [5.8] and [8.0] are the magnitudes in Vega system in the channels 1, 2, 3 and 4 respectively). We point out that this selection criterion does not select AGN in any specific redshift range. We applied this selection technique to find the AGN candidates in our 70 fields and observed a large field-to-field variation of the number of mid-infrared selected AGN candidates. In order to be able to compare them directly, we cut the AGN catalogues of each field to a comparable depth. We adopted the 5σ flux limits of the ISS (see chapter 5), i.e., 6.4, 8.8, 51 and 50μm for channels 1, 2, 3 and 4 respectively. At these 5σ limits, the number of AGN expected in ISS for such an area is about 3.22. Fig. 6.2 presents the number of AGN found in each field at these limits. We highlight in filled red circles, the four densest fields. We already knew from the results of chapter 2 and 3 that the field around 7C 1756+6520 was much denser than average. In light of this new study, it seems that 7C 1756+6520 is indeed a very peculiar field. We also notice that the field around 7C 1805+6332 is overdense in mid-infrared selected AGN candidates. We isolated the evolved population at high redshift in this field using combined optical and near-infrared colour cuts (see Appendix of chapter 2) but did not find any particular overdensity of red objects. We can not affirm at this point that the detected excess of AGN candidates is associated with the radio galaxy. If confirmed however, it would show again the importance of multiwavelength studies to probe the full diversity of sources that constitutes a galaxy cluster. Red open circles in Fig. 6.2 indicate the particular examples of known protoclusters fields including the well studied PKS 1138-262 (the Spiderweb galaxy) and the protocluster TNJ 1338-1942 (see previous section).

However, this is a work in progress. More extensive study of the HzRG sample will try to answer open questions like: What is the spatial distribution of the AGN in the different fields and are they preferentially found concentrated near the HzRG as expected from the results of chapter 5? Can we derive any clues concerning the cosmic evolution of AGN based on our sample and push the analysis of chapter 5 up to $z = 5$? We will also combine our IRAC data with the MIPS 24μm data available for the majority of our 70 fields to derive further properties of high redshift galaxy clusters associated with HzRGs.

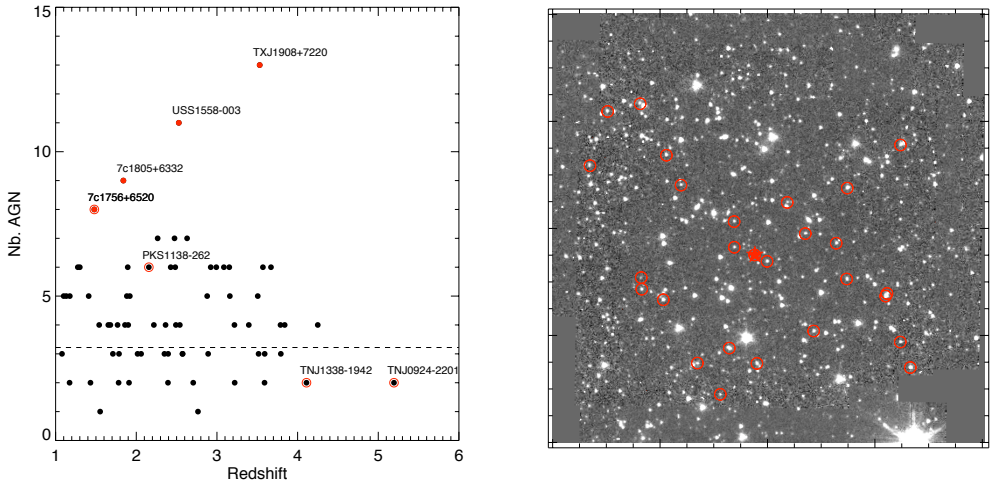

Figure 6.2. Mid-infrared selected AGN candidates in our 70 radio galaxies fields. *Left:* Number of AGN found for each radio galaxy field versus redshift. The expected number of AGN for such area in ISS is 3.22 (see horizontal dashed line). *Right:* Example of spatial distribution of AGN candidates in a combined IRAC1+IRAC2 image of TXJ 1908+7220, our densest field. The radio galaxy is indicated by the red star.

Appendix A

Wide-field near-infrared data

For a long time, the study of high redshift galaxy clusters has been limited by telescope sensitivity. High redshift galaxies are faint and their restframe optical light migrates to the near-infrared where it becomes more challenging to observe faint galaxies due to the increasing sky brightness. The small field of view of the past near-infrared instruments was also limiting the study of large galaxy systems at high redshifts. Thanks to the advent of new wide-field near-infrared cameras such as the CFHT/WIRCam and VLT/HAWK-I, such studies are now possible. In this thesis, we often made use of near-infrared data e.g., CFHT/WIRCAM (see chapter 2) or VLT/HAWK-I (see chapter 4). The following section describes the main steps of the reduction of near-infrared data illustrated by the description of the MVM reduction pipeline. The second section details two artifacts that can commonly be observed in near-infrared data: the crosstalk and the persistence.

A.1 Reducing near-infrared imaging data

We will briefly describe here the main steps of the reduction of near-infrared wide-field data through the example of the 'Multi-scale Vision Model' (MVM) pipeline we used to reduce our HAWK-I data (chapter 4). The ESO/MVM (or 'alambic') is an image reduction system originally developed by Benoit Vandame and taken over by the Virtual Observatory Systems department at ESO to process optical and near-infrared data (e.g. VIMOS, FORS2, ISAAC, SOFI) and was lately adapted to HAWK-I (see section A.2.1 for a description of the instrument). The full pipeline is described in Vandame (2004). We present here the main reduction steps as well as our personal experience with the pipeline.

A first step consists in preparing the data (splitting the multi extension files if needed, checking keyword and chip position etc.). MVM reads the keyword of the raw images and grouped them by filters, exposure time and types: flats, dark, bias, science images. Preparing the reduction also consists in providing the necessary tools for the pipeline (astrometric catalogues, reference grid for the final mosaic etc.). The choice of the astrometric catalogue is particularly important for multi-chip instruments like HAWK-I. MVM can automatically retrieve a star catalogue from the GSC2.2 catalogue using the header keywords. However, we systematically created our own astrometric catalogue since the default catalogue usually does not contain a sufficient number of stars for an optimal astrometry. In this thesis, we are in particular working with colours and relative astrometry between images of different filters is crucial. We therefore usually reduce our bluer band first — J or Y-band where the stars are brighter — using a standard catalogue like the USNO-B1.0 (Monet et al. 2003) catalogue and then extract a source catalogue derived from this image to astrometrically calibrate our redder bands data. This way, all final mosaics are perfectly aligned on the same astrometric grid.

The reduction procedure then follows a classical path schematized in Fig. A.1:

- Creation of master dark, bias and flat
- Creation of a 'bad pixel' (cold/hot) and weight maps
- Correction of fringing and production of background maps
- Harmonization of the gain for multi chips instruments
- Illumination-error correction
- Reduction of the science data and photometric standard
- Instrumental effect removal
- Small scale background removal
- Large-scale background removal
- Relative astrometry, warping and stacking - for each chip separately
- Absolute astrometry - for the final mosaic aligning all chips on the same final grid
- Production of the final image - Final stacking in the case of multi chip instruments

The user is free to change the default parameters of the configuration file of MVM in every step of the reduction. However, intense tests were run on raw images and the default parameters are optimized to produce an exploitable final image.

We should precise however that between the science verification run at the end of January 2008 and the start of operation in ESO Period 81, the entrance window of HAWK-I suffered a significant degradation (a damaged coating of the window). The problem was resolved in August 2008 by replacing the damaged window by a spare window without coating. However, all the data taken before repairs show a cross-hatched pattern in the background of the image. Fig. A.2 shows an example of cross-hatched pattern in the background of one of our control fields (Ks-band). This cross-pattern is basically the result of the convolution of the coating defect pattern with the pupil image. This effect would subtract well in a difference image. However, the pupil rotates — as HAWK-I is mounted on the Nasmyth platform — and a little cross-shaped spider pattern remains[1]. One post-processing solution proposed by the HAWK-I team was to optimize our background subtraction for our set of data. We optimised the pipeline and in particular the sky subtraction, limiting the number of frames used for our sky estimation to the immediate 'neighbours' set of frames. Some of our data were fortunately re-observed in the next periods with smaller DIT*NDIT which reduced the cross-hatch pattern. We were finally able to exploit the large majority of our HAWK-I data after optimization of the pipeline for each field and each filter; only the Ks-band of one of our control field was unexploitable (see Fig. A.2).

[1] More details on the entrance window problem are provided at http://www.eso.org/sci/facilities/paranal/instruments/hawki/doc/HAWKI-NEWS-2008-07-11.pdf

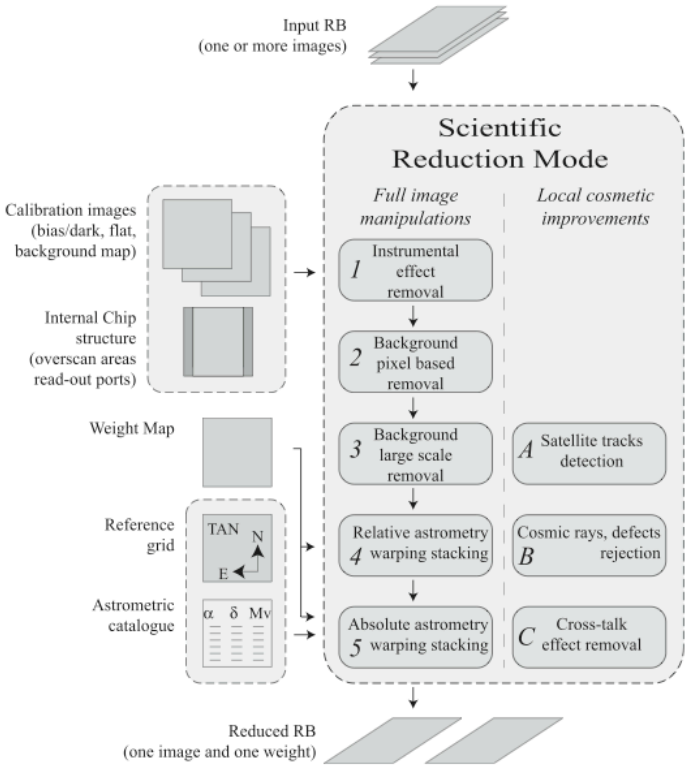

Figure A.1. From Vandame 2004. Main step of a Reduction Mode used to reduce a scientific reduction block containing several images into a reduced image with its corresponding weight-map. See text for details.

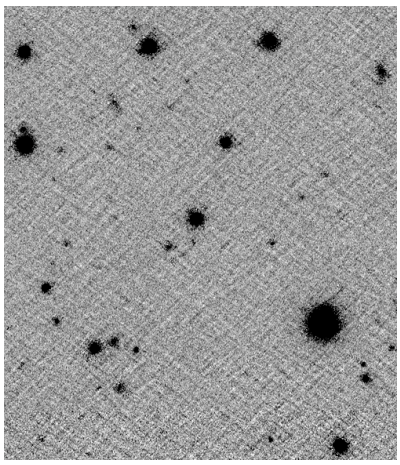

Figure A.2. Cross-hatched pattern in the background of HAWK-I data due to sky subtraction problems after degradation of the entrance window of HAWK-I.

A.2 Data artifact in near-infrared

A.2.1 Crosstalk

If a bright source is imaged by the detector, 'shadows' of this source can be observed on some of the amplifiers, This phenomenon is called the crosstalk and can be summarized as an 'inter-channel capacitive coupling'.

CFHT/WIRCam

The Wide-field InfraRed Camera (WIRCam; Puget et al. 2004) is the near-infrared wide-field imager of the Canada-France-Hawaii Telescope (CFHT) and has been in operation since November 2005. It contains four 2048 × 2048 pixels HAWAII2-RG detectors and covers a field of view of $20' \times 20'$ with a pixel scale of 0.3 arcsec/pixel. Each HAWAII-2RG array is read using 32 amplifiers (horizontal stripes). Until March 2008, WIRCam data present three different types of crosstalk[2]:

- 'Edge' crosstalk: caused by any fast-varying pixels values (star or hot pixels) anywhere on the detector which produces a edge-like shape (3D effect) of ~ 50 adu amplitude on all the 32 amplifiers.
- 'Negative' crosstalk: caused by bright sources which produced a black doughnut-shaped hole of $\sim 50 - 100$ adu amplitude on all the 32 amplifiers.
- 'Positive' crosstalk: affect only the 8 channels that is not seen in any of our data.

Fig. A.3 gives examples of an 'edge' and 'negative' crosstalk on our J-band data of our 7C 1756+6520 field. Several studies have been made to reduce or remove the crosstalk but the different profiles that the crosstalk presents make it very challenging to implement a systematic software correction. Our WIRCam data were some of the first taken after the installation of the camera (beginning of 2006) and the Terapix team, in charge of the reduction pipeline of WIRCam was still at that epoch working on correction methods for the different types of crosstalk. We studied the particular case of the negative crosstalk in our data and estimated that its brightness was a factor of $-1/600$ of the brightness of the object causing the crosstalk. At the depth of our WIRCam data, the crosstalk is clearly detectable out of the background for all objects brighter than $J_{AB} = 16$. We decided to flag the regions affected by the crosstalk in our image. We located the crosstalk by detecting its negative component on an inverted version of our images (using SExtractor) and flag a small area around each position. The crosstalk was flagged using circular boxes of 14 pixels diameters. A visual inspection was also conducted to flag regions affected by fainter crosstalk. Fig. A.4 illustrates this flagging method on a subset of one of our WIRCam J-band data.

In 2007, many improvements on the instrument, both hardware and software have permitted to limit the effects of the crosstalk significantly. For example, cables were changed in July 2007 to eliminate the negative crosstalk.

VLT/HAWK-I

The High Acuity Wide field K-band Imager (HAWK-I; Casali et al. 2006) on the Very Large Telescope (VLT) is a wide-field imager on UT4 with a field of view of $7.5' \times 7.5'$ composed of

[2]For details, see http://www.cfht.hawaii.edu/Instruments/Imaging/WIRCam/WIRCamCrosstalks.html

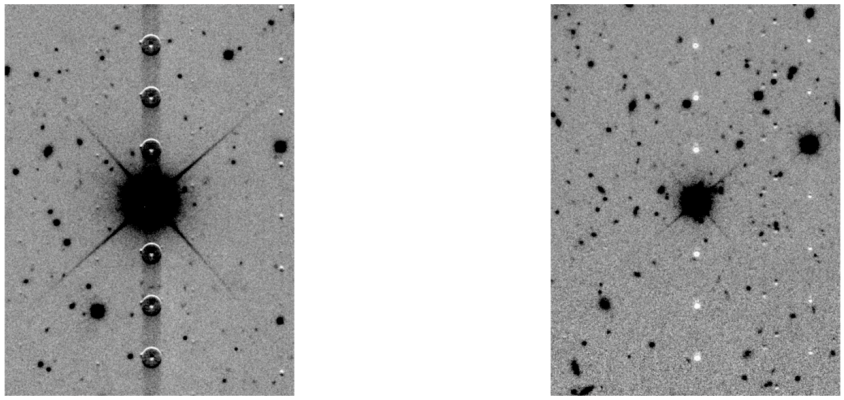

Figure A.3. Example of crosstalk in our WIRCAM *J*-band data of the 7C 1756+6520 field (see chapter 2). Left: 'Edge' crosstalk. Right: 'Negative' crosstalk.

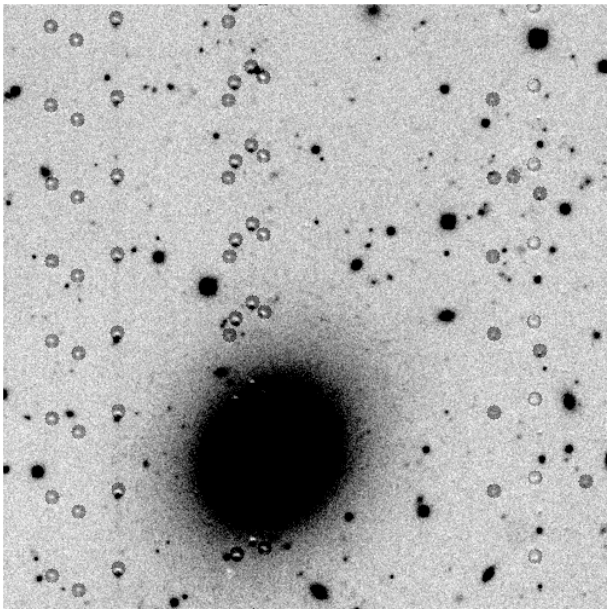

Figure A.4. Example of a $2.5' \times 2.5'$ region of the same *J*-band as Fig. A.3 with crosstalk flag boxes overlaid. Circular boxes of 14 pixels diameters were chosen to flag regions affected by crosstalk before source extraction.

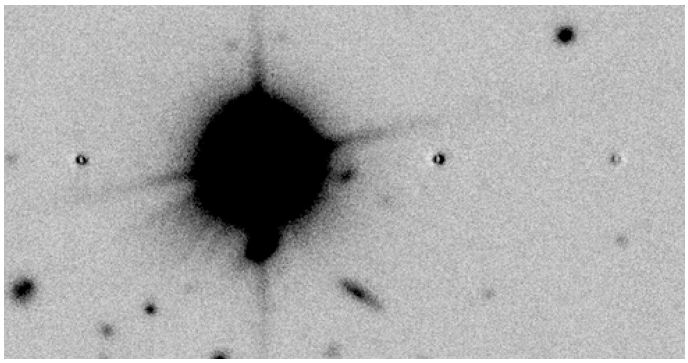

Figure A.5. Example of crosstalk in our HAWK-I Y-band data of the MRC 0156-262 field (see chapter 4).

four 2048 × 2048 pixels HAWAII-2RG detectors separated by a gap of 15″. The pixel scale is 0.1064″. As from WIRCam, 32 amplifiers (but this time organized in vertical stripes) permit a faster readout of the detector. In the case of HAWK-I, the strength of the crosstalk follows an irregular pattern and may be small or negligible for adjacent amplifiers (for details on the HAWK-I crosstalk, see Finger et al. 2008). During our data reduction, we interacted closely with the HAWK-I team, and in particular the detector group in Garching (Gert Finger and Reinhold Dorn). After noticing the important effects of crosstalk in our images, they realised that this effect can be reduced by lowering the detector read speed and changing the bias voltages. Unfortunately, these changes were not implemented before the remainder of our data were obtained. As a result, in all our data, crosstalk is clearly visible for sources with $K_{AB} < 15.5$. The crosstalk of HAWK-I data has only one profile, a crater-like shape with two strong and opposite components: one positive that can be confused with a real source and its negative counterpart. An example of crosstalk in our HAWK-I data is given in Fig. A.5. As for the data from WIRCam, we did not attempt to correct the crosstalk of the images but rather flagged the affected zone by flag boxes. The crosstalk of the HAWK-I data is more important in our 'bluer' bands data (Y and J) since we designed them to be deeper. Stars are also brighter in those bands. We therefore first identified the crosstalk in our Y or J-band. A map was created to flag the crosstalk-affected pixels by $4'' \times 4''$ squared masks. The flag area accounts for less than 2% for most of our fields.

A.2.2 Persistence

'Persistence' refers to the part of the signal that remains on a pixel after being saturated by a very bright source. This residual decreases with time but results in 'ghosts' in the subsequent images. Near-infrared detectors are particularly sensitive to this problem.

To elude this problem, especially when considering high redshift wide field observations, one can avoid including very bright stars on the field observed. In all the near-infared data we have been using in this thesis, only one image shows this persistence effect, the Y-band of our targeted radio galaxy at $z = 1.77$, MRC 1017-220 taken by HAWK-I. HAWK-I detectors suffer of persistence[3] at the level of $10^{-3} - 10^{-4}$ (depending on how badly the pixels were saturated) that decays slowly over minutes (about 5minutes for the maximum tolerated saturation level). No observation in service mode is accepted with this instrument if the field contains objects brighter than $J_{Vega} = 8.8$. Bright objects still however produce a noticeable persistence. MRC 1017-220 is

[3] See HAWK-I User Manual: http://www.eso.org/sci/facilities/paranal/instruments/hawki/doc/

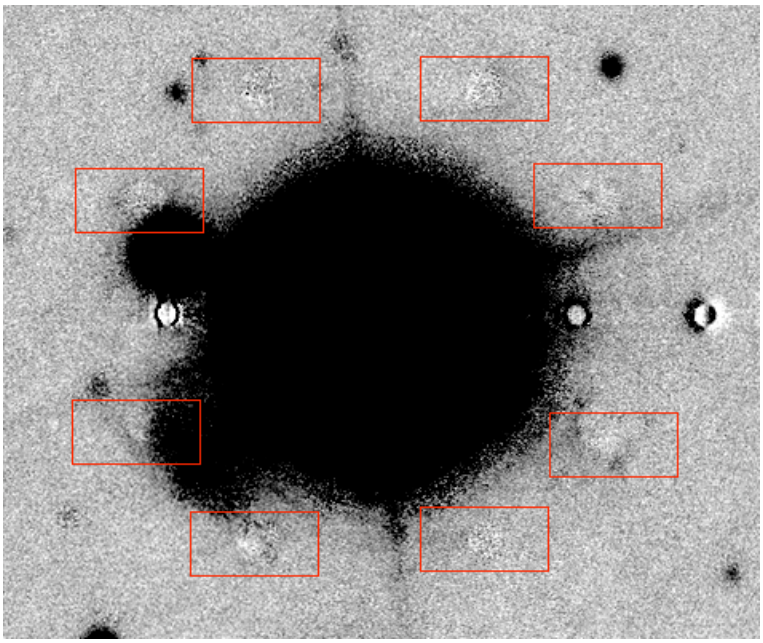

Figure A.6. Persistence in our Y-band HAWK-I data of MRC 1017-220. Ghosts of the saturated star are marked by the red boxes. Crosstalk is also observed, repeating horizontally the signal of the bright star on each amplifier.

unfortunately in a field with many bright stars and despite the optimization of our final covered field, one star with $J_{Vega} \sim 10$ was also observed. The final reduced image is worth showing as another non negligible artifact of near-infrared detectors (see Fig. A.6). The persistence is only visible in the Y-band, the star being much brighter in Y than in the other filters, H and Ks. As for the crosstalk, we flagged the regions of the image affected by persistence.

Appendix B

Source lists

This appendix lists the candidate cluster members described in chapters 2 and 4.
Notes on all tables: Magnitudes are derived using SExtractor MAG_AUTO, with the appropriate Galactic extinction correction applied. The colour selection for the pBzK*, sBzK, zJK, r-YHK and b-YHK galaxies have been made from aperture magnitudes which give slightly different values. Magnitudes are provided in the AB photometric system. ID numbers of all tables correspond to their Ks-band ID number in our SExtractor source catalogues.

B.1 Source lists of chapter 2:

Table B.1. *pBzK** galaxies in the field of 7C 1756+6520

ID	R.A. hms	Dec. dms	*B* (AB)	*z* (AB)	*J* (AB)	*Ks* (AB)	ID	R.A. hms	Dec. dms	*B* (AB)	*z* (AB)	*J* (AB)	*Ks* (AB)
3680	17:57:46.32	65:13:54.5	26.69	21.55	20.60	20.11	4628	17:58:01.68	65:15:14.7	26.78	22.39	20.93	20.15
5321	17:55:50.88	65:16:20.6	24.63	22.91	21.16	20.33	5671	17:58:10.56	65:16:56.6	25.65	22.71	21.59	20.57
7240	17:57:19.19	65:19:31.1	25.94	22.72	21.57	20.67	7325	17:58:26.40	65:19:35.4	26.45	24.22	22.78	21.77
7359	17:57:12.48	65:19:45.1	26.65	22.63	21.37	20.18	8121	17:56:30.72	65:20:52.4	25.20	23.24	22.43	20.99
8267	17:56:16.80	65:21:10.4	23.49	21.90	21.58	20.55	8438	17:56:48.48	65:21:22.0	25.01	23.14	22.04	20.97
9570	17:56:52.56	65:22:59.5	26.88	23.70	22.55	20.71	5624	17:57:01.68	65:16:50.2	>27.1	24.18	22.91	22.03
7317	17:57:12.48	65:19:41.9	>27.1	23.04	21.84	20.63	2516	17:57:20.40	65:11:51.0	>27.1	23.03	22.08	20.92
2738	17:57:12.48	65:12:10.5	>27.1	23.68	22.63	21.30	3078	17:57:53.76	65:12:45.7	>27.1	23.29	21.95	21.09
3363	17:57:33.12	65:13:13.4	>27.1	24.11	22.58	21.81	3503	17:57:28.80	65:13:28.2	>27.1	23.45	21.99	21.18
3662	17:57:11.04	65:13:46.9	>27.1	22.25	21.12	20.44	3927	17:57:40.08	65:14:08.9	>27.1	23.28	22.30	21.33
4060	17:57:41.76	65:14:17.9	>27.1	24.25	22.97	21.71	4505	17:57:26.40	65:14:59.3	>27.1	23.88	22.45	21.74
4698	17:57:52.56	65:15:16.9	>27.1	23.76	22.93	21.57	4736	17:57:40.32	65:15:23.4	>27.1	23.13	21.53	20.51
4948	17:57:16.56	65:15:43.9	>27.1	22.79	21.46	20.49	4963	17:58:06.48	65:15:47.2	>27.1	23.13	21.96	20.74
5019	17:58:13.92	65:15:51.1	>27.1	22.08	20.95	20.11	5130	17:56:55.68	65:16:00.5	>27.1	23.81	22.13	21.20
5488	17:56:25.44	65:16:36.1	>27.1	23.37	22.80	21.57	5620	17:58:19.68	65:16:50.5	>27.1	23.39	21.94	21.20
5858	17:57:44.40	65:17:14.3	>27.1	23.80	23.56	21.62	5914	17:57:40.08	65:17:17.5	>27.1	23.32	21.84	21.10
5957	17:57:33.84	65:17:20.8	>27.1	23.22	22.70	21.58	6245	17:56:43.92	65:17:50.6	>27.1	23.43	22.99	21.69
6601	17:58:29.04	65:18:25.2	>27.1	22.34	20.83	20.33	6691	17:56:32.64	65:18:32.8	>27.1	23.79	22.25	21.46
6870	17:56:48.96	65:18:50.8	>27.1	23.70	22.65	21.32	6864	17:56:52.32	65:18:52.2	>27.1	22.55	21.21	20.31
7174	17:57:28.32	65:19:24.6	>27.1	21.91	20.82	19.93	7380	17:57:13.92	65:19:44.1	>27.1	23.16	21.82	20.79
7428	17:57:22.80	65:19:45.5	>27.1	23.17	22.39	21.46	7401	17:57:58.08	65:19:44.4	>27.1	23.91	22.33	21.40
7523	17:57:05.04	65:19:54.5	>27.1	23.47	22.48	21.31	7866	17:56:42.72	65:20:27.2	>27.1	23.11	21.91	20.93
8002	17:57:21.36	65:20:52.1	>27.1	22.50	21.38	20.30	8263	17:57:52.08	65:21:07.9	>27.1	23.70	22.17	21.48
8348	17:56:55.44	65:21:15.5	>27.1	22.97	21.78	20.80	8523	17:57:40.08	65:21:26.6	>27.1	24.75	22.31	22.10
8484	17:58:16.56	65:21:24.1	>27.1	23.18	21.74	20.92	8466	17:56:19.44	65:21:25.9	>27.1	22.05	20.52	19.87
8567	17:56:35.28	65:21:32.8	>27.1	23.85	22.83	21.33	8828	17:56:50.16	65:21:56.9	>27.1	23.88	22.62	21.54
8918	17:56:50.16	65:22:05.9	>27.1	23.16	22.22	20.94	9022	17:58:36.96	65:22:09.5	>27.1	23.63	22.46	21.20
9139	17:56:12.00	65:22:19.9	>27.1	23.45	21.74	21.25	9166	17:56:25.20	65:22:23.9	>27.1	24.13	22.69	21.42
9271	17:55:31.68	65:22:36.8	>27.1	21.72	21.03	20.14	9812	17:55:55.44	65:23:17.5	>27.1	22.99	22.05	21.32
9869	17:57:33.36	65:23:21.8	>27.1	24.34	23.25	21.83	9988	17:56:54.48	65:23:35.1	>27.1	22.41	21.25	20.23
10169	17:58:07.69	65:23:50.6	>27.1	21.89	20.63	19.79	10254	17:57:11.04	65:23:56.8	>27.1	23.40	22.51	21.20
10235	17:57:25.20	65:23:58.2	>27.1	23.45	22.86	21.76	10512	17:56:49.44	65:24:21.2	>27.1	23.41	22.36	21.13
10665	17:57:45.84	65:24:34.6	>27.1	23.62	21.77	21.39	10904	17:55:42.72	65:24:56.9	>27.1	22.80	21.30	20.43
10985	17:58:14.88	65:25:05.2	>27.1	22.59	21.22	20.32	11081	17:57:00.00	65:25:12.4	>27.1	23.54	22.16	21.73
11220	17:57:54.72	65:25:25.7	>27.1	24.14	22.42	21.53	11217	17:55:33.60	65:25:26.4	>27.1	22.99	21.66	20.56
12866	17:55:57.84	65:25:37.6	>27.1	22.63	21.51	20.59	12994	17:57:39.12	65:25:40.1	>27.1	23.87	23.07	21.62
13007	17:55:57.84	65:25:40.8	>27.1	23.65	22.21	21.36	12759	17:57:16.08	65:26:01.7	>27.1	23.72	22.19	21.36
11707	17:55:55.44	65:26:12.8	>27.1	23.79	22.19	21.43	11677	17:55:39.60	65:26:21.8	>27.1	23.32	21.52	20.83
12035	17:57:05.28	65:27:21.6	>27.1	23.99	22.63	21.80	14470	17:55:29.76	65:27:33.8	>27.1	22.55	21.14	20.41
12008	17:55:46.56	65:27:32.8	>27.1	23.65	22.54	21.64	14436	17:57:28.80	65:27:34.2	>27.1	23.20	22.42	20.72
14533	17:56:58.80	65:27:39.2	>27.1	23.06	22.19	20.44	11906	17:55:59.28	65:27:41.8	>27.1	22.63	22.03	20.78
14570	17:57:35.04	65:27:38.9	>27.1	23.74	22.16	21.30	11555	17:55:57.12	65:27:48.2	>27.1	22.30	20.81	20.18
11952	17:55:57.84	65:27:49.0	>27.1	24.36	22.55	21.85	14428	17:56:49.68	65:27:56.2	>27.1	22.60	21.37	20.63
14524	17:56:42.48	65:28:17.4	>27.1	24.19	22.86	21.62	13997	17:56:47.28	65:28:36.5	>27.1	23.48	22.06	21.32
13794	17:57:06.00	65:29:08.5	>27.1	23.90	23.24	21.40	2365	17:57:34.32	65:11:39.1	>27.1	22.33	20.73	19.78
3178	17:57:10.08	65:12:55.4	>27.1	22.81	21.83	20.89	3223	17:57:09.84	65:12:59.4	>27.1	23.63	22.73	21.49
3731	17:57:36.48	65:13:50.2	>27.1	23.85	22.20	21.32	3686	17:58:14.64	65:13:46.6	>27.1	24.21	22.10	21.00
3791	17:56:41.04	65:13:55.9	>27.1	23.91	21.91	20.98	3786	17:57:46.56	65:13:56.3	>27.1	22.46	21.05	20.25
3920	17:57:34.56	65:14:06.4	>27.1	23.83	22.59	21.18	4351	17:56:25.68	65:14:45.6	>27.1	23.93	21.77	21.30
4592	17:57:59.28	65:15:07.9	>27.1	23.44	22.46	21.03	4777	17:57:19.44	65:15:24.5	>27.1	23.54	22.48	21.45
4852	17:57:53.76	65:15:33.1	>27.1	23.45	22.21	21.02	4910	17:56:53.04	65:15:38.9	>27.1	24.05	22.25	21.31
5079	17:58:14.88	65:15:55.5	>27.1	23.18	21.64	20.29	5773	17:57:26.16	65:17:08.5	>27.1	23.07	21.68	20.60
5885	17:57:51.36	65:17:17.9	>27.1	22.78	21.52	20.46	5959	17:57:21.12	65:17:24.7	>27.1	21.95	21.02	19.94
6356	17:57:59.76	65:18:01.8	>27.1	23.70	22.07	21.16	6624	17:55:27.12	65:18:25.6	>27.1	23.61	21.80	21.03
6666	17:56:33.60	65:18:31.0	>27.1	23.94	22.12	21.18	7069	17:58:21.12	65:19:13.8	>27.1	22.86	21.52	20.31
7269	17:57:29.28	65:19:33.6	>27.1	22.70	21.30	20.16	7982	17:57:10.08	65:20:39.5	>27.1	23.78	22.58	21.48
8264	17:56:53.76	65:21:07.5	>27.1	23.76	22.40	21.20	8535	17:58:22.80	65:21:31.3	>27.1	22.41	20.66	19.95
8787	17:56:55.20	65:21:54.0	>27.1	23.65	21.54	20.59	9193	17:56:45.84	65:22:27.5	>27.1	23.42	21.49	20.71
9356	17:57:02.40	65:22:40.4	>27.1	23.42	22.80	20.94	9886	17:57:12.48	65:23:25.8	>27.1	23.42	21.83	20.58
10430	17:56:46.80	65:24:14.8	>27.1	23.29	21.48	20.69	10535	17:58:11.04	65:24:22.7	>27.1	23.72	22.77	21.36
10832	17:56:18.96	65:24:50.4	>27.1	23.91	22.89	21.34	10871	17:57:58.56	65:24:52.9	>27.1	23.55	21.78	20.96
12956	17:56:16.56	65:25:41.9	>27.1	23.79	22.87	21.47	12435	17:55:55.20	65:26:33.3	>27.1	22.44	21.36	20.48
12240	17:56:50.16	65:27:05.0	>27.1	23.71	22.70	21.23	12221	17:56:33.36	65:27:03.2	>27.1	22.20	21.04	20.11
11850	17:56:15.12	65:27:56.5	>27.1	22.93	21.63	20.52	14037	17:56:13.20	65:28:44.8	>27.1	22.70	21.20	20.19
13662	17:57:48.72	65:29:17.9	>27.1	22.98	21.43	20.01							

Table B.2. *sBzK* galaxies in the field of 7C 1756+6520

ID	R.A. hms	Dec. dms	*B* (AB)	*z* (AB)	*J* (AB)	*Ks* (AB)	ID	R.A. hms	Dec. dms	*B* (AB)	*z* (AB)	*J* (AB)	*Ks* (AB)
3977	17:56:57.84	65:14:14.6	23.18	22.50	21.31	20.36	4989	17:57:08.16	65:15:46.8	24.44	23.61	22.80	21.55
5115	17:56:51.12	65:15:58.7	25.63	23.82	22.45	21.35	5761	17:56:53.76	65:17:04.2	24.76	24.02	22.23	21.02
6259	17:56:59.04	65:17:54.6	23.22	22.41	21.42	20.26	6933	17:57:00.00	65:18:57.6	24.42	23.59	22.90	21.19
7021	17:57:29.04	65:19:08.4	26.55	23.74	22.13	21.02	7311	17:57:21.12	65:19:36.5	26.24	23.45	22.66	21.24
7506	17:56:43.44	65:19:52.7	24.20	23.29	60.86	20.93	7687	17:57:03.60	65:20:15.7	24.53	22.98	21.61	20.51
8185	17:55:51.13	65:20:58.9	26.08	23.36	22.58	21.40	8285	17:55:34.32	65:21:09.4	23.45	23.00	22.20	21.04
8475	17:56:28.08	65:21:24.5	23.51	24.35	22.10	21.20	8379	17:57:30.72	65:21:21.3	24.05	21.80	20.86	19.44
8490	17:55:52.56	65:21:25.2	25.13	23.63	22.44	21.43	8761	17:56:56.88	65:21:53.6	23.35	22.83	21.61	20.37

Table B.2. continued.

ID	R.A. hms	Dec. dms	*B* (AB)	*z* (AB)	*J* (AB)	*Ks* (AB)	ID	R.A. hms	Dec. dms	*B* (AB)	*z* (AB)	*J* (AB)	*Ks* (AB)
9053	17:56:21.84	65:22:16.0	24.90	23.50	21.28	20.62	10357	17:58:05.52	65:24:06.5	25.95	23.94	23.18	21.90
10497	17:57:34.80	65:24:19.5	25.69	23.53	21.97	21.06	14663	17:57:12.72	65:27:06.5	25.96	23.67	22.58	20.64
14471	17:56:10.32	65:27:39.2	24.70	22.64	21.50	20.53	11935	17:57:01.20	65:27:44.6	25.36	23.23	23.24	21.47
14376	17:57:28.32	65:27:58.3	26.31	24.26	22.19	21.27	1301	17:57:25.92	65:09:43.6	22.85	22.60	21.29	21.50
1467	17:57:47.04	65:09:58.3	25.18	23.26	22.21	22.01	1535	17:57:35.04	65:10:09.1	22.76	21.54	20.64	20.18
1661	17:58:03.84	65:10:16.7	24.56	24.14	60.86	22.26	1668	17:57:49.68	65:10:18.1	24.71	23.93	23.65	21.94
1809	17:58:04.79	65:10:32.5	23.50	23.69	23.14	22.96	1810	17:57:50.16	65:10:34.7	24.46	23.39	23.37	22.13
1883	17:57:59.28	65:10:40.4	24.46	23.73	22.67	22.85	1880	17:57:28.80	65:10:44.0	24.54	23.27	22.39	21.86
2013	17:57:27.84	65:10:55.6	25.62	23.85	23.64	22.87	2137	17:56:52.56	65:11:09.9	24.09	23.96	22.66	22.61
2476	17:58:11.52	65:11:42.7	26.61	24.20	22.55	22.06	2837	17:58:12.73	65:12:16.6	23.61	23.07	22.12	22.66
2998	17:56:56.40	65:12:32.8	24.19	23.79	23.00	22.88	3042	17:57:03.12	65:12:43.2	23.91	22.79	22.15	21.34
3098	17:57:04.32	65:12:46.8	24.13	23.09	22.06	21.16	3511	17:57:40.32	65:13:27.5	26.16	24.38	23.58	22.03
3471	17:57:41.76	65:13:23.9	24.05	23.46	22.81	22.56	3586	17:58:05.76	65:13:33.6	24.34	23.42	23.26	22.40
3534	17:58:01.68	65:13:31.1	23.73	22.84	22.55	21.82	3796	17:58:03.61	65:13:54.5	25.22	23.86	22.20	21.75
3718	17:58:01.20	65:13:48.7	22.65	21.75	21.92	21.76	4131	17:57:35.52	65:14:24.3	25.78	24.01	22.75	22.17
4119	17:57:30.96	65:14:25.1	22.67	21.66	21.62	21.11	4367	17:57:29.28	65:14:48.1	25.04	22.98	21.95	21.47
4449	17:57:47.28	65:14:51.7	24.93	23.89	23.96	23.02	4858	17:57:48.72	65:15:31.0	24.18	22.85	22.72	22.14
5102	17:57:57.60	65:15:55.1	23.59	22.84	22.58	22.21	5169	17:56:57.60	65:16:02.6	23.65	23.47	22.50	22.39
5235	17:58:11.04	65:16:11.3	23.72	22.46	21.88	21.33	5265	17:56:46.32	65:16:14.5	24.17	23.10	21.92	21.31
5254	17:56:32.88	65:16:16.7	20.14	19.70	19.71	19.04	5573	17:57:46.80	65:16:43.0	24.70	23.54	22.81	21.89
5466	17:56:27.12	65:16:32.5	22.46	22.40	22.99	22.40	5542	17:56:15.60	65:16:40.8	22.17	23.32	22.71	21.78
5633	17:56:30.00	65:16:50.9	23.95	23.36	22.57	22.49	5658	17:58:15.11	65:16:53.0	25.24	24.15	23.28	22.33
5699	17:57:44.16	65:16:56.3	25.89	24.20	23.19	22.71	5674	17:56:52.56	65:16:56.6	23.21	22.14	21.41	20.89
5759	17:56:55.20	65:17:01.3	23.20	23.87	22.81	22.96	5717	17:56:03.12	65:16:58.1	23.59	23.37	22.56	21.93
5728	17:56:51.60	65:17:05.3	23.45	22.11	21.35	20.25	5898	17:56:55.20	65:17:13.9	23.49	23.88	22.87	23.16
5860	17:57:35.28	65:17:13.6	22.96	22.35	21.98	21.31	5934	17:57:42.00	65:17:18.6	25.37	23.61	22.44	21.83
5920	17:57:50.88	65:17:17.2	24.66	22.50	22.42	21.69	5955	17:56:19.68	65:17:21.5	23.88	22.99	22.36	21.58
6117	17:56:22.08	65:17:37.7	23.98	23.86	23.19	22.38	6028	17:56:28.08	65:17:29.8	22.87	23.04	22.19	21.04
6247	17:56:44.64	65:17:50.3	24.16	23.54	23.30	21.65	6337	17:55:46.80	65:17:57.8	24.64	23.11	22.21	21.42
6330	17:57:36.96	65:17:57.8	23.82	23.23	22.88	21.94	6355	17:57:59.51	65:18:00.0	24.36	23.34	22.44	21.54
6379	17:56:23.76	65:18:00.7	23.96	24.13	23.26	23.09	6408	17:55:47.28	65:18:05.8	24.56	23.34	22.39	21.80
6434	17:56:16.08	65:18:10.8	24.57	23.08	22.95	21.60	6537	17:55:46.80	65:18:15.8	24.14	23.71	23.23	22.29
6562	17:55:59.76	65:18:18.0	23.36	22.90	22.77	22.43	6886	17:57:37.69	65:18:53.3	25.82	23.25	22.23	21.70
6858	17:56:58.08	65:18:50.1	23.06	23.11	22.16	21.02	6997	17:57:24.47	65:19:03.0	25.21	24.21	23.09	22.56
7100	17:57:57.37	65:19:12.0	26.34	24.48	60.86	22.07	7078	17:57:28.08	65:19:12.4	23.98	22.74	22.19	21.65
7159	17:57:28.56	65:19:17.1	24.70	23.05	22.95	22.44	7150	17:58:36.48	65:19:14.2	24.01	23.03	22.16	22.14
7208	17:57:18.48	65:19:25.0	24.93	23.46	22.17	21.60	7231	17:56:42.48	65:19:27.8	24.47	23.60	22.56	21.34
6910	17:56:01.68	65:18:54.7	20.19	22.48	21.60	21.04	7290	17:56:51.36	65:19:32.9	23.95	23.51	23.35	22.37
7277	17:56:32.40	65:19:28.6	23.02	23.94	60.86	22.82	7432	17:57:15.84	65:19:45.1	25.45	24.15	23.20	22.02
7437	17:56:50.64	65:19:44.1	24.23	24.04	60.86	22.68	7524	17:57:06.48	65:19:53.0	24.60	23.10	60.86	22.19
7612	17:56:14.16	65:20:02.4	23.71	23.02	22.62	21.85	7589	17:56:04.80	65:20:00.6	23.79	22.51	22.97	21.96
7556	17:57:46.56	65:19:59.5	20.97	20.77	20.72	20.35	7678	17:56:08.40	65:20:08.2	24.69	23.76	23.42	21.89
7629	17:58:28.56	65:20:03.8	22.03	21.43	21.01	20.71	7624	17:56:33.12	65:20:04.2	22.51	22.39	21.82	21.30
7813	17:55:30.00	65:20:20.0	24.55	23.34	22.50	21.61	7921	17:56:39.84	65:20:30.1	22.73	23.67	60.86	22.79
7895	17:57:05.04	65:20:31.6	22.70	21.75	60.86	20.94	8162	17:58:03.84	65:20:53.2	26.25	24.31	23.14	22.08
8078	17:56:46.56	65:20:48.5	22.65	22.75	21.92	21.36	8332	17:58:12.48	65:21:10.4	24.85	23.53	22.33	22.00
8410	17:57:25.20	65:21:16.9	25.37	23.75	22.89	21.90	8393	17:55:45.12	65:21:15.1	24.19	23.72	22.41	22.02
8443	17:58:35.28	65:21:16.9	24.49	23.22	23.16	22.26	8465	17:56:28.80	65:21:23.4	22.48	23.68	22.66	21.96
8435	17:56:56.40	65:21:20.5	23.08	22.65	23.25	21.84	8474	17:57:02.40	65:21:22.7	23.69	23.66	23.14	22.52
8366	17:56:39.60	65:21:18.0	22.17	22.33	22.96	21.55	8631	17:56:31.45	65:21:41.4	23.90	23.06	23.49	21.36
8666	17:58:26.64	65:21:37.8	24.74	24.32	23.43	23.09	8668	17:57:52.56	65:21:42.1	23.55	22.57	22.35	21.77
8775	17:57:31.44	65:21:51.1	25.41	23.74	22.58	22.10	8799	17:57:11.52	65:21:53.6	23.59	22.26	22.25	21.14
8902	17:57:15.84	65:22:04.1	24.28	22.93	22.85	21.88	8953	17:58:01.20	65:22:04.8	24.42	23.55	22.61	22.44
8911	17:57:08.87	65:22:05.5	24.92	23.48	21.89	21.24	8958	17:56:24.72	65:22:05.9	22.93	23.53	22.44	22.60
9077	17:55:56.88	65:22:13.8	24.04	23.41	21.89	22.32	9140	17:55:56.17	65:22:17.8	24.07	24.29	22.53	22.56
9006	17:56:28.80	65:22:10.2	22.95	22.84	22.59	22.27	9164	17:55:59.04	65:22:22.4	23.60	23.15	22.78	21.26
9371	17:57:33.84	65:22:41.2	25.74	24.30	22.83	22.18	9330	17:57:32.64	65:22:36.8	24.25	23.67	22.60	22.61
9345	17:56:47.05	65:22:40.8	23.82	22.73	21.92	21.02	9430	17:55:53.51	65:22:47.3	23.44	22.79	22.25	21.73
9510	17:56:05.04	65:22:51.6	24.33	23.58	22.75	22.60	9464	17:57:32.88	65:22:51.6	24.68	22.91	22.36	21.58
9550	17:58:01.68	65:22:55.9	24.57	22.78	22.32	21.85	9635	17:57:42.96	65:23:02.4	24.68	23.84	60.86	22.46
9622	17:57:21.84	65:23:05.3	24.00	22.78	21.04	20.38	9844	17:57:16.32	65:23:20.0	26.00	24.18	60.86	21.99
9788	17:55:49.44	65:23:15.4	23.93	22.98	20.85	22.18	9872	17:56:06.00	65:23:20.4	25.13	23.72	22.23	22.38
9820	17:58:16.80	65:23:18.2	24.13	22.66	22.08	21.39	9879	17:57:04.08	65:23:22.9	25.45	23.67	60.86	21.82
9924	17:57:14.40	65:23:26.9	24.82	23.41	22.13	21.36	10026	17:58:07.20	65:23:36.2	24.40	23.09	22.58	21.90
10279	17:57:22.32	65:23:57.1	24.55	23.94	23.24	22.26	10298	17:57:15.84	65:24:01.4	25.00	23.38	22.73	21.41
10344	17:56:31.45	65:24:05.0	25.55	23.46	23.48	21.91	10463	17:56:57.12	65:24:14.4	24.74	23.82	60.86	23.02
10572	17:56:36.73	65:24:25.2	24.12	23.38	22.46	22.28	10672	17:57:49.92	65:24:32.4	25.00	23.93	23.78	22.70
10656	17:58:11.28	65:24:32.4	23.94	22.84	22.14	21.58	10714	17:56:27.12	65:24:39.6	25.77	23.66	22.38	21.62
10753	17:55:29.28	65:24:40.0	24.13	22.77	22.03	21.64	10752	17:55:48.96	65:24:41.8	25.54	23.66	20.93	20.39
10808	17:57:59.28	65:24:44.3	25.48	24.39	22.91	22.94	10853	17:55:40.56	65:24:47.2	25.04	24.34	22.80	22.58
10852	17:56:24.96	65:24:48.9	25.25	23.71	23.20	22.90	10795	17:57:28.56	65:24:46.5	24.60	23.32	22.27	22.03
10933	17:56:34.32	65:24:59.8	23.69	22.32	21.86	21.72	10968	17:55:29.76	65:24:59.8	23.94	23.49	22.91	22.39
10876	17:57:14.64	65:24:55.1	23.57	22.63	21.77	21.56	11080	17:57:34.08	65:25:11.3	25.08	23.82	22.74	22.51
11094	17:55:42.24	65:25:13.1	24.41	22.38	22.25	21.60	11112	17:58:21.84	65:25:12.0	24.80	23.17	22.81	22.19
11159	17:56:41.04	65:25:20.6	25.92	24.08	22.85	22.01	11168	17:56:58.08	65:25:19.5	25.46	23.93	22.85	22.37
11175	17:55:51.84	65:25:18.8	25.27	23.42	22.94	22.46	11154	17:58:18.01	65:25:18.8	24.77	23.42	22.29	21.86
11226	17:57:19.44	65:25:24.6	24.45	23.83	23.85	23.19	11243	17:58:01.44	65:25:26.4	24.47	24.03	23.24	22.33
13654	17:58:25.92	65:25:27.1	24.67	23.56	23.06	22.10	13015	17:58:24.72	65:25:30.7	24.75	23.67	22.53	22.18
11725	17:56:30.24	65:25:31.4	22.35	21.78	21.30	21.00	12921	17:56:38.87	65:25:36.1	23.99	22.88	22.49	21.20
12992	17:57:44.64	65:25:42.6	25.09	23.73	22.92	22.38	12902	17:55:55.68	65:25:42.9	24.73	23.62	23.06	22.05
12114	17:57:53.28	65:25:47.6	24.96	23.95	23.34	22.42	12753	17:57:14.88	65:25:52.0	24.50	23.65	23.23	22.84
12772	17:57:38.64	65:25:50.9	24.12	23.04	22.32	22.27	12770	17:55:29.52	65:26:02.4	24.19	22.96	22.48	21.83
12786	17:55:30.00	65:25:59.2	20.95	20.80	20.97	20.36	12626	17:57:42.00	65:26:06.3	25.67	23.94	60.86	22.53
12685	17:57:29.51	65:26:09.2	23.52	22.57	22.24	21.34	12562	17:56:32.64	65:26:14.6	24.71	24.00	23.07	22.82
12583	17:58:26.40	65:26:05.3	23.45	23.03	22.65	22.39	12359	17:55:45.36	65:26:33.7	24.35	23.75	23.17	23.16
12407	17:56:56.64	65:26:36.2	25.02	24.33	23.51	22.99	14648	17:57:12.00	65:26:48.1	24.28	22.61	21.92	20.54
12276	17:57:14.15	65:26:49.9	24.42	23.68	22.23	22.10	14665	17:56:14.88	65:26:50.7	24.90	23.99	22.85	22.41

Table B.2. continued.

ID	R.A. hms	Dec. dms	*B* (AB)	*z* (AB)	*J* (AB)	*Ks* (AB)	ID	R.A. hms	Dec. dms	*B* (AB)	*z* (AB)	*J* (AB)	*Ks* (AB)
14769	17:56:28.08	65:26:51.4	24.84	23.20	23.39	21.92	14661	17:55:51.60	65:27:11.5	25.13	23.20	23.05	21.92
14725	17:58:02.88	65:27:07.9	23.70	23.62	23.10	22.51	12119	17:57:45.12	65:27:13.0	24.12	22.73	22.85	22.03
12106	17:57:06.00	65:27:19.4	24.63	23.34	22.48	21.91	14660	17:55:35.76	65:27:28.4	24.11	23.08	22.83	21.88
14512	17:57:38.64	65:27:38.2	25.82	23.40	23.16	22.81	14466	17:57:54.72	65:27:37.1	24.96	23.57	23.36	22.66
14315	17:58:05.76	65:27:53.3	25.17	24.29	23.32	22.78	11942	17:58:02.16	65:27:47.5	23.69	24.33	60.86	23.10
14162	17:57:16.80	65:27:55.8	25.71	24.25	23.41	22.93	13074	17:57:21.36	65:27:59.0	25.13	23.59	22.91	21.81
14445	17:58:03.84	65:27:57.6	23.51	22.61	21.39	20.83	11933	17:58:04.08	65:27:59.8	23.16	23.22	60.86	21.35
14291	17:58:25.44	65:28:09.5	24.51	23.08	22.16	21.09	11541	17:57:32.64	65:28:05.2	24.31	22.80	22.55	22.28
13674	17:58:10.32	65:29:27.9	25.13	23.66	22.66	22.53	13680	17:57:51.60	65:29:25.8	25.19	23.08	22.75	21.47
13765	17:57:56.40	65:29:16.8	24.41	24.11	22.95	22.84	13852	17:58:10.80	65:29:04.2	23.24	21.48	20.67	20.07
13541	17:57:59.28	65:29:38.8	22.54	23.51	22.51	22.45	11776	17:57:03.60	65:29:18.3	23.58	22.68	22.37	22.11
13436	17:56:12.48	65:28:43.0	25.06	22.99	22.02	22.03	14116	17:58:00.72	65:28:29.3	24.21	23.43	22.92	21.35
13484	17:56:32.88	65:28:46.2	25.33	23.89	23.10	22.65	14141	17:57:54.24	65:28:40.1	23.52	23.85	22.99	22.29
14177	17:57:07.92	65:28:21.4	25.17	23.65	22.18	21.72	13588	17:58:00.24	65:29:18.3	22.76	23.38	22.93	22.74

Table B.3. *pBzK** galaxies in the field of 7C 1751+6809

ID	R.A. hms	Dec. dms	*B* (AB)	*z* (AB)	*J* (AB)	*Ks* (AB)	ID	R.A. hms	Dec. dms	*B* (AB)	*z* (AB)	*J* (AB)	*Ks* (AB)
2172	17:51:44.88	67:59:43.1	25.24	23.73	22.58	21.05	4886	17:51:07.92	68:04:10.9	25.82	22.36	21.12	20.16
9428	17:49:31.44	68:11:44.5	24.74	22.67	21.59	20.47	9414	17:51:31.68	68:11:42.7	25.17	24.10	22.51	21.30
10769	17:49:57.37	68:13:54.5	24.40	21.77	20.98	19.81	12257	17:50:52.08	68:15:00.7	25.35	22.37	60.86	20.07
11739	17:50:05.76	68:16:30.4	24.22	22.96	21.71	20.70	13618	17:51:49.92	68:17:51.4	24.54	23.33	21.86	20.53
1462	17:50:09.12	67:58:32.2	>27.1	23.93	22.96	21.10	1563	17:51:38.65	67:58:41.2	>27.1	24.51	22.31	21.43
2013	17:49:57.12	67:59:24.3	>27.1	23.94	22.39	21.33	3050	17:51:50.64	68:01:09.8	>27.1	22.62	21.36	20.57
3183	17:50:32.16	68:01:21.4	>27.1	24.21	22.35	21.29	3261	17:51:06.48	68:01:28.9	>27.1	22.77	21.67	20.85
4119	17:51:24.96	68:02:54.2	>27.1	22.22	21.31	20.07	4582	17:51:43.20	68:03:38.5	>27.1	22.85	21.61	20.90
4879	17:49:00.00	68:04:08.4	>27.1	22.24	21.48	20.51	4943	17:51:19.44	68:04:14.9	>27.1	24.07	21.75	21.59
5084	17:52:10.56	68:04:24.6	>27.1	24.07	21.95	21.88	5184	17:49:42.48	68:04:32.5	>27.1	24.74	22.41	21.83
5215	17:52:21.36	68:04:39.0	>27.1	23.67	22.08	20.80	5478	17:50:19.44	68:05:04.9	>27.1	24.23	22.71	21.37
5541	17:48:53.52	68:05:08.5	>27.1	23.30	22.03	21.28	5543	17:49:42.00	68:05:11.1	>27.1	22.93	21.42	20.66
5720	17:49:38.16	68:05:25.4	>27.1	23.86	21.96	21.18	6112	17:50:35.52	68:06:08.6	>27.1	23.52	22.14	21.17
6309	17:51:19.44	68:06:30.6	>27.1	23.66	22.15	21.00	6616	17:51:52.80	68:07:06.6	>27.1	21.75	20.94	19.63
6636	17:51:04.56	68:07:06.6	>27.1	23.25	21.73	20.76	6788	17:49:10.56	68:07:18.1	>27.1	23.16	21.99	20.91
7092	17:52:22.56	68:07:51.6	>27.1	24.63	22.13	20.98	7159	17:49:01.68	68:07:58.1	>27.1	24.03	22.04	21.35
7356	17:50:49.92	68:08:26.2	>27.1	22.40	21.11	20.04	7381	17:51:13.93	68:08:27.6	>27.1	22.67	20.83	20.18
7358	17:48:52.32	68:08:26.2	>27.1	24.12	22.16	21.11	7379	17:51:13.44	68:08:29.8	>27.1	23.53	21.78	20.94
7449	17:51:24.96	68:08:33.7	>27.1	22.69	21.51	20.70	7800	17:49:14.64	68:09:10.1	>27.1	22.80	21.14	20.29
7850	17:49:08.40	68:09:12.6	>27.1	22.95	21.62	20.38	8248	17:48:50.64	68:09:53.3	>27.1	23.23	21.20	20.59
8966	17:49:46.80	68:11:01.7	>27.1	23.56	21.75	21.12	9164	17:50:17.52	68:11:20.1	>27.1	23.80	21.95	21.20
9193	17:48:48.23	68:11:30.8	>27.1	20.56	19.37	18.57	9488	17:48:53.52	68:11:47.1	>27.1	23.43	21.59	20.93
9493	17:49:08.87	68:11:48.5	>27.1	22.81	21.63	20.77	9661	17:51:53.76	68:12:02.5	>27.1	23.88	60.86	21.69
9815	17:49:8.16	68:12:18.4	>27.1	22.87	21.24	20.56	9893	17:49:6.24	68:12:28.1	>27.1	22.25	20.96	20.14
10024	17:49:7.92	68:12:38.9	>27.1	23.82	21.41	20.92	10562	17:50:18.72	68:13:32.2	>27.1	23.49	22.18	21.03
10630	17:51:42.24	68:13:40.1	>27.1	23.91	21.51	20.99	12746	17:49:40.32	68:14:17.2	>27.1	23.94	22.02	21.41
12372	17:50:53.52	68:14:39.5	>27.1	21.91	20.97	20.17	12485	17:49:59.04	68:14:35.2	>27.1	22.70	21.21	20.49
12327	17:49:07.92	68:14:43.8	>27.1	24.21	22.36	21.04	14599	17:52:06.72	68:15:00.4	>27.1	23.30	21.11	20.91
12245	17:51:12.00	68:15:07.6	>27.1	22.94	20.98	20.43	14525	17:52:10.32	68:15:21.2	>27.1	21.95	20.51	19.74
14335	17:49:55.68	68:16:18.5	>27.1	23.12	21.69	20.88	12398	17:50:04.80	68:16:25.7	>27.1	22.90	21.45	20.63
14057	17:49:57.37	68:16:37.9	>27.1	22.92	21.47	20.60	14098	17:50:43.20	68:16:52.3	>27.1	21.61	20.86	19.92
14053	17:50:57.84	68:16:50.5	>27.1	24.32	22.01	21.12	13468	17:51:59.76	68:18:07.6	>27.1	22.84	21.36	20.59
1754	17:49:59.76	67:58:59.5	>27.1	24.38	22.23	21.42	3331	17:50:49.92	68:01:34.3	>27.1	22.91	21.27	20.39
3394	17:51:24.72	68:01:41.9	>27.1	23.38	21.41	20.17	4196	17:51:19.44	68:03:00.0	>27.1	23.79	21.87	20.74
4456	17:51:30.48	68:03:27.4	>27.1	23.35	21.46	20.57	4569	17:51:40.32	68:03:37.1	>27.1	23.81	22.06	20.96
5298	17:49:20.64	68:04:45.8	>27.1	23.38	21.49	20.50	5542	17:50:47.52	68:05:13.9	>27.1	23.70	22.34	20.82
5985	17:52:06.96	68:06:02.9	>27.1	18.65	60.86	16.64	6151	17:52:10.08	68:06:22.0	>27.1	18.43	60.86	16.13
6606	17:48:54.00	68:07:07.3	>27.1	19.29	60.86	16.74	6659	17:50:38.40	68:07:05.9	>27.1	24.09	21.95	21.26
6680	17:49:56.88	68:07:07.7	>27.1	24.29	22.79	21.27	6747	17:52:05.75	68:07:12.4	>27.1	24.28	22.03	20.88
6782	17:49:41.04	68:07:18.1	>27.1	23.47	21.69	20.97	6871	17:50:23.28	68:07:29.3	>27.1	23.53	21.94	20.76
7106	17:49:43.92	68:07:54.1	>27.1	23.74	21.90	21.21	7280	17:51:15.60	68:08:19.0	>27.1	24.08	22.32	21.41
7355	17:50:48.96	68:08:24.7	>27.1	23.21	20.80	20.48	7582	17:51:40.56	68:08:47.0	>27.1	23.41	21.79	20.77
7677	17:49:06.49	68:08:57.1	>27.1	23.07	21.03	20.19	7703	17:51:29.51	68:09:00.7	>27.1	23.48	22.13	20.65
7805	17:50:32.64	68:09:07.9	>27.1	24.08	21.79	20.92	8355	17:49:22.09	68:10:08.0	>27.1	23.01	21.30	20.35
8444	17:51:35.04	68:10:12.4	>27.1	23.73	21.89	21.38	9076	17:49:16.80	68:11:15.0	>27.1	22.42	21.14	20.13
9707	17:52:28.56	68:12:09.7	>27.1	24.15	21.54	20.70	10183	17:51:29.04	68:12:57.6	>27.1	23.37	21.09	20.84
10312	17:49:36.48	68:13:08.8	>27.1	23.81	21.36	20.94	10405	17:48:56.16	68:13:18.8	>27.1	22.75	21.14	19.94
10701	17:48:58.08	68:13:43.7	>27.1	23.67	22.19	20.83	10717	17:51:21.36	68:13:49.1	>27.1	23.07	21.53	20.64
12825	17:50:05.52	68:14:05.6	>27.1	22.95	21.00	20.57	12741	17:49:06.96	68:14:19.3	>27.1	23.11	21.22	20.36
12780	17:50:05.04	68:14:22.6	>27.1	23.35	60.86	20.56	12090	17:49:13.92	68:14:31.6	>27.1	22.52	60.86	19.85
11443	17:51:16.08	68:14:49.2	>27.1	23.81	22.27	20.93	12214	17:49:55.92	68:15:12.2	>27.1	23.70	21.68	20.88
12175	17:51:12.48	68:15:11.5	>27.1	23.55	21.50	20.79	11413	17:51:24.00	68:15:33.8	>27.1	23.80	21.69	21.21
11784	17:49:24.72	68:15:47.2	>27.1	23.93	22.54	21.30	13618	17:51:49.92	68:17:51.4	>27.1	23.53	60.86	20.53

Table B.4. *sBzK* galaxies in the field of 7C 1751+6809

ID	R.A. hms	Dec. dms	*B* (AB)	*z* (AB)	*J* (AB)	*Ks* (AB)	ID	R.A. hms	Dec. dms	*B* (AB)	*z* (AB)	*J* (AB)	*Ks* (AB)
1210	17:50:48.48	67:58:04.1	25.15	22.95	21.33	20.34	1538	17:51:48.48	67:58:50.9	22.66	24.00	22.16	21.05
1790	17:50:12.48	67:59:04.9	24.66	23.56	21.81	20.90	2225	17:51:48.96	67:59:46.0	23.08	24.08	22.92	21.56
2551	17:52:04.80	68:00:19.1	23.00	23.93	21.04	20.53	3018	17:50:00.48	68:01:07.0	24.13	23.51	21.59	20.78

Table B.4. continued.

ID	R.A.	Dec.	*B*	*z*	*J*	*Ks*	ID	R.A.	Dec.	*B*	*z*	*J*	*Ks*
	hms	dms	(AB)	(AB)	(AB)	(AB)		hms	dms	(AB)	(AB)	(AB)	(AB)
3180	17:50:01.44	68:01:19.2	24.07	24.56	22.73	22.16	3519	17:51:04.08	68:01:52.0	22.39	23.39	21.25	20.90
4238	17:52:04.80	68:03:10.1	20.06	19.73	16.89	16.99	5502	17:50:05.76	68:05:07.8	24.03	23.70	22.06	21.03
5639	17:51:32.16	68:05:22.2	23.96	23.11	22.51	20.49	6274	17:49:12.95	68:06:23.4	22.39	23.66	22.44	21.16
6672	17:50:54.96	68:07:06.6	23.82	23.84	60.86	21.07	6613	17:51:42.96	68:07:03.0	22.81	22.58	21.01	19.97
6275	17:50:24.96	68:06:32.0	18.11	19.57	16.51	17.06	6628	17:51:12.00	68:07:07.3	23.13	22.96	21.10	20.46
6969	17:50:13.20	68:07:43.3	23.14	23.78	21.66	20.49	7162	17:48:48.23	68:07:59.2	22.65	23.32	20.96	20.29
7243	17:51:02.64	68:08:06.7	23.21	24.63	60.86	23.25	7302	17:49:17.28	68:08:22.6	23.92	23.95	20.97	20.37
7759	17:48:48.96	68:09:08.3	23.84	23.32	21.95	20.47	8074	17:51:26.40	68:09:35.3	25.14	23.38	21.93	21.04
8133	17:49:19.44	68:09:42.1	23.52	22.77	20.78	20.21	8238	17:50:34.56	68:09:55.8	24.09	24.19	20.89	20.58
9473	17:50:40.32	68:11:48.1	25.03	23.62	21.97	20.98	9420	17:51:27.60	68:11:49.9	24.74	23.55	20.53	19.99
10812	17:50:17.04	68:13:55.6	25.38	24.69	22.02	21.56	10853	17:49:02.40	68:13:54.9	24.65	24.65	23.82	22.24
10889	17:52:05.75	68:14:00.6	22.93	23.35	60.86	20.82	12744	17:51:16.32	68:14:24.0	23.87	24.16	22.16	21.17
12090	17:49:13.92	68:14:31.6	23.78	22.85	21.16	19.85	12461	17:50:19.19	68:14:50.3	24.29	23.81	21.73	20.72
14603	17:50:25.68	68:15:28.8	24.05	23.13	21.40	20.62	14576	17:50:52.56	68:15:48.2	25.46	24.25	22.97	21.78
11791	17:49:08.87	68:15:43.6	23.67	24.38	21.73	21.15	11974	17:49:29.52	68:15:45.4	25.73	23.79	21.98	21.30
14621	17:52:12.24	68:15:46.8	22.50	23.57	21.10	20.77	14038	17:50:05.28	68:17:22.5	23.59	22.97	21.00	20.41
1762	17:51:53.28	67:58:59.9	23.19	23.77	21.88	22.56	2020	17:49:56.64	67:59:24.3	23.99	24.02	22.11	21.74
2340	17:51:31.44	67:59:57.1	24.20	23.55	22.49	22.09	2377	17:50:15.12	67:59:58.9	23.44	24.17	23.47	22.90
2513	17:50:29.51	68:00:18.0	22.55	22.81	21.30	20.76	2644	17:51:44.40	68:00:28.4	23.58	24.11	23.42	22.72
3047	17:51:53.28	68:01:07.0	24.72	24.05	22.63	22.27	3120	17:51:44.64	68:01:16.3	23.94	23.30	21.99	21.77
3329	17:50:38.64	68:01:32.5	24.57	24.39	22.81	22.00	3228	17:51:20.16	68:01:27.5	22.06	21.38	20.88	20.06
3370	17:50:31.44	68:01:37.6	23.08	23.69	22.19	21.65	3660	17:51:23.05	68:02:05.3	24.02	23.52	22.46	21.87
3823	17:52:00.71	68:02:19.7	22.95	23.87	23.35	23.13	3686	17:51:53.28	68:02:12.9	18.91	18.04	16.91	17.28
3909	17:51:28.80	68:02:30.1	21.11	23.37	21.78	21.70	4072	17:50:27.12	68:02:45.6	23.52	24.25	23.30	22.31
4101	17:51:32.16	68:02:47.4	24.90	23.89	22.66	22.75	4248	17:50:16.32	68:03:00.7	23.49	24.09	60.86	22.94
3856	17:50:09.84	68:02:37.7	18.39	18.26	16.49	17.04	4527	17:50:17.52	68:03:30.3	23.41	23.98	22.55	22.16
4918	17:49:42.00	68:04:08.4	25.55	23.97	22.65	23.14	4889	17:50:05.04	68:04:09.8	24.45	23.47	22.34	21.75
5050	17:49:52.32	68:04:22.4	22.86	23.01	22.39	21.65	5097	17:51:33.36	68:04:27.1	23.86	23.26	21.66	21.40
5208	17:50:01.44	68:04:36.8	22.75	23.66	23.16	22.31	5223	17:51:37.68	68:04:37.2	23.86	23.17	21.74	21.09
5291	17:50:45.60	68:04:43.3	25.19	24.87	60.86	22.43	5231	17:51:03.12	68:04:39.0	23.88	23.35	21.85	21.41
5371	17:49:54.72	68:04:50.9	23.88	23.88	22.49	22.10	5396	17:49:48.24	68:04:52.7	23.66	24.27	22.78	22.56
5421	17:52:27.36	68:04:54.1	25.25	23.61	21.94	21.49	5459	17:49:53.04	68:05:00.2	23.63	23.89	23.05	22.10
5611	17:51:48.72	68:05:14.6	23.18	24.24	22.59	22.77	5665	17:52:10.08	68:05:18.6	23.70	24.20	22.45	22.81
5640	17:50:40.07	68:05:18.6	23.46	23.83	21.92	22.05	5793	17:50:15.12	68:05:32.3	23.65	23.60	23.29	22.63
5810	17:49:17.76	68:05:33.0	23.64	23.37	22.54	22.04	5812	17:49:16.32	68:05:34.1	23.45	24.24	22.62	22.16
5911	17:49:48.24	68:05:43.1	23.30	23.35	22.80	23.05	5946	17:49:45.12	68:05:47.8	23.46	23.57	23.15	22.64
5849	17:49:03.36	68:05:36.6	22.59	23.10	22.56	22.47	5951	17:48:49.20	68:05:49.9	22.95	22.51	21.76	20.64
5977	17:51:34.56	68:05:55.0	25.52	23.37	22.15	21.61	5935	17:49:46.08	68:05:49.9	22.65	22.89	21.62	21.14
5981	17:50:52.32	68:05:55.0	23.61	22.94	22.53	21.88	6080	17:50:02.41	68:06:03.2	24.37	24.44	22.04	22.55
6104	17:50:15.60	68:06:05.4	24.18	23.54	22.46	21.62	6087	17:51:26.40	68:06:02.5	24.04	23.42	22.57	22.81
6067	17:49:36.73	68:06:02.5	22.12	23.70	23.48	22.41	6225	17:50:10.56	68:06:16.9	23.94	23.93	21.39	22.16
6226	17:50:52.80	68:06:16.9	23.38	23.97	22.97	23.20	6355	17:51:18.48	68:06:30.6	24.70	24.35	22.86	22.34
6442	17:51:16.32	68:06:39.2	23.44	23.91	22.99	22.04	6513	17:49:40.32	68:06:46.4	23.87	24.27	22.92	22.61
6502	17:49:18.48	68:06:43.9	22.95	24.19	23.51	23.24	6586	17:49:12.24	68:06:54.7	24.90	23.78	22.50	21.91
6792	17:51:19.68	68:07:16.3	23.36	23.40	22.44	22.55	6865	17:49:35.28	68:07:24.9	23.85	24.51	60.86	22.20
6941	17:51:13.44	68:07:32.9	23.96	23.92	60.86	22.87	6981	17:49:45.84	68:07:38.3	24.09	23.54	22.59	21.67
7007	17:50:01.20	68:07:39.7	23.88	24.28	22.93	23.04	7040	17:51:18.48	68:07:46.6	23.42	23.78	22.36	21.94
7168	17:51:09.36	68:08:01.3	25.10	23.86	23.10	22.03	7232	17:50:01.92	68:08:06.4	23.31	23.75	22.60	22.13
7175	17:50:51.12	68:08:01.7	22.81	23.77	21.65	21.26	7276	17:51:49.68	68:08:10.7	24.89	24.00	22.87	22.81
7095	17:51:30.72	68:07:52.3	22.04	23.66	60.86	21.73	7307	17:51:35.04	68:08:16.8	23.97	23.67	22.40	21.86
7397	17:51:30.96	68:08:27.2	23.34	22.75	22.16	21.32	7473	17:50:56.40	68:08:31.2	22.98	23.54	23.47	23.23
7558	17:50:19.19	68:08:42.7	23.15	23.87	23.14	21.98	7586	17:51:47.04	68:08:43.8	24.73	23.47	22.56	22.31
7521	17:51:09.60	68:08:41.6	23.52	23.24	22.04	20.72	7612	17:49:20.88	68:08:49.6	23.58	23.00	21.36	20.92
7767	17:51:26.88	68:09:01.4	22.68	23.64	23.38	21.78	7834	17:49:18.96	68:09:08.3	23.71	23.33	22.34	22.14
7780	17:49:39.60	68:09:02.9	22.61	23.44	22.43	22.06	7797	17:51:00.96	68:09:06.5	23.62	23.29	22.42	21.62
7783	17:50:18.96	68:09:08.6	23.11	22.45	21.76	21.14	7880	17:50:50.40	68:09:13.7	22.94	23.16	22.50	22.25
7956	17:51:06.48	68:09:19.1	23.76	23.77	22.74	22.49	7981	17:52:28.32	68:09:19.8	24.14	24.26	22.73	22.95
7960	17:50:45.60	68:09:23.0	22.38	23.63	21.08	21.15	8012	17:48:56.16	68:09:28.1	23.10	22.98	21.70	20.84
8058	17:51:07.20	68:09:29.9	23.43	23.71	23.26	22.57	8081	17:50:16.56	68:09:33.8	24.06	24.69	60.86	22.86
8097	17:50:54.72	68:09:36.7	23.66	23.77	23.11	21.90	8038	17:50:58.33	68:09:30.6	21.96	23.15	22.30	21.34
8068	17:49:14.15	68:09:34.9	22.79	23.24	21.99	20.97	8043	17:49:11.04	68:09:28.4	22.40	22.60	21.82	20.86
8230	17:50:35.52	68:09:55.8	22.79	22.93	20.12	19.94	8310	17:51:15.84	68:09:58.3	23.76	24.00	22.99	22.51
8327	17:51:15.36	68:10:00.8	22.47	22.74	22.01	21.87	8583	17:51:00.72	68:10:24.2	23.03	23.26	22.27	21.44
8784	17:49:24.00	68:10:41.5	23.97	24.64	22.55	22.98	8715	17:49:16.08	68:10:33.3	22.21	24.00	22.94	22.86
8816	17:51:00.00	68:10:44.4	22.39	23.97	22.40	22.83	8897	17:50:14.64	68:10:54.1	23.70	23.83	23.27	22.26
8957	17:48:53.04	68:10:55.9	24.96	24.25	22.14	21.97	8885	17:51:12.00	68:10:53.0	23.17	23.53	21.98	21.57
8963	17:51:30.96	68:10:59.9	23.77	23.49	22.72	21.87	8981	17:50:11.76	68:11:03.5	23.51	23.57	22.96	21.75
8969	17:51:19.68	68:11:02.4	23.67	23.87	22.96	22.20	9029	17:50:34.56	68:11:04.6	23.36	24.16	22.34	22.12
9149	17:50:21.12	68:11:17.9	22.64	22.42	21.58	20.87	9227	17:51:05.52	68:11:24.0	24.08	24.03	22.65	21.85
9320	17:50:47.04	68:11:32.3	23.49	23.17	22.01	21.58	9419	17:50:54.72	68:11:42.0	23.54	23.64	23.34	22.52
9208	17:52:04.32	68:11:23.7	20.94	20.32	20.36	19.36	9410	17:52:09.36	68:11:41.6	23.50	24.47	22.79	21.70
9495	17:51:46.56	68:11:45.6	22.82	24.19	23.26	23.03	9605	17:50:35.04	68:11:56.7	23.45	23.29	22.82	22.39
9563	17:50:02.88	68:11:56.0	22.61	23.06	22.50	21.58	9627	17:49:33.84	68:12:03.2	23.75	23.25	22.18	21.25
9759	17:50:21.84	68:12:12.6	23.33	23.23	21.89	21.78	9743	17:50:10.32	68:12:15.5	22.46	21.15	20.40	19.48
9801	17:51:13.20	68:12:16.2	23.37	23.90	22.48	22.08	9941	17:51:10.32	68:12:29.9	22.62	24.57	22.81	22.48
9859	17:49:59.28	68:12:25.6	21.65	22.42	21.65	21.02	10076	17:48:59.04	68:12:51.5	21.22	19.97	19.44	18.93
10205	17:50:49.19	68:12:54.7	23.19	23.99	23.13	22.80	10215	17:49:45.60	68:12:56.9	23.01	24.42	22.35	22.92
10257	17:48:55.68	68:13:00.1	22.95	24.85	23.22	23.02	10307	17:49:30.00	68:13:04.8	23.68	24.06	23.44	23.04
10324	17:49:38.87	68:13:07.7	22.17	24.66	22.67	22.30	10254	17:51:45.60	68:13:02.3	23.07	22.63	21.76	21.32
10383	17:49:34.80	68:13:13.8	23.61	23.05	21.47	21.01	10355	17:50:48.48	68:13:16.0	23.59	22.72	21.89	21.07
10350	17:49:39.12	68:13:12.7	23.42	23.79	22.08	21.69	10356	17:51:35.04	68:13:10.9	21.62	23.79	20.90	21.78
10311	17:49:06.96	68:13:11.6	22.65	22.18	20.90	20.00	10447	17:52:21.60	68:13:17.4	23.28	24.35	23.14	22.80
10468	17:49:05.52	68:13:18.5	23.18	24.79	24.32	22.73	10696	17:49:03.36	68:13:41.5	22.74	22.85	22.18	21.49
10827	17:51:02.40	68:13:54.1	24.30	24.77	21.52	22.75	10856	17:50:58.80	68:13:55.9	23.90	24.79	23.18	23.19
11510	17:51:39.60	68:14:10.0	24.15	23.08	22.98	21.63	12610	17:49:43.44	68:14:15.7	23.85	23.75	22.51	22.09
11499	17:48:53.04	68:14:10.3	24.26	23.52	22.10	21.17	12742	17:49:53.76	68:14:20.0	23.30	24.09	24.16	22.87
12700	17:50:42.73	68:14:18.3	23.31	22.99	21.84	21.53	12594	17:49:50.40	68:14:21.8	22.78	23.84	22.98	22.87

Table B.4. continued.

ID	R.A. hms	Dec. dms	*B* (AB)	*z* (AB)	*J* (AB)	*Ks* (AB)	ID	R.A. hms	Dec. dms	*B* (AB)	*z* (AB)	*J* (AB)	*Ks* (AB)
12416	17:48:54.96	68:14:22.6	24.01	24.05	22.31	21.34	12674	17:50:20.16	68:14:32.6	23.33	23.66	23.25	22.67
12794	17:52:05.28	68:14:19.3	19.10	17.55	16.37	16.66	12652	17:49:18.96	68:14:23.6	22.56	23.50	22.19	22.93
12555	17:50:39.36	68:14:40.2	22.09	22.43	21.39	20.45	12098	17:50:41.52	68:15:01.1	23.33	23.73	21.92	21.84
12056	17:48:55.68	68:15:35.3	23.70	24.27	22.67	21.33	12004	17:49:08.40	68:15:37.4	22.98	23.53	23.20	21.66
11987	17:52:11.52	68:15:44.3	23.35	23.85	21.80	22.22	14642	17:50:05.04	68:15:51.8	24.08	24.44	22.72	21.64
14267	17:50:48.24	68:15:56.5	22.64	23.49	22.16	21.15	14475	17:51:36.24	68:16:12.0	24.23	23.76	22.77	22.44
14330	17:51:46.08	68:16:16.7	22.21	21.59	21.22	20.72	14340	17:51:11.28	68:16:12.0	22.15	23.52	22.73	21.85
14154	17:51:06.72	68:16:44.4	23.13	22.71	21.69	20.95	14128	17:50:34.08	68:16:54.5	22.80	24.60	23.54	22.30
11644	17:50:11.76	68:17:24.4	24.24	24.46	22.44	21.56	13915	17:51:38.88	68:17:29.8	24.00	24.00	23.35	22.35
13555	17:50:32.16	68:17:43.4	22.71	23.25	22.18	22.13	13631	17:51:57.12	68:17:33.4	23.80	23.89	22.35	22.08

Table B.5. *zJK* galaxies in 7C 1805+6332 field

ID	R.A. hms	Dec. dms	*z* (AB)	*J* (AB)	*Ks* (AB)	ID	R.A. hms	Dec. dms	*z* (AB)	*J* (AB)	*Ks* (AB)
2257	18:06:15.60	63:23:22.9	23.88	22.34	21.46	3341	18:06:23.76	63:24:40.7	22.46	21.17	20.22
4336	18:06:06.72	63:25:48.4	22.58	21.14	19.95	4563	18:06:48.48	63:25:54.8	23.62	21.64	21.52
4945	18:06:21.60	63:26:24.0	23.51	21.98	20.90	5256	18:05:24.00	63:26:55.7	19.88	17.11	17.45
5485	18:06:11.04	63:27:11.9	18.37	17.11	17.51	5295	18:06:55.92	63:26:47.4	22.80	21.49	20.66
5353	18:06:10.08	63:26:53.2	23.73	22.20	20.95	6249	18:06:20.39	63:28:00.8	23.72	22.40	21.47
6501	18:05:43.44	63:28:12.0	24.13	21.94	21.06	7001	18:06:40.80	63:28:48.7	22.99	21.60	20.77
7177	18:06:30.48	63:28:56.6	24.06	22.59	21.92	7047	18:06:39.36	63:28:53.8	22.47	20.88	19.81
7481	18:07:14.64	63:29:19.0	21.69	19.83	20.09	7511	18:04:53.04	63:29:27.2	21.82	19.61	19.13
7816	18:04:54.47	63:29:43.4	22.57	20.43	19.77	8001	18:07:12.72	63:29:55.3	23.44	20.96	19.98
8030	18:07:13.93	63:29:56.4	23.82	21.74	20.59	8169	18:05:30.48	63:30:07.2	22.87	21.53	20.44
8470	18:04:52.32	63:30:25.6	23.67	21.90	21.41	8614	18:04:29.52	63:30:39.6	22.31	21.36	20.54
8987	18:06:13.93	63:31:09.8	18.75	17.19	17.68	9585	18:06:10.08	63:31:49.4	23.95	22.19	21.47
9589	18:06:17.28	63:31:54.8	22.68	20.48	20.12	9919	18:04:50.64	63:32:14.6	22.52	20.71	20.01
10072	18:05:08.64	63:32:24.0	22.79	21.38	20.57	10510	18:06:53.28	63:32:53.2	23.59	22.01	20.96
10591	18:04:59.04	63:32:57.8	23.71	21.24	20.86	10569	18:06:12.96	63:32:57.5	23.40	21.11	20.66
10897	18:05:51.36	63:33:17.6	22.86	21.11	20.49	11320	18:05:31.20	63:33:45.0	23.40	21.81	20.77
11683	18:04:24.24	63:33:59.0	22.58	20.66	19.79	11641	18:04:23.76	63:34:00.5	23.43	21.91	20.87
11688	18:05:31.20	63:34:04.4	22.25	20.65	20.01	11850	18:06:30.00	63:34:10.9	22.62	21.92	20.82
11972	18:07:05.28	63:34:20.3	23.52	21.92	21.07	12381	18:06:05.52	63:34:43.7	23.47	21.21	20.58
12694	18:04:43.92	63:35:02.0	23.22	21.76	21.01	12821	18:07:04.32	63:35:10.0	23.37	21.80	20.77
13102	18:07:34.32	63:35:28.0	23.66	19.84	21.47	13097	18:07:35.28	63:35:31.9	23.95	19.97	20.99
13150	18:04:39.36	63:35:32.6	21.86	21.17	20.35	13452	18:07:19.20	63:35:53.5	23.82	22.01	21.15
13746	18:07:09.60	63:36:11.5	23.34	21.02	20.47	13902	18:04:43.44	63:36:18.0	22.68	21.60	20.58
14147	18:04:25.20	63:36:30.2	22.27	20.64	19.86	14697	18:07:08.88	63:37:00.5	23.97	22.71	21.47
14654	18:04:37.44	63:37:06.6	24.05	22.18	21.77	14916	18:06:36.96	63:37:21.7	23.70	22.39	21.44
15006	18:06:58.33	63:37:23.5	23.63	21.62	21.09	14988	18:06:26.16	63:37:29.6	23.61	20.02	19.79
15062	18:07:04.08	63:37:27.1	22.91	21.33	20.75	15166	18:06:58.80	63:37:32.2	24.15	21.96	21.26
15215	18:06:17.04	63:37:33.6	22.55	19.24	20.63	15284	18:07:29.04	63:37:36.8	23.96	21.27	20.94
15612	18:05:25.44	63:37:58.1	22.58	21.61	20.94	15711	18:06:59.04	63:37:59.9	23.88	21.72	20.74
15763	18:06:52.08	63:38:04.9	23.74	21.60	21.04	16044	18:06:41.28	63:38:22.2	23.51	21.89	21.36
16823	18:04:27.84	63:38:58.2	21.88	20.56	19.61	18612	18:06:58.80	63:39:22.3	22.58	21.19	20.92
18555	18:04:34.32	63:39:28.4	22.89	21.15	20.33	18454	18:05:48.48	63:39:39.6	23.01	21.89	20.97
18365	18:07:19.68	63:39:43.9	23.37	21.69	20.46	22006	18:04:42.72	63:39:54.7	23.60	21.74	20.91
21884	18:06:38.88	63:40:17.0	24.39	21.90	21.14	21766	18:05:04.80	63:40:23.5	23.34	21.77	21.03
17868	18:06:32.88	63:40:29.6	22.39	20.73	19.84	21141	18:07:26.40	63:41:16.4	23.18	20.73	20.26
20998	18:06:18.72	63:41:34.8	23.32	21.71	20.95	20979	18:04:40.08	63:41:39.1	24.08	22.11	20.97
20934	18:04:30.48	63:41:42.4	24.03	22.40	21.64	20927	18:06:29.76	63:42:19.8	23.26	20.60	20.34
20556	18:06:06.72	63:42:22.7	23.43	22.29	21.09	19432	18:06:03.61	63:43:41.9	23.88	21.60	21.11
18852	18:07:08.88	63:44:19.7	23.48	21.67	20.70						

B.2 Source lists of chapter 4:

Table B.6. r-*YHK* galaxies in the field of MRC 1017-220

ID	R.A.	Dec.	*Y*	*H*	*Ks*	ID	R.A.	Dec.	*Y*	*H*	*Ks*
	hms	dms	(AB)	(AB)	(AB)		hms	dms	(AB)	(AB)	(AB)
106	10:19:36.98	-22:22:02.4	23.33	20.46	20.39	209	10:19:55.62	-22:21:44.8	24.63	22.53	21.81
257	10:19:52.35	-22:21:33.2	23.25	21.72	21.31	389	10:19:38.36	-22:21:07.0	24.09	22.66	23.15
499	10:20:01.80	-22:20:41.4	24.08	22.19	21.72	511	10:19:50.97	-22:20:37.3	23.14	21.04	20.60
537	10:19:48.88	-22:20:35.8	25.78	23.31	23.05	720	10:20:05.51	-22:19:57.9	24.33	22.43	21.84
733	10:19:56.52	-22:19:55.3	24.69	22.49	22.02	819	10:20:05.43	-22:19:37.9	23.26	21.26	20.89
948	10:20:07.20	-22:19:08.3	25.04	23.17	22.96	1020	10:20:09.24	-22:18:52.4	25.37	23.16	22.67
1088	10:19:37.97	-22:18:36.2	22.63	20.73	21.67	1087	10:19:45.83	-22:18:35.6	24.16	22.00	21.57
1222	10:19:42.78	-22:17:59.7	24.15	22.19	22.00	1390	10:19:41.35	-22:17:23.0	25.72	24.27	22.85
1412	10:19:39.61	-22:17:18.1	25.89	23.05	22.59	1423	10:19:38.45	-22:17:12.1	24.00	21.70	21.30
1525	10:19:56.71	-22:16:49.7	25.05	22.66	21.90	1678	10:19:44.07	-22:14:55.3	24.17	22.27	21.66
2107	10:20:07.34	-22:15:20.0	25.39	22.44	22.06	1776	10:20:08.97	-22:15:59.5	23.15	21.43	20.98
1956	10:20:09.45	-22:16:05.6	23.47	21.24	20.92	1987	10:20:08.97	-22:15:44.5	24.68	22.88	22.41
1758	10:19:57.47	-22:15:49.5	24.18	22.48	22.26	1723	10:20:09.59	-22:16:07.1	24.00	22.02	21.53
1843	10:20:09.75	-22:16:01.6	24.58	22.83	22.51	1768	10:20:08.86	-22:16:10.7	24.73	22.98	22.28

Table B.7. b-*YHK* galaxies in the field of MRC 1017-220

ID	R.A.	Dec.	*Y*	*H*	*Ks*	ID	R.A.	Dec.	*Y*	*H*	*Ks*
	hms	dms	(AB)	(AB)	(AB)		hms	dms	(AB)	(AB)	(AB)
44	10:20:01.59	-22:22:17.3	24.82	23.16	23.12	66	10:20:09.62	-22:22:12.9	24.23	22.90	22.88
71	10:20:03.36	-22:22:10.1	22.88	21.88	21.71	77	10:20:07.58	-22:22:09.1	23.90	23.27	22.88
83	10:19:42.93	-22:22:07.8	22.89	22.03	21.79	133	10:19:57.17	-22:21:57.9	22.06	21.19	20.99
157	10:19:39.76	-22:21:55.4	22.56	21.73	21.53	162	10:19:50.21	-22:21:52.9	22.53	21.49	21.21
164	10:19:39.02	-22:21:56.3	24.07	23.00	22.80	163	10:20:02.31	-22:21:54.6	23.49	22.13	21.72
170	10:19:38.55	-22:21:52.7	23.85	22.56	22.72	204	10:20:04.73	-22:21:46.9	24.11	22.96	23.12
201	10:19:41.68	-22:21:46.8	24.36	22.70	22.14	213	10:19:37.04	-22:21:41.4	20.02	19.25	19.58
219	10:19:59.17	-22:21:41.3	22.68	21.60	21.29	237	10:19:48.94	-22:21:41.1	24.15	23.36	24.42
254	10:20:06.53	-22:21:35.0	22.67	21.89	21.99	253	10:19:40.39	-22:21:34.8	22.54	21.22	20.97
256	10:19:37.42	-22:21:34.6	22.09	21.00	20.77	298	10:19:50.05	-22:21:26.9	24.15	22.68	22.36
309	10:19:56.47	-22:21:22.2	22.34	21.27	20.96	323	10:19:58.00	-22:21:21.5	24.12	22.63	22.31
327	10:19:48.08	-22:21:18.8	23.72	22.40	22.02	350	10:20:00.57	-22:21:13.2	22.57	21.88	22.06
343	10:20:06.55	-22:21:16.4	23.84	22.76	22.98	352	10:19:55.46	-22:21:14.1	23.67	22.32	22.99
360	10:19:56.36	-22:21:12.8	23.33	22.30	22.28	363	10:19:58.57	-22:21:09.6	22.12	21.30	21.04
387	10:19:54.70	-22:21:06.2	23.13	22.61	22.34	393	10:19:44.35	-22:21:05.3	24.55	23.24	23.06
410	10:20:05.84	-22:20:54.3	20.52	19.76	19.58	445	10:19:49.41	-22:20:53.3	23.79	23.34	24.09
458	10:20:10.53	-22:20:48.4	21.95	20.68	20.34	531	10:20:05.63	-22:20:31.2	23.27	22.18	22.13
544	10:20:01.06	-22:20:31.5	23.93	22.57	22.46	578	10:19:47.01	-22:20:27.0	25.10	23.34	22.93
603	10:19:44.32	-22:20:24.3	25.45	23.36	23.46	641	10:19:50.94	-22:20:15.3	23.71	22.53	23.13
658	10:19:52.24	-22:20:11.5	23.87	22.95	23.33	662	10:19:59.39	-22:20:09.1	22.88	21.97	21.80
666	10:19:43.98	-22:20:10.4	24.34	23.32	23.83	688	10:19:46.13	-22:20:02.8	22.89	22.18	21.98
725	10:19:37.72	-22:19:56.9	22.73	21.55	21.71	759	10:20:09.29	-22:19:52.5	24.30	23.33	24.23
769	10:20:05.69	-22:19:50.7	24.84	23.01	22.61	775	10:19:47.79	-22:19:46.5	21.97	20.80	20.57
778	10:19:47.85	-22:19:48.2	23.54	22.12	21.70	808	10:19:42.81	-22:19:45.9	23.85	22.48	22.23
831	10:20:01.20	-22:19:40.2	23.99	22.40	22.98	812	10:19:50.50	-22:19:42.5	23.91	22.91	22.80
817	10:20:09.59	-22:19:38.3	22.47	21.51	21.16	827	10:19:38.37	-22:19:39.5	22.89	21.94	21.90
833	10:19:40.71	-22:19:39.5	24.15	23.22	22.98	850	10:19:46.96	-22:19:32.6	23.39	22.00	21.48
889	10:20:03.10	-22:19:23.4	24.30	23.59	23.60	884	10:20:02.25	-22:19:21.8	23.54	22.10	22.28
982	10:19:44.60	-22:19:00.7	23.65	22.73	22.57	977	10:20:10.51	-22:19:02.6	24.72	23.74	24.15
997	10:20:04.04	-22:18:58.1	22.89	22.00	21.87	1002	10:19:57.48	-22:18:57.0	23.29	21.94	21.63
1008	10:20:05.41	-22:18:56.2	23.72	22.56	23.00	1030	10:20:05.47	-22:18:50.0	24.93	22.99	23.86
1043	10:20:05.91	-22:18:43.7	22.00	21.15	20.97	1056	10:19:58.09	-22:18:44.3	24.50	23.78	23.34
1059	10:19:59.81	-22:18:43.8	23.86	22.65	23.36	1068	10:19:51.64	-22:18:40.9	23.08	22.07	21.96
1064	10:20:06.28	-22:18:41.7	24.83	23.08	22.89	1094	10:19:49.83	-22:18:30.4	23.06	21.99	21.64
1111	10:19:46.65	-22:18:23.5	21.95	21.19	20.98	1157	10:19:57.42	-22:18:16.3	23.37	22.62	22.36
1148	10:19:56.19	-22:18:15.8	22.95	21.88	21.58	1172	10:20:03.39	-22:18:12.5	24.00	22.77	22.98
1220	10:19:45.10	-22:18:01.0	24.40	23.82	23.77	1233	10:19:40.94	-22:17:58.8	24.08	24.08	23.39
1262	10:19:38.80	-22:17:50.1	24.60	23.92	23.29	1286	10:19:53.83	-22:17:42.4	21.90	21.08	22.76
1273	10:20:00.74	-22:17:45.4	25.26	23.97	23.95	1300	10:19:44.82	-22:17:40.6	23.53	22.71	22.54
1306	10:19:56.17	-22:17:39.8	24.04	23.14	23.01	1302	10:19:49.84	-22:17:39.7	24.38	23.38	23.26
1340	10:19:54.77	-22:17:30.6	22.18	20.82	20.81	1341	10:19:54.25	-22:17:33.5	23.35	22.41	23.77
1406	10:19:42.39	-22:17:19.2	23.29	22.44	22.85	1443	10:20:02.79	-22:17:10.0	22.88	22.02	21.88
1447	10:20:02.27	-22:17:07.9	22.33	21.15	20.74	1458	10:19:42.66	-22:17:08.6	24.43	23.47	23.34
1477	10:19:48.76	-22:17:03.9	24.57	23.56	23.71	1474	10:20:04.17	-22:17:02.6	23.81	22.44	22.04
1510	10:19:58.29	-22:16:53.5	22.65	21.94	21.70	1518	10:19:45.45	-22:16:52.6	22.95	21.81	21.62
1533	10:19:47.06	-22:16:49.1	25.97	23.81	23.79	1610	10:19:42.15	-22:14:35.5	22.36	21.56	21.57
1623	10:19:58.16	-22:14:38.5	23.57	22.94	22.77	1649	10:19:42.27	-22:14:47.1	22.71	21.49	21.11
1647	10:19:41.92	-22:14:46.2	23.90	22.75	22.64	1658	10:20:06.36	-22:14:50.0	24.34	22.85	23.66
1661	10:19:43.38	-22:14:50.7	24.68	23.79	22.88	2009	10:20:00.58	-22:15:17.2	23.61	22.55	22.09
1970	10:20:03.55	-22:15:18.3	22.78	21.39	20.88	1812	10:19:42.92	-22:16:09.0	25.52	24.03	24.24
1765	10:19:38.48	-22:16:02.4	22.13	20.90	21.50	1762	10:20:06.76	-22:16:09.7	23.95	22.88	23.24
1922	10:19:48.46	-22:16:32.4	22.81	21.62	21.35	2096	10:20:08.74	-22:15:26.9	23.99	22.48	22.07
1919	10:20:06.78	-22:16:29.3	23.83	23.16	23.43	1822	10:20:09.99	-22:16:21.3	23.83	22.31	22.71
1856	10:20:02.17	-22:16:18.9	23.09	22.11	21.96	2109	10:20:02.15	-22:16:01.7	23.28	21.88	21.76
1730	10:19:45.90	-22:15:02.5	23.75	22.97	23.99	1895	10:19:59.55	-22:15:33.1	22.75	21.92	21.66
1896	10:19:45.87	-22:16:37.6	22.30	21.54	21.17	1752	10:19:49.38	-22:15:53.6	22.96	21.91	21.77
1944	10:19:55.48	-22:16:39.0	23.78	22.21	22.04	1837	10:19:39.65	-22:16:37.9	24.86	23.86	24.13
1853	10:19:46.36	-22:15:32.4	25.94	24.54	23.73	1780	10:20:04.99	-22:15:55.3	24.83	23.12	23.12

Table B.8. r-*YHK* galaxies in the field of MRC 0156-252

ID	R.A. hms	Dec. dms	*Y* (AB)	*H* (AB)	*Ks* (AB)	ID	R.A. hms	Dec. dms	*Y* (AB)	*H* (AB)	*Ks* (AB)
37	01:58:46.13	-25:04:50.1	23.53	21.68	21.33	40	01:58:50.44	-25:04:50.6	24.88	23.52	23.58
86	01:58:31.72	-25:04:34.9	22.81	21.17	20.80	93	01:58:44.59	-25:04:36.2	25.28	23.48	23.06
96	01:58:27.97	-25:04:31.4	23.46	22.02	21.46	113	01:58:50.04	-25:04:29.6	24.52	23.09	22.73
139	01:58:27.40	-25:04:23.5	25.70	22.42	21.83	149	01:58:34.69	-25:04:22.6	24.62	22.68	22.45
187	01:58:54.87	-25:04:12.7	23.75	22.00	21.48	200	01:58:26.00	-25:04:09.1	23.15	21.59	21.30
193	01:58:34.78	-25:04:12.0	25.09	23.18	22.49	210	01:58:40.72	-25:04:08.2	24.88	22.61	21.95
234	01:58:34.67	-25:04:00.0	24.79	22.72	22.33	276	01:58:28.35	-25:03:51.5	25.26	23.15	22.94
311	01:58:31.41	-25:03:41.9	23.79	22.34	21.77	347	01:58:47.94	-25:03:35.8	26.04	23.40	22.97
369	01:58:28.24	-25:03:32.8	25.59	23.80	23.42	367	01:58:46.46	-25:03:29.9	23.80	22.26	21.95
402	01:58:55.95	-25:03:23.9	23.99	22.30	21.94	400	01:58:46.68	-25:03:23.6	25.03	22.48	21.72
428	01:58:34.87	-25:03:19.9	24.87	22.71	22.45	477	01:58:20.94	-25:03:07.2	21.76	17.34	18.29
493	01:58:53.73	-25:03:08.7	24.30	22.59	22.05	514	01:58:38.42	-25:03:03.2	24.14	22.65	22.11
522	01:58:56.56	-25:03:03.1	24.71	22.39	22.36	535	01:58:45.78	-25:02:59.5	24.83	22.91	22.29
541	01:58:35.13	-25:02:59.6	25.15	23.99	24.02	549	01:58:49.83	-25:02:55.5	24.80	23.06	22.45
577	01:58:31.87	-25:02:52.2	24.88	23.06	23.68	572	01:58:23.06	-25:02:53.1	25.53	23.66	23.31
563	01:58:20.90	-25:02:48.3	21.40	18.33	18.46	593	01:58:34.33	-25:02:46.6	23.48	21.74	21.43
625	01:58:49.11	-25:02:42.0	24.29	22.48	22.05	675	01:58:44.51	-25:02:33.8	24.41	22.80	22.53
674	01:58:44.15	-25:02:32.7	24.37	22.18	21.75	756	01:58:50.85	-25:02:15.4	25.55	23.65	23.16
770	01:58:24.71	-25:02:12.2	24.30	22.56	22.93	812	01:58:37.63	-25:02:02.5	24.82	23.07	23.56
814	01:58:46.97	-25:02:00.5	24.58	22.88	22.39	819	01:58:46.68	-25:01:58.5	24.08	22.09	21.96
829	01:58:51.90	-25:01:54.2	23.01	21.36	20.88	831	01:58:26.42	-25:01:54.7	23.22	21.53	21.26
878	01:58:53.49	-25:01:49.4	25.01	23.49	23.46	880	01:58:49.82	-25:01:47.4	25.13	22.76	22.02
935	01:58:23.71	-25:01:38.6	24.11	21.94	21.55	947	01:58:49.81	-25:01:35.8	25.06	22.69	21.96
975	01:58:30.61	-25:01:30.6	23.75	22.12	21.85	1055	01:58:35.76	-25:01:13.1	24.31	22.12	21.62
1073	01:58:53.93	-25:01:06.6	23.69	22.27	21.98	1102	01:58:51.72	-25:01:03.9	26.15	23.59	22.90
1139	01:58:45.64	-25:00:55.5	24.37	22.24	21.87	1222	01:58:33.04	-25:00:33.6	23.70	22.01	21.48
1229	01:58:32.28	-25:00:32.7	23.46	21.78	21.40	1239	01:58:45.63	-25:00:28.0	22.23	20.54	20.17
1234	01:58:39.45	-25:00:31.0	24.78	22.78	22.02	1255	01:58:39.28	-25:00:25.0	23.91	22.01	21.29
1253	01:58:26.32	-25:00:25.9	24.95	22.82	22.12	1304	01:58:52.13	-25:00:12.2	23.98	22.35	21.88
1333	01:58:38.11	-25:00:07.2	23.66	22.14	21.74	1351	01:58:52.65	-25:00:06.2	25.43	23.32	22.59
1367	01:58:53.46	-25:00:01.5	23.83	21.81	21.36	1368	01:58:55.40	-25:00:02.5	23.89	22.40	21.75
1396	01:58:23.29	-24:59:55.6	23.70	21.88	21.42	1398	01:58:53.75	-24:59:56.8	24.98	23.15	22.86
1434	01:58:30.93	-24:59:50.1	24.92	23.51	23.14	1429	01:58:32.48	-24:59:49.6	25.15	23.46	22.95
1455	01:58:54.37	-24:59:47.2	25.53	23.37	22.86	1449	01:58:35.50	-24:59:46.1	24.04	21.82	21.48
1478	01:58:33.48	-24:59:32.0	21.47	19.45	18.68	1495	01:58:39.67	-24:59:36.6	24.50	22.63	22.09
1518	01:58:25.75	-24:59:30.9	25.16	23.21	22.66	1526	01:58:33.87	-24:59:28.8	24.31	22.19	21.65
1562	01:58:32.65	-24:59:22.8	25.30	23.87	24.32	1569	01:58:37.38	-24:59:21.5	25.45	23.30	23.27
1595	01:58:38.79	-24:59:17.4	23.77	22.35	21.80	1589	01:58:36.14	-24:59:17.9	24.26	22.43	21.98
1585	01:58:30.78	-24:59:17.7	23.95	22.02	21.46	1647	01:58:23.73	-24:59:05.3	24.55	23.12	22.90
1650	01:58:34.12	-24:59:05.2	24.78	22.80	22.81	1658	01:58:22.62	-24:59:03.4	26.40	23.15	22.36
1665	01:58:38.86	-24:59:01.1	24.67	22.71	22.24	1702	01:58:26.63	-24:56:42.0	19.09	15.59	16.46
1715	01:58:40.09	-24:56:42.0	23.23	19.96	20.18	1725	01:58:25.64	-24:56:46.8	24.19	22.02	21.48
2220	01:58:23.15	-24:57:56.8	23.76	22.19	21.91	1788	01:58:41.88	-24:58:11.2	24.15	21.97	21.68
1809	01:58:31.55	-24:58:10.4	25.30	23.80	23.77	1847	01:58:44.69	-24:58:11.4	22.99	21.53	21.11
1834	01:58:56.21	-24:58:09.6	24.13	22.17	21.58	2146	01:58:37.96	-24:58:11.4	24.20	22.17	21.57
1787	01:58:23.27	-24:58:31.7	24.94	23.35	22.94	1977	01:58:53.41	-24:58:40.8	24.59	22.44	21.95
1802	01:58:43.79	-24:58:42.1	23.99	21.87	21.61	1930	01:58:29.20	-24:58:46.7	24.44	22.31	22.52
2001	01:58:55.90	-24:57:36.0	25.41	22.39	21.83	1909	01:58:23.23	-24:57:09.0	25.34	22.71	23.40
2025	01:58:29.00	-24:58:51.6	24.69	22.29	21.88	1823	01:58:30.29	-24:57:11.1	24.01	22.49	22.03
2107	01:58:36.81	-24:57:21.3	25.20	22.53	22.07	2080	01:58:22.79	-24:57:34.6	24.74	22.76	22.44
2079	01:58:29.75	-24:57:15.9	25.22	22.23	22.15	2099	01:58:24.80	-24:57:27.1	24.39	22.59	22.16
2139	01:58:38.11	-24:57:33.8	23.90	22.35	21.88	1884	01:58:55.24	-24:58:25.4	24.20	21.96	21.97
2167	01:58:45.11	-24:57:44.8	25.12	23.36	24.12						

Table B.9. b-*YHK* galaxies in the field of MRC 0156-252

ID	R.A. hms	Dec. dms	*Y* (AB)	*H* (AB)	*Ks* (AB)	ID	R.A. hms	Dec. dms	*Y* (AB)	*H* (AB)	*Ks* (AB)
14	01:58:41.63	-25:04:55.3	23.08	22.20	22.22	24	01:58:24.11	-25:04:52.3	23.15	22.59	21.88
23	01:58:53.79	-25:04:53.7	23.82	22.61	22.74	25	01:58:51.69	-25:04:53.0	23.47	22.75	22.91
56	01:58:38.18	-25:04:45.9	23.69	22.30	22.27	73	01:58:51.46	-25:04:40.3	21.95	21.15	20.92
94	01:58:52.64	-25:04:34.7	23.34	22.54	22.25	144	01:58:24.53	-25:04:23.7	23.78	22.99	22.95
151	01:58:23.70	-25:04:20.9	23.41	22.15	21.79	156	01:58:49.98	-25:04:18.5	22.11	20.87	20.39
213	01:58:48.67	-25:04:07.6	23.05	22.11	22.24	185	01:58:46.88	-25:04:15.6	24.61	23.51	23.64
198	01:58:37.38	-25:04:09.5	22.73	21.76	21.53	226	01:58:27.70	-25:04:04.5	23.87	23.15	23.89
228	01:58:53.69	-25:04:03.7	23.87	22.44	22.06	230	01:58:54.42	-25:04:02.8	24.11	22.91	22.87
242	01:58:39.31	-25:03:58.2	22.32	21.32	21.30	239	01:58:22.52	-25:03:57.3	22.48	21.37	21.12
278	01:58:41.94	-25:03:51.8	23.98	22.98	23.53	284	01:58:23.31	-25:03:49.8	23.35	22.24	22.13
301	01:58:46.89	-25:03:43.8	22.79	21.38	20.96	303	01:58:36.81	-25:03:44.6	23.22	21.85	21.54
313	01:58:26.28	-25:03:41.9	23.08	22.15	23.51	324	01:58:35.08	-25:03:40.1	22.29	21.30	21.22
315	01:58:47.17	-25:03:44.2	24.62	24.09	24.64	265	01:58:45.76	-25:03:40.0	22.80	21.87	21.60
362	01:58:23.35	-25:03:33.8	24.02	23.28	23.38	384	01:58:42.40	-25:03:26.8	22.15	21.20	21.19
389	01:58:56.75	-25:03:28.0	23.77	22.68	22.73	410	01:58:30.11	-25:03:23.7	24.26	23.44	22.84
418	01:58:24.31	-25:03:22.1	23.73	22.45	22.39	420	01:58:23.61	-25:03:20.7	23.54	22.70	22.42
431	01:58:49.95	-25:03:19.0	22.84	22.09	21.90	433	01:58:42.69	-25:03:20.0	24.35	23.40	24.15
429	01:58:23.53	-25:03:13.7	22.01	20.84	20.32	443	01:58:46.71	-25:03:15.1	23.31	21.96	21.48
446	01:58:26.01	-25:03:16.3	23.90	22.53	22.08	460	01:58:23.07	-25:03:13.9	23.65	22.64	22.93
467	01:58:39.67	-25:03:13.1	23.52	22.57	22.26	465	01:58:26.97	-25:03:13.8	24.85	23.71	23.71
482	01:58:50.19	-25:03:11.1	23.66	22.79	22.64	483	01:58:43.98	-25:03:11.2	24.29	23.39	23.35
488	01:58:38.83	-25:03:10.9	23.64	22.75	23.25	492	01:58:28.34	-25:03:08.2	22.26	21.33	21.02
489	01:58:28.02	-25:03:10.9	24.65	23.97	23.95	507	01:58:21.46	-25:03:04.1	22.21	21.14	20.75
511	01:58:33.70	-25:03:03.7	22.87	22.02	21.88	542	01:58:39.64	-25:02:58.0	23.15	22.09	21.79
562	01:58:45.49	-25:02:52.9	22.84	21.71	22.21	540	01:58:38.65	-25:02:59.2	24.42	23.30	23.09

Table B.9. continued.

ID	R.A. hms	Dec. dms	*Y* (AB)	*H* (AB)	*Ks* (AB)	ID	R.A. hms	Dec. dms	*Y* (AB)	*H* (AB)	*Ks* (AB)
569	01:58:36.59	-25:02:53.7	24.84	23.93	23.97	579	01:58:40.55	-25:02:51.3	24.63	23.59	23.31
602	01:58:40.64	-25:02:47.6	24.38	23.32	23.85	601	01:58:46.32	-25:02:47.7	24.64	23.367	23.10
604	01:58:57.29	-25:02:46.6	23.23	22.28	22.14	612	01:58:23.36	-25:02:46.0	24.30	23.59	23.82
637	01:58:44.60	-25:02:40.2	23.17	22.35	22.17	652	01:58:42.38	-25:02:38.6	24.42	23.38	23.61
651	01:58:32.34	-25:02:36.9	22.76	21.67	21.49	645	01:58:29.64	-25:02:40.4	25.59	24.63	24.22
664	01:58:45.34	-25:02:36.2	24.21	23.61	24.32	659	01:58:41.04	-25:02:37.2	24.25	23.53	23.19
671	01:58:54.53	-25:02:35.3	24.22	23.45	23.69	680	01:58:47.08	-25:02:31.4	23.70	22.46	22.04
681	01:58:53.33	-25:02:31.3	23.91	22.60	22.61	686	01:58:48.82	-25:02:29.1	22.80	21.96	21.76
683	01:58:45.48	-25:02:29.9	24.08	23.18	22.79	688	01:58:40.03	-25:02:27.6	23.25	21.81	21.72
697	01:58:30.24	-25:02:25.6	23.97	23.25	22.78	759	01:58:53.65	-25:02:15.2	25.13	23.89	23.69
789	01:58:27.83	-25:02:06.1	22.26	21.43	21.15	828	01:58:37.34	-25:01:56.5	23.00	22.16	22.01
833	01:58:50.82	-25:01:55.8	24.23	22.87	22.40	851	01:58:42.28	-25:01:50.9	22.94	21.83	21.65
865	01:58:22.04	-25:01:49.6	21.55	20.60	20.37	852	01:58:48.89	-25:01:53.2	26.96	24.40	23.17
868	01:58:32.88	-25:01:51.4	24.49	23.33	23.98	891	01:58:39.72	-25:01:46.9	23.58	22.46	22.31
900	01:58:48.83	-25:01:46.5	24.67	23.66	23.70	909	01:58:30.91	-25:01:43.5	23.28	22.29	22.34
913	01:58:52.17	-25:01:42.5	23.56	22.58	22.43	921	01:58:42.67	-25:01:41.8	24.08	23.12	22.70
922	01:58:23.82	-25:01:41.5	24.62	23.51	23.27	930	01:58:30.84	-25:01:40.6	24.49	23.35	22.98
932	01:58:49.30	-25:01:40.8	24.69	23.28	23.05	937	01:58:51.71	-25:01:40.6	25.88	23.57	24.57
942	01:58:40.22	-25:01:37.5	23.46	22.38	22.09	948	01:58:30.07	-25:01:37.0	24.09	23.32	22.93
979	01:58:53.33	-25:01:28.2	22.34	21.14	20.79	974	01:58:51.50	-25:01:30.6	23.55	22.54	22.50
980	01:58:42.07	-25:01:29.9	23.96	23.16	23.07	1049	01:58:48.67	-25:01:15.5	23.89	23.11	23.81
1076	01:58:48.77	-25:01:09.8	24.50	23.58	23.76	1082	01:58:36.08	-25:01:08.4	24.34	23.12	23.42
1117	01:58:53.44	-25:01:01.7	24.07	23.16	23.16	1153	01:58:35.28	-25:00:51.1	24.50	24.60	24.19
1156	01:58:40.64	-25:00:49.8	23.71	22.48	22.09	1209	01:58:31.05	-25:00:38.0	24.57	23.48	23.31
1236	01:58:36.79	-25:00:32.2	24.22	24.30	23.35	1244	01:58:48.24	-25:00:30.2	24.28	23.31	22.87
1233	01:58:25.16	-25:00:31.5	24.60	23.63	23.12	1248	01:58:23.63	-25:00:29.5	24.21	23.35	23.22
1274	01:58:50.06	-25:00:22.0	23.86	23.12	23.06	1277	01:58:36.42	-25:00:20.2	23.80	23.06	22.63
1293	01:58:36.22	-25:00:17.0	25.15	23.68	23.73	1296	01:58:27.70	-25:00:16.4	24.98	23.54	23.61
1334	01:58:27.87	-25:00:05.5	22.88	21.56	21.01	1403	01:58:52.72	-24:59:54.2	24.04	23.06	22.92
1412	01:58:39.42	-24:59:53.9	23.64	23.05	23.50	1410	01:58:44.12	-24:59:53.2	23.81	23.36	23.16
1425	01:58:47.62	-24:59:50.0	23.37	22.30	22.26	1476	01:58:37.34	-24:59:40.1	22.65	21.77	21.60
1458	01:58:52.02	-24:59:46.1	24.27	23.28	22.95	1481	01:58:56.38	-24:59:39.2	22.69	21.80	21.63
1473	01:58:31.90	-24:59:42.1	25.31	24.24	22.95	1482	01:58:36.20	-24:59:40.5	24.53	23.44	24.15
1486	01:58:22.95	-24:59:39.2	24.17	22.93	22.96	1491	01:58:32.09	-24:59:37.7	24.36	23.53	23.02
1507	01:58:57.33	-24:59:35.5	23.03	22.36	22.88	1520	01:58:43.13	-24:59:30.7	24.04	23.04	22.90
1532	01:58:32.21	-24:59:29.2	24.43	23.09	22.66	1539	01:58:55.91	-24:59:26.5	23.48	22.23	21.82
1542	01:58:22.21	-24:59:27.4	24.06	23.14	23.44	1546	01:58:37.68	-24:59:26.8	25.42	24.21	24.05
1560	01:58:23.90	-24:59:20.3	22.33	20.92	20.45	1579	01:58:43.07	-24:59:20.7	23.71	22.82	22.99
1573	01:58:27.89	-24:59:17.2	22.97	21.68	21.33	1590	01:58:33.66	-24:59:19.4	24.57	23.53	23.73
1603	01:58:31.15	-24:59:16.6	23.65	22.51	22.28	1607	01:58:36.12	-24:59:15.2	23.18	21.81	21.57
1614	01:58:47.33	-24:59:15.1	24.84	23.50	23.01	1644	01:58:30.33	-24:59:07.2	24.14	23.05	22.57
1688	01:58:39.29	-24:58:55.4	22.25	21.43	21.31	1687	01:58:33.15	-24:58:57.3	24.33	23.28	24.06
1734	01:58:42.04	-24:56:50.6	23.17	22.32	22.01	1741	01:58:24.30	-24:56:52.5	25.37	23.96	23.64
1744	01:58:53.31	-24:56:53.3	24.98	23.70	23.89	1776	01:58:33.10	-24:57:06.8	24.65	22.98	23.57
2132	01:58:43.09	-24:57:44.1	24.20	23.11	23.62	2156	01:58:51.39	-24:57:46.7	22.95	21.95	21.80
2224	01:58:50.83	-24:57:53.7	24.77	23.77	23.93	1998	01:58:23.35	-24:57:38.8	23.81	22.45	22.08
2186	01:58:54.60	-24:57:58.0	24.12	23.49	23.42	1698	01:58:39.31	-24:57:59.6	23.49	22.60	22.65
1807	01:58:26.96	-24:58:10.1	23.63	22.86	22.88	2034	01:58:21.90	-24:58:04.2	23.22	22.76	22.85
1810	01:58:32.03	-24:58:03.1	23.31	21.96	21.69	1849	01:58:35.85	-24:58:07.7	24.37	23.51	25.05
1842	01:58:34.88	-24:58:08.5	24.73	23.46	23.84	2171	01:58:55.07	-24:58:07.7	24.94	23.92	23.38
2006	01:58:34.74	-24:58:51.3	24.30	22.95	22.57	1784	01:58:49.02	-24:58:23.2	24.40	23.51	24.50
1910	01:58:33.46	-24:58:29.0	23.96	23.08	22.82	1951	01:58:36.14	-24:58:44.5	23.05	22.27	22.41
1941	01:58:55.17	-24:58:29.0	22.47	21.56	21.16	2110	01:58:27.90	-24:58:29.5	24.64	23.54	24.00
1911	01:58:30.82	-24:58:21.2	25.02	23.67	23.60	1963	01:58:55.10	-24:58:32.6	23.80	22.53	22.12
1971	01:58:29.72	-24:58:34.3	24.55	23.87	24.01	2049	01:58:28.71	-24:58:50.0	23.96	22.57	22.20
1990	01:58:24.49	-24:58:42.7	23.38	22.42	22.29	1983	01:58:54.95	-24:58:39.8	23.35	22.42	22.06
2007	01:58:35.42	-24:57:15.0	22.97	22.09	21.79	2041	01:58:23.24	-24:57:29.8	21.67	20.37	22.25
2010	01:58:27.30	-24:57:24.2	25.27	24.54	24.61	1796	01:58:50.70	-24:58:01.6	24.45	24.00	23.27
1960	01:58:40.28	-24:57:42.4	23.76	22.71	22.46	1816	01:58:32.57	-24:58:44.0	23.59	22.17	21.78
2201	01:58:23.01	-24:57:53.7	23.82	23.04	22.72						

Appendix C

Publication List

- Galametz et al. to be submitted to A&A: "Spectroscopic confirmation of a galaxy cluster associated with 7C 1756+6520 at z=1.416 ": Audrey Galametz, Daniel Stern, Adam Stanford, Carlos De Breuck, Joël Vernet, Fiona Harrison, Roger Griffith

- Galametz et al. to be submitted: "IR survey of high redshift radio-selected protoclusters candidates. I- Galaxy cluster candidates at $1.6 < z \lesssim 2$": Audrey Galametz, Joël Vernet, Carlos De Breuck, George Miley, Nina Hatch, Bram Venemans, Tadayuki Kodama, Jaron Kurk

- Galametz et al. 2009B : "Large Scale Structures Around Radio Galaxies at $z \sim 1.5$" - *A&A*, **507**, 131: Audrey Galametz, Carlos De Breuck, Joël Vernet, Daniel Stern, Alessandro Rettura, Chiara Marmo, Alain Omont, Mark Allen, Nick Seymour

- Galametz et al. 2009A : "The Cosmic Evolution of Active Galactic Nuclei in Galaxy Cluters" - *ApJ*, **694**, 1309-1316: Audrey Galametz, Daniel Stern, Peter R. M. Eisenhardt, Mark Brodwin, Michael J. I. Brown, Arjun Dey, Anthony H. Gonzalez, Buell T. Jannuzi, Leonidas A. Moustakas, S. Adam Stanford

- Brodwin, M. et al. 2008: "A Large Population of High Redshift Galaxy Clusters in the IRAC Shallow Survey" - *ASPC*, **399**, 322: Mark Brodwin, Peter R. Eisenhardt, Anthony H. Gonzalez, Adam Stanford, Daniel Stern, Leonidas A. Moustakas, Michael J. I. Brown, Ranga-Ram Chary, Audrey Galametz

- Eisenhardt, P. et al. 2008: "Clusters of Galaxies in the First Half of the Universe fron the IRAC Shallow Survey" - *ApJ*, **684**, 905-932: Peter R. M. Eisenhardt, Mark Brodwin, Anthony H. Gonzalez, S. Adam Stanford, Daniel Stern, Pauline Barmby, Michael J. I. Brown, Kyle Dawson, Arjun Dey, Mamoru Doi, Audrey Galametz, B. T. Jannuzi, C. S. Kochanek, Joshua Meyers, Tomoki Morokuma, Leonidas A. Moustakas

- Seymour, N. et al. 2007: "Mid-infrared Spectra of High-Redshift ($z > 2$) Radio Galaxies - *ApJ*, **681**, L1-L4: Nick Seymour, Patrick Ogle, Carlos De Breuck, Giovanni Fazio, Audrey Galametz, Martin Haas, Mark Lacy, Anna Sajina, Daniel Stern, Steve Willner, Joël Vernet

Bibliography

Abraham, R. G. et al. 2004, AJ, 127, 2455

Andreon, S., Maughan, B., Trinchieri, G., & Kurk, J. 2008, ArXiv:0812.1699

Assef, R. J. et al. 2010, ArXiv:1001.4529

Bahcall, J. N., Schmidt, M., & Gunn, J. E. 1969, ApJ, 157, L77

Barrientos, L. F. et al. 2004, ApJS, 153, 397

Becker, R. H., White, R. L., & Helfand, D. J. 1995, ApJ, 450, 559

Bell, E. F. et al. 2004, ApJ, 608, 752

Bertin, E. & Arnouts, S. 1996, A&AS, 117, 393

Best, P. N., Kauffmann, G., Heckman, T. M., et al. 2005, MNRAS, 362, 25

Best, P. N. et al. 2003, MNRAS, 343, 1

Bignamini, A., Tozzi, P., Borgani, S., Ettori, S., & Rosati, P. 2008, A&A, 807

Birkinshaw, M. 1999, Phys. Rep., 310, 97

Bîrzan, L. et al. 2004, ApJ, 607, 800

Bonamente, M. et al. 2006, ApJ, 647, 25

Borgani, S., Rosati, P., Tozzi, P., et al. 2001, ApJ, 561, 13

Bower, R. G., Lucey, J. R., & Ellis, R. S. 1992, MNRAS, 254, 601

Brand, K. et al. 2006, ApJ, 641, 140

Brodwin, M., Gonzalez, A. H., Moustakas, L. A., et al. 2007, ApJ, 671, L93

Brodwin, M. et al. 2006, ApJ, 651, 791

Brodwin, M. et al. 2008, ApJ, 687, L65

Brown, M. J. I. et al. 2006, ApJ, 638, 88

Bruzual, G. & Charlot, S. 2003, MNRAS, 344, 1000

Butcher, H. & Oemler, Jr., A. 1984, ApJ, 285, 426

Cappi, M. et al. 2001, ApJ, 548, 624

Cardelli, J. A., Clayton, G. C., & Mathis, J. S. 1989, ApJ, 345, 245

Carilli, C. L. et al. 2002, ApJ, 567, 781

Carlberg, R. G. 1984, ApJ, 286, 403

Casali, M. et al. 2006, in SPIE, Vol. 6269, Society of Photo-Optical Instrumentation Engineers (SPIE) Conference Series

Castellano, M. et al. 2007, ApJ, 671, 1497

Chabrier, G. 2003, PASP, 115, 763

Chen, H.-W. et al. 2002, ApJ, 570, 54

Cimatti, A. et al. 1999, A&A, 352, L45

Cimatti, A. et al. 2000, MNRAS, 318, 453

Cimatti, A. et al. 2002, A&A, 381, L68

Cimatti, A. et al. 2008, A&A, 482, 21

Coil, A. L., Hennawi, J. F., Newman, J. A., Cooper, M. C., & Davis, M. 2007, ApJ, 654, 115

Condon, J. J. 1992, ARA&A, 30, 575

Condon, J. J., Cotton, W. D., Greisen, E. W., et al. 1998, AJ, 115, 1693

Cool, R. J. 2007, ApJS, 169, 21

Cowie, L. L., Songaila, A., Hu, E. M., & Cohen, J. G. 1996, AJ, 112, 839

Croft, S., de Vries, W., & Becker, R. H. 2007, ApJ, 667, L13

Croft, S., Kurk, J., van Breugel, W., et al. 2005, AJ, 130, 867

Croom, S. M., Smith, R. J., Boyle, B. J., et al. 2004, MNRAS, 349, 1397

Croom, S. M. et al. 2005, MNRAS, 356, 415

Daddi, E. et al. 2000, A&A, 361, 535

Daddi, E. et al. 2004, ApJ, 617, 746

De Breuck, C. et al. 2004, A&A, 424, 1

De Lucia, G. et al. 2004, ApJ, 610, L77

De Lucia, G. et al. 2006, MNRAS, 366, 499

De Lucia, G. et al. 2007, MNRAS, 374, 809

de Vries, W. H., Morganti, R., Röttgering, H. J. A., et al. 2002, AJ, 123, 1784

Dey, A. et al. 2008, ApJ, 677, 943

Dickinson, M. 1993, in Astronomical Society of the Pacific Conference Series, Vol. 51, Observational Cosmology, ed. G. L. Chincarini, A. Iovino, T. Maccacaro, & D. Maccagni, 434

Doherty, M. et al. 2010, A&A, 509, 83

Donley, J. L., Rieke, G. H., Perez-Gonzalez, P. G., & Barro, G. 2008, ApJ, 687, 111

Dressler, A., Thompson, I. B., & Shectman, S. A. 1985, ApJ, 288, 481

Dunlop, J. S. & Peacock, J. A. 1990, MNRAS, 247, 19

Eales, S. A. & Rawlings, S. 1996, ApJ, 460, 68

Eastman, J., Martini, P., Sivakoff, G., et al. 2007, ApJ, 664, L9

Ebeling, H., Edge, A. C., & Henry, J. P. 2001, ApJ, 553, 668

Eckart, M. E., McGreer, I. D., Stern, D., Harrison, F. A., & Helfand, D. J. 2010, ApJ, 708, 584

Eckart, M. E., Stern, D., Helfand, D. J., et al. 2006, ApJS, 165, 19

Eggen, O. J., Lynden-Bell, D., & Sandage, A. R. 1962, ApJ, 136, 748

Eisenhardt, P. R. et al. 2004, ApJS, 154, 48

Eisenhardt, P. R. M. et al. 2008, ApJ, 684, 905

Eke, V. R., Cole, S., Frenk, C. S., & Patrick Henry, J. 1998, MNRAS, 298, 1145

Elston, R. J. et al. 2006, ApJ, 639, 816

Elvis, M. et al. 1994, ApJS, 95, 1

Faber, S. M. et al. 2003, in SPIE Conference Series, Vol. 4841, Society of Photo-Optical Instrumentation Engineers (SPIE) Conference Series, 1657–1669

Farouki, R. T. & Shapiro, S. L. 1982, ApJ, 259, 103

Fazio, G. G. et al. 2004, ApJS, 154, 10

Finger, G. et al. 2008, in SPIE, Vol. 7021, Society of Photo-Optical Instrumentation Engineers Conference Series

Finkelstein, S. L., Rhoads, J. E., Malhotra, S., Pirzkal, N., & Wang, J. 2007, ApJ, 660, 1023

Finlator, K. et al. 2000, AJ, 120, 2615

Fioc, M. & Rocca-Volmerange, B. 1997, A&A, 326, 950

Franx, M. et al. 2003, ApJ, 587, L79

Galametz, A. et al. 2009, A&A, 507, 131

Galametz, A. et al. 2009, ApJ, 694, 1309

Gawiser, E. et al. 2006, ApJS, 162, 1

Gawiser, E. et al. 2007, ApJ, 671, 278

Gehrels, N. 1986, ApJ, 303, 336

Gilbank, D. G. et al. 2008, ApJ, 673, 742

Gladders, M. D., Lopez-Cruz, O., Yee, H. K. C., & Kodama, T. 1998, ApJ, 501, 571

Gladders, M. D. & Yee, H. K. C. 2000, AJ, 120, 2148

Gorjian et al. 2008, ApJ, 679

Grazian, A. et al. 2006a, A&A, 453, 507

Grazian, A. et al. 2006b, A&A, 449, 951

Grazian, A. et al. 2007, A&A, 465, 393

Gunn, J. & Weinberg, D. 1995, in Wide Field Spectroscopy and the Distant Universe, ed. S. J. Maddox & A. Aragon-Salamanca, 3

Halverson, N. W. et al. 2009, ApJ, 701, 42

Hartley, W. G. et al. 2008, MNRAS, 1280

Hawarden, T. G. et al. 2001, MNRAS, 325, 563

Hayashi, M. et al. 2009, ArXiv:0911.2530

Hewett, P. C. et al. 2006, MNRAS, 367, 454

Hilton, M. et al. 2007, ApJ, 670, 1000

Hilton, M. et al. 2009, ApJ, 697, 436

Hogg, D. W. et al. 2002, AJ, 124, 646

Huang, J.-S. et al. 2001, A&A, 368, 787

Imai, K. et al. 2008, ApJ, 683, 45

Jannuzi, B. T. & Dey, A. 1999, in Astronomical Society of the Pacific Conference Series, Vol. 191, Photometric Redshifts and the Detection of High Redshift Galaxies, ed. R. Weymann, L. Storrie-Lombardi, M. Sawicki, & R. Brunner, 111

Joy, M. et al. 2001, ApJ, 551, L1

Kajisawa, M. et al. 2000, PASJ, 52, 61

Kajisawa, M. et al. 2006, MNRAS, 371, 577

Kapahi, V. K. et al. 1998, ApJS, 118, 275

Kenter, A. et al. 2005, ApJS, 161, 9

Kodama, T. et al. 1998, A&A, 334, 99

Kodama, T. et al. 2005, PASJ, 57, 309

Kodama, T. et al. 2007, MNRAS, 377, 1717

Kong, X. et al. 2006, ApJ, 638, 72

Kriek, M. et al. 2008, ApJ, 677, 219

Kümmel, M. W. & Wagner, S. J. 2001, A&A, 370, 384

Kurk, J. et al. 2009, ArXiv:0906.4489

Kurk, J. D. et al. 2004a, A&A, 428, 793

Kurk, J. D. et al. 2004b, A&A, 428, 817

Kurk, J. D. et al. 2008a, ArXiv:0804.4126, 804

Kurk, J. D. et al. 2008b, in Astronomical Society of the Pacific Conference Series, Vol. 381, Infrared Diagnostics of Galaxy Evolution, 303

Lacy, M., Rawlings, S., Hill, G. J., et al. 1999, MNRAS, 308, 1096

Lacy, M., Rawlings, S., & Warner, P. J. 1992, MNRAS, 256, 404

Lacy, M. et al. 2004, ApJS, 154, 166

Lacy, M. et al. 2005, ApJS, 161, 41

Landolt, A. U. 1992, AJ, 104, 340

Lane, K. P. et al. 2007, MNRAS, 379, L25

Lidman, C. et al. 2004, A&A, 416, 829

Lidman, C. et al. 2008, A&A, 489, 981

Lin, Y.-T. & Mohr, J. J. 2007, ApJS, 170, 71

Magliocchetti, M. et al. 2008, MNRAS, 383, 1131

Magorrian, J. et al. 1998, AJ, 115, 2285

Maihara, T. et al. 2001, PASJ, 53, 25

Makovoz, D. & Khan, I. 2005, in Astronomical Society of the Pacific Conference Series, Vol. 347, Astronomical Data Analysis Software and Systems XIV, ed. P. Shopbell, M. Britton, & R. Ebert, 81–+

Marmo, C. 2007, in Astronomical Society of the Pacific Conference Series, Vol. 376, Astronomical Data Analysis Software and Systems XVI, ed. R. A. Shaw, F. Hill, & D. J. Bell, 285–+

Martini, P., Kelson, D. D., Kim, E., Mulchaey, J. S., & Athey, A. A. 2006, ApJ, 644, 116

Martini, P., Kelson, D. D., Mulchaey, J. S., & Trager, S. C. 2002, ApJ, 576, L109

Martini, P., Mulchaey, J. S., & Kelson, D. D. 2007, ApJ, 664, 761

Massey, P. & Gronwall, C. 1990, ApJ, 358, 344

Matthews, T. A., Morgan, W. W., & Schmidt, M. 1964, ApJ, 140, 35

McCarthy, P. J., Persson, S. E., & West, S. C. 1992, ApJ, 386, 52

McCarthy, P. J. et al. 1996, ApJS, 107, 19

McNamara, B. R. et al. 2000, ApJ, 534, L135

Mei, S. et al. 2006, ApJ, 644, 759

Mei, S. et al. 2009, ApJ, 690, 42

Metcalfe, N., Shanks, T., Fong, R., & Jones, L. R. 1991, MNRAS, 249, 498

Metcalfe, N., Shanks, T., Fong, R., & Roche, N. 1995, MNRAS, 273, 257

Metcalfe, N. et al. 2006, MNRAS, 370, 1257

Miley, G. & De Breuck, C. 2008, A&A Rev., 15, 67

Miley, G. K. et al. 2004, Nature, 427, 47

Miley, G. K. et al. 2006, ApJ, 650, L29

Mobasher, B. et al. 2004, ApJ, 600, L167

Monet, D. G. et al. 2003, AJ, 125, 984

Moy, E. et al. 2003, A&A, 403, 493

Mullis, C. R. et al. 2005, ApJ, 623, L85

Murray, S. S. et al. 2005, ApJS, 161, 1

Oke, J. B. et al. 1995, PASP, 107, 375

Overzier, R. A. et al. 2008, ApJ, 673, 143

Pentericci, L. et al. 2000, A&A, 361, L25

Pentericci, L. et al. 2001, ApJS, 135, 63

Poggianti, B. M. et al. 2009, ApJ, 697, L137

Pope, A. et al. 2006, in BAAS, Vol. 38, Bulletin of the American Astronomical Society, 1172

Postman, M. et al. 2005, ApJ, 623, 721

Puget, P. et al. 2004, in SPIE, Vol. 5492, Ground-based Instrumentation for Astronomy. Edited by Alan F. M. Moorwood and Iye Masanori., ed. A. F. M. Moorwood & M. Iye, 978–987

Quadri, R. et al. 2007, AJ, 134, 1103

Quadri, R. F., Williams, R. J., Lee, K., et al. 2008, ApJ, 685, L1

Reddy, N. A. et al. 2006, ApJ, 644, 792

Rettura, A. et al. 2008, ApJ, 806

Retzlaff, J. 2009, ArXiv:0912.1306

Richards, G. T. et al. 2006, ApJS, 166, 470

Rosati, P., Borgani, S., & Norman, C. 2002, ARA&A, 40, 539

Rosati, P. et al. 2004, AJ, 127, 230

Rosati, P. et al. 2009, ArXiv:0910.1716

Ruderman, J. T. & Ebeling, H. 2005, ApJ, 623, L81

Sandage, A. 1972, ApJ, 176, 21

Sandage, A., Freeman, K. C., & Stokes, N. R. 1970, ApJ, 160, 831

Santini, P. et al. 2009, ArXiv:0905.0683

Saracco, P. et al. 2001, A&A, 375, 1

Sarazin, C. L. 1988, X-ray emission from clusters of galaxies, ed. C. L. Sarazin

Schlegel, D. J., Finkbeiner, D. P., & Davis, M. 1998, ApJ, 500, 525

Schmidt, M. 1968, ApJ, 151, 393

Serjeant, S., Gruppioni, C., & Oliver, S. 2002, MNRAS, 330, 621

Seymour, N. et al. 2007, ApJS, 171, 353

Simcoe, R. A., Metzger, M. R., Small, T. A., & Araya, G. 2000, in Bulletin of the American Astronomical Society, Vol. 32, Bulletin of the American Astronomical Society, 758–+

Skrutskie, M. F. et al. 1997, in ASS Library, Vol. 210, The Impact of Large Scale Near-IR Sky Surveys, ed. F. Garzon, N. Epchtein, A. Omont, B. Burton, & P. Persi, 25–+

Skrutskie, M. F. et al. 2006, AJ, 131, 1163

Stanford, S. A., Eisenhardt, P. R., & Dickinson, M. 1998, ApJ, 492, 461

Stanford, S. A. et al. 2005, ApJ, 634, L129

Stanford, S. A. et al. 2006, ApJ, 646, L13

Staniszewski, Z. et al. 2009, ApJ, 701, 32

Stern, D., Djorgovski, S. G., Perley, R. A., de Carvalho, R. R., & Wall, J. V. 2000, AJ, 119, 1526

Stern, D., Holden, B., Stanford, S. A., & Spinrad, H. 2003, AJ, 125, 2759

Stern, D. et al. 2005, ApJ, 631, 163

Stern, D. et al. 2009, ArXiv:0907.3149

Stott, J. P., Pimbblet, K. A., Edge, A. C., Smith, G. P., & Wardlow, J. L. 2009, MNRAS, 394, 2098

Sunyaev, R. A. & Zeldovich, Y. B. 1970, Comments on Astrophysics and Space Physics, 2, 66

Sunyaev, R. A. & Zeldovich, Y. B. 1972, Comments on Astrophysics and Space Physics, 4, 173

Tanaka, M., Kodama, T., Arimoto, N., & Tanaka, I. 2006, MNRAS, 365, 1392

Tanaka, M. et al. 2005, MNRAS, 362, 268

Tanaka, M. et al. 2007, MNRAS, 377, 1206

Tanaka, M. et al. 2009, ArXiv:0909.3160

Teplitz, H. I., McLean, I. S., & Malkan, M. A. 1999, ApJ, 520, 469

Terlevich, A. I., Caldwell, N., & Bower, R. G. 2001, MNRAS, 326, 1547

Tran, K. et al. 2005, ApJ, 627, L25

Ueda, Y., Akiyama, M., Ohta, K., & Miyaji, T. 2003, ApJ, 598, 886

Vandame, B. 2004, PhD Thesis, Nice University, France

Venemans, B. P. et al. 2002, ApJ, 569, L11

Venemans, B. P. et al. 2004, A&A, 424, L17

Venemans, B. P. et al. 2005, A&A, 431, 793

Venemans, B. P. et al. 2007, A&A, 461, 823

Vikhlinin, A. et al. 2009, ApJ, 692, 1033

White, S. D. M. & Rees, M. J. 1978, MNRAS, 183, 341

Williams, R. E. et al. 1996, AJ, 112, 1335

Wilson, G. et al. 2009, ApJ, 698, 1943

Yan, L. et al. 1998, ApJ, 503, L19+

York, D. G. et al. 2000, AJ, 120, 1579

Zirm, A. W. et al. 2008, ApJ, 680, 224